University of Sheffield

INFLUENCE OF HIGH HUMIDITY ENVIRONMENT ON PERFORMANCE AND RELIABILITY OF POWER MODULES USED IN OFFSHORE WIND TURBINES

Mark Peter Sherriff

Supervised by Prof. Antonio Griffo

A thesis submitted in partial fulfilment of the requirements for the degree of

Doctor of Philosophy

Department of Electrical and Electronic Engineering

Faculty of Engineering

The University of Sheffield

May 2024

This page intentionally left blank.

For Kate, my wife,
I could not have done this without you.
As long as winds blow and rivers flow.

Thank you.

This page intentionally left blank.

Abstract

The world is reliant on growth in renewable energy generation sectors such as offshore wind to meet the ever-increasing demand for energy and facilitate the drive towards a net zero economy. The ambient environment around the power converters used in such applications poses significant reliability concerns due to the high temperatures, high humidity, and presence of corrosion-causing contaminants. Degradation mechanisms for power electronics modules with respect to temperature stress are widely studied, but the other environmental factors have only recently received significant attention. This thesis studies the impact of the high-temperature high-humidity environment on samples representative of the insulation structures found in typical high power devices. The primary encapsulant material chosen for use within high power modules is often silicone gel, a crosslinked polymer providing a strong dielectric barrier between the conductive elements, good thermal conductivity which facilitates proper cooling, and a pliant conformal nature giving way to thermal expansions of the internal components, reducing thermomechanical fatigue. The ability of this material to guard against the ingress of moisture has been called into question in recent years, prompting much research.

The humidity-driven changes in the electrical properties of the gel are measured in a configuration representative of the substrate and die attach layer. The diffusion of moisture within the gel is shown to have a significant influence on its permittivity, resistance, and dielectric loss. The dynamics agree with non-Fickian diffusion under the Langmuir model, and the rate of changes are shown to be a function of the coating thickness. Comparisons are made of the switching performances of high voltage insulated gate bipolar transistors in dry and humid environments. It is revealed that although the gel is significantly influenced by humidity, these changes are not sufficient to alter the switching behaviours in a meaningful way. Partial discharge testing is carried out on gel-encapsulated substrates taken from power modules with fast positive square pulses. Two distinct behaviours of partial discharge are observed, which are categorised by their relative amplitudes. Strong discharges do not vary with humidity and are conceptually attributed to voids within the ceramic of the substrate. Weak discharges are significantly influenced by the ambient humidity and are conceptually attributed to the gel-substrate interface known as the triple interface.

This page intentionally left blank.

Acknowledgements

A great many people have supported my PhD, to all of which I owe my deepest and most heartfelt gratitude.

Foremost are sincere thanks to my academic supervisor, Professor Antonio Griffo, whose insight into the field and guidance were invaluable during my study.

Thanks also to my industrial supervisors Dr Chunjiang Jia and Dr Chong Ng, whose experience and recommendations were greatly appreciated. I must also show my appreciation to my colleagues in the Powertrain Research Hub, without whom this PhD would not have been possible.

The University of Sheffield has been a part of my life for nearly the last decade. I have come to truly appreciate the hard work and support of my colleagues in the EEE department and EMD group. Thanks especially to Imogen Rogers and Professor David A. Stone.

My friends and family, who have had to bear with me during the preparation of this thesis, have shown endless patience and provided me with boundless support. Without them and the love, support and encouragement of my wife Kate, this thesis would have remained but a single blank page. Words cannot begin to convey the depth of my appreciation.

This page intentionally left blank.

Table of Contents

List of Acronyms

ABS	Acrylonitrile Butadiene Styrene
AC	Alternating Current
ACW	AC Withstand
AFM	Atomic Force Microscopy
AH	Absolute Humidity
Al	Aluminium
Al_2O_3	Aluminium Oxide, Alumina
AlN	Aluminium Nitride
AMB	Active Metal Brazed
ATH	Aluminium Trihydrate
$BaTiO_3$	Barium Titanate
BMRS	Balancing Mechanism and Reporting Scheme
BSF	Band-stop Filter
BSI	British Standards Institute
BW	Bandwidth
CA	Cyanoacrylate
CDF	Cumulative Distribution Function
CM	Condition Monitoring
CO_2	Carbon Dioxide
cps	Counts Per Second
cRIO	Compact RIO
DBC	Direct Bonded Copper
DC	Direct Current
DEA	Dissociative Electron Attachment
DFIG	Doubly-fed Induction Generator
DPT	Double Pulse Test
DUT	Device Under Test
ECM	Electrochemical Migration
EDS	Energy Dispersive X-ray Spectroscopy
EEDF	Electron Energy Distribution Function
EIS	Electrical Insulation System
EMC	Electromagnetic Compatibility
EMI	Electromagnetic Interference
EU	European Union
EU-27	EU 27 Member States
EV	Electric Vehicle
eV	Electron-volt
FBG	Fibre Bragg Grating
FDC	Field-dependent Conductivity
FDP	Field-dependent Permittivity
FEA	Finite Element Analysis
FS	Field Stop
FWD	Free-wheeling Diode
GaN	Gallium Nitride
GE	General Electric

GF/PA	Glass Fibre Reinforced Polyamide
GSC	Grid Side Converter
HAWT	Horizontal Axis Wind Turbine
HF	High Frequency
HFCT	High-frequency Current Transformer
HHT	Hilbert-Huang Transform
Hi-Pot	High Potential Test
HPF	High-pass Filter
HSEP	Humidity Sensitive Electric Parameter
HTV	High Temperature Vulcanising
HV	High Voltage
IC	Integrated Circuit
IDC	Interdigital Capacitor
IEA	International Energy Agency
IEC	International Electrotechnical Committee
IGBT	Insulated Gate Bipolar Transistor
IPA	Isopropyl Alcohol
IPM	Intelligent Power Module
IR	Insulation Resistance
ITU	International Telecommunications Union
LCOE	Levelized Cost of Energy
LOLE	Loss of Load Expectation
LOLP	Loss of Load Probability
LPA	Log-periodic Antenna
LSR	Liquid Silicone Rubber
MMSD	Mean of Moving Standard Deviation
MOSFET	Metal-oxide-semiconductor Field-effect Transistor
MPPT	Maximum Power Point Tracking
MSC	Machine Side Converter
NDC	Nationally Determined Contributions
NG	National Grid
NG-ESO	NG Electricity System Operator
NI	National Instruments
NIST	United States National Institute of Standards and Technology
NPT	Non Punch-through
OEM	Original Equipment Manufacturer
OFDR	Optical Frequency Domain Reflectometry
OWT	Offshore Wind Turbine
PCB	Printed Circuit Board
PD	Partial Discharge
PDDV	Partial Discharge Detection Voltage
PDEV	Partial Discharge Extinction Voltage
PDIV	Partial Discharge Inception Voltage
PDMS	Polydimethylsiloxane
PEM	Power Electronic Module
PMMA	Polymethyl Methacrylate
PMSG	Permanent Magnet Synchronous Generator
PP	Polypropylene

PPD	Primary Partial Discharge
PRPD	Phase-resolved Partial Discharge
PSH	Pumped Storage Hydro
PSU	Power Supply Unit
Pt	Platinum
PT	Punch-through
PTFE	Polytetrafluoroethylene
PVC	Polyvinyl Chloride
PWM	Pulse Width Modulation
RF	Radio Frequency
RH	Relative Humidity
RPDEV	Repeat Partial Discharge Extinction Voltage
RPDIV	Repeat Partial Discharge Inception Voltage
RTV-1	One-part Room-temperature Vulcanising Silicone Rubber
RTV-2	Two-part Room-temperature Vulcanising Silicone Rubber
SCR	Silicon-controlled Rectifier
SEM	Scanning Electron Microscopy
Si	Silicon
Si_3N_4	Silicon Nitride
SiC	Silicon Carbide
SiO_2	Silicon Dioxide
SNR	Signal-to-noise Ratio
SOA	Safe Operating Area
SPD	Secondary Partial Discharge
SPMA	Schleich Potted Monopole Antenna
SVA	Spectrum and Vector Network Analyser
TCAD	Technology Computer-aided Design
TG	Tracking Generator
TRPD	Time-resolved Partial Discharge
TSEP	Temperature Sensitive Electric Parameter
UHF	Ultra-high Frequency
UK	United Kingdom
UN	United Nations
USA	United States of America
UWB	Ultra-wideband
VHF	Very High Frequency
VNA	Vector Network Analyser
VSI	Voltage Source Inverter
VSWT	Variable-speed Wind Turbine
WBG	Wide Bandgap
WECS	Wind Energy Conversion System
WT	Wind Turbine
XLPE	Cross-linked Polyethylene

List of Figures

Nomenclature

This list of nomenclature is provided in order of symbol use, without repetition.

NOMENCLATURE

Symbol	Meaning	Unit(s)
P_m	Mechanical power	W
ρ	Air density	$kg \cdot m^{-3}$
v	Air velocity	$m \cdot s^{-1}$
K_p	Performance coefficient	—
ϑ	Pitch angle	°
λ	Turbine tip speed ratio	—
t_{GP}	Miller plateau width	s
R_G	Gate resistance	Ω
$C_{GC,av}$	Average of Miller capacitance during turn-off	F
V_{DC}	DC-link voltage	V
$V_{CE(on)}$	On-state collector-emitter voltage drop	V
I_L	Load current	A
g_m	Transconductance	S
V_{TH}	Device threshold voltage	V
RH	Relative humidity	%
P_w	Water vapour partial pressure	Pa
P_{ws}	Saturation vapour pressure	Pa
$\mathcal{A}$	Empirical constant	—
$\mathcal{B}$	Empirical constant	—
$\mathcal{C}$	Empirical constant	—
T	Temperature	$°C, K$
AH	Absolute humidity	$g \cdot m^{-3}$
m_v	Mass of water vapour in air	kg
$\mathcal{V}$	Volume of air-water mixture	m^3
R_w	Specific gas constant for water vapour	$J \cdot kg^{-1} \cdot K^{-1}$
q	Specific humidity	$g \cdot kg^{-1}$
m_g	Mass of dry air	kg
r	Mixing ratio	—
C	Electrical capacitance	F
ε_0	Permittivity of free space	$F \cdot m^{-1}$
ε_r	Relative permittivity, dielectric constant	—
A	Area	m^2
d	Distance	m
μ_0	Vacuum permeability	$H \cdot m^{-1}$
c	Speed of light	$m \cdot s^{-1}$

κ	Relative permittivity, dielectric constant	—
ε	Absolute permittivity	—
$\underline{D}$	Electric flux density	$C \cdot m^{-2}$
$\underline{E}$	Electric field strength	$V \cdot m^{-1}$
$\underline{P}$	Polarisation density of material	$C \cdot m^{-2}$
χ	Susceptibility to polarisation	—
ε_r^*	Complex relative permittivity	—
ε_r'	Real component of complex permittivity	—
ε_r''	Imaginary component of complex permittivity	—
ω	Angular frequency	rad
j	Imaginary operator	—
δ	Loss angle	rad
I	Electrical current	A
Z	Electrical impedance	Ω
θ	Phase angle	rad
R	Electrical resistance	Ω
X	Electrical reactance	Ω
Q	Quality factor	—
J	Diffusion flux	$kg \cdot m^{-2} \cdot s^{-1}$
D	Coefficient of diffusion	$m^2 \cdot s^{-1}$
c	Concentration of diffusant (usually moisture)	$kg \cdot m^{-3}$
x	Axial direction, abscissa	—
y	Axial direction, ordinate	—
z	Axial direction, applicate	—
∇	Nabla operator	—
ℓ	Length or thickness	m
M	Moisture content	%
G	Time-dependent Fickian diffusion parameter	—
M_m	Saturation moisture content of material	%
M_i	Initial moisture content of material	%
D_x	Coefficient of diffusion in x-direction	$m^2 \cdot s^{-1}$
h	Material thickness	m
s	Twice material thickness ($s = 2h$)	m
$m(t)$	Relative mass increase of material at time t	kg
m_∞	Relative saturation mass value	kg
r	Ratio of absorption	—
Δc_t	Relative moisture concentration increase at time t	—
Δc_∞	Steady-state moisture concentration	—
D_f	Coefficient of Fickian diffusion for free molecules	$m^2 \cdot s^{-1}$
c_f	Moisture concentration of free molecules	—
c_b	Moisture concentration of bound molecules	—

α	Bonding coefficient	—
β	De-bonding coefficient	—
$g(t)$	Form of Fickian diffusion model	—
ε_{mix}	Relative permittivity of mixture	—
ϕ_n	Volume fraction of constituent n	—
ε_n	Relative permittivity of constituent n	—
ε_{im}	Relative permittivity of interface medium	—
ε_t	Relative permittivity at time t	—
$\mathcal{L}(t)$	Form of Langmuir diffusion model	—
ε_∞	Relative permittivity at maximal moisture uptake	—
ε_s	Relative permittivity of dry material	—
C_{UC}	Capacitance of a unit cell	F
N	Number of unit cells	—
$K(k)$	Complete elliptic integral of the first kind	—
h	Height of trace	m
a	Trace separation	m
b	Width of unit cell	m
$AGM(p,q)$	Arithmetic geometric mean of p and q	—
σ	Electrical conductivity	$S \cdot m^{-1}$
D_0	Pre-exponential factor relating to diffusion coefficient	$m^2 \cdot s^{-1}$
E_a	Material activation energy	J
$\mathcal{R}$	Universal gas constant	$J \cdot mol^{-1} \cdot K^{-1}$
C^*_{ies}	Device input capacitance, after moisture absorption	F
C_{ies}	Device input capacitance	F
C^*_{oes}	Device output capacitance, after moisture absorption	F
C_{oes}	Device output capacitance	F
C^*_{res}	Device Miller capacitance, after absorption	F
C_{res}	Device Miller capacitance	F
L	Electrical inductance	H
V_{BD}	Breakdown voltage	V
p	Gas pressure	Pa
γ	Townsend secondary ionisation coefficient	—
w	Electron population energy	eV
E_i	Field strength for partial discharge inception	$V \cdot m^{-1}$
V_{PDIV}	Partial discharge inception voltage	V
t_r	Pulse rise time	s

This page intentionally left blank.

Chapter 1: Introduction

1.1 Motivation

In 2022, the United Nations (UN) reported that the global human population reached 7.9 billion people, with projections of 8.5 billion by 2030, and 9.6 billion by 2050 [1]. Since the second industrial revolution, electrification of almost all aspects of life has been on the rise, with global electrification rates reaching 89% in 2019 [2]. For most developed nations this is 100%, and reliable access to electricity is a fundamental part of the workings of modern societies and economies. The demand for electrical energy is anticipated to increase by an average of 3.4% annually through to 2026 [3], with most (85%) of the additional demand coming from outside advanced economies.

Traditionally, coal, oil and natural gas were the primary fuel sources for energy generation, and modern understanding of the negative impact that these fossil fuels can have on the environment is a major driver of change to alternative sources [4]. Fossil fuels are recognised as a principal carbon dioxide (CO_2) emission source [5], and are hence a major contributor to the global climate crisis. This is leading to: raising global sea levels [6], which threatens many businesses and lives; reduced water quality [6], [7], [8]; unpredictable and inclement weather [9]; and significant deforestation from ever increasing global temperatures [10].

Many policies and agreements are being signed the world over, committing to action on this front. The Paris Agreement is an international treaty dedicated to combatting climate change, and was signed in 2015 by 196 national Parties including the G20 [11]. It put forth a plan to reduce global emissions by way of nationally determined contributions (NDCs) on a five-year cycle. An initiative called Mission 2020 was launched in April of that year, and using data from 2017 [12] gathered by the Global Carbon Project recognises a so-called "Carbon Crunch" – a budget of 600 Gt of CO_2 remained until the planet is warmed to dangerous levels, a rise of 1.5–2 °C. Limiting global warming to 1.5 °C is increasingly more difficult, but not impossible, according to the International Energy Agency (IEA) in their 2023 outlook [13]. Bloomberg NEF also reported that 2020 was tied with 2016 as the "warmest year on record" [14]. A report produced by the Potsdam Institute of Climate Impact Research called for 2020

to be the 'peak' of global emissions, highlighting that not only is a shift towards renewable energy generation desirable and in fact necessary, it is already well underway [15].

In 2021, a report published by Agora Energiewende and Ember showed that renewable energy generation in the EU-27 (the 27 European Union, EU, member states after the UK left in 2020) overtook fossil fuels in terms of percentage share of generation for the first time [16] (38% of gross energy generation from renewables versus 37% from fossil fuels). The United States of America (USA) is also increasing renewable energy generation, with net installed capacity reaching 284 GW in 2020 [17], a notable increase from 114 GW in 2000 [18]. Renewable energy generation encompasses a wide array of generation sources such as solar photovoltaic (PV), wind, bioenergy, hydropower and geothermal. According to a report in 2020 by the IEA, wind energy was expected to increase the most in terms of absolute generation capacity among renewables [19]. According to Energy Dashboard, which presents data from the Elexon Balancing Mechanism and Reporting Scheme (BMRS) and National Grid Electricity System Operator (ESO), generation from wind sources in the United Kingdom (UK) is increasing steadily year on year. A total of 64 TWh, 79 TWh, and 81 TWh of electrical energy was generated by wind sources in 2021, 2022 and 2023, respectively (1st January to 31st December). Over the period 01/05/23 to 01/05/24, a total of 84 TWh was generated, accounting for 29.8% of the annual generation mix [20]. The full electricity generation mix for this period is presented in Fig. 1.1.

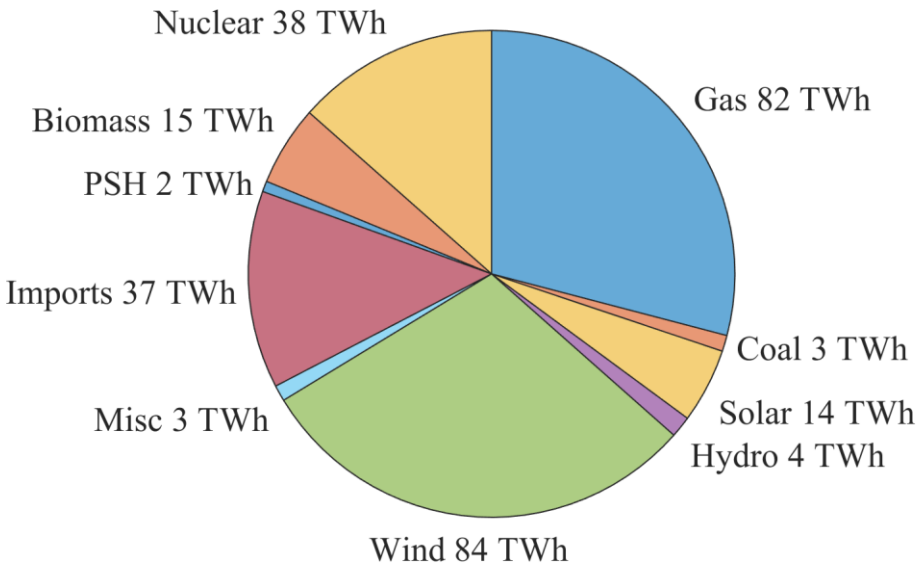

Fig. 1.1 UK energy generation mix from 01/05/23 to 01/05/24. Data obtained from Energy Dashboard [20]. PSH is pumped storage hydro. Reported total generation 282 TWh.

Wind energy generation is a core component in meeting the UK's net zero emissions target of 2050. Offshore wind is seeing significant growth, accounting for 17.4% of all electricity generated in the UK in 2023 [21]. The 2022 British Energy Security Strategy sets out a desired 50 GW of installed generation capacity from offshore wind by 2030. The current installed capacity is 14.67 GW, second globally only to China, and will require an estimated £50 billion in investment in the sector to meet the ambitious 2030 targets [21], [22]. The installed capacity of onshore and offshore wind is shown in Fig. 1.2, alongside total annual electricity generation from each source, showing that significant investment in the sector is required. A key facet in the success of the sector is the evaluation and understanding of the reliability of offshore wind turbines (OWTs) and the components that constitute them. In 2011, a questionnaire survey put to semiconductor manufacturers and professionals across other sectors such as aerospace, automotive and utility power, identified power semiconductor devices as the most fragile component in the field of power electronics [23]. More recently in 2019, a large-scale study covering ~7,400 years of operating data across many wind turbine (WT) manufacturers and constructions in both onshore and offshore scenarios globally, highlighted the phase-module components of WTs as the largest contributor to failures in WTs [24]. Phase-module components include: the power electronic module (PEM), usually insulated gate bipolar transistors (IGBTs); associated driver boards; DC-link

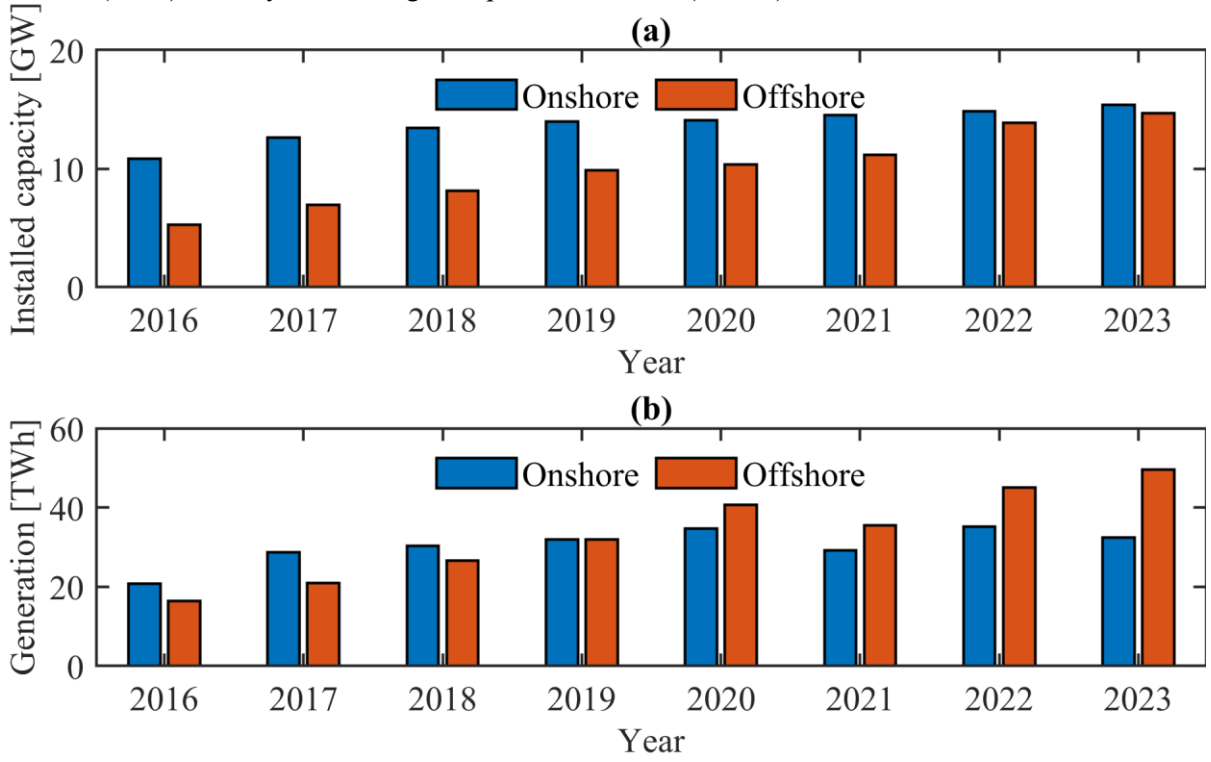

Fig. 1.2 UK wind energy metrics in period 2016–2023. (a) Installed capacity, (b) annual electricity generated from wind sources. Data provided by UK Department for Energy Security & Net Zero [21].

capacitors; and connection busbars. These failures contribute to the increase in the levelized cost of energy (LCOE) experienced by consumers, in part due to costly maintenance and repair works which are only exacerbated by the difficulty of these operations in offshore environments. The same authors later concluded that a considerable degree of studied failures could be attributed to environmental factors including humidity, rather than thermally-induced degradation mechanisms. This was followed up in 2021, where clear seasonal patterns in failures were observed, concluding that the climate inside converter cabinets played a key role in the failures of phase modules [25]. Last year the authors further confirmed humidity about converters as a statistically likely failure driver [26]. OWT system reliability is paramount to consumers, original equipment manufacturers (OEMs) and energy suppliers. Increasing system robustness depends on understanding the influence of harsh environments including humidity on the phase-module components.

1.2 Scope and Aim of the Thesis

This thesis aims to build on the body of pre-existing work in the field of PEM reliability to aid in reliability-oriented WT converter designs and provide a platform on which future humidity-robust module designs can be based. The scope is limited to the influence of humidity on the performance and reliability of existing IGBT modules used in OWT installations. This is due to the frequency of their failure relative to other components in the OWT structure, and the thoroughly acknowledged detriment of high humidity environments on their lifetime. Modules in aerospace applications, electric vehicles and grid tie inverters may also experience harsh environments. However, this work acknowledges the support of its industrial sponsors and chooses to focus solely on the offshore wind application. Three main questions are asked in this thesis, which are addressed in turn by the experiment chapters (3–5):

i. How are the electrical properties of the primary encapsulant within power IGBTs influenced by a harsh environment consisting of high-temperature and high-humidity?
ii. Do these changes in the electrical properties of the gel cause any significant barrier or limitation on operation of IGBTs in a hard-switching scenario representative of use in OWTs?
iii. Is the behaviour of partial discharge (PD) on power module substrates exacerbated in any meaningful way due to the absorption of moisture within the encapsulant gel?

1.3 Contribution

The contributions this thesis makes to the field of PEM operation and reliability in harsh environment conditions are summarised below, corresponding to each major experiment chapter.

Chapter 3: Impact of High Humidity Environment on Electrical Properties of Silicone Gel Used for Power Module Encapsulation

- Confirms the negligible influence of temperature increase on the electrical properties of silicone gel encapsulation used in power modules, in the temperature range 20–90 °C.
- Evaluates the limited influence of a high-humidity low-temperature condition on the electrical properties of silicone gel power module encapsulant in the range 30–90% relative humidity (RH).
- Validates the permittivity increase at the bottom of a silicone gel mass, commensurate with die attach region of IGBT, due to moisture absorption in a high-temperature high-humidity environment.
- Demonstrates recoverability of electrical property change in silicone gel due to high-temperature high-humidity environment, when the environmental stress is removed.
- Establishes a firm case for the modelling of moisture transport through silicone gels using Langmuir-type diffusion rather than Fickian, which is currently the predominant model used in the literature.
- Highlights that the orientation of power modules is likely to influence moisture absorption timescales in the short term, which could be utilised in reliability-oriented converter designs for use in OWTs.

Chapter 4: Short-Term Influence of Humid Environment on Performance of IGBT Power Modules

- Shows the limited increase in IGBT device input capacitance cause by the absorption of moisture within the encapsulating dielectric gel via simulation and practical measurements under bias.

- Increases the operational confidence for the use of power modules in high-temperature high-humidity conditions by demonstrating negligible impact of moisture on hard switching performance, with double pulse testing.
- Reveals the potential of increased ringing and reduced electromagnetic compatibility (EMC) of power modules when operating in high-humidity environments.

Chapter 5: Partial Discharge Characteristics of Power Module Substrates Under High Humidity

- Highlights a need for improved reliability test standards for modern IGBTs considering test voltages representative of field operation, in harsh environments.
- Establishes a link between moisture infiltration into power modules with an increasing quantity of PD, which could potentially reduce insulation quality in the gel over time due to the dissociative electron attachment (DEA) process.
- Identifies two distinct behaviours of PD, which are attributed to physical location on the power module substrate. The behaviour of stronger discharges does not vary with humidity and are ascribed to the ceramic portion of the substrate. The weaker discharges are influenced by the absorption of moisture within the gel and are hence expected to occur therein.
- Explores the limited applicability of traditional electrostatic simulation methods for PD modelling used for PD mitigation, which typically involve reduction of the electric field strength at the triple interface. Although useful in most cases, this approach is unable to adequately capture the influence of moisture on PD dynamics.

1.4 Publications and Outputs

i. Journal publications

M. Sherriff, A. Griffo, C. Jia, C. Ng, Z. -Q. Zhu and D. A. Stone, "Partial Discharge in Silicone Gel on Power Module Substrates in High-Humidity Conditions," in *IEEE Transactions on Dielectrics and Electrical Insulation*, 2024, doi: 10.1109/TDEI.2024.3404367.

ii. Conference proceedings

M. Sherriff, A. Griffo, C. Jia, and C. Ng, "Investigation of the Impact of Temperature and Humidity on the Capacitance of Dielectric Gel Used for Power Electronics," in *11th International Conference on Power Electronics, Machines and Drives (PEMD 2022)*, 2022, pp. 91–96. doi: 10.1049/icp.2022.1023.

iii. Other

M. Sherriff, A. Griffo, C. Jia, and C. Ng, "Influence of High Humidity Environment on Partial Discharge Behaviours of Silicone Gel Encapsulated Power Module Substrates,"

Poster presentation at *Centre for Power Electronics (CPE 2024)*, 2024.

M. Sherriff, A. Griffo, C. Jia, and C. Ng, "Partial Discharge in Silicone Gel on Power Module Substrates in High-Humidity Conditions,"

Poster presentation at *Centre for Power Electronics (CPE 2023)*, 2023.

Awarded 2nd place poster prize for early career researchers.

M. Sherriff, A. Griffo, C. Jia, and C. Ng, "Investigation of the Impact of Temperature and Humidity on the Capacitance of Dielectric Gel Used for Power Electronics,"

Oral presentation at *IMAPS-UK iPower 4 Conference*, 2022.

M. Sherriff, A. Griffo, C. Jia, and C. Ng, "Investigations of Silicone Gel Used for Power Modules in Harsh Environment Operation,"

Poster presentation at *Centre for Power Electronics (CPE 2022)*, 2022.

Awarded 2nd place poster prize for early career researchers.

1.5 Thesis Outline

The thesis is organised into six chapters as follows:

i. Introduction

This chapter sets the context of the thesis, explaining current and future trends in electrical energy generation, the increase in demand due to increased electrification and population growth. It highlights the core focus for the thesis, which is the relative unknown quantity that is the reduced performance and reliability of PEMs due to the harsh environments typical of OWT applications. It also highlights the contributions made by the thesis, publications and outputs arising from the work herein, and gives a brief overview of the structure.

ii. Background, Theory and Literature

A solid foundation for the concepts explored in the thesis is provided in this chapter. It explains the necessary theoretical background for the experiments carried out. By discussing the current state of the art in the field of PEM reliability, with a specific focus on humidity robustness, gaps in the field are established, which this work aims to explore.

iii. Impact of High Humidity Environment on Silicone Gel Used for Power Module Encapsulation

The change due to ambient environment in the electrical properties of silicone gel, the primary encapsulant material used in high voltage (HV) PEMs, is studied extensively in this chapter. Experiments subject cured gel samples to a variety of environmental stresses with varying temperature-only, humidity-only, and combined temperature and humidity conditions. Gel electrical property changes are evaluated based on measurements taken of interdigital capacitor (IDC) sensors placed beneath the cured gel. Results confidently indicate the strong influence of absorbed moisture on electrical properties. The influence of gel thickness as a barrier to moisture ingress is discussed, and relative permittivity results are presented in the context of common diffusion models. Additionally, the orientation of samples representative of PEMs is shown to influence moisture absorption dynamics, highlighting a potential for improvements in humidity-robust converter designs.

iv. Short-term Influence of Humid Environment on Performance of IGBT Power Modules

This chapter explores a notable gap in the current body of work in the field, aiming to ascertain the influence of humid environments on the performance of HV-IGBT modules. This is done by first evaluating module input capacitance (the sum of the gate-to-emitter and gate-to-collector parasitic capacitances, measured at the device terminals) as a salient parameter, and then by measurement of switching performance over time in a high-temperature high-humidity environment using the industry standard double pulse test (DPT). The results indicate that although humidity absorbed by the gel causes a slight increase in input capacitance, the hard switching behaviour of modules is largely unaffected. A notable increase in gate-emitter voltage oscillation is observed, however, raising concerns about spurious switching and EMC.

v. Partial Discharge Characteristics of Gel Encapsulated Power Module Substrates Under High Humidity

Building on the previous two experimental chapters which addressed the properties of the gel and performance of modules in high-temperature high-humidity conditions respectively, this chapter aims to address the question of module reliability. An extensive series of experiments are performed on direct bonded copper (DBC) substrates taken from real PEMs and encapsulated in fresh silicone gel. These experiments subject the samples to HV pulses representative of hard switching in the OWT converter application, and studies the characteristics of the ensuing PD. Two PD categories are identified, which based on their changing behaviour (or lack thereof) when subjected to the high humidity environment, are attributed to different locations on the DBC substrate.

vi. Conclusions and Future Work

This chapter summarises the experimental results, placing them into the wider context of the research field. The key findings are reiterated and used to comment on potential avenues for future research, with the intent of improving PEM reliability and robustness for OWT converter operation.

Chapter 2: Background, Theory and Literature

This chapter provides a foundation for the concepts explored in the thesis, and explains the necessary theoretical background required to understand the experiments that are performed within it. It offers a brief history of the IGBT and explains its role in wind energy conversion systems (WECS). By discussing the current state of the art in the field of PEM reliability with a specific focus on humidity robustness, vital gaps in the field are identified. These open avenues of research will provide a clearer understanding of the influence of humidity on PEMs in use in WECS today.

2.1 Role of Power Modules in Wind Energy Conversion Systems

The primary purpose of a typical WECS is to harness the free and inexhaustible power of wind currents, which are converted into electrical power by way of a generator. Primarily, variable-speed WTs (VSWTs) are used for the large-power installations that make up the lion's share of offshore wind energy generation, facilitating easier grid interconnection and compliance and providing higher power output than fixed-speed alternatives [27]. The preferred axis orientation for large-scale generation has long been a horizontal axis WT (HAWT) [28], for which the mechanical wind power captured by the turbine blades and provided to the generator can be given by (1) [29]:

$$P_m = \frac{1}{2} \cdot \rho \cdot A \cdot v^3 \cdot K_p(\vartheta, \lambda) \qquad [W] \quad (1)$$

where P_m is the mechanical power input to the generator; ρ is the air density about the turbine blades, in kg·m^{-3}; A is the area the blades cover during rotation, called the 'swept area', in m^2; v is the velocity of the air moving through the swept area, in m·s^{-1}; and K_p is the performance coefficient (C_p in [29] and generally, changed in this work to avoid confusion) of the turbine blade, which is a function of the pitch angle ϑ, in degrees, and the tip speed ratio λ.

Blade pitch angle is adjusted to achieve the desired performance coefficient by the pitch actuators at the base of each blade; generally this is done as part of a maximum power point tracking (MPPT) scheme [30]. The swept area is one of the key drivers behind the ever increasing size of WTs, with General Electric (GE) producing 14 MW turbines with 107 m blades planned to be fully operational in Dogger Bank C in the North Sea off the English coast by 2026 [31], [32]. Recent prototypes for 15 MW

turbines and concepts for 22 MW turbines have also been shown, with 236 m and 310 m rotor diameters, respectively, requiring further increases to hub heights [33], [34]. Increased hub height of WTs has been shown to be an important parameter for both WT power output and failure rate [35]. Although increased hub heights are linked to more frequent failures, the added power output afforded more than offsets the negatives in terms of overall system reliability metrics such as loss of load probability (LOLP) and loss of load expectation (LOLE). Nevertheless, reducing failure rates is a primary focus of WECS research to date. A diagram of the geometric parameters of a typical WT is provided in Fig. 2.1, alongside the primary construction components (Fig. 2.1(b)).

To facilitate variable speed operation and ensure correct and safe connection to the grid, all VSWTs require some form of power converter. Two of the most prevalent three-phase generator topologies used in offshore WECS are the permanent-magnet synchronous generator (PMSG) and the doubly-fed induction generator (DFIG). In configurations utilising the PMSG, a full-scale power converter is required to provide the necessary speed control for the turbine and perform appropriate conversion to meet grid compliance. As converters in this configuration are required to handle the full load, the power electronics involved are required to have higher ratings, which comes with added cost [36]. In

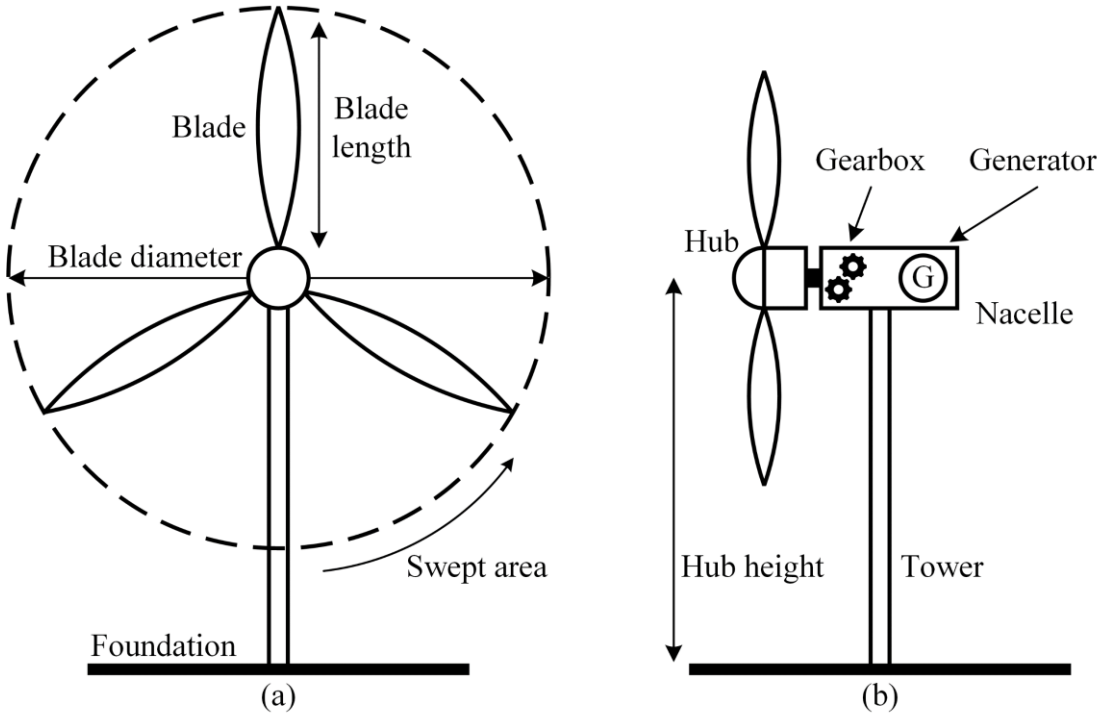

Fig. 2.1 Diagram of a typical HAWT. (a) face-on, showing blade diameter, blade length and swept area; (b) side-on, showing nacelle components and hub height. Based on [29].

configurations including the DFIG, the stator of the generator is tied directly to the grid and speed control is primarily performed via gearing. The rotor frequency and current are further controlled by an attached power converter, which handles approximately 30% of the power of the generator. This reduced rating provides the ability to use smaller, individual power electronics components but can come at the expense of lower grid fault tolerance [36]. Nevertheless, although the DFIG has traditionally been the dominating topology for WECS [37], the market share is becoming increasingly more diverse considering WT architectures [27], [38]. Diagrams of the PMSG and DFIG architecture are provided in Fig. 2.2. Regardless of the choice of architecture, the inclusion of power electronics is unavoidable due to their critical role in the generation powertrain. Most architectures utilise a combination of back-to-back power converters with a combination of active braking, choppers, and snubbers to ensure PEMs are kept within their safe operating area (SOA). A 2019 study of WT failures using data from 2003–2017 found no significant bias towards failures in either the machine side converter (MSC), or the grid side converter (GSC) [24]. The authors note that if the observed failures were purely due to thermal

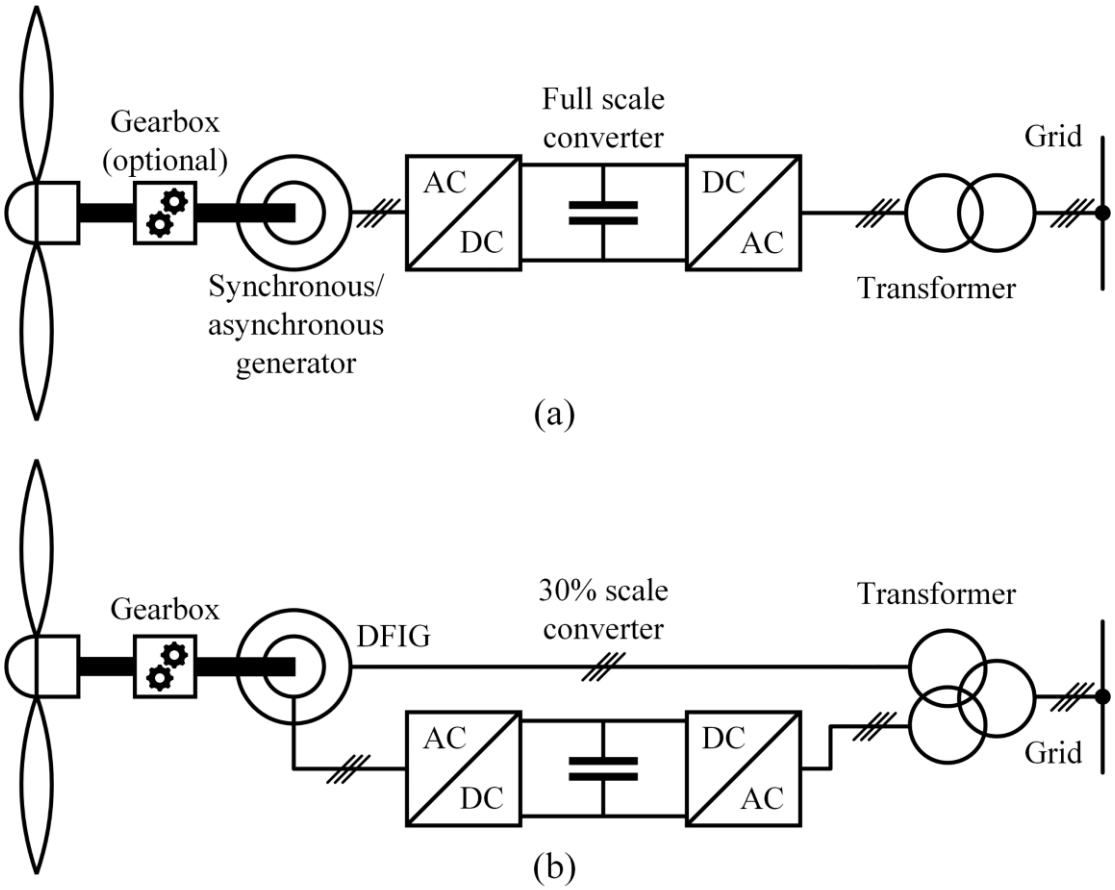

Fig. 2.2 Common WT architectures. (a) PMSG topology with full-scale power converter, (b) DFIG topology with 30% scale power converter. Based on [27], [37].

cycles and the ensuing fatigue of related components, the distribution of failures would lean more heavily towards the MSC due lower switching frequencies compared to the GSC. Instead, the authors attributed failures to seasonal variation of the ambient environment. The typical structure of a two-level voltage source converter (VSC) as is commonly utilised in WT generation architectures is shown in Fig. 2.3 [24]. This topology was identified as the prevailing choice in WTs as of 2019 and utilises an MSC and GSC in a back-to-back configuration [24]. Each IGBT-diode-pair shown represents many such devices in parallel as required to handle the rated WT power. In most cases, the converter is also used in conjunction with grid- and machine-side harmonic filters, choppers, and snubbers. These help to improve the performance of the converter as a whole and ensure that devices are kept within their respective SOAs.

Inside the nacelle of an OWT, the ambient environment can vary significantly. The converter microclimate can closely match the external macroclimate, ranging between 3.3–82% RH and 15.2–45.9 °C according to reported field measurements [39]. Dehumidification of the converter cabinet alongside temperature regulation are the prevailing environmental control methodologies [40], but these approaches introduce additional costs. During long-term idle or dormant periods with no electrical load

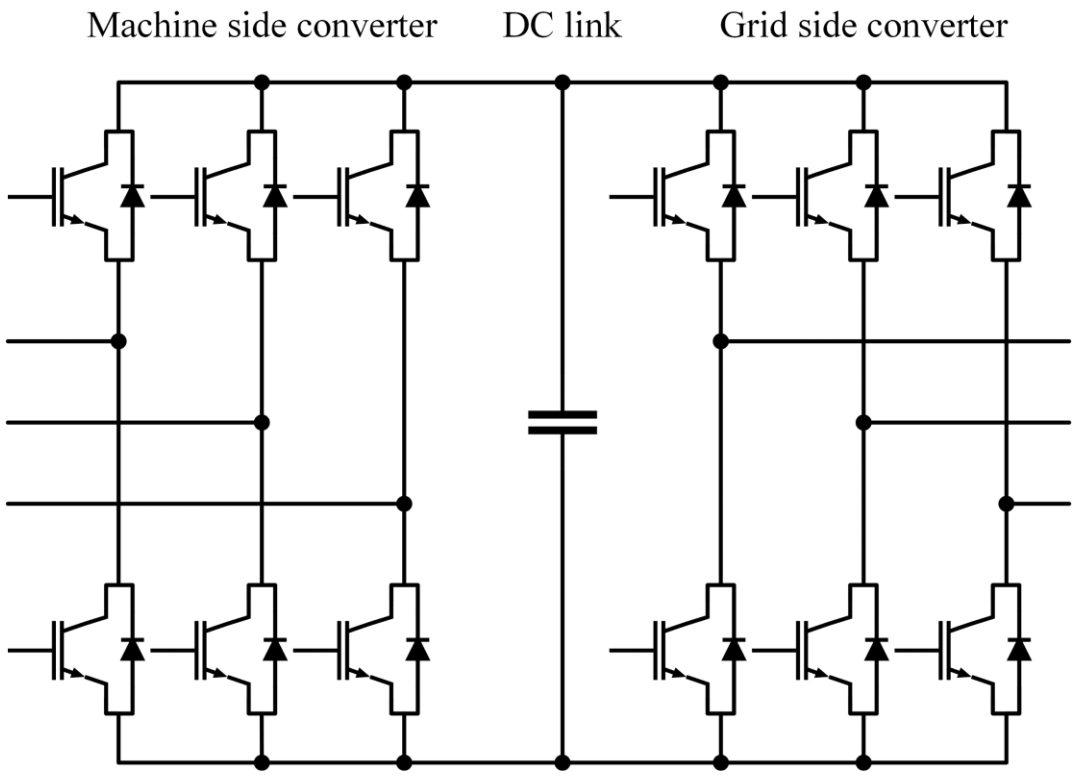

Fig. 2.3 Two-level converter as is commonly used in WTs, based on [24].

moisture pervades the module insulation causing degradation. Consequently, a considerable proportion of converter failures are observed when starting after these conditions [39]. Manufacturer guidance highlights procedures involving preliminary heating of the converter cabinet to drive off moisture [41], but seasonal variations in converter failures are still observed [24]. Qualification of modules for harsh environment operation is performed via industry standard testing such as the high humidity high temperature reverse bias test (H3TRB) [42]. These are discussed in detail in § 2.5.

2.2 A Brief History of the Insulated Gate Bipolar Transistor

Power devices have been used in WT-based generation since the early 1970s, when diode bridges and silicon-controlled rectifiers (SCRs) were used to facilitate variable-speed operation of large scale WTs with AC grid interconnection [43]. The IGBT itself was first shown by Baliga in 1979 and then in the early 1980s alongside other authors [44], [45], [46], and reached markets in 1983 [47]. Offering faster switching speeds for power applications than alternatives at the time [48], the IGBT saw significant adoption across many sectors of power electronics, but mainly in high-power applications such as traction, industry, and generation [47]. Since then, significant improvements have been made to the IGBT structure, allowing for smaller chip sizes, improved thermal reliability and reduced switching losses [49]. These are granted by use of the field-stop IGBT (FS-IGBT) cell structure, explained in the next section, and from improved thermal management from more recent packaging and interconnection technologies. Currently, a wide array of ratings are available for IGBT devices, with regular commercial availability in the 600–6500 V range, with current ratings up to thousands of amps [50]. This affords engineers the opportunity to tailor device choices to the target application, reducing capital expenditure and overheads.

Recent developments with wide bandgap (WBG) devices provide competition across the board for the mature silicon-based IGBT. Silicon carbide (SiC) metal-oxide-semiconductor field-effect transistors (MOSFETs) and gallium nitride (GaN) devices now offer increased switching speeds, reduced losses and improved thermal performance when compared with silicon (Si) [49], [51] in the $\geq$1200 V and <1200 V ranges, respectively.

The complexity of gate drive design is a limitation holding back the widespread adoption of GaN devices, with the difficulty of maintaining proper charge on high side bootstrap capacitors resulting in more sophisticated drives [52]. Additionally, the unavoidable performance degrading presence of package-related parasitics is yet a confounding factor, leading to monolithic integrated circuit (IC) approaches [53]. These limit the benefits gained by utilising GaN, with recent works in this field showing promise [52], [53]. Nevertheless, these alternatives are not yet mature and hence involve increased upfront costs, which make the established Si-IGBT still an attractive and affordable choice in many applications. Comparisons between the performance in terms of output and LCOE for Si-IGBT and SiC-MOSFET-based WT systems are still ongoing [54], but the industry has not yet seen widespread adoption of WBG devices for use in WECS. Consequently, there are many OWT fleets both operational and in commissioning that are based on IGBT platforms.

2.3 Structure of Modern IGBT Power Modules

Modern high power IGBT modules typically consist of multiple individual IGBT dies arranged in configurations that enable the many extant converter topologies. The dies are generally mounted together with requisite free-wheeling diodes (FWDs) on a common substrate, either DBC or active metal brazed (AMB), depending on performance requirements, and connected with aluminium bond wires. For high current ratings (≥100 A), several such 'rafts' may be connected in parallel, as is seen in the decapsulated Infineon FF1000R17IE4 half-bridge module shown in Fig. 2.4, which has a continuous current rating of 1 kA. Many configurations of IGBT modules, as well as discrete devices, are commercially available to suit user requirements, such as: booster modules incorporating SiC Schottky diodes, chopper circuits, three-level neutral point clamped (NPC) circuits, single half bridges, and two-pack, four-pack, six-pack and twelve-pack half bridge configurations [50].

The conventional epitaxial structure at the single-cell die level of a traditional vertical IGBT is shown in Fig. 2.5, demonstrating the punch-through (PT) construction, so called due to the electric field 'punching through' the drift region to the buffer layer. The conventional structure is akin to a vertical MOSFET but uses a p^+ substrate, which forms a pn junction with the following n^+ buffer epilayer and injects minority carriers into the drift region [47]. The gate terminal is insulated from the rest of the

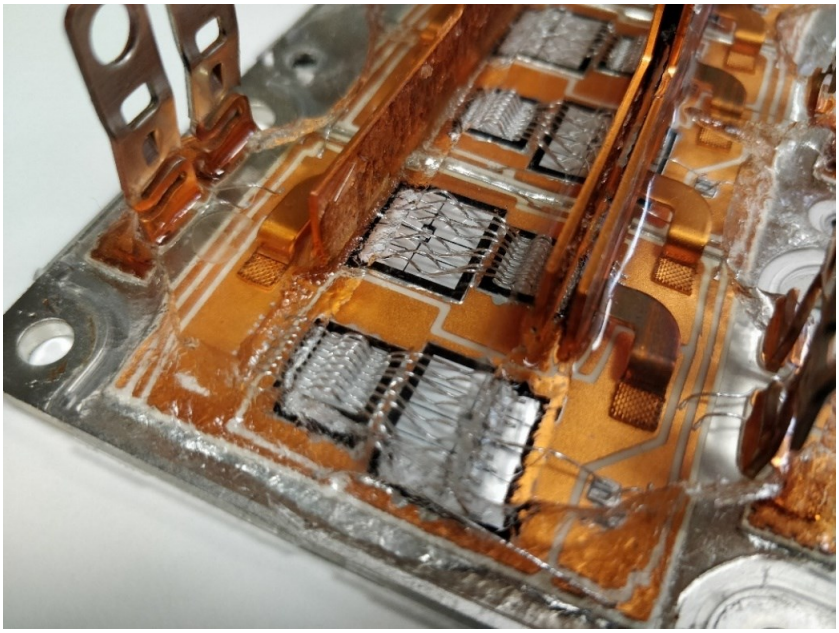

Fig. 2.4 Portion of a decapsulated IGBT half-bridge module. Model is FF1000R17IE4, manufactured by Infineon. Ratings: 1.7 kV, 1 kA.

device using a dielectric layer, the gate oxide, usually fabricated from silicon dioxide (SiO2). In the non-PT (NPT) construction, the manufacturing is performed via diffusion processes which can be less expensive. In NPT-IGBTs a thicker n^- drift region is used, fully containing the depletion region under the maximum allowable electric field. This allows the removal of the n^+ buffer layer, and the p^+ substrate thickness can also be reduced.

Most NPT-IGBTs generally provide lower switching losses and better ruggedness to short circuit failure but have a higher on-state voltage drop ($V_{CE(sat)}$, also $V_{CE(on)}$) than PT-IGBTs due to the thicker n^- layer, potentially resulting in higher on-state losses. NPT-IGBTs do not require the implementation

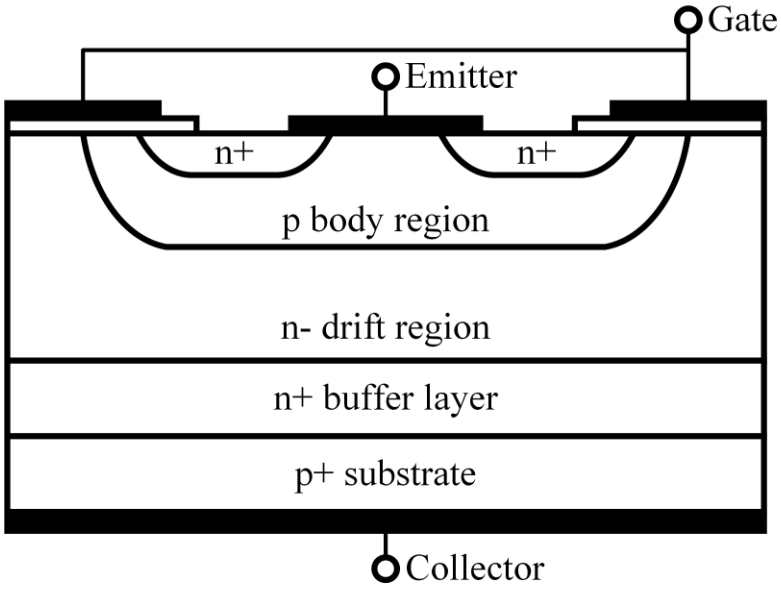

Fig. 2.5 Vertical epitaxial cross section structure of a traditional PT-IGBT, based on [47].

lifetime killing techniques in the n^- base layer unlike PT-IGBTs, which more easily provides reduced turn-off times, potentially mitigating switching losses over the turn-off interval. Over time there have been many improvements to the IGBT structure such as field stop (FS), trench gate and trench stop IGBTs, but the underlying structure is generally similar. In a FS-IGBT, an n-doped FS layer is implanted between the n^- drift layer and the now very thin p^+ substrate, allowing the base region to be thinner still, and further reducing $V_{CE(sat)}$. Most modern HV-IGBTs are of the trench gate FS (also called trench stop) construction, wherein the gate structures are placed within trenches etched through the body region and into the drift region, a simplified diagram of which is shown in Fig. 2.6 [55], [56]. This provides further reduced switching losses and $V_{CE(sat)}$, as well as reduced Miller capacitance, C_{res}, due to the reduced width of the gate. An exhaustive overview of the various IGBT constructions, their advantages, disadvantages, and most suitable applications is beyond the scope of this thesis. The brief overview given here is intended mainly as reference and to highlight the ever-increasing complexity of these devices, while bringing potentially unintended coupled parasitics due to packaging more and more into the spotlight. Outside of the chip structure, PEM layout design and optimisation generally focuses on reducing parasitic inductance and improving thermal conductivity, as these are the most salient factors impacting proper operation and reliability of the power converter.

A simplified model of a typical IGBT including parasitics is shown in Fig. 2.7. Parasitic inductances are especially a growing concern for ever increasing dv/dt requirements for modern converter

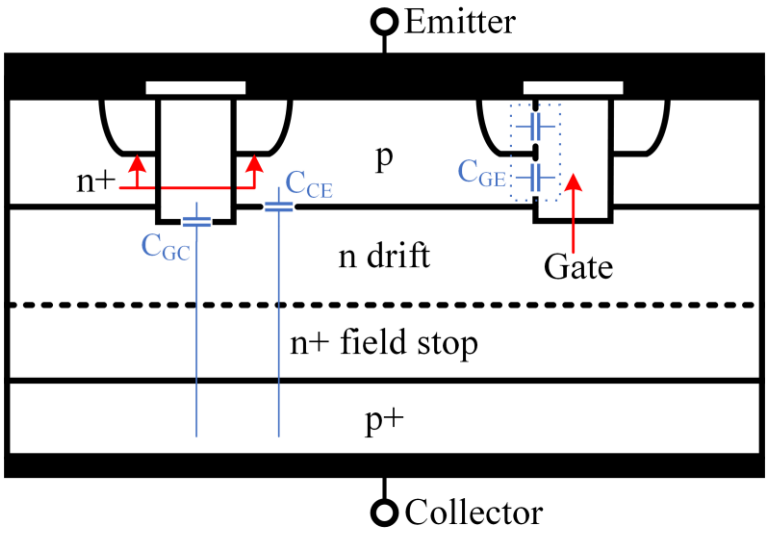

Fig. 2.6 Vertical epitaxial cross section structure of a modern trench stop IGBT. Parasitic capacitances related to the chip structure are shown in blue font face. Based on [55], [56].

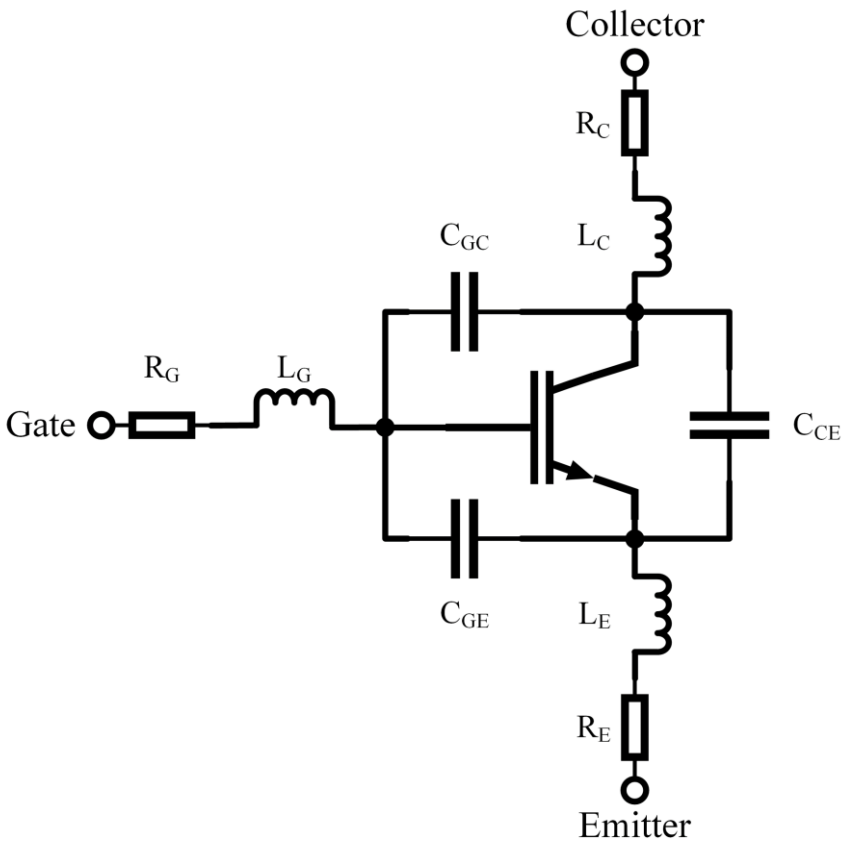

Fig. 2.7 Model of IGBT including die capacitances, terminal and lead parasitic inductances and resistances.

solutions and can cause significant switching oscillation, radiated EMI, and elevated electrical stress. The parasitic inductances are primarily caused by the bond wires required to connect the chips, the length of the copper pads of the DBC and the connection busbar terminals themselves. These busbar and bond wire connections, as well as the silicone structure, also provide small parasitic resistances. On the gate side, the parasitic gate inductance L_G can cause unintended switching of the device when oscillations are present that exceed the device threshold voltage, $V_{GE(th)}$. In combination with the internal gate resistance R_G, slight variations in the bond wire lengths for multi-chip modules can cause minute changes in the respective turn-on times of each chip due to the individual differences in L_G. This can result in improper load sharing between the chips, causing increased electrical stress which damages the module over time, and limiting the module's reliability. The parasitic emitter inductance L_E serves to lengthen the turn-off time of the device by reducing the voltage applied to the gate, due to the reducing collector current. The package stray inductances may also cause peaks during the switching intervals which may place the device operation outside its SOA [47].

The typical dynamic capacitance behaviours of a standard IGBT are shown in representative terms in Fig. 2.8. The input capacitance (C_{ies}) of the device is the sum of the gate-emitter (C_{GE}) and gate-collector (C_{GC}) capacitances, and together with L_G, limits the bandwidth (BW) of the device to the gate drive signals. To allow the device to begin to turn on, C_{ies} must first be charged to $V_{GE(th)}$, and for turn-off this must be discharged to the plateau, or Miller, voltage V_{GEP}. Consequently, an increase in the drive impedance or the input capacitance causes longer switching delays. The output capacitance (C_{oes}) of the device is the sum of C_{GC} and the collector-emitter capacitance (C_{CE}). This is a critical parameter for soft switching applications as it influences circuit resonant behaviours. Finally, the Miller capacitance, also called the reverse transfer capacitance C_{res}, is equal to C_{GC}. As C_{GC} forms part of the input capacitance, the reverse transfer capacitance also plays a major role in switching delays. Increases in either C_{GE} or C_{GC} increase the turn-on and turn-off delay times and limit the slew rate of the current through the device, di_c/dt, causing slower switching. In particular, C_{GC} is a factor in the Miller plateau width according to (2) [57]:

$$t_{GP} = \frac{R_G \cdot C_{GC,av} \cdot \left(V_{DC} - V_{CE(on)}\right)}{\frac{I_L}{g_m} + V_{TH}} \tag{2}$$

where t_{GP} is the Miller plateau width, in s; $C_{GC,av}$ is the average value of the reverse transfer capacitance during turn-off, in F; V_{DC} is the applied DC-link voltage, in V; $V_{CE(on)}$ is the on-state voltage

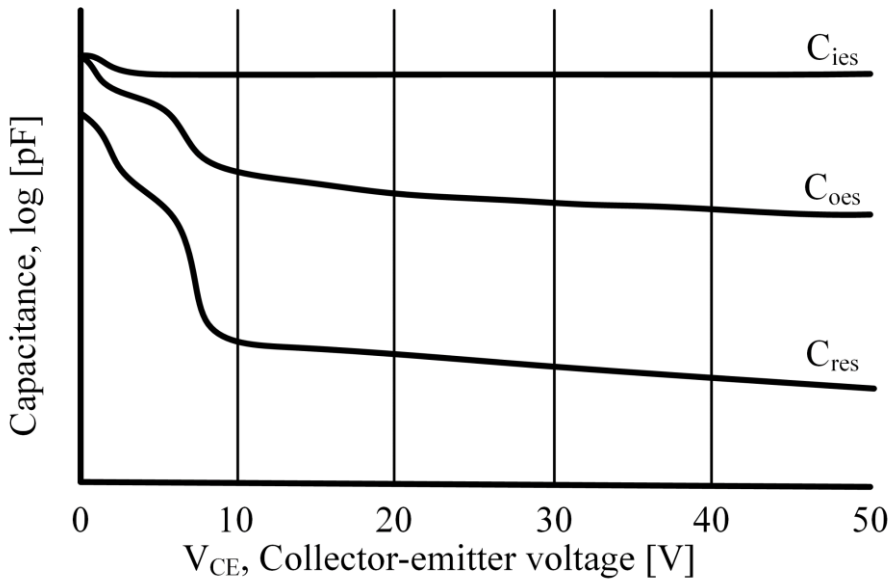

Fig. 2.8 Representative typical dynamic capacitance behaviours of an IGBT, based on [55].

drop across the device, in V; I_L is the load current through the device during conduction until turn-off, in A; g_m is the device transconductance, in S; and V_{TH} is the threshold voltage of the device, in V.

In [57], this relation is used to estimate the junction temperature of an IGBT during operation, proposing the use of t_{GP} as a new temperature sensitive electric parameter (TSEP) for use in online condition monitoring (CM). TSEPs are commonly used to estimate the junction temperature of devices, which is a critical part of CM and reliability metrics [58]. The switching intervals of the IGBT are dominated by internal parasitics, package parasitics, and parasitics in the external circuitry such as the drive arrangement. Reduced switching speeds could result in increased switching losses within the devices, leading to reliability concerns due to elevated junction temperatures. The IGBT die parasitic capacitances as quoted in most datasheets are specified in terms of the typical characterisation configuration, and under a specific collector-emitter bias (V_{CE}). This is due to the dynamic behaviour of these capacitances depending on the applied bias, generally reducing steeply (less so in the case of C_{ies}) until about $V_{CE} = 10\ V$, and then continuing to reduce at a significantly slower rate until up to several hundreds of volts, depending on the device. Manufacturer datasheets for HV-IGBTs typically state device capacitances at $V_{CE} = 25\ V$, due to the relative lack of further variation beyond this point.

Most PEMs are packaged with the bare dies supported by a substrate or lead frame for the purposes of ease of manufacture and distribution of the thermal loads under operation. These substrates are usually placed on baseplates which further thermally interface with heatsinks and cooling systems, with the entire system providing a low thermal resistance pathway to allow for efficient cooling of the module. This helps avoid thermal stresses within the module, and mitigates junction temperature increase, which is a significant parameter influencing the performance of the dies. Thermal stresses cannot be entirely avoided however, and so the substrate is often designed from a combination of ceramic and copper, bonded together in such a way as to match their coefficients of thermal expansion (CTEs). Common techniques to achieve these structures are DBC, usually utilising alumina (Al_2O_3), and AMB which normally includes silicon nitride (Si_3N_4) or aluminium nitride (AlN) ceramics. Resistance to mechanical damage, form factor uniformity and identification of modules can be provided by an adequate plastic (usually glass fibre reinforced polyamide, GF/PA) housing. The material above

the substrate, around the die attach layer, bond wires, and terminal busbars must meet several requirements: it must have a high thermal conductivity, so that thermal stresses can be mitigated; it must yield to deformation, such that thermal expansion of module components can occur relatively freely and without undue stress; it must provide significant electrical insulation strength, especially when considering the move to higher operating voltages; and it must provide some measure of barrier against the harmful influence of an environment high in moisture and corrosion-causing contaminant species.

Modern HV power modules are the product of several manufacturing stages, beginning with the initial semiconductor substrate wafer which is usually p^+ [47]. A series of procedural epitaxial growth, oxidation, photolithography, etching and diffusion process are used to fabricate the actual devices on the substrate wafer. The full scope of these processes is not germane to the topics covered in this thesis. Individual IGBT bare dies are sectioned off from the wafer by dicing methods such as scribe and break or diamond saws. Bare dies are bonded to a metal leadframe or ceramic substrate. Die attach processes include eutectic bonding (soldering) and more recently, sintering [59]. Typically for high-power modules, a ceramic insulating substrate is chosen due to the higher thermal conductivity. Interconnecting bond wires (or ribbons [60]) made of gold, aluminium or copper are attached to the device and substrate either by thermo-compression (in the case of gold) or ultrasonic wedge bonding. Additional electrical interconnects and terminal busbars are then bonded to the device to provide the electrically complete package. In the case of power modules, several individual devices are packaged together on a common baseplate, usually made of aluminium, which provides a thermal interface for cooling. A plastic housing is then attached to the configuration either by an overmoulding process or bonded by adhesives. Generally, the void inside the package is then filled with a dielectric (usually silicone) gel. The result is then placed under vacuum to remove any air voids entrained within the gel, which would cause weakness in the insulation. This process is known as degassing. A diagram showing the cross-sectional structure of a typical IGBT module utilising a DBC substrate and silicone gel encapsulation is shown in Fig. 2.9.

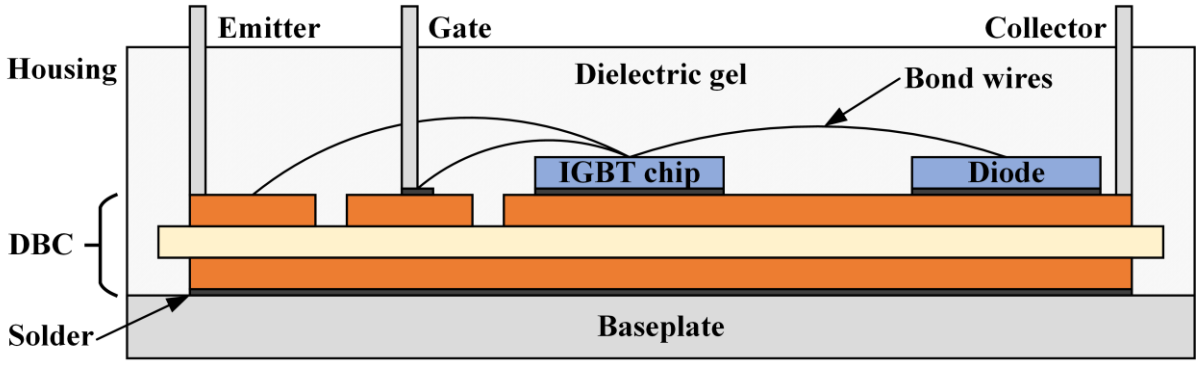

Fig. 2.9 Typical IGBT module construction utilising DBC substrate and silicone gel encapsulation.

The choice of traditionally packaged modules as described above, or the hermetically sealed press-pack structure generally comes down to availability and cost. Hitachi Energy and Infineon both offer press-pack devices and modules [61], [62]. The lowest voltage rating of these is 4.5 kV, making it unsuitable for typical converter topologies in WECS, and the cost of individual devices can be in excess of £4000 making it undesirable when non-hermetic modules are available for a fraction of the price. The appeal of increasing the reliability and performance of the more cost effective packaging technologies is readily evident.

Recently, humidity-robust platforms such as the Semikron SKiiP 7 intelligent power module (IPM) have reached mass market, available in 1.2 kV and 1.7 kV ratings for 500 A or 600 A loads in six-pack or half bridge configurations [63]. Though the manufacturers claim this module has increased ruggedness in harsh environment operation, this is substantiated only through improved performance in standardised test scenarios which are discussed in § 2.5 and the choice of sintered die attach rather than a more traditional solder layer. Although additional improvements such as a hermetically sealed packaging structure are possible, this information is not readily available from the manufacturer.

2.4 Overview of Silicone Gel

The materials long used for the encapsulation of power electronics are silicone gels [64]. These gels are a family of polysiloxane elastomers, chemically similar to polydimethylsiloxane (PDMS) but often supplied with additives or fillers to achieve specific desired properties for the target application [65], [66], [67].Power devices based on Si, SiC, and GaN are usually packaged in modules using similar encapsulation techniques [68], [69], [70], and are subsequently limited by the same packaging-related reliability concerns. Generally, silicones are classified into several categories: 1-part room-temperature

vulcanising silicone rubbers (RTV-1), 2-part room-temperature vulcanising silicone rubbers (RTV-2), liquid silicone rubber (LSR), and high-temperature vulcanising silicone rubber (HTV). The prevailing types used are RTV-2 and HTV, for PEM encapsulation and composite insulators in transmission systems, respectively. Regardless of type, the uncured component(s) are vulcanised into a rubber elastomer during the curing process. For RTV-2 silicones, which are the primary focus of this work, two pourable components are intermixed and poured into the PEM housing and cured in place either at room-temperature or at a higher temperature (heat-curing), which increases mechanical performance and reduces cure times.

The advantages offered by RTV-2 silicone gels for PEMs are numerous: they are low in viscosity (~1000 mPa·s), able to flow to fill the module housing and evenly coat the internal components; have good thermal conductivity (0.2 $W \cdot mK^{-1}$); a linear thermal expansion coefficient of 3×10^{-4} $m \cdot mK^{-1}$; and provide a high dielectric strength exceeding 23 $kV \cdot mm^{-1}$ in most cases. Alongside an inherent tackiness when mixed, and a typical service temperature in the range -50 °C to 180 °C, these are all favourable characteristics for the potting of PEMs. Due to ease of use in manufacturing, addition-curing RTV-2 gels are often selected, such as Wacker SilGel 612, which is consequently a common choice for this type of research [71], [72], [73], [74], [75]. The dielectric strength of this gel has been measured as 32.5 $kV \cdot mm^{-1}$ by other authors [76]. The basic chemical structure of silicone gel curing is shown in Fig. 2.10. One component contains polymer and a crosslinking agent, and the other component contains polymer and the catalyst, which in this case is platinum (Pt). When mixed, a siloxane (Si–O) elastomer is formed through Pt-catalysed hydrosilylation, which causes the polymer chains to cross link via

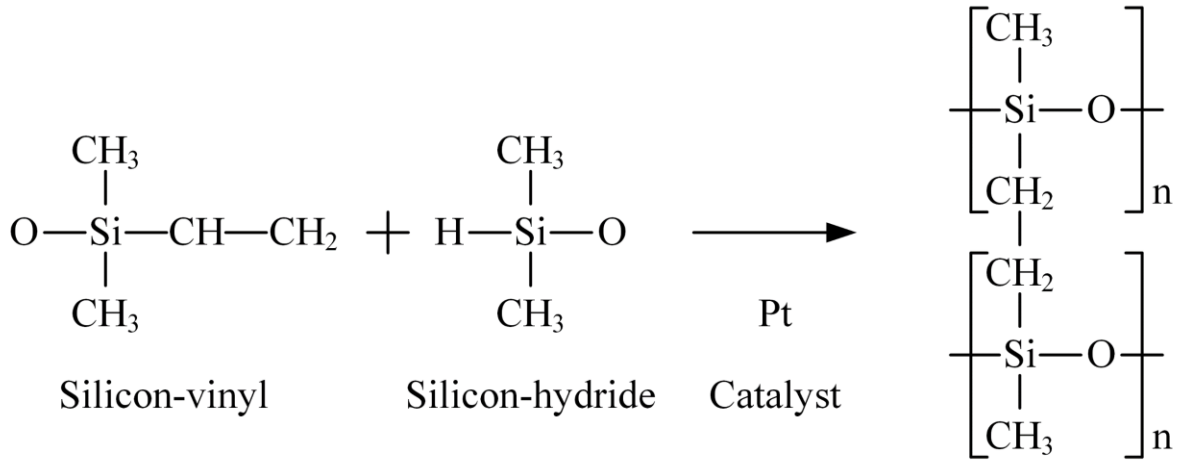

Fig. 2.10 Chemical structure of RTV-2 addition curing silicone gels, showing crosslinking, based on [77], [78].

CH_2–CH_2 bonds [77], [78]. This results in a mesh of siloxane backbone, which surrounds regions of uncured silicone fluid, giving the gel its desirable pliant nature.

However, these gels are not entirely immune to moisture absorption, and many power modules are not fully hermetically sealed, with large gaps between terminals and the housing. These gaps provide ingress routes for moisture, which can result in a local environment within the plastic housing that consists of moist air ready to be absorbed by the gel. Moisture is easily accommodated by the loose structure of the crosslinked network of the gel [79], this is shown graphically in Fig. 2.11. Diffusion of moisture through the plastic housing is also possible, as demonstrated on surface mount power electronics packages in [80] and TO-247 package IGBTs in [81], however this is expected to occur on a far longer timescale than through the gel, such that other degradation mechanisms and processes are the more pressing concern from a reliability standpoint. The moisture absorption dynamics of silicone gel encapsulation have long been studied from various perspectives, with more recent approaches focusing mostly on their influence on insulation quality [42], [79], [82], [83], [84], [85], [86].

The two main degradation mechanisms for silicone gel are “electrical treeing” and “water treeing” [87], [88]. The former is effectively a PD process, wherein inhomogeneities in the insulation structure

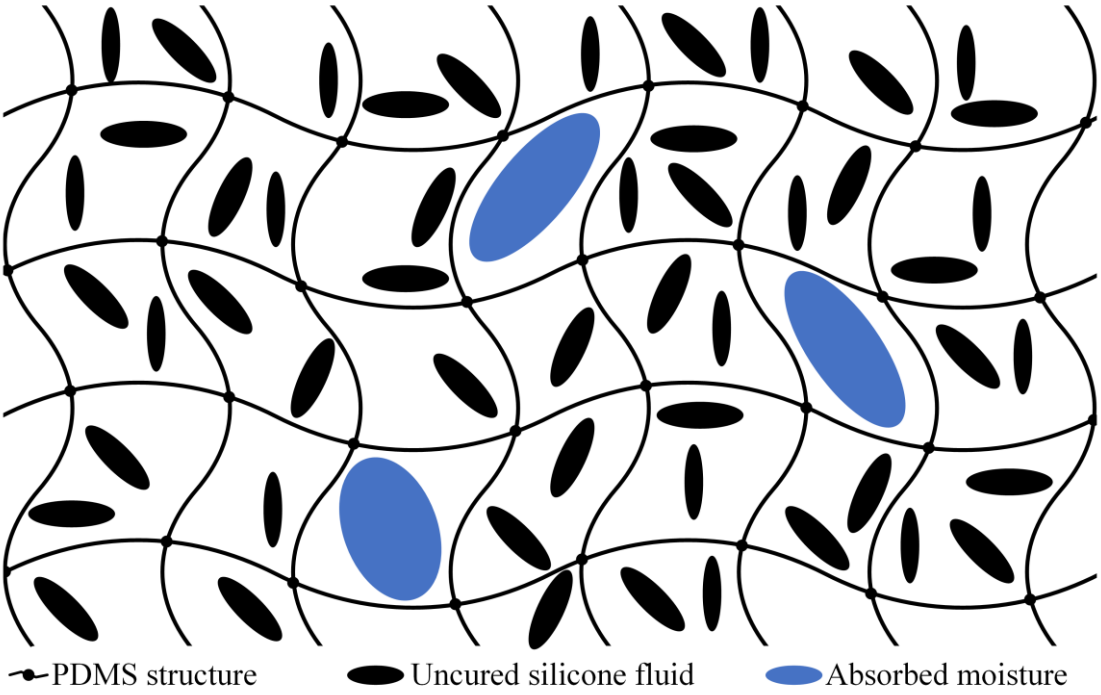

Fig. 2.11 Silicone gel structure showing crosslinked network, enclosed uncured silicone fluids, and a small amount of absorbed moisture. Based on [79].

of a device during operation causes regions of high electric field, sufficient to cause a localised breakdown. The field is enhanced by defects such as cracks, sharp edges, and voids in the insulation. Moisture intrusion into the encapsulation has also been shown to enhance the electric field local to the guard rings of IGBT devices in technology computer-aided design (TCAD) simulations [89], which is likely to exacerbate PD at this critical region. PD is discussed separately in depth in a later section. Water treeing is one term used to describe the previously discussed diffusion of moisture through the encapsulation structures. This diffusion may be exacerbated by the presence of an electric field and may result in lower impedance channels which are more likely to break down [71], [85]. Additionally, the absorption of moisture in the encapsulation and subsequent condensation at the die attach layer causes corrosion [74], which is discussed in more detail in the next section.

The RH inside different thicknesses of silicone gel was measured in [84] using commercial humidity sensors (Sensirion SHT71) embedded in gel samples. The authors demonstrated an increase in the RH inside the gel due to exposure to a high humidity (80% RH) environment, with up to 10 mm samples reaching steady-state at the sensor by 10 hours. The thickness of the gel above the sensor was shown to influence the rate of change in this parameter, presumably owing to a longer diffusion path length. In terms of mass increase by absorption of moisture in silicone gel, the authors of [42] show a steady-state value of about 0.07% in an 85 °C / 85% RH environment based on gravimetric analysis, demonstrating that the absolute quantity of absorbed moisture is minor. Gravimetric analysis is also performed in [83] for silicone rubber samples, comparing fresh rubber disc samples to field-operated ones. This work showed a significant increase in the moisture content for exposure to a high humidity environment (20 °C / 90% RH), which was significantly more prevalent in the aged samples. Mass increase in silicone gel was again measured via gravimetric analysis in [86]. However, gravimetric analysis alone provides little information as to the dielectric condition, so this is often presented alongside measurements of electrical properties [83], [90]. Gravimetric analysis also requires either measurements to be made in situ of the harsh environment, which limits the use of precision balances sufficient to measure the slight mass gain, or measurements are made ex situ wherein the samples will be desorbing moisture due to the changed moisture concentration gradient. There are no discussions in the literature

relating to samples sealed in situ for ex situ gravimetric analysis. Gravimetric analysis may not be a suitable technique to adequately determine moisture content within the gel, based on the competing absorption desorption process identified in [79], considering the complex nature of the interaction of the silicone gel chemical makeup with the absorbed moisture. It is worth noting that in field operation, the application of electrical stress may impact the diffusion dynamics of the encapsulation, as shown for silicone rubber samples in [85]. Therein, the authors conclude that although an applied AC stimulus has negligible impact on the moisture absorption rate of samples, an applied DC field results in a reduced absorption rate due to the orientation of water molecules with the field, and hence reduced free motion as required for diffusion. As a result of the above investigations, it is preferable from many avenues to investigate the influence of the moisture content in the gel on its electrical properties, rather than to quantify the moisture content by gravimetric analysis.

2.5 Influence of Temperature and Humidity on Power Module Performance and Reliability

Power converters in offshore energy generation, aerospace, and automotive applications are subjected to many environmental stressors including high temperatures, high ambient humidity, and contamination [91], [92], [93], [94]. Though the influence of each of these environmental factors does not act independently in field operation [95], [96], [97], [98], they are more often studied individually in order to better isolate the selected factor.

The influence of high temperatures on the performance and reliability of PEMs is the subject of much research [99], [100], [101], [102]. Conduction and switching losses within PEMs results in variable heating of the materials around the semiconductor die. The heating and cooling process is repeated many times during operation and is known as temperature cycling when the temperature is externally applied, and power cycling when the module is operated to generate heat via internal losses. Temperature cycling of any kind can cause degradation of the power module over time due to the mismatched coefficients of thermal expansion (CTEs) of the module components, which is often most severe closest to the die, at attachment layers [103]. Solder fatigue can occur in the form of non-recoverable deformation, i.e. creep [104], [105], or desquamation [106]. This fatigue can occur not only

within the solder attaching the die to the substrate, but also between substrate and baseplate [106]. Bond-wire lift off or heel cracking [107], [108], [109], or even delamination of the components within the PEM may also occur due to thermal cycling [59], causing increased thermal resistance and greater losses leading to greater damage. These thermomechanical degradation mechanisms generally all result in a reduced lifetime of the device, and reduced SOAs.

Offline characterisation of the lifetimes of PEMs is performed through stress testing to develop lifetime reliability models, which take in current operating conditions and operating history and determine the device's remaining useful life (RUL) and aid in planned maintenance cycles [110]. As the damage caused by thermomechanical degradation can be described by the Arrhenius relation [111], accelerated tests can be performed at temperatures higher than those experienced by the PEM during operation [112]. This allows lifetime data to be obtained much more quickly than the tens of years of expected operation. Online CM approaches often involve the tracking of degradation through the continuous measurement of so-called temperature sensitive electric parameters (TSEPs), which are highly influenced by the semiconductor device junction temperature, T_j [113]. These at-the-terminal measurable device parameters change as the rate of the degradation increases. Estimation of T_j via measurement of TSEPs, or by inference through temperature measurements of the die surface using sensors is also important in power cycling tests (PCT) to control the junction temperature variation, ΔT_j [114], [115], [116], [117], [118]. Common TSEPs for PEMs include: the on-state voltage of devices, $V_{CE(on)}$ [119], [120], [121]; on-state resistance, R_{on} [122]; threshold voltage, V_{th} [123], [124]; rate of change of collector voltage, dV_{CE}/dt [125]; rate of change of collector current, di_C/dt [126]; gate charge, Q_G [127]; turn off delay, $t_{d(off)}$ [128], [129], [130]; and many others. It is understood that the topic of IGBT-based PEM reliability from a purely thermomechanical perspective is well saturated and leaves little room for innovation for the reliability of mature device technologies.

The ingress of moisture into PEMs has several long term effects which limit reliability and often result in catastrophic failure of the converter. Almost all humidity-related PEM reliability research with accelerated testing is performed using the well-known HV high humidity high temperature reverse bias test (HV-H3TRB), which has seen significant development over the years to become the industry

standard assessment for humidity-robustness of power electronics [131], [132], [133], [134], [135], [136], [137], [138], [139]. In the most general case, this test involves placing the device under test (DUT) in a controlled climate chamber with fixed temperature and humidity. Typically, setpoints of 85 °C / 85% RH are used. A bias of 80% of the device's rating is applied while under blocking mode, and the leakage current through the device is periodically measured. Older forms of the test used an 80–100 V bias (H3TRB), but this was determined to be inadequate to cause representative degradation [132]. The modern test lasts for 1200 hours or until a threshold for the leakage current is exceeded, typically 10 times the initial measured value.

The increase in leakage current through the device is due to corrosion caused by the absorption of moisture, which eventually migrates to the die attach layer of the module [140]. The rate of absorption for modern PEMs is significantly shorter than the length of the H3TRB test [42]. This could indicate that although moisture is present at the die attach layer almost immediately, corrosion is not a significant concern until much later. Nevertheless, corrosion in the form of dendritic growth from copper (Cu) or silver (Ag) components has been observed in PEM substrates under as low as 4 V bias in under an hour [74]. This time is reduced further in the presence of contaminant species such as hydrogen sulphide (H_2S), sulphuric acid (H_2SO_4), or hydrochloric acid (HCl). Previous authors stated the combination of stress factors such as humidity, bias, and contamination all co-operate to accelerate corrosion in low-power electronic devices [141]. The disagreement between the rapid onset of corrosion compared to the far later increase in leakage current could be due to the presence of the passivation layer, which is generally manufacturer and device dependent. Moisture can eventually infiltrate the passivation layer, either through diffusion or wicking under delamination, causing aluminium (Al) corrosion about the edge termination and guard rings of Si-IGBT modules [142], [143], [144]. The quality of the passivation layer was again shown to be a significant factor in leakage current tests including a pulsed variant on 3.3 kV IGBTs [145]. A more recent work highlighted the improved robustness of the passivation of modern discrete TO-packaged SiC-IGBT devices to this type of degradation [146].

The presence of ambient humidity (70%–90% RH) in low temperature air (10–30 °C) has been shown to reduce the temperature increase of a converter under laboratory test conditions [147].

Conversely, investigations of the power cycling capability of PEMs in high humidity conditions indicates a reduction in cycles-to-failure (N_f) caused by moisture uptake in the thermal interface material (TIM) [148]. Similarly, earlier research highlights a growing concern for thermal cycling of power module substrates in high humidity (83% RH) [98], where the authors concluded that the silicone gel encapsulant was degraded. Consecutive H3TRB and PCT testing of IGBT modules has shown a reduction in N_f by up to 20% when compared with PCT alone [149], and PCT followed by H3TRB shows some evidence of reduced humidity-ruggedness [150]. The influence of humidity on PCT performance in general is still new ground for reliability research, leading to the development of improved test methodologies and simulation approaches incorporating combined environmental stress [151], [152], though these have yet to see significant use in the literature.

Almost all recent reliability research on PEMs in humid environments deals with long-term degradation via corrosion. Even adapted PCT with humidity, or PCT with consecutive H3TRB testing only looks at the lifespan of the device. There are no examples in the literature of how the behaviour of PEMs changes in the short-term due to the absorption of moisture, which is a potential research avenue to aid in reliability-oriented WT converter designs and control strategies.

2.6 Relevant Theory for Moisture Absorption in High Humidity Environments

As stated in the previous section, the ambient environment about OWTs consists of many stressors for PEMs. One major stressor and reliability concern for power modules is moisture. In this thesis, relative humidity is the primary metric in the interest of easy comparison with the literature, but there are many useful terms which bear clarification.

2.6.1 Definition of Terms Associated with Humidity

The information below is a summary of definitions found in various standards, as well as commonly accepted terms, which are pertinent to this thesis [153], [154], [155], [156]. Many different symbols are used in the literature and standards to represent humidity-related parameters, with a single symbol for each chosen for use in this thesis in the interest of clarity. RH is the most common metric for humidity and is defined as the percentage of the water vapour in the air relative to the maximum the air can hold,

at a given temperature and pressure. At 100% RH, water vapour in the air will begin to condense into liquid water. RH can be given by (3).

$$RH = \frac{P_w}{P_{ws}} \times 100\% \tag{3}$$

where P_w is the actual partial pressure exerted by the water vapour in air at a given temperature, and P_{ws} is the saturation vapour pressure which describes the pressure of the water vapour at full saturation in air, i.e. at thermodynamic equilibrium over an open mass of water. When $P_w > P_{ws}$, water will condense out of the air, and when $P_w < P_{ws}$, water will evaporate out of the liquid.

There are several relations presented in the literature to estimate the saturation vapour pressure of water at a given temperature. Due to its validity over the temperature ranges used in this thesis, the empirical Antoine equation is used in this work to estimate P_{ws} [157], using constants published in the US National Institute of Standards and Technology (NIST) Chemistry Webbook [158] (valid over the temperature range 255.9–373.0 K). This is given by (4):

$$\log_{10}(P_{ws}) = \mathcal{A} - \frac{\mathcal{B}}{\mathcal{C} + T} \rightarrow P_{ws} = 10^{\left(\mathcal{A} - \frac{\mathcal{B}}{\mathcal{C}+T}\right)} \qquad [bar] \tag{4}$$

where $\mathcal{A}$, $\mathcal{B}$, and $\mathcal{C}$ are empirical constants equal to 4.6543, 1435.264, and -64.848, respectively, and T is the ambient temperature in Kelvin.

Absolute humidity (AH) is the term used to describe the mass or density of water vapour per unit volume of air, often represented in g·m^{-3}. The British Standards Institute (BSI) notes that this is often a loose term, interchangeably describing either the mixing ratio, specific humidity, or volumetric humidity. It can be given by (5):

$$AH = \frac{m_v}{\mathcal{V}} = \frac{RH}{100} \cdot \frac{P_{ws}}{R_w \cdot T} \qquad [g \cdot m^{-3}] \tag{5}$$

where m_v is the mass of the water vapour in air; $\mathcal{V}$ is the volume of the air and water mixture; R_w is the specific gas constant for water vapour equal to 461.5 J·kg^{-1}·K^{-1} [159], representing the energy required to heat a mass of material by a given temperature. As AH is usually represented in g·m^{-3}, care must be taken in conversion of units.

Specific humidity (q) is the mass fraction of water vapour in the air per unit mass of the air at the given pressure, and can be represented with (6):

$$q = \frac{m_v}{m_v + m_g} \qquad [g \cdot kg^{-1}] \quad (6)$$

where m_g is the mass of the dry air in the same volume as the water vapour. It is often shown in relation to the mixing ratio (r), which shows instead the ratio of the relative masses of water vapour and dry air in a given volume (7):

$$r = \frac{m_v}{m_g} \quad (7)$$

2.6.2 Capacitance and Dielectric Theory Pertaining to Moisture Absorption in Gel Insulation

Previous studies have shown that the presence of moisture around the active area of a power device can significantly influence the local electric field [89], and it is well understood that it plays a significant role in damage-causing phenomena such as PD [160].

Capacitance is the measure of a system's ability to store energy in an electric field. The simplest capacitor consists of two parallel conductive plates separated by some distance, with an applied external electric field. Rather than air, a dielectric material is placed between, with properties that increase the energy storing ability of the system. A simplified diagram of this capacitor is provided in Fig. 2.12.

For the parallel plate capacitor of Fig. 2.12 the capacitance can be given by (8):

$$C = \frac{\varepsilon_0 \varepsilon_r A}{d} \qquad [F] \quad (8)$$

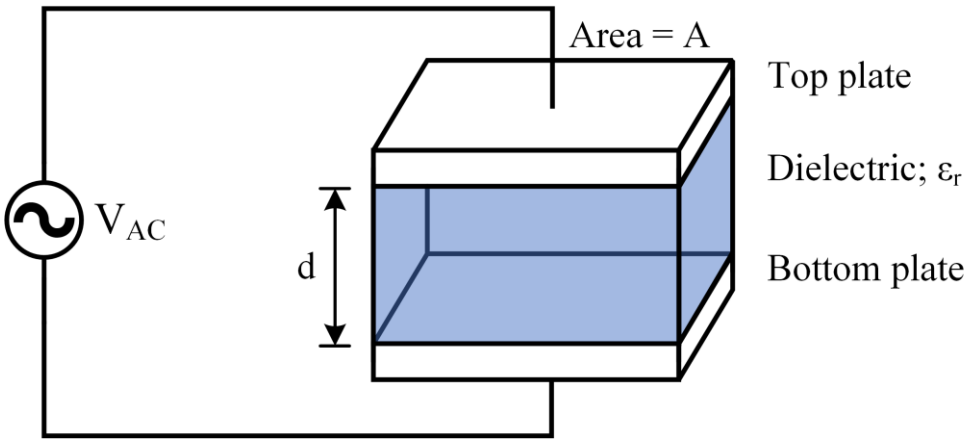

Fig. 2.12 Diagram of components in a parallel plate capacitor, highlighting the dielectric material.

where C is the capacitance of the system, in F; ε_0 is the vacuum permittivity; ε_r is the relative permittivity of the material placed between the plates; A is the plate area, in m^2; and d is the distance to which the plates are separated, in m. The constant ε_0 is also known the permittivity of free space, and is given by (9):

$$\varepsilon_0 = \frac{1}{\mu_0 c^2} \approx 8.8542 \times 10^{-12} \qquad [F \cdot m^{-1}] \quad (9)$$

where c is the vacuum speed of light, and μ_0 is the vacuum permeability – a measure of the resistance to the development of a magnetic field in a vacuum.

The relative permittivity is the ratio of the absolute permittivity (ε) of the material and the vacuum permittivity (ε_0) as given in (10):

$$\kappa = \varepsilon_r = \frac{\varepsilon}{\varepsilon_0} \qquad (10)$$

where κ is equivalent to ε_r and is termed the dielectric constant of the material. The absolute permittivity is a proportionality factor representing the interaction of a material with an externally applied electric field.

Historically, the electric flux density (electrical displacement) between the two plates (avoiding polarisation of the material for now) was given by (11) [161]:

$$\underline{D} = \varepsilon \underline{E} \qquad [C \cdot m^{-2}] \quad (11)$$

where $\underline{D}$ is the electric flux density; ε is the absolute permittivity, $\varepsilon = \varepsilon_0 \varepsilon_r$; and $\underline{E}$ is the applied electric field.

High permittivity materials are those that significantly displace the electric field, resulting in a greater degree of energy from that field stored within the material. The polarisation of a material is a measurable quantity which represents the complete influence of an externally applied electric field on that material. The polarisation of an isotropic material is linearly related to the external electric field by (12) [162]:

$$\underline{P} = \varepsilon_0 \cdot \chi \cdot \underline{E} \qquad [C \cdot m^{-2}] \quad (12)$$

where $\underline{P}$ represents the polarisation density of the material, χ is the dimensionless material property called electric susceptibility, and $\underline{E}$ is the externally applied electric field.

Considering (12), it is appropriate to describe the electric displacement of (11) in a way that includes the polarisation of the material, which is given in (13):

$$\underline{D} = \varepsilon_0 \cdot \underline{E} + \underline{P} \qquad [C \cdot m^{-2}] \quad (13)$$

Combining (10), (11), (12), and (13), the relative permittivity of the material can be represented in terms of its susceptibility to polarisation, given in (14):

$$\varepsilon_r = 1 + \chi \quad (14)$$

Materials such as air ($\varepsilon_r \approx 1$) are far less susceptible to polarisation than materials made up of freely moving polar molecules, such as water ($\varepsilon_r \approx 81$ at 25 °C). At the base level, the capacitance of the parallel plate capacitor described by (8) relies only on its geometry and the choice of dielectric material. Considering the geometry to be fixed, the capacitance increases linearly with the dielectric constant (its relative permittivity). No real-world capacitor is ideal and free of losses, so to include a measure of the losses of the material, its relative permittivity is often represented as a frequency-dependent complex property with real and imaginary parts, as shown in (15) [163]:

$$\varepsilon_r^*(\omega) = \varepsilon_r'(\omega) - j\varepsilon_r''(\omega) \quad (15)$$

where ε_r^* is the complex relative permittivity; ε_r' is the real component relating to polarisation of the material and energy storage; ε_r'' is the imaginary component relating to losses within the material; ω is angular frequency, $\omega = 2\pi f$; and j is the imaginary operator, $j^2 = -1$.

The simple parallel-plate model of Fig. 2.12 can be modified include the loss proportion as a parallel resistance (R_p), more accurately describing a lossy dielectric material. A diagram of this system is shown in Fig. 2.13 alongside a phasor representation of the same (Fig. 2.13(b)). Note that ε_r' and ε_r'' in (15) are functions of frequency. Generally, both reduce with increasing frequency as the contributions from lower frequency polarisation mechanisms become less pronounced. Localised peaks exist due to resonance effects with certain polarisation mechanisms [164], [165], [166].

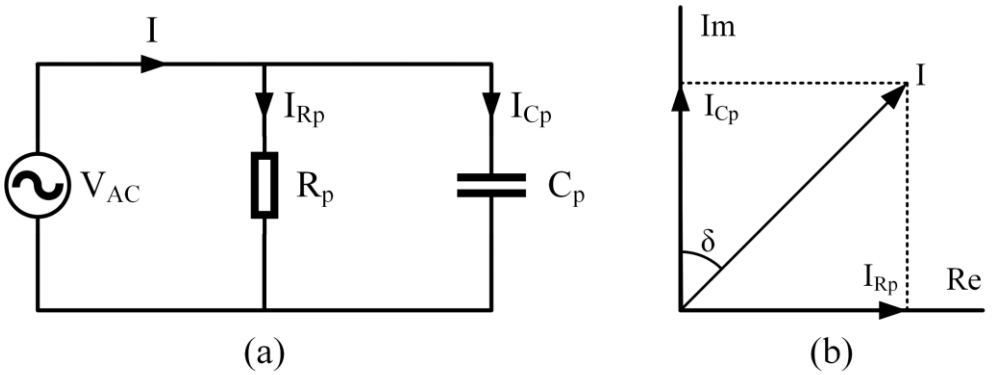

Fig. 2.13 Equivalent representations for a dielectric material. (a) parallel RC model, (b) phasor diagram.

A simplified overview of the behaviours of the main polarisation mechanisms for a given material is shown in Fig. 2.14. Space charge (or interfacial) polarisation occurs when mobile charges in a material accumulate on either the surface of applied electrodes, or in the case of heterogeneous materials, at boundaries. Dipolar (or orientation) polarisation requires the existence of polar molecules (such as H_2O) within the material, which experience a turning torque when an external electric field is applied. Ionic polarisation occurs mainly in solid materials, in which opposingly charged ions within a compound (such as NaCl) are displaced relative to one another by an external electric field, resulting in a net dipole moment. Atomic (or electronic) polarisation occurs when any atom is exposed to an electric field, wherein the centre of positive and negative charges of that atom are displaced relative to one another. Each of these polarisation mechanisms results in increased electric flux density in the material

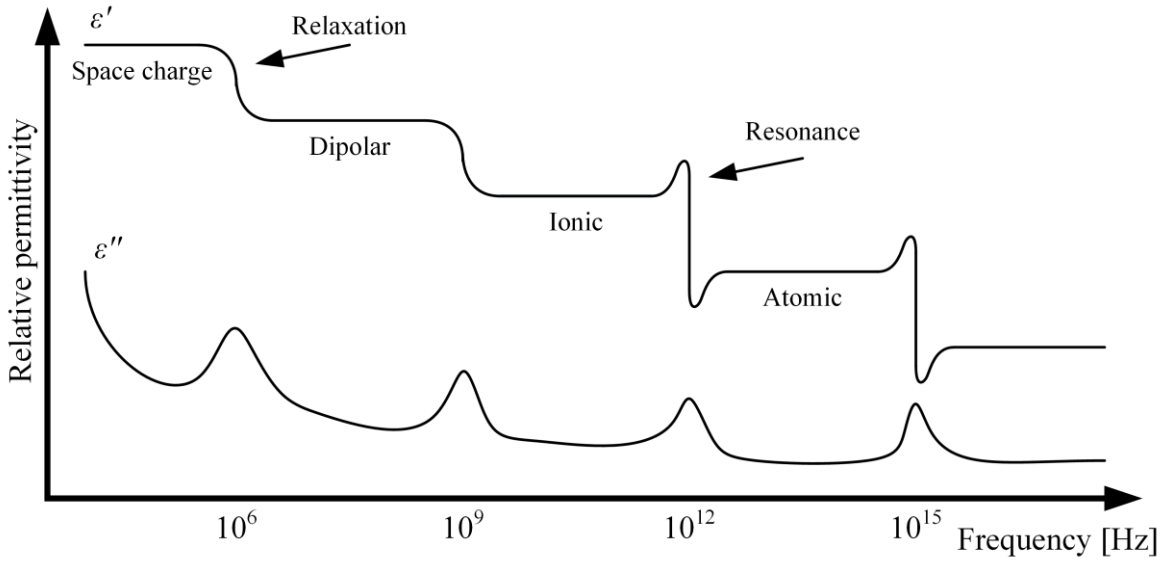

Fig. 2.14 Simplified overview of complex relative permittivity of a material against frequency. Polarisation mechanisms are highlighted. Based on [164], [165], [166].

due to the dipole alignments with the applied electric field. It is beyond the scope of this thesis to give full mathematical descriptions of these independent mechanisms.

The losses in a dielectric are usually represented by the so-called loss tangent, $tan(\delta)$, which in practical terms for model of a lossy dielectric shown in Fig. 2.13 can be found using the relationships given in (16):

$$tan(\delta) = \frac{\varepsilon''}{\varepsilon'} = \frac{\varepsilon_r''}{\varepsilon_r'} = \frac{I_{R_p}}{I_{C_p}} = \frac{1}{\omega C_p R_p} \tag{16}$$

For realistic measurement of these parameters, the parallel resistance and capacitance are taken from measurements of system impedance magnitude and phase using appropriate equipment. This is performed by first converting the impedance magnitude ($|Z|$) and phase (θ) to the equivalent series resistance (R_s) and series capacitive reactance (X_s) as in (17):

$$|Z|\angle\theta \rightarrow \begin{cases} R_s = |Z| \cdot \cos(\theta) \\ X_s = |Z| \cdot \sin(\theta) \end{cases} \tag{17}$$

Then the Q factor of the system is found by the ratio of the reactive and real portions with (18):

$$Q = Q_s = Q_p = \frac{X_s}{R_s} \tag{18}$$

where Q_s and Q_p are the Q factors in series and parallel models, respectively.

Equating Q_s and Q_p facilitates conversion from the series to the parallel model with (19) and (20):

$$R_p = R_s(1 + Q^2) \quad [\Omega] \tag{19}$$
$$X_p = X_s(1 + Q^{-2}) \quad [\Omega] \tag{20}$$

The remaining operation is simply to convert the retrieved parallel capacitive reactance (X_p) to the parallel capacitance (C_p) as needed. This is easily done using the standard relation shown in (21):

$$C_p = \frac{1}{\omega \cdot X_p} \quad [F] \tag{21}$$

2.6.3 Moisture Absorption Modelling

The absorption of moisture into a material is effectively a diffusion process, whereby moisture follows a concentration gradient of high moisture concentration (i.e. humid air) into a low concentration (i.e. dry silicone gel) to reach an equilibrium. This is widely studied, and almost all examples of moisture diffusion are based on Fick's first and second laws. Fick's first law, given in (22), describes diffusion flux as proportional to the concentration gradient, scaled by the coefficient of diffusion for that material [79], [90], [167]:

$$J = -D\frac{dc}{dx} \qquad [kg \cdot m^{-2} \cdot s^{-1}] \quad (22)$$

where J is the diffusion flux describing the amount of the diffusant moving through a given region over a given time in the x direction, which in units mol·m^{-2}·s^{-1} would instead describe the movement of a number of particles; D is the coefficient of diffusion of the material, generally given with units m^2·s^{-1}; and c is the concentration of the diffusant with units kg·m^{-3}.

Considering a 3-dimensional system as shown in Fig. 2.15, (22) can be adjusted to obtain (23):

$$J = -D\left(\frac{\partial c}{\partial x} + \frac{\partial c}{\partial y} + \frac{\partial c}{\partial z}\right) = -D \cdot \nabla \mathrm{c} \qquad (23)$$

where ∇ is the del, or *nabla*, operator; and x, y, and z are the axes of the concentration gradient.

It is useful to consider the rate of change of the concentration of moisture within the material, which requires the assumption that no reaction of the materials occurs, and is given by (24):

$$\frac{\partial c}{\partial t} = div(\mathrm{D} \cdot \nabla \mathrm{c}) = D \cdot \nabla^2 c = D\left(\frac{\partial^2 c}{\partial x^2} + \frac{\partial^2 c}{\partial y^2} + \frac{\partial^2 c}{\partial z^2}\right) \qquad (24)$$

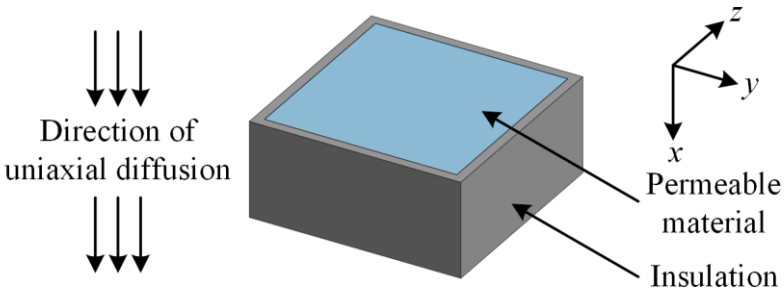

Fig. 2.15 Diffusion dynamics reference frame.

where ∇^2 is the Laplacian operator, representing the divergence ($\nabla \cdot$) of the gradient (∇f) of c.

The uniaxial (or one-dimensional) case is most common for diffusion modelling in the literature, as assumptions are made that only the 'top' of power modules is open for the ingress of humidity. In almost every case this is a reasonable assumption, as the rate of diffusion through the silicone gel is significantly higher than through the housing, which is usually GF/PA, and generally HV power module housings have small gaps for the terminals which are not hermetically sealed. The one-dimensional case, with convention being to take x as the diffusion gradient axis normal to the surface plane of the material, of (24) is Fick's second law, given by (25):

$$\frac{\partial c}{\partial t} = D\frac{\partial^2 c}{\partial x^2} \tag{25}$$

The initial and boundary conditions for the case of moisture absorption into a material with thickness ℓ are given in (26) [79]:

$$c = \begin{cases} c = c_0, & & t = 0 \\ c = c_1, & x = 0, & t \geq 0 \\ c = c_2, & x = \ell, & t \geq 0 \end{cases} \tag{26}$$

where c_0 is the initial moisture concentration in the material, c_1 is the moisture concentration at the interface of the material and the moist air above, ℓ is the thickness of the material, and c_2 is the moisture concentration at ℓ.

The moisture content within the material during the diffusion process can be given by (27) [168]:

$$M = G(M_m - M_i) + M_i \tag{27}$$

where M is the percent moisture content of the material, M_m is the steady-state moisture content of the material for a given ambient environment, M_i is the initial moisture content of the material before exposure to moisture, and G is a time dependent parameter given by (28):

$$G = 1 - \frac{8}{\pi^2}\sum_{j=0}^{\infty}\frac{\exp\left[-(2j+1)^2\pi^2\left(\frac{D_x t}{s^2}\right)\right]}{(2j+1)^2} \tag{28}$$

where D_x is the x-direction coefficient of diffusion, and s is twice the thickness of the material ($s = 2h$; where h is the thickness, assuming single-sided absorption).

Choosing to investigate only relative mass gain as in [90], and using the approximation of (28) from [168] results in a more workable case as in (29):

$$\frac{m(t)}{m_\infty} \approx 1 - \exp\left[-7.3\left(\frac{D \cdot t}{s^2}\right)^{0.75}\right] \tag{29}$$

where $m(t)$ is the relative mass increase of the material due to moisture absorption at time t, and m_∞ is the relative steady-state mass value.

These parameters are related to (27) by (30):

$$\frac{m(t)}{m_\infty} = \frac{M - M_i}{M_m - M_i} \tag{30}$$

In [79], which looks at the moisture concentration increase rather than mass gain, the relative changes are more clearly denoted by prepending Δ, with the remainder of the solution being the same, this is given here by (31) for completeness and future reference:

$$\curlyvee = \frac{\Delta c_t}{\Delta c_\infty} = \frac{c_t - c_0}{c_\infty - c_0} = 1 - \sum_{n=0}^{\infty} \frac{8}{(2n+1)^2\pi^2} \exp\left[\frac{-D((2n+1)^2\pi^2)t}{\ell^2}\right] \tag{31}$$

where $\curlyvee$ is the ratio of absorption, equivalent to G in (28); Δc_t is the relative moisture concentration increase at time t; Δc_∞ is the relative moisture increase at steady-state; c_t is the moisture concentration in the material at time t; c_0 is the initial moisture concentration inside the material, as in (26); c_∞ is the moisture concentration in the material at steady-state; and ℓ is the thickness of the material as in (26), equivalent to s or $2h$ in (28).

Evidently, since the ratio of absorption can be linked to relative mass increase or relative moisture concentration increase, it is possible to investigate the growth of any material property that changes based on Fickian diffusion in a similar manner.

One of the main assumptions that validate Fickian diffusion is that there is no interaction between the absorbed water molecules and the material into which they are absorbed. This is not true in every case, with a pertinent example being that of silicone gels filled with additives such as aluminium trihydrate (ATH) filler, which is hydrophilic [90], [169]. There are also strong indications that moisture absorption into silicone gel without filler also forms some chemical bonds, at the very least in the case of hydrolysis of the siloxane backbone as commented on in [79]. Such phenomena are called anomalous, or non-Fickian, diffusion, and the pervading modelling technique is based on the Langmuir diffusion theory [82]. The core basis of the Langmuir type diffusion model is that water molecules have a certain propensity to becoming bound in the material. There are then two states of water molecules in the system: those that are bound, and those that are free. An assumption is made that the free molecules act as in the case of Fickian diffusion, and indeed the diffusion process under the Langmuir model can be described by altering Fick's second law using (32) and (33) [90]:

$$D_f \frac{\partial^2 c_f}{\partial x^2} = \frac{\partial c_f}{\partial t} + \frac{\partial c_b}{\partial t} \tag{32}$$

$$\frac{\partial c_b}{\partial t} = \alpha c_f - \beta c_b \tag{33}$$

where D remains the diffusion coefficient as previously defined, although here it represents the Fickian diffusion of free molecules only; c is the moisture concentration, also as previously defined; new subscripts f and b are introduced to represent free and bound portions, respectively; α is the bonding coefficient representing the probability of a free molecule becoming bound; and β is the de-bonding coefficient representing the probability of a bound molecule becoming free. The boundary conditions for (32) are the same as those for (25).

In a similar approach to the previous analysis for Fickian diffusion as previously explained, the relative mass increase in the material by under Langmuir diffusion can be given as (34):

$$\frac{m(t)}{m_\infty} = \frac{\beta}{\alpha+\beta}\exp(-\alpha t)\cdot g(t) + 1 - \exp(-\beta t) + \frac{\beta}{\alpha+\beta}[\exp(-\beta t) - \exp(-\alpha t)] \tag{34}$$

where $g(t)$ is the form of Fickian diffusion given in (28).

Whether the Fickian or Langmuir type diffusion model fits best for a given material depends on the interaction of the material's chemistry with water molecules. In the case of the silicone gel studied in this thesis, to which no filler is added, this interaction is relatively unquantified. Therefore, fits of the data to each model will be provided, with the aim of identifying which best suits diffusion of moisture through silicone gel.

2.6.4 Mixture of Two Dielectrics

Based on evidence in the literature, the relative permittivity of the gel is expected to increase due to the absorption of water via diffusion processes caused by the moisture concentration gradient [79]. Two diffusion models are considered in this thesis: Fickian diffusion and Langmuir diffusion (non-Fickian). The effect of moisture absorption by the gel is to change its electrical properties, namely its relative permittivity, and the actual proportion of moisture absorbed by the gel is somewhat debated by the literature. Consequently, it is useful to identify what influence mixtures of dielectrics (the gel and the water) have on the permittivity of the resultant material. The traditional model for this in the literature is the Lichtenecker-Rother logarithmic dielectric mixing theory, which is used for a wide array of composite materials [90], [170], [171]. According to the Lichtenecker-Rother relation, the permittivity of a homogeneous mixture of any number of dielectrics is given by (35):

$$\log \varepsilon_{mix} = \sum_{n} \phi_n \cdot \log \varepsilon_n \tag{35}$$

where ε_{mix} is the permittivity of the mixture of the dielectrics; ϕ_n represents the volume fraction of each constituent component, satisfying $\sum_n \phi_n = 1$ [90]; and ε_n represents the permittivity of each constituent material.

In the case of a mixture of only two dielectrics, which is the focus of this work considering water and silicone gel only, (35) may be rewritten as (36):

$$\log \varepsilon_{mix} = \phi_1 \cdot \log \varepsilon_1 + \phi_2 \cdot \log \varepsilon_2 \ = \phi \cdot \log \varepsilon_1 + (1 - \phi) \log \varepsilon_2 \tag{36}$$

where ϕ_i represents the volume fractions of the constituent materials, with $\phi \ = \phi_1 \ = \ 1 - \phi_2$; and ε_i represents the permittivities of the constituent materials, $i = 1, 2$.

Based on the work in [172], (35) and (36) can result in (37) and (38), respectively:

$$\varepsilon_{mix} = \prod_n \varepsilon_n^{\phi_n} \tag{37}$$

$$\frac{\varepsilon_{mix}}{\varepsilon_1} = \left(\frac{\varepsilon_2}{\varepsilon_1}\right)^{\alpha} \tag{38}$$

where α is now the volume fraction of the constituent material with permittivity ε_2, for clarity.

This makes use of the inherent symmetry in the Langmuir model for two-component mixtures, i.e., which subscript is assigned to which component does not matter, if the volume fraction labels are also reassigned. For legibility and clear understanding, the volume fraction α of material two which has permittivity ε_2 is equivalent to $\phi_2 = 1 - \phi$ as in (36).

Other relations for determining the resultant permittivity of a mixture of dielectrics are given in the literature. The Landau-Lifshitz-Looyenga formula discussed in [173] is provided in (39), and the Maxwell-Garnett relation as discussed in [174] is provided in (40). These are also discussed in [90], from which the convention is kept.

$$\varepsilon_{mix}^{1/3} = \sum_n \phi_n \cdot \varepsilon_n^{1/3} \tag{39}$$

$$\frac{\varepsilon_{mix} - \varepsilon_{im}}{\varepsilon_{mix} + 2\varepsilon_{im}} = \sum_n \phi_n \cdot \frac{\varepsilon_n - \varepsilon_{im}}{\varepsilon_n + 2\varepsilon_{im}} \tag{40}$$

where ε_{im} is a relative permittivity determined by the so-called interface medium between the constituent materials, for which no firm value can be provided in the case of water and silicone gel.

Non-uniform concentrations of moisture absorbed into silicone rubber showing good agreement with the Langmuir diffusion model are discussed in [90], [175], where the authors note that the Langmuir model is suitable to partly capture the chemical changes due to moisture absorption in silicone rubber. Consequently, the Lichtenecker-Rother dielectric mixing formula is pursued in this work. The relative permittivity of the gel at time t can be given by (41) for the uniform absorption case (i.e., the bulk of the gel absorbs moisture evenly throughout its thickness), and (42) for the non-uniform absorption case (i.e., the gel closest the diffusant absorbs moisture first) , based on the work in [90]. As the behaviours

of silicone rubber, which the observations suiting the Langmuir model are based around, and silicone gel may differ in practice, the choice of both diffusion model and dielectric mixing theory is unclear.

$$\varepsilon_t = \mathcal{L}(t)(\varepsilon_\infty - \varepsilon_s) + \varepsilon_s \tag{41}$$

$$\varepsilon_t = \frac{\varepsilon_s}{1 - \mathcal{L}(t) \cdot \left(1 - \frac{\varepsilon_s}{\varepsilon_\infty}\right)} \tag{42}$$

where ε_t is the permittivity of the dielectric mixture at time t; ε_s is the permittivity of the dry silicone gel; ε_∞ is the permittivity of the silicone gel at maximal moisture uptake; and $\mathcal{L}(t)$ is the Langmuir diffusion model as given in (34), permitted here by the relation shown in (43):

$$\frac{m(t)}{m_\infty} = \frac{\varepsilon_t - \varepsilon_s}{\varepsilon_\infty - \varepsilon_s} \cdot \frac{\varepsilon_\infty}{\varepsilon_t} \tag{43}$$

2.7 Partial Discharge in Relation to Power Modules

PD is an electrical discharge which does not fully bridge the conductive elements of a system, occurring within the insulation structures often due to voids or flaws. The minimum voltage at which this occurs is known as the PD inception voltage (PDIV). Generally, a higher PDIV indicates insulation structures that are less prone to the occurrence of PD and are hence more rugged to this type of fault. PD can occur within power modules due to weaknesses in the insulation structure from ageing or unintentional manufacturing faults, or high local electric fields caused by ever increasing operating voltages. This is most prevalent at the triple interface where the dielectric gel meets with the copper and ceramic of the substrate, or with the copper and semiconductor die at the die-attach region, as shown in Fig. 2.16. Although the term ‘triple junction’ is commonly used in the literature when describing this section of the geometry, this work chooses to avoid any possible confusion with the semiconductor device junction itself. Here, the combination of the interfaces and the sharp geometries causes significant enhancement of the local electric field, which in some cases is sufficient to overcome the insulation and result in a localised discharge. The electric field strength is greatest when flaws such as unfilled voids in the insulation, microcracks in the ceramic, or sharp defects in the copper are present. PD is known to damage insulation structures over time, with increasing PD magnitude correlating with a reduced insulation lifetime. For WBG devices this is a well-acknowledged reliability limitation, but PD can still occur in PEMs with lower switching speeds such as IGBTs [176], [177], [178], [179]. This

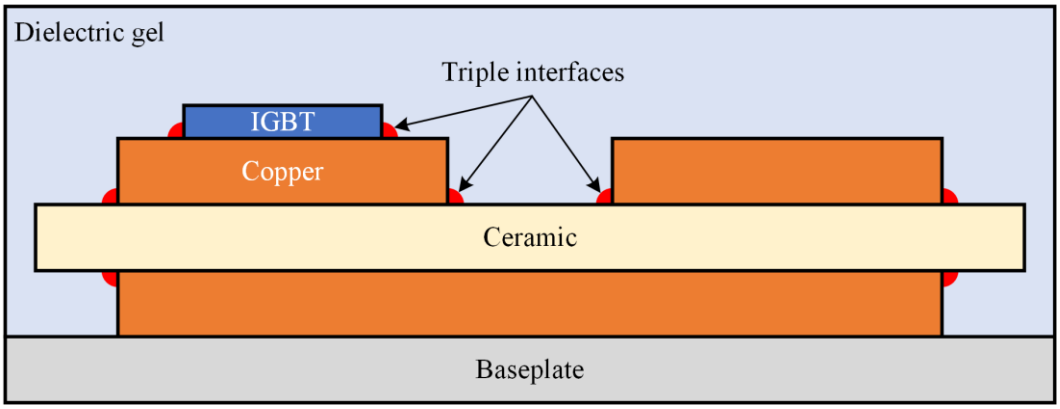

Fig. 2.16 Cross-section diagram of typical DBC and silicone gel encapsulation of IGBT modules, with triple interfaces shown in red, annotated.

can also occur within IGBTs in blocking mode [180]. Consequently, significant effort is taken in the design of HV power modules to mitigate the impact of PD-driven degradation [181], [182]. Usually this is done by reducing the electric field at critical regions in the packaging structure, by geometrical variations or by careful material selection. However, these must also be balanced against design constraints such as: minimised parasitics, good thermal performance, and weight and volume constraints. Moreover, these mitigation approaches must be cost effective and fit easily into the production pipeline in terms of ease of implementation and production time. Macroclimate approaches towards reducing hazardous environments within control cabinets can prove effective in some cases [40], but cost and volume constraints limit their feasibility for every application.

Early studies on the PD behaviours of silicone gel were performed in 2006 [183], concluding that increasing temperature had little impact on the PDIV. This disagreed with contemporary research for solid insulation such as high-voltage cabling in [184], or insulated stator bars in [185], which showed that PD activity was exacerbated or PDIV reduced with increasing temperature. Studies investigated the breakdown characteristics of silicone gel thoroughly under various conditions [186], [187], concluding that proper degassing of the material can help eliminate the presence of voids within the gel or at interfaces and reduce the quantity of uncured silicone fluid, both of which generally increased the breakdown strength under 50 Hz AC stimulus. Later, ceramic substrates were incorporated in testing, showing again that for silicone gel insulation the PDIV was not impacted in a significant manner by increasing temperature [188]. However, this study revealed that the absolute number of PD events was increased with increasing temperature. Additionally, the authors here reasoned that the PDs occurred

within the substrate itself, and not the gel. Though a 2007 study highlighted the severe reduction in insulation quality of silicone gel in high humidity [189], the picture is not clear when considering combined temperature and humidity stress for solid insulation.

An earlier study on enamelled magnet wires showed that increasing ambient humidity at low temperatures (30 °C) reduced PDIV but had little impact at higher temperatures (≥ 60 °C) [190]. The same authors found a strong dependence on temperature in the humidity-driven change of PDIV on similar samples with PD measured by optical emission spectroscopy in 2010 [191] and investigate the combined impact in [192]. More recently it was shown that increasing temperature served generally to reduce PDIV, especially at lower ambient humidity, for solid insulation [193]. This is somewhat in disagreement with the later results of [194] that the impact of temperature and humidity on the PD characteristics of solid insulation is strongly nonlinear. The variation could be due to the test stimulus applied, as the former utilised surge voltage for PDIV measurement, while the latter used 50 Hz AC as per international standard IEC 60034-18-41 [195].

For gel insulation, the authors of [98] thermally aged silicone gel encapsulated DBC substrate samples in high and low humidity environments. The latter had little bearing on the PD and breakdown behaviours, but the former showed a multifaceted impact: PDIV was increased, but the variation was also significantly increased with a few instances of significantly reduced PDIV. The authors observe the same reduction in breakdown voltage for the humid-aged samples as reported by the previous work in [189], and also comment on the inability of contemporary standard IEC 61287:2006 [196] to stress the substrate in a fully representative manner. The recent version of this standard and other relevant current standards do not yet ameliorate this issue [197], [198], [199].

PD research for power module substrates nevertheless continues with improvements on test structure and detection methodology. Recently, the authors of [200] showed that higher temperatures reduce PDIV and increase PD amplitude under both unipolar square pulses and AC stimulus. The importance of the applied waveform is also investigated in this work: AC stimulus resulted in a lower PDIV than square pulses, which demonstrated elevated PDIV for higher slew rate and pulse width. The noted impacts agree with earlier work on similar samples [201]. Conversely, HV power modules which pass

standard PD tests at 50 Hz AC are shown to fail when subjected to pulse width modulation (PWM) stress in [202], indicating potential disagreement in the literature.

Most often in the literature, reduction of PD activity and hence reduction of damage to insulation caused by PD [203], [204], [205], [206], [207] is achieved either by altering the composition of the insulating components inside the power module, or by varying the geometry of the substrate. Already by 2010 the silicone gel within power modules was considered a target for reliability improvement, with [208] adding barium titanate ($BaTiO_3$) to the gel to reduce the field strength at the edge of DBC metallisation and thereby enhancing sample PDIV under 50 Hz AC stimulus. Resistive coatings applied to the edge of AlN ceramic showed promise in reducing PD activity in gel encapsulated samples in [181], but this has yet not seen widespread adoption, likely owing to the move towards higher switching speeds at which this technique is less effective. More recently, charged-film electrets have been shown to reduce electric fields considerably compared to uncharged films when subjected to unipolar square wave stress [209], but this has yet to be experimentally verified in fully representative samples. SiC-filled epoxy resin applied about the triple interface of copper, ceramic and gel was shown in [210] to reduce PD activity under AC stress. This technique shows significant promise and is already being pursued in new high-voltage packaging designs to enhance PD ruggedness [211].

From a geometrical standpoint, increasing the trench width between top copper on the DBC enhances PDIV as shown in [201], where it was also shown that increasing the bend radius starting from 0.3 mm could enhance PDIV. Increasing the thickness of the ceramic is shown via simulation in [182] to reduce the electric field near the triple interface and is experimentally demonstrated to enhance PDIV under 50 Hz AC stress. The authors propose further modification of the DBC geometry with a protruding cap design, which is similar to the mesa concept put forth in [212]. Both designs reduce the electric field about the triple interface in simulation, but the latter also fabricates samples for PD testing under 50 Hz AC stimulus, where the mesa design proves to be effective in enhancing the so-called PD detection voltage (PDDV). Combined material and geometric variations are shown to reduce the electric field stress in critical regions in simulation works performed by [213], [214] but there is only sparse

evidence of practical implementations and therefore the current mature power module packaging types are expected to still be in use for several years to come.

There is uncertainty regarding geometric and material variations to power module designs to increase PD ruggedness, and these approaches are not yet mature for field operation. PD behaviours have shown a complex nonlinear relationship with temperature and humidity for gel encapsulation which is not yet fully understood. The test waveform is also highly sensitive parameter, and the test configuration of current standards is not sufficient to stress substrates fully. Consequently, there is a need to test real field operating substrates in representative environmental conditions, with test stimuli representative of field operation.

2.8 Summary

Although there is growing interest in the hygrothermal reliability of power modules due to the push for higher operating voltages, faster switching speeds and harsh application environments, this research is still somewhat nascent. Standard approaches for hygrothermal reliability testing are yet to be solidly defined and are likely to be application-specific due to the influence of the operating environment, which may vary significantly. Current works look mainly at adaptations of existing long-term reliability tests such as the H3TRB or PCT, showing that hygrothermal stress, when combined with electrical bias, can reduce the power-cycling capability of modules. Characterising lifetime in terms of N_f is important research and will help improve the longevity of converters for use in OWTs in years to come. However, an opportunity arises to address the lack of information about moisture-driven changes in performance in the short-term, which could lead to new understanding of harsh environment operation.

Moisture absorption within the PEM package can occur rapidly in harsh environments, and can lead to near immediate corrosion, which is generally only mitigated by the presence of passivation films. Advances in passivation for newer modules highlight significant advances in humidity-robustness, but this is not yet mature for field operation in high-power PEMs. Silicone gel is revealed to be no significant barrier to moisture ingress and may exacerbate moisture-driven degradation through storage and condensation mechanisms in the presence of forced cooling. The diffusion dynamics within silicone gel are not yet fully understood, and many different approaches have been used in the literature to model

these behaviours. There is little information generally about the behaviours of silicone gel from an electrical perspective at the die attach layer, as this research is more often performed with bulk samples. Nor is there yet an understanding of how moisture retention in the gel may influence the switching performance of devices, which could potentially require additional de-rating or reduction of SOAs to enhance device longevity. The insulation quality of silicone gel is likely to reduce by the mere presence of ambient moisture due to hydrolysis, which has been shown to reduce its crosslinking density. Gravimetric measurements of moisture uptake in gels have been shown to have limited use due to competing absorption-desorption processes whereby gel mass may be lost over time in high humidity.

PD can degrade the insulation over time and is exacerbated by field-enhancing regions such as sharp edges or defects. Such defects may be readily provided by dendritic growth or voids in the insulation structures. Inhomogeneous electric fields about critically weak regions of the die attach or substrate may reduce the PD-ruggedness of modules, leading to early failure. Most research into mitigation of PD in silicone gel encapsulation or PEMs appears to be focused on the substrate geometry or fillers in the gel, with little regard for the presence of moisture due to harsh environment operation. The typical approach is based on electrostatic simulation, which may not adequately capture the complex behaviours at the triple interface when moisture is involved. Fillers such as ATH or $BaTiO_3$ in the gel intended for field stress mitigation may accelerate the rate of moisture absorption within the gel due to their hydrophilic nature, but this is not yet investigated. No comparison of PD behaviours in situ of dry and humid conditions is yet shown in the literature in the context of PEMs, which provides an avenue for critical research underpinning reliability-oriented designs and operation in harsh environments.

This chapter presented the requisite theory of capacitance, permittivity and diffusion modelling which will be used to expand on the gaps identified in the body of work relating to the influence of moisture on performance and reliability of power modules. Equations (16)–(21) will be used in impedance measurements of gel in humid environments, indicative of the moisture absorption in the gel. This will be related to the increase in the dielectric gel's relative permittivity using theory based on (8)–(10). Fits of permittivity data will be performed using (28), (29), (34) and (42), aiming to compare the applicability of Fickian and non-Fickian diffusion models for moisture absorption in silicone gel.

Chapter 3: Impact of High Humidity Environment on Electrical Properties of Silicone Gel Used for Power Module Encapsulation

In this chapter, the impact of moisture absorption by silicone gel encapsulation used for power modules is investigated by capacitance measurements at the bottom of freshly cured gel using bespoke interdigital sensors. As discussed in the previous chapter, the absorption of moisture, which has a high permittivity, by silicone gel is expected to significantly change its electrical properties. Many of the methods and results described in this chapter were presented in [215] but are restated here for clarity.

3.1 Preliminary Investigations

Preliminary investigations into the influence of temperature and humidity on the electrical properties of silicone gel were performed by impedance measurement using an Omicron Bode-100 vector network analyser (VNA) in the range 1 kHz – 50 MHz. Samples were parallel-plate capacitors with silicone gel dielectric, created by sandwiching gel taken from a power module between two flat square copper electrodes (copper-backed FR4; 15 mm^2). A 2.5 mm separation distance was achieved with Nylon nuts. Fig. 3.1 shows photographs of a single sample (Fig. 3.1(a)) and of all samples used in situ (Fig. 3.1(b)). Four samples were placed inside a programmable environment chamber and subjected to varying temperature and humidity stress over 24 h. The chamber was not able to pressurise, so samples were subjected to standard atmospheric pressure only. Impedance measurements were taken every 2 minutes

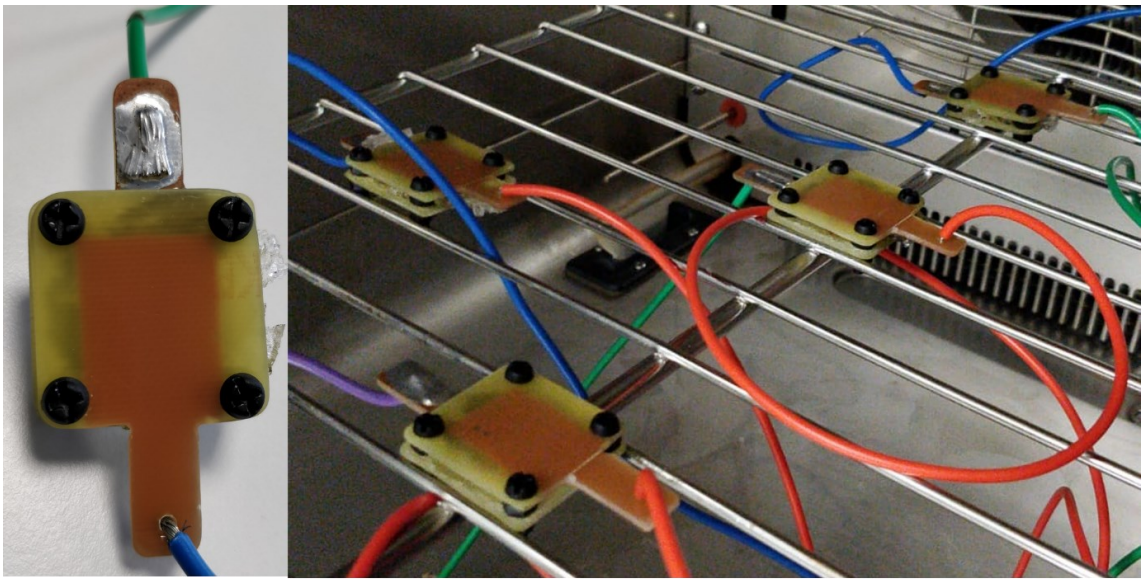

(a) (b)

Fig. 3.1 Parallel-plate capacitor samples used in preliminary investigations. (a) ex situ, (b) in situ.

via automated control of the VNA and a programmable relay board which selected samples as required. Although the interface between the gel and copper was not ideal for these investigations, the intent was to gauge whether any change in electrical parameters was at all evident due to the influence of a varying environment, and worthy of more sophisticated investigation. For this and all subsequent investigations involving the use of the Bode-100 VNA, the influence of measurement leads is mitigated by performing open-short-load compensation. The setpoints for the environment chamber are provided in Table 3.1. The temperature and humidity setpoints were designed to provide significant difference from their low and high values such that any parameter changes were clear, and the duration of test steps was based on expectations of steady-state of the changes in electrical properties based on work of other authors [42].

TABLE 3.1
ENVIRONMENT CHAMBER SETPOINTS FOR PRELIMINARY INVESTIGATIONS

Stage	Temperature [°C]	Relative humidity [% RH]	Sequential duration [h]
1	30	30	2
2	90	30	1
3	90	90	18
4	90	30	1
5	30	30	2

The chamber humidity and temperature over the course of the test are shown in Fig. 3.2. Before the commencement of the test, the temperature and relative humidity in the chamber were 25.6 °C and 94.5% RH, respectively, but the first setpoint (30 °C / 30% RH) was reached after 30 minutes.

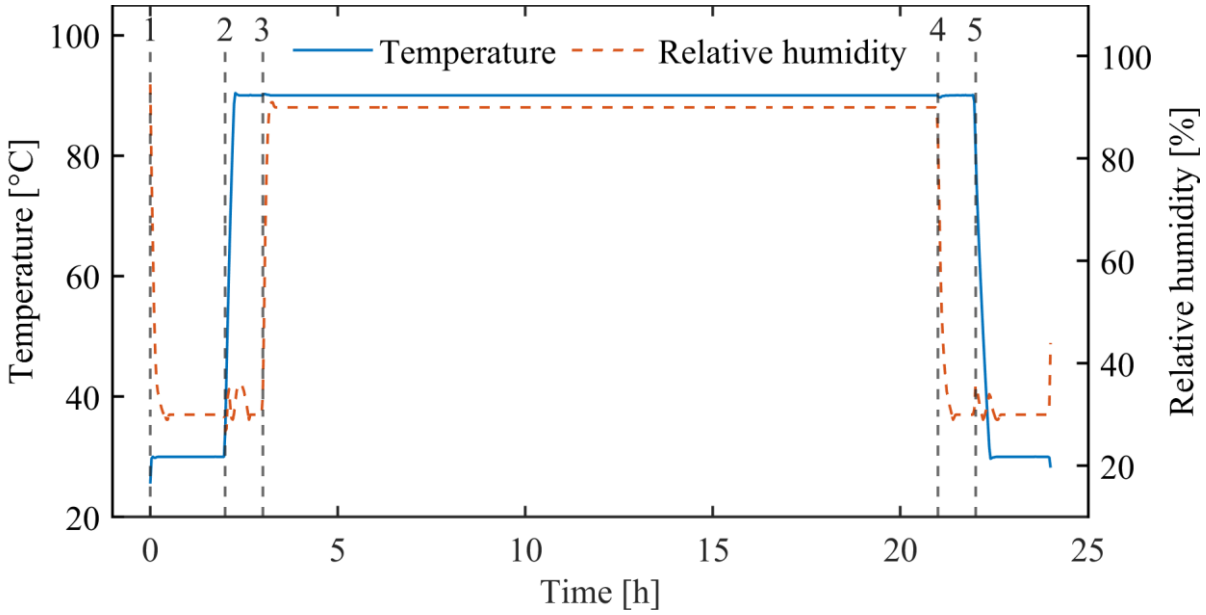

Fig. 3.2 Temperature (blue, solid) and relative humidity (orange, dashed) vs. duration of the preliminary test. Beginning of test stages outlined in Table 3.1 are indicated by the numbered vertical dashed lines.

The humidity in the chamber fluctuates around the temperature transition times, but the extent is limited (+6% RH, -3.25% RH). The initial frequency sweeps taken at the start of the test are shown via Bode plot in Fig. 3.3 and demonstrate the samples acting in a primarily capacitive manner until resonance at about 21 MHz. The samples are also shown to be well matched, and so henceforth the mean ($N = 4$) value will be presented instead.

For clarity, the following visualisations choose a fixed frequency of 2.5 kHz to clearly highlight the variations with the changing environment. Measured impedance and derived parallel model parameters are shown in Fig. 3.4, and derived $tan(\delta)$ is shown in Fig. 3.5. From the brief preliminary investigations, the following conclusions can be drawn in support of further investigations with a more sophisticated test procedure and better sample preparation:

i. An increase in ambient temperature with fixed ambient humidity about the samples reduces impedance magnitude and increases impedance phase. Correspondingly, derived parallel capacitance and resistance are increased and reduced, respectively.

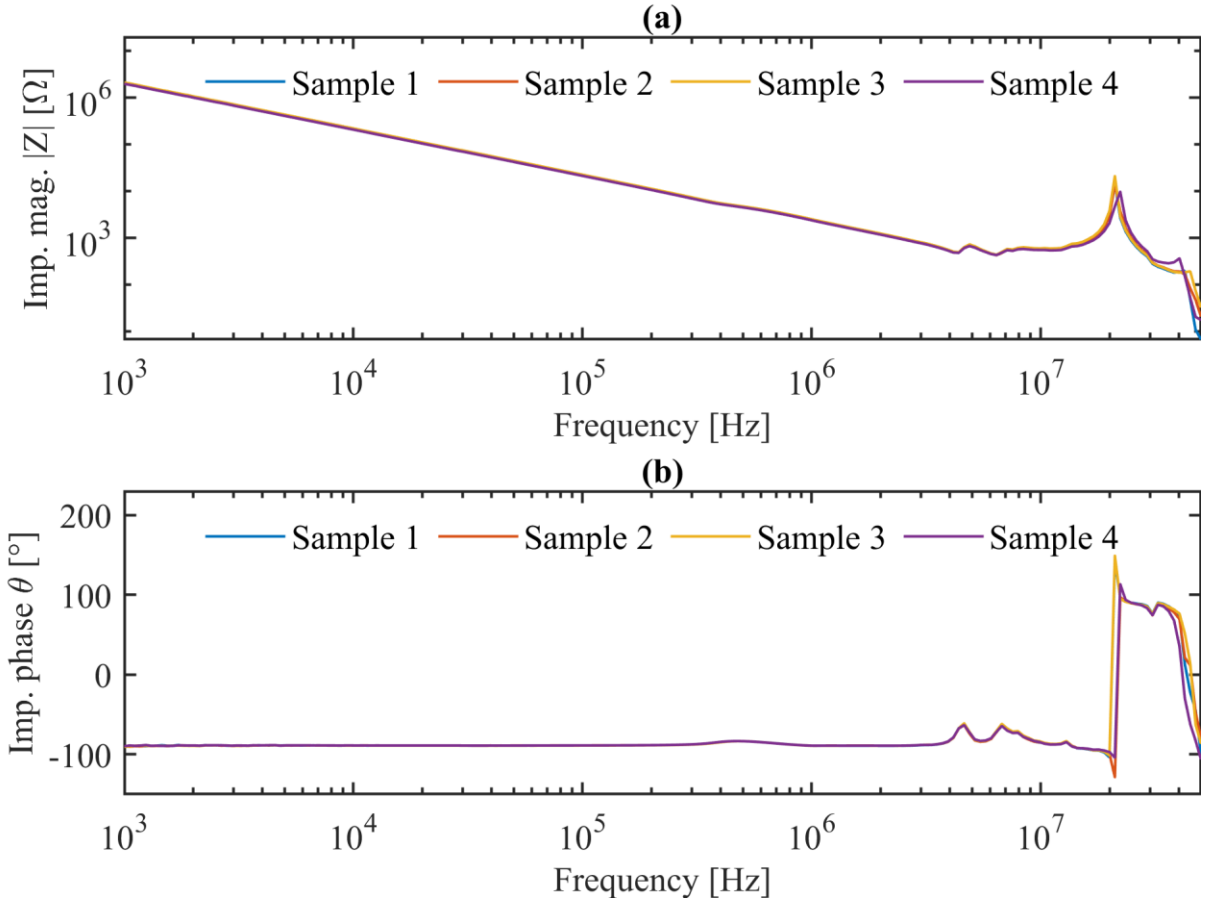

Fig. 3.3 Initial results of impedance measurement for parallel-plate capacitor samples. Values from start of test. (a) impedance magnitude, (b) impedance phase.

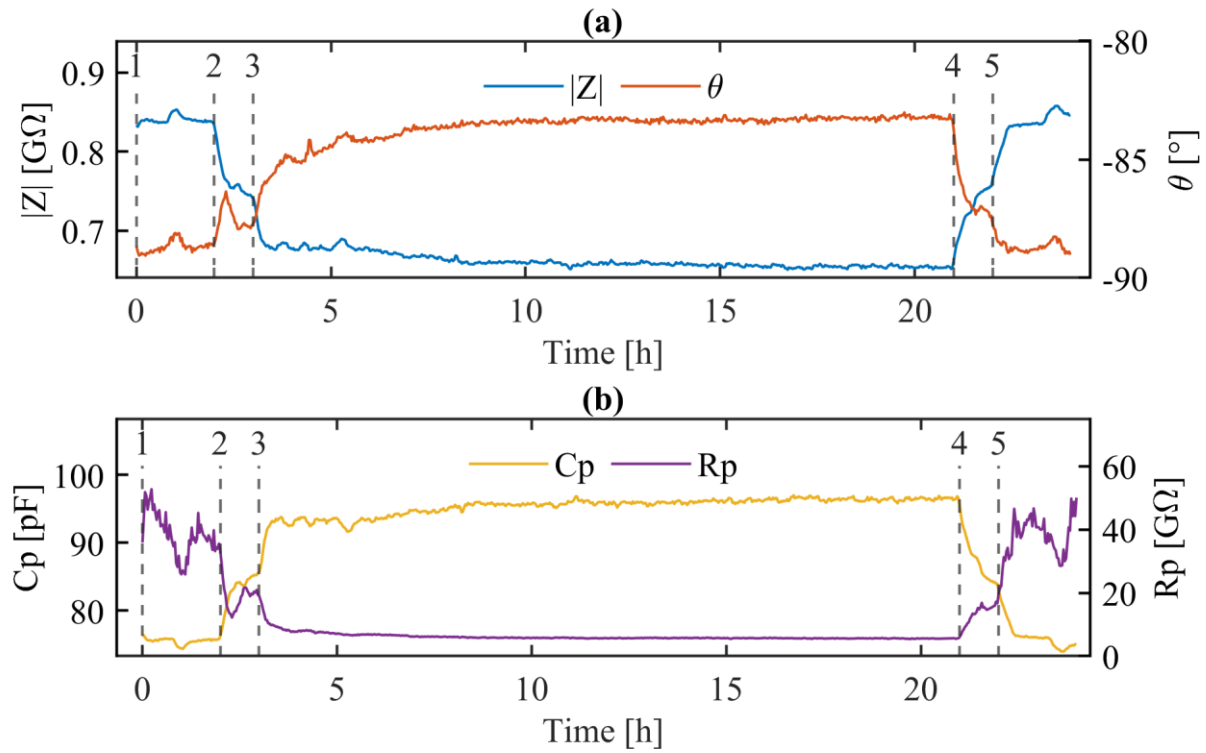

Fig. 3.4 Impedance measurement results for varying temperature and humidity stress (as in Fig. 3.2). (a) impedance magnitude (blue) and phase (orange), (b) parallel capacitance (yellow) and parallel resistance (purple). Only 2.5 kHz values from frequency sweeps are shown for clarity. Values are means across 4 samples. Beginning of test stages outlined in Table 3.1 are indicated by the numbered vertical dashed lines.

ii. The same is true for increasing ambient humidity with fixed temperature, therefore both ambient temperature and humidity are shown to change the electrical properties of the samples investigated.

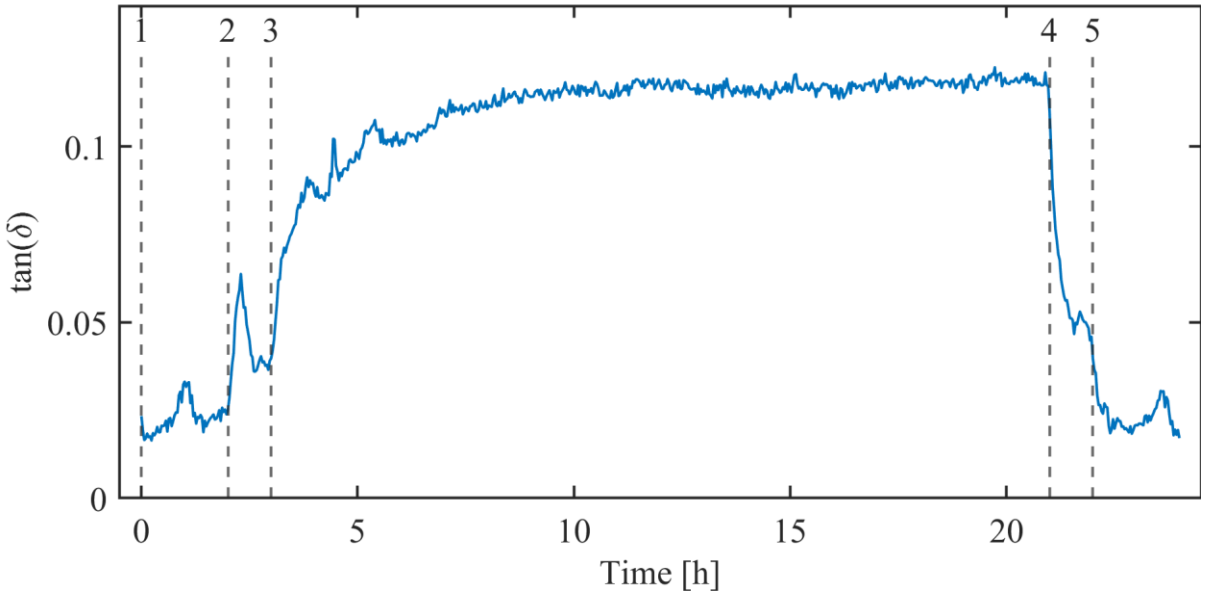

Fig. 3.5 Measured dielectric loss tangent ($tan(\delta)$) for varying temperature and humidity stress (as in Fig. 3.2). Only 2.5 kHz values taken from frequency sweeps are shown for clarity. Values are means across 4 samples. Beginning of test stages outlined in Table 3.1 are indicated by the numbered vertical dashed lines.

iii. Increasing ambient temperature results in an increased $tan(\delta)$ initially, but this relaxes shortly after temperature stabilisation. Increasing the ambient humidity in the chamber results in a further increase in $tan(\delta)$ which does not relax back and appears to saturate after around 8 h.

iv. All changes are in general recoverable upon removal of the high humidity and high temperature stress.

Consequently, it was determined to be worthwhile to evaluate the influence of temperature and humidity stress more thoroughly on the electrical properties of capacitors using silicone gel as a dielectric. This aimed to provide a basis for understanding probable changes in performance and degradation of power modules which use the silicone gel as the primary encapsulation material.

3.2 Embedded Capacitive Sensors

The literature holds several examples of sensing and measuring the presence of moisture within silicone gel. The gravimetric method has already been discussed, but it is also possible to apply the parallel-plate capacitor formula of (8) to suitably dimensioned samples [90]. Such samples require the dielectric to be placed between two electrodes however, which is not representative of the power module application. Fibre-optic sensors have been used for the detection of temperature and RH (T-RH) through several means in the literature, potentially offering minimally invasive embedded measurement approaches. An all-silica combined T-RH sensor was presented in [216], using a porous silica layer coating around a silica micro-wire for the measurement of humidity. Hygroscopic polyimide coatings were applied to fibre-optic cabling to induce strain therein, which was measured using optical frequency domain reflectometry (OFDR) in a 64 m long distributed sensor in [217]. The coatings were improved in their subsequent work [218]. Similar works were performed by other authors at the same time in [219]. Fibre Bragg gratings (FBGs) are also shown in the literature to be effective in T-RH measurements, again using either polyimide or bespoke coatings [220], [221]. These fibre-optic methods all require careful etching processes and calibration and are not demonstrated in embedded applications for either solid or gel insulation. Use of embedded commercial RH sensors has been demonstrated in several cases in the literature. In [84], Sensirion SHT71 T-RH sensors were potted under silicone gel, similar to the later work of [222] which chose to use Sensirion SHT31 sensors. More

recently, commercial temperature and humidity sensors were placed inside the gel encapsulation of power modules under various conditions. SiC power modules with embedded temperature (Analog Devices TS-TMP37) and humidity (Honeywell HIH-5030) sensors were subjected to temperature and humidity stress via a controlled external environment and active heating/cooling of the module baseplate in [156]. Field operation data was applied to stress IGBT modules in a power converter system from a wind power application with embedded sensors (Sensirion SHT35) in [39]. These commercial sensors generally make use of internal capacitive elements, usually combined with a film that absorbs moisture from the ambient environment. Although these sensors were demonstrated successfully in an embedded application in [223], they obfuscate the change in electrical properties of the gel, which was desired in the current work. Consequently, a different sensor solution was sought.

Interdigital sensors of varying geometries were reviewed for a variety of applications in [224], demonstrating their applicability to the parallel RC model of a dielectric material shown in Fig. 2.13. A later review paper explains the IDC approach used in many of the widespread commercial humidity sensors at the time [225]. Nanometre thickness coatings of hafnium dioxide (HfO_2) were used in the fabrication of small IDCs, showing that successful design of the sensors using electrostatic simulation was possible [226]. A fractal spiral capacitor intended for RF applications was demonstrated in [227], highlighting the difficulty of manufacture of such geometries with small dimensions on printed circuit boards (PCBs) at the time. More recently, IDCs printed in silver (Ag) on flexible polymer substrates and potted with silicone gel were shown, demonstrating the feasibility of such sensors for use in PEMs [228]. This approach was followed up in [229], further demonstrating the technique's suitability for use in moisture detection in silicone gel. The last work was presented after much of the experimental work carried out in this chapter was already complete.

3.2.1 Theory of Interdigital Capacitor

This section details the theory behind the IDC structure and demonstrate how the relative permittivity of silicone gel can be obtained via impedance measurement, provided the sensor geometry is known. The IDC sensor concept was pursued in this work to investigate the moisture-induced changes

in electrical properties of the silicone gel at a position representative of the die attach layer in a power module.

Fig. 3.6 shows the general construction of an IDC from a top-down perspective (Fig. 3.6(a)), 3D render (Fig. 3.6(b)) and a cross-section showing one unit cell (Fig. 3.6(c)). The unit cell represents the minimum geometry for calculations, the result of which can be scaled to give the final result. The capacitance of the IDC includes not only the parallel-plate capacitance between the PCB traces within the unit cell, but also contributions from the fringing electric field above and below the traces. The total capacitance for the IDC is product of the capacitance of one unit cell, the effective digit length, and the number of unit cells. This is shown in (44)–(48) [224], [230].

$$C = C_{UC}(N-1)\cdot L \quad [F] \quad (44)$$

$$C_{UC} = C_1 + C_2 + C_3 \quad [F] \quad (45)$$

$$C_1 + C_3 = \varepsilon_0 \cdot \frac{\varepsilon_1 + \varepsilon_3}{2} \cdot \frac{K\left(\sqrt{1-k^2}\right)}{K(k)} \quad [F] \quad (46)$$

$$C_2 = \varepsilon_0 \varepsilon_2 \cdot \frac{h}{a} \quad [F] \quad (47)$$

$$k = \frac{a}{b} \quad (48)$$

where C is the total capacitance of the IDC; C_{UC} is the capacitance of one unit cell; N is the number of digits; L is the effective digit length; C_1 is the partial capacitance due to the fringe electric field in

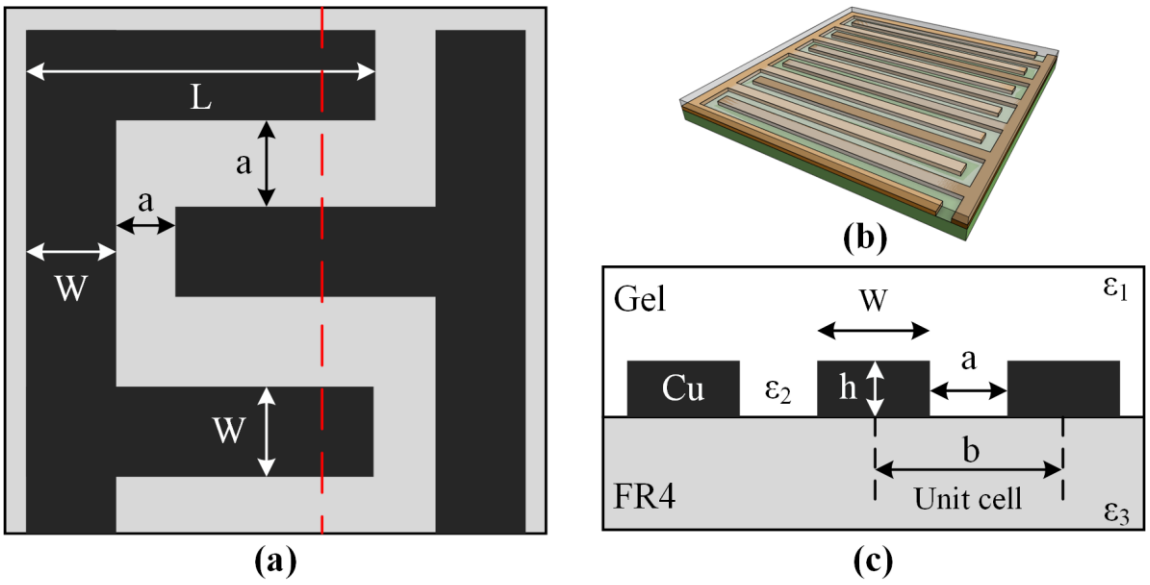

Fig. 3.6 Diagram of major IDC dimensions. (a) top-down view, (b) simple 3D render, (c) cross-section view (cut-plane represented by red dashed line on Fig. 3.6(a)).

the material above the PCB traces; C_2 is the partial capacitance resulting from the parallel-plate arrangement of the PCB traces; C_3 is the partial capacitance due to the fringe electric field in the material below the PCB traces; ε_i represents the relative permittivity of the material above, between and below the traces ($i = 1,2,3$); $K(k)$ is the complete elliptical integral of the first kind; h is the height of the PCB traces; a is the trace separation distance; and b is the width of a single unit cell.

It is possible to use measured capacitance to find the relative permittivity of the material of interest, assuming the geometry of the IDC is known. Assuming that the material above and between the traces is the same ($\varepsilon_1 = \varepsilon_2$), the parameter ε_1 can be found by (49):

$$\varepsilon_1 = \frac{a\left[2C \cdot K(k) - (N-1)L \cdot \varepsilon_0\varepsilon_3 \cdot K\left(\sqrt{1-k^2}\right)\right]}{(N-1)L \cdot \varepsilon_0 \cdot \left[2h \cdot K(k) + a \cdot K\left(\sqrt{1-k^2}\right)\right]} \tag{49}$$

In this work, the parallel capacitance of the IDC is assumed to represent the parallel capacitance of the model for a lossy dielectric system as shown in Fig. 2.13. The parallel resistance of the potted IDC is similarly attributed to the model. The complete elliptic integral of the first kind, $K(k)$, is defined as (50), and is computed here using the arithmetic–geometric mean method (51) [231], [232].

$$K(k) \coloneqq \int_0^{\frac{\pi}{2}} \frac{d\theta}{\sqrt{1-k^2\sin^2\theta}}; \quad 0 < k < 1 \tag{50}$$

$$K(k) = \frac{\pi}{2 \cdot AGM\left(1, \sqrt{1-k^2}\right)} \tag{51}$$

where the real number k is known as the modulus of the elliptic integral, and the real number $k' = \sqrt{1-k^2}, \quad (0 < k' < 1)$ is termed the complementary modulus.

The arithmetic-geometric mean of two numbers is defined as the value at which two interdependent sequences, a_i (the arithmetic mean) and g_i (the geometric mean), converge (i.e., the mutual limit). It can be written as $AGM(p, q)$ based on the following:

$$\begin{aligned} a_0 &= p, & g_0 &= q \\ a_{n+1} &= \frac{1}{2}(a_n + g_n), & g_{n+1} &= \sqrt{a_n \cdot g_n} \end{aligned} \tag{52}$$

3.2.2 Selection of Sensor Geometry via Simulation

It is understood from the theory that the capacitance of the IDC is the sum of the capacitance contributions from the fields between, above, and below the traces. The trace height, minimum trace separation and width are limited to that available from commercial PCB fabricators. The sensitivity of this capacitor to changes in the material above and between the traces is increased if the total capacitance arising from those regions is increased. It is pertinent to identify which controllable design parameters are the most salient for increasing device sensitivity, given practical limitations. The pertinent capabilities of the commercial PCB fabricator used for this work are as follows: minimum trace width 0.127 mm (1 oz.), 0.2 mm (2 oz.); minimum trace separation 0.127 mm (1 oz.), 0.2 mm (2 oz.). As previously stated, electrostatic simulation is a useful tool in designing IDCs, and similar approaches to [226] were used to select sensor geometry for this work. To select which combination of copper weight and trace separation is used, electrostatic simulations of a unit cell were performed in ANSYS Maxwell 2D. The simulation geometry is shown in Fig. 3.7. The values used for each scenario are given in Table 3.2, which also includes the simulated capacitance results for the unit cell in each case. The silicone gel and FR4 Y-axis heights were set to 0.5 mm, with a balloon boundary condition applied. The full thickness of the materials was not required, simplifying the simulation geometry. The excitations used for this simulation were 1 V and 0 V applied to the drive and sense copper traces, respectively.

TABLE 3.2
GEOMETRIC PARAMETERS USED IN ELECTROSTATIC SIMULATION OF IDC

Copper weight [oz.]	a [mm]	b [mm]	h [µm]	W [mm]	C_{UC} [pF]
1	0.127	0.254	35	0.127	47.265
2	0.2	0.4	70	0.2	49.673

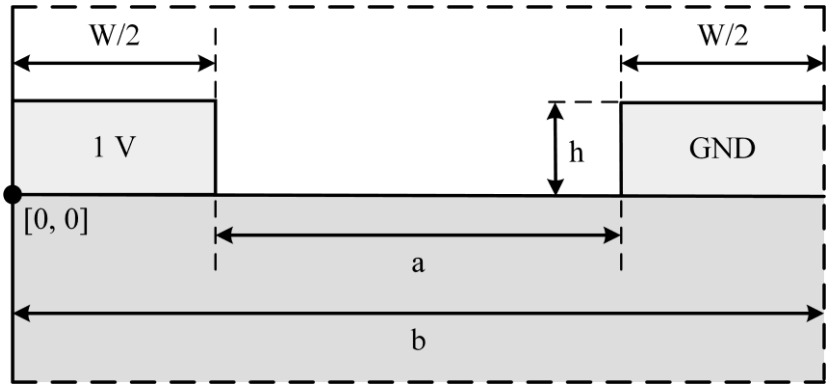

Fig. 3.7 Geometry used for electrostatic simulation of IDC designs. Materials are silicone gel (white background), copper (light grey background) and FR4 (darker grey background). Balloon boundaries are applied to all outer edges.

The difference between the two geometries is minor (2.408 pF, 5.15%) but could amount to a sizeable change in overall capacitance depending on the effective length of the digits (L), and the number of digits (N) chosen for the sensors. Therefore, the geometry using a 2 oz. copper pour was chosen. The remaining design parameters were limited only by the availability and machinability of suitable mould materials, and by the internal envelope of the environment chamber. Note that this simulation captures the influence of both the parallel-plate and fringing field contributions.

Polytetrafluoroethylene (PTFE) was chosen for the mould material to house the sensors and gel, as it was not expected to inhibit the curability of the silicone gel, is easily machinable, can withstand continuous operating temperatures up to 260 °C and is generally understood to not absorb moisture from an ambient environment. Moisture absorption was consequently expected to occur only within the gel, as desired. The resultant outer dimensions for the IDC sensor boards were 60 × 75 mm. Providing adequate spacing for mounting holes limited the final IDC envelope to 58 × 58 mm. A tab was included to support connection points, such that these would not be potted by the silicone gel, and hence influence the measurement due to moisture absorption about the connectors. Given the envelope, the choice of unit cell design parameters and the PCB fabricator capabilities, the final design used $N = 145$ and $L = 57.8$ mm. According to the theory of the IDC previously defined, the total capacitance of the sensor is expected to be 404.32 pF using geometric parameters for the 2 oz. copper weight and with $\varepsilon_1 = 2.7$ and $\varepsilon_3 = 4.4$. Using the C_{UC} value from the simulation in (44), the resultant capacitance should be 413.44 pF, an increase of only 2.26% over the theoretical estimate. Note that these simulations were performed under the assumption of a homogeneous ambient environment in terms of humidity, and an inhomogeneous environment was deemed out of scope.

3.2.3 Sample Preparation

The IDC sensors were placed in pockets of varying depths milled into PTFE moulds. The gel depth measured on a commercial IGBT half bridge module (FF1000R17IE4) was 10 mm above the DBC layer. To ensure the investigations were representative of field operation for a variety of module sizes, the following pocket depths were created in the moulds: 20 mm, 15 mm, 10 mm, 5 mm (measured from the top of the IDC sensors). The silicone gel chosen for this study was Wacker SilGel 612 [75], an

RTV-2 silicone rubber, recommended by the manufacturer for use in the potting of power electronics. Previous authors have measured the breakdown strength of this gel at 32.5 kV·mm^{-1} [76]. The connector tab portion of the sensor boards required the creation of tape dams applied to the mould to avoid leakage of the gel. The mould and sensors were degreased with isopropyl alcohol (IPA) before application of the gel. The gel was mixed in a 1A:1B ratio in clean lab glassware and degassed at approximately 30 mBar in a vacuum chamber to remove any entrained air, before being poured from a low height into the moulds and degassed once more. Per manufacturer guidelines, the degassing stages were designed to ensure collapse of the mixture within 10 minutes [66]. The moulds were then placed inside a controlled environment chamber and left to cure for 8 hours at 30 °C / 30% RH. The addition cure nature of the silicone gel results in no volatile gaseous products. A photograph of the cured IDC samples inside the PTFE mould is provided in Fig. 3.8.

To verify the correct operation of the IDC boards received from the PCB manufacturer, brief investigations were performed with the capacitors uncoated and in free air, submerged in demineralised water (conductivity, $\sigma < 5\ \mu S \cdot cm^{-1}$), submerged in regular domestic water ($\sigma \approx 2500\ \mu S \cdot cm^{-1}$), and after potting with the silicone gel encapsulant ($\sigma \approx 1 \times 10^{-9}\ \mu S \cdot cm^{-1}$). All measurements were taken in room temperature laboratory conditions ($T = 22\ ^{\circ}C,\ RH = 40\%$). A total of 4 sensors were measured for validation purposes. The mean values of these capacitance measurements are shown in

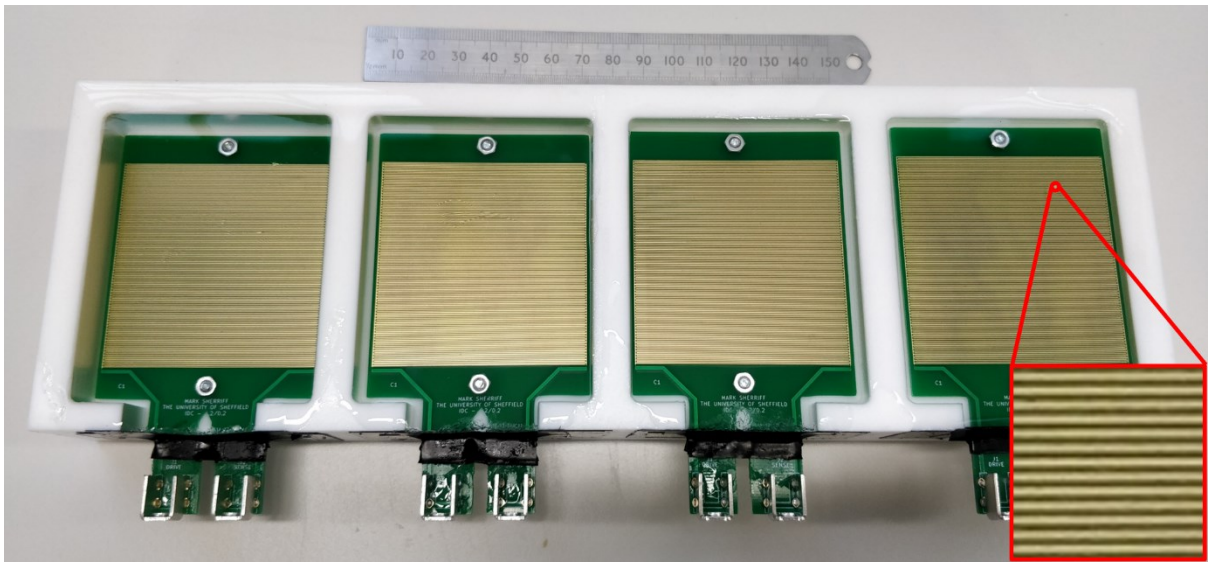

Fig. 3.8 Photograph of IDC sensors in PTFE mould with dielectric gel cured over top. Gel depths measured from top of IDC boards, left to right: 20 mm, 15 mm, 10 mm, 5 mm. Inset: zoom-in on section showing individual PCB traces constituting IDC structure.

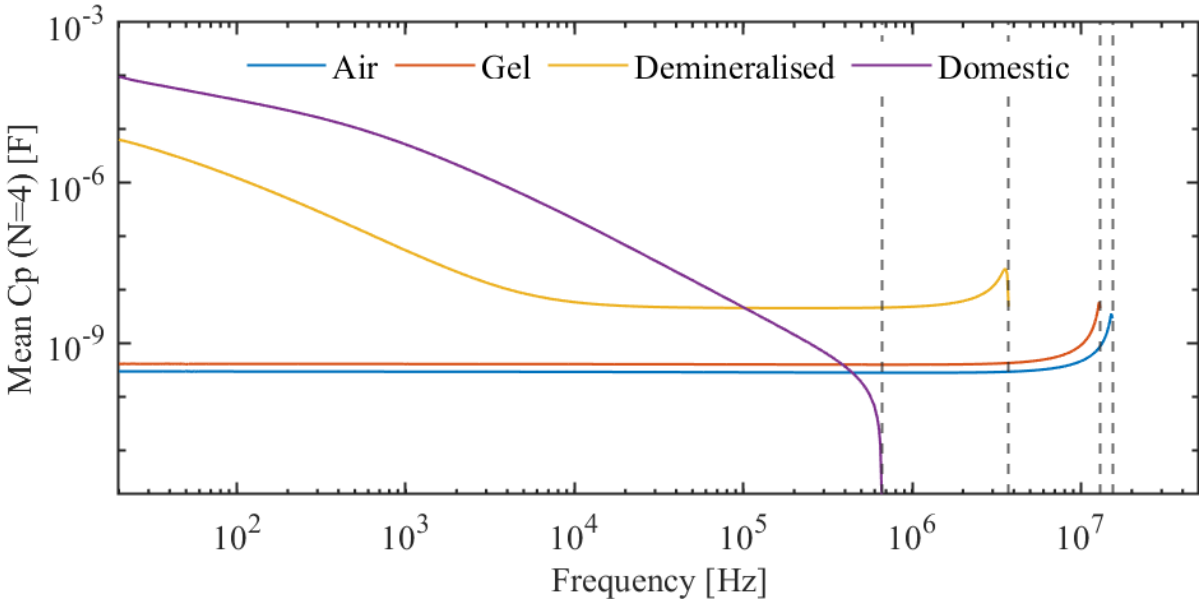

Fig. 3.9 Mean capacitance ($N = 4$) of IDCs in various fluids. Results until resonance due to logarithmic scale. In air (blue), in dielectric gel (orange), in demineralised water (yellow) and in domestic water (purple).

Fig. 3.9. In free air, the capacitance ranges from 279–296 pF, decreasing slightly as the measurement frequency increases. The value increases at higher frequencies due to resonance, which in air occurs at 15.89 MHz. A significant increase in the capacitance is seen across the full frequency range when the dielectric is changed. For silicone gel encapsulant, the capacitance ranged from 394.93–409.21 pF, with resonance at 5.85 MHz. This is close to the theoretical and simulated capacitance values determined previously (404.32 pF and 413.44 pF, respectively), indicating good agreement between the theory, simulation, and the finalised sensors.

When the bare sensors are submerged in water, a significant increase in the mean measured capacitance is observed due to the high relative permittivity of the water (~81). When demineralised water is used, the 20 Hz capacitance is increased to 6.44 µF. This plateaus to 45.16 nF at 218.6 kHz before increasing due to resonance, which occurs at 3.73 MHz. When submerged in domestic water, the mean capacitance of the bare sensors at 20 Hz was increased to 93.40 µF, falling until resonance at 660.05 kHz. The high relative permittivity alone is not sufficient to describe the nonlinear change in capacitance with frequency when the bare sensors are submerged in water. As previously discussed, relative permittivity depends on the sum contributions of various polarisation phenomena. The increase of capacitance over the air and gel cases in the flat portion of the demineralised water case (20 kHz – 10 MHz) is likely due to dipole orientation polarisation of the water molecules. As the conductivity of

the water increases, the number of mobile ions present in the water is increased. Demineralised water is not completely free of contaminants. At lower frequencies, these free charges are given sufficient time under the external electric field to accumulate around the corresponding conductor surfaces each half cycle. Consequently, the increase in low frequency capacitance can be explained by space charge (interfacial) polarisation. As the dry silicone gel absorbs moisture, the capacitance measurement is expected to saturate at some value between the dry gel and submerged cases shown here, and similar frequency-driven trends determined by polarisation mechanisms are expected to occur. While modern power modules switch at higher frequencies than the range at which significant capacitance increase is observed here, the fact that capacitance is increased across the range of measurement is worthy of further investigation. Additionally, modulation techniques may introduce low frequency switching components sufficient in magnitude to drive the low-frequency polarisation mechanisms.

3.3 Capacitance Measurements in Various Environments

3.3.1 Measurement System

The moisture absorption steady-state time of the silicone gel given in the literature ranges was on the order of hours or days [42], [79], [229]. The rate of moisture absorption over time was the focus of this study, so periodic measurement using an automated system was required. A graphical diagram of the measurement system is provided in Fig. 3.10. Samples were placed inside a temperature and humidity chamber (Espec SH-662) and connected via high-temperature hookup wire. A Bode-100 VNA was used to take periodic frequency sweeps (1 kHz – 50 MHz) of impedance and phase, with a period of 120 s. The MATLAB-based timing software ran on a nearby PC. Measurements received from the chamber were checked against an additional T/RH sensor (TE Connectivity HTM2500LF) during commissioning and showed good agreement. Photographs of the measurement equipment and the

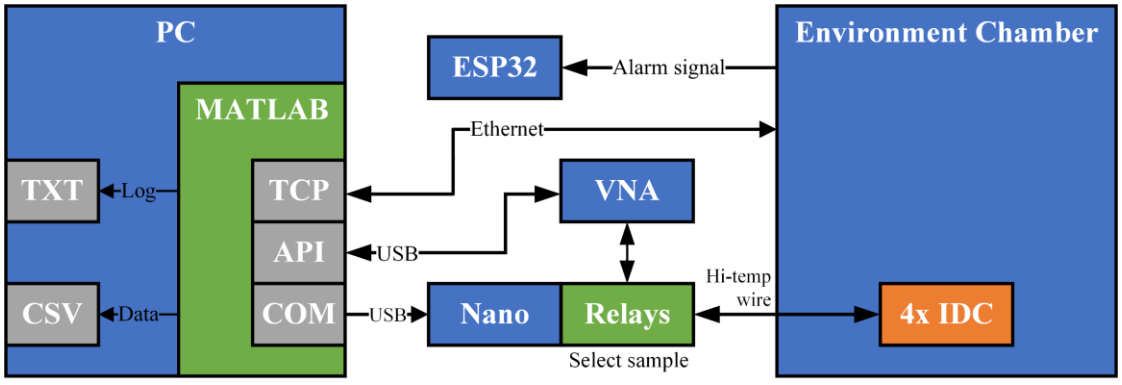

Fig. 3.10 Diagram of key components of automated impedance measurement platform.

samples in situ are shown in Fig. 3.11. The Bode-100 application programming interface (API) for MATLAB was used to calibrate, trigger measurements, and receive the measurement data from the VNA. An Arduino Nano was used to interpret serial commands from the software to a relay board, which was used to select the DUT. The software saved the measurement data locally and provided a log for debugging in case of error. The error reporting capability of the environment chamber was

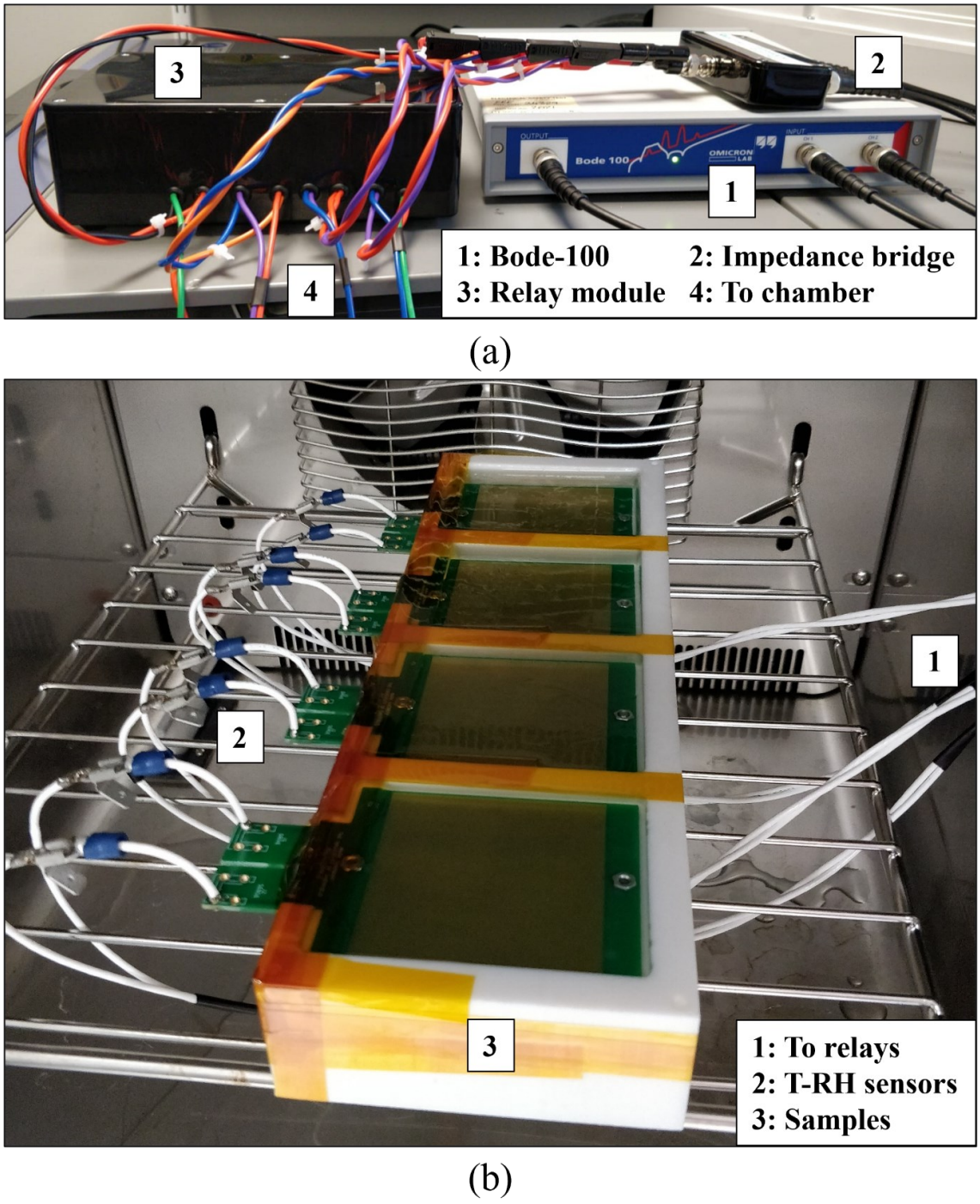

Fig. 3.11 Photographs of: (a) measurement equipment for testing, showing VNA and relay module connections on top of the environment chamber, and; (b) gel-encapsulated IDC samples in situ of the environment chamber highlighting location of T-RH sensors.

interfaced with an ESP32 microcontroller to send email alerts in case of fault states such as: low water, chamber door open, or temperature and humidity exceeding preprogrammed limits.

3.3.2 Temperature-only Testing

i. Test Procedure

To examine the change of the gel's electrical properties solely due to variation in the ambient temperature, testing was performed at various temperatures with a fixed ambient humidity (20% RH). This was intended to characterise the temperature dependence of the dielectric properties of the gel for use in future works, and to possibly rule out permittivity variation with temperature as a confounding factor in other experiments. Samples were placed in the environment chamber and connected to the measurement system, before being subjected to a forced dry-out condition of 95 °C / 20% RH for 24 hours before the application of test setpoints. The setpoints for the temperature-only testing are provided in Table 3.3. The temperature was reduced in a stepwise fashion every 15 hours from the dry-out condition rather than changing from the dry-out condition to a low temperature first and then increasing. This was intended to provide the best chance of avoiding any unintentional moisture absorption in the samples when transitioning from the preconditioning phase to the first setpoint.

TABLE 3.3
SETPOINTS FOR TEMPERATURE-ONLY TESTING

Stage	Temperature [°C]	Relative humidity [% RH]	Absolute humidity [$g \cdot m^{-3}$]	Sequential duration [h]
0	95	20	98.402	24
1	95	20	98.402	15
2	80	20	58.192	15
3	60	20	26.247	15
4	40	20	10.354	15
5	20	20	3.446	15

ii. Results

The temperature and relative humidity for the test are shown in Fig. 3.12. These parameters are measured by the environment chamber in the upper-rear corner, using wet and dry bulb sensors. The chamber holds to the setpoints well in all but the following cases: on reduction of the temperature from 60 °C to 40 °C the humidity jumps to 45% RH, stabilising in 20 minutes, and on reduction to 20 °C the chamber cannot maintain the 20% RH setpoint, with a mean value during this period of about 26% RH.

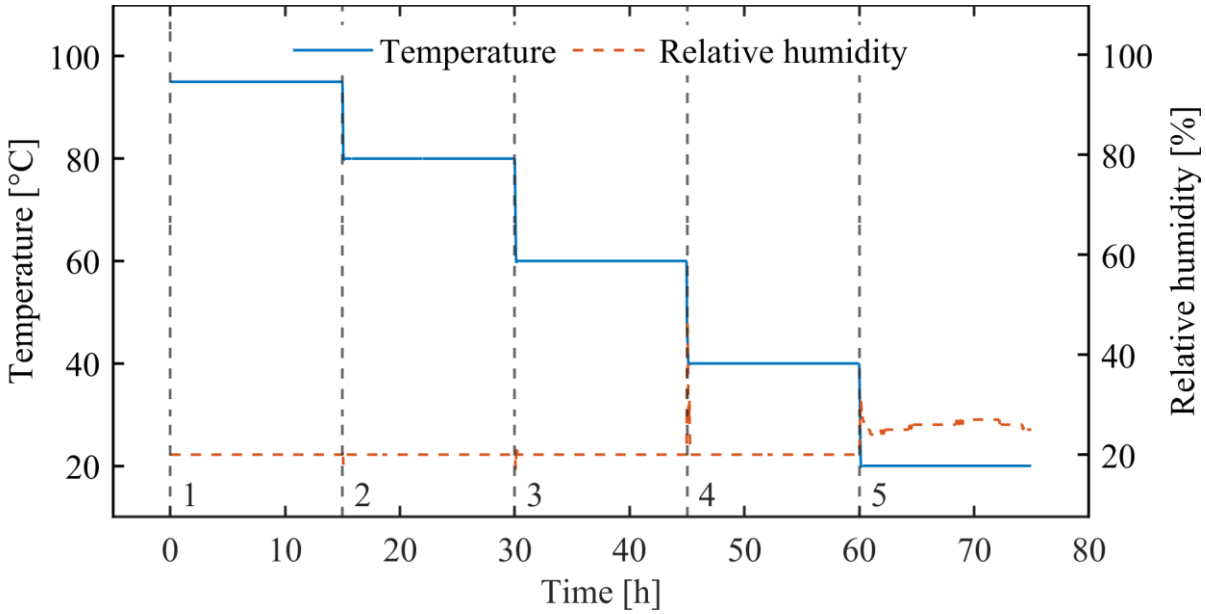

Fig. 3.12 Temperature (blue) and relative humidity (orange, dashed) as measured by the environment chamber over the course of the temperature-only test. Beginning of test stages outlined in Table 3.3 are indicated by the numbered vertical dashed lines. Data not recorded during preconditioning (Stage 0).

Consequently, any sudden changes in the electrical properties at these times could in part be explained by the inability of the environment chamber to maintain setpoints. Fig. 3.13 shows impedance phase and magnitude, inferred sample parallel capacitance, and inferred parallel resistance for each sample at the end of each setpoint, demonstrating the inability of this visualisation to capture the change in sample behaviours over time. Fig. 3.13 highlights measurement error in parallel resistance before 10 kHz, which could be reflected in the other measurement parameters. The source level of the Bode-100 VNA (13 dBm) may result in low signal-to-noise ratio (SNR) due to the high impedance of the samples. The Bode-100 VNA required the use of an external measurement bridge adapter for high impedance measurement, which could cause additional error due to poor matching over the range of sample impedance. Similar errors are observed in inferred parallel resistance above 30 MHz, potentially due to inadequate compensation. Due to the nature of the in situ environmental testing, 1 m of cabling is required to connect the samples to the VNA in each direction. Given the measurement error at low and high frequencies, 10 kHz values are shown in the following plots to investigate the change in electrical properties over time under test. Fig. 3.14 shows the 10 kHz values of inferred parallel capacitance, inferred parallel resistance, $tan(\delta)$, and relative permittivity calculated using (49), for the temperature-only testing. To demonstrate relative change in the parameters, rather than absolute, Fig. 3.15 shows the percentage difference in the 10 kHz values over time from the start-of-test values.

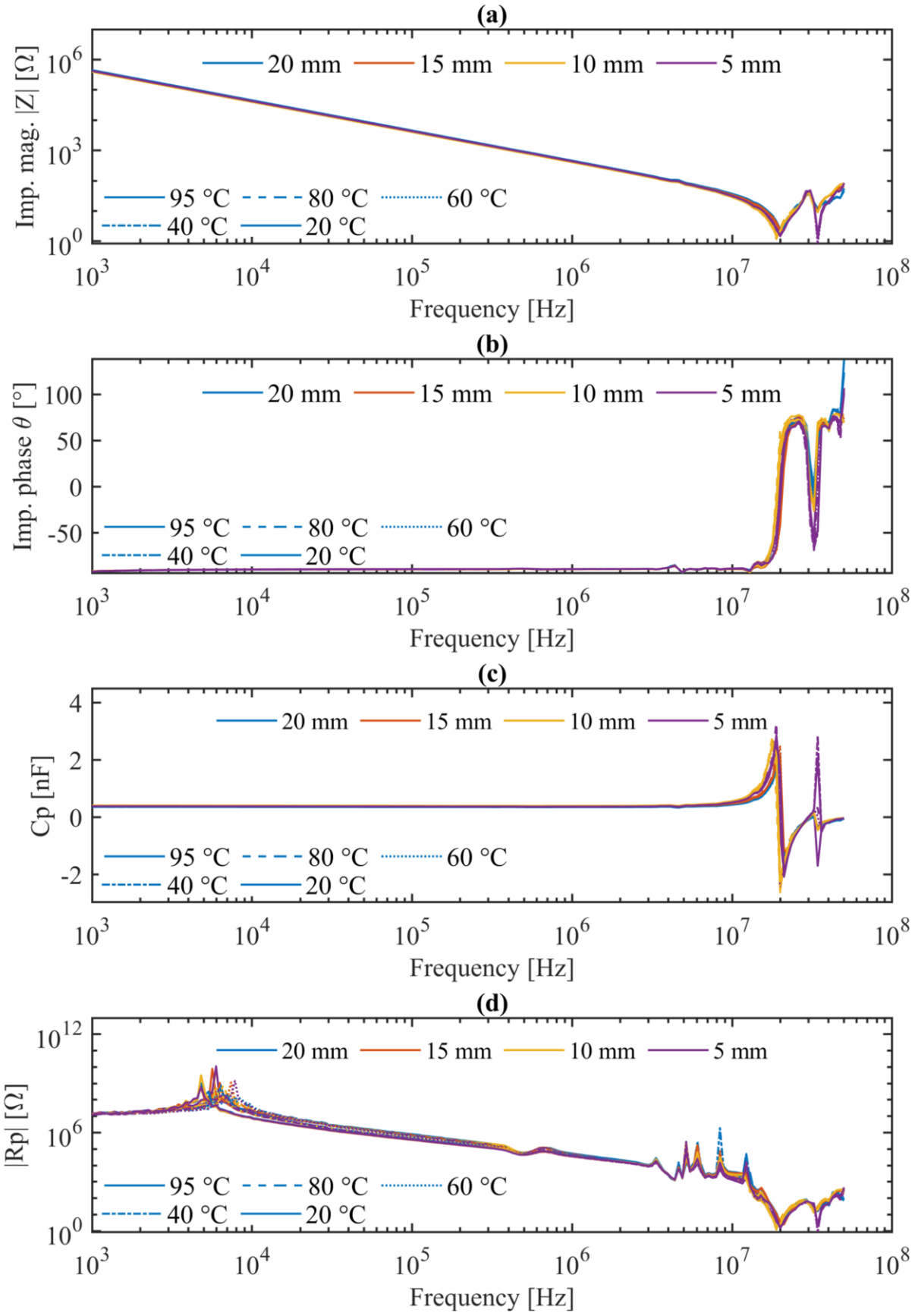

Fig. 3.13 Plots of sample electrical parameters against frequency for individual points in time over the course of the temperature-only testing. (a) impedance magnitude, (b) impedance phase, (c) inferred parallel capacitance, (d) inferred parallel resistance. Sample gel depth represented by plot colour: 20 mm (blue), 15 mm (orange), 10 mm (yellow), 5 mm (purple). Values are taken from end of each temperature setpoint (after 15 hours).

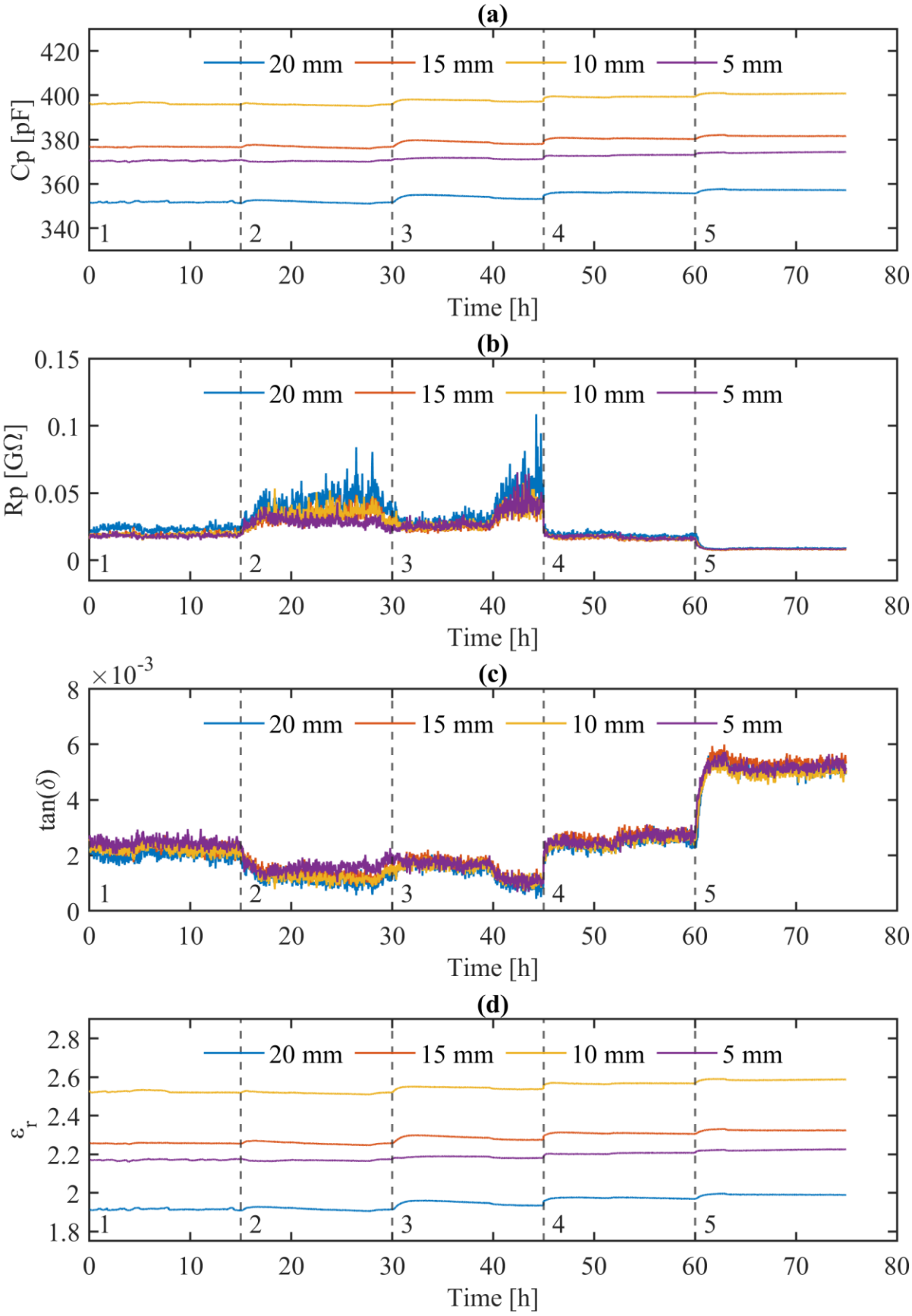

Fig. 3.14 Plots of 10 kHz values recorded over time for the temperature-only testing with gel encapsulated DBC samples. (a) inferred parallel capacitance, (b) inferred parallel resistance, (c) derived $tan(\delta)$, and (d) relative permittivity calculated using (49). Gel depths indicated by trace colour: 20 mm (blue), 15 mm (orange), 10 mm (yellow), and 5 mm (purple). Test stages indicated by vertical dashed lines.

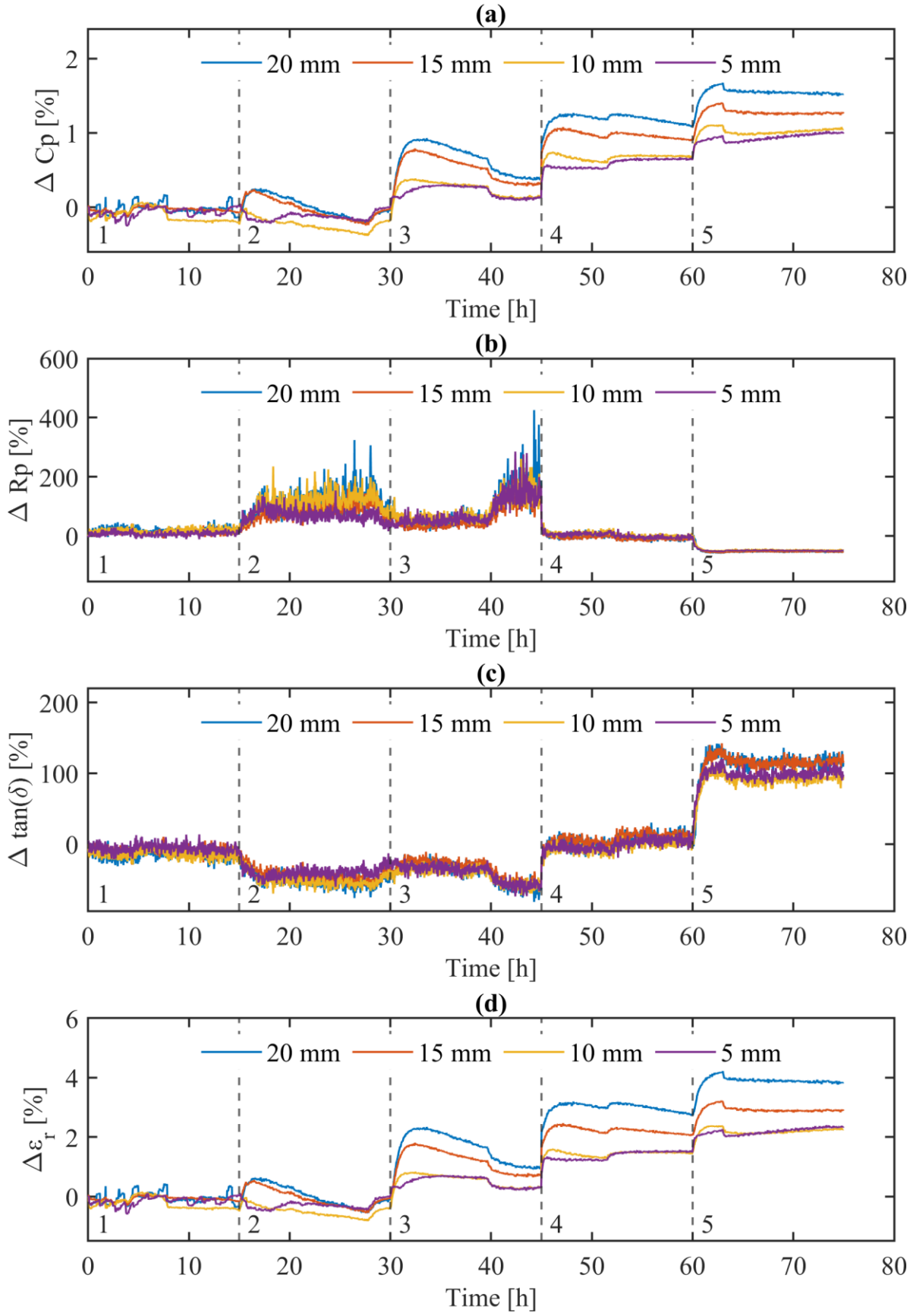

Fig. 3.15 Plots of percentage change in 10 kHz parameters from start-of-test values for the temperature-only testing with gel encapsulated DBC samples. (a) inferred parallel capacitance, (b) inferred parallel resistance, (c) derived $tan(\delta)$, and (d) relative permittivity calculated using (49). Gel depths indicated by trace colour: 20 mm (blue), 15 mm (orange), 10 mm (yellow), and 5 mm (purple). Test stages indicated by vertical dashed lines.

As previously stated, the temperature-only test was performed in steps of reducing temperature to avoid the effect of moisture absorption when changing from the preconditioning (95 °C / 20% RH) stage to the start of test. It is useful to reverse the temperature direction and examine the behaviour of the relative permittivity of the material in terms of temperature, using the end-of-setpoint values. These results are shown in Fig. 3.16, including both ε_r' and ε_r''. Generally, both the real and complex parts of relative permittivity appear to reduce for increasing temperature. For ε_r', the percentage reduction from 20–95 °C implies a function of the gel thickness, with total reductions of 2.2%, 2.6%, 3.0%, and 4.0% for the 5 mm, 10 mm, 15 mm, and 20 mm gel depths, respectively. This result could be due to the

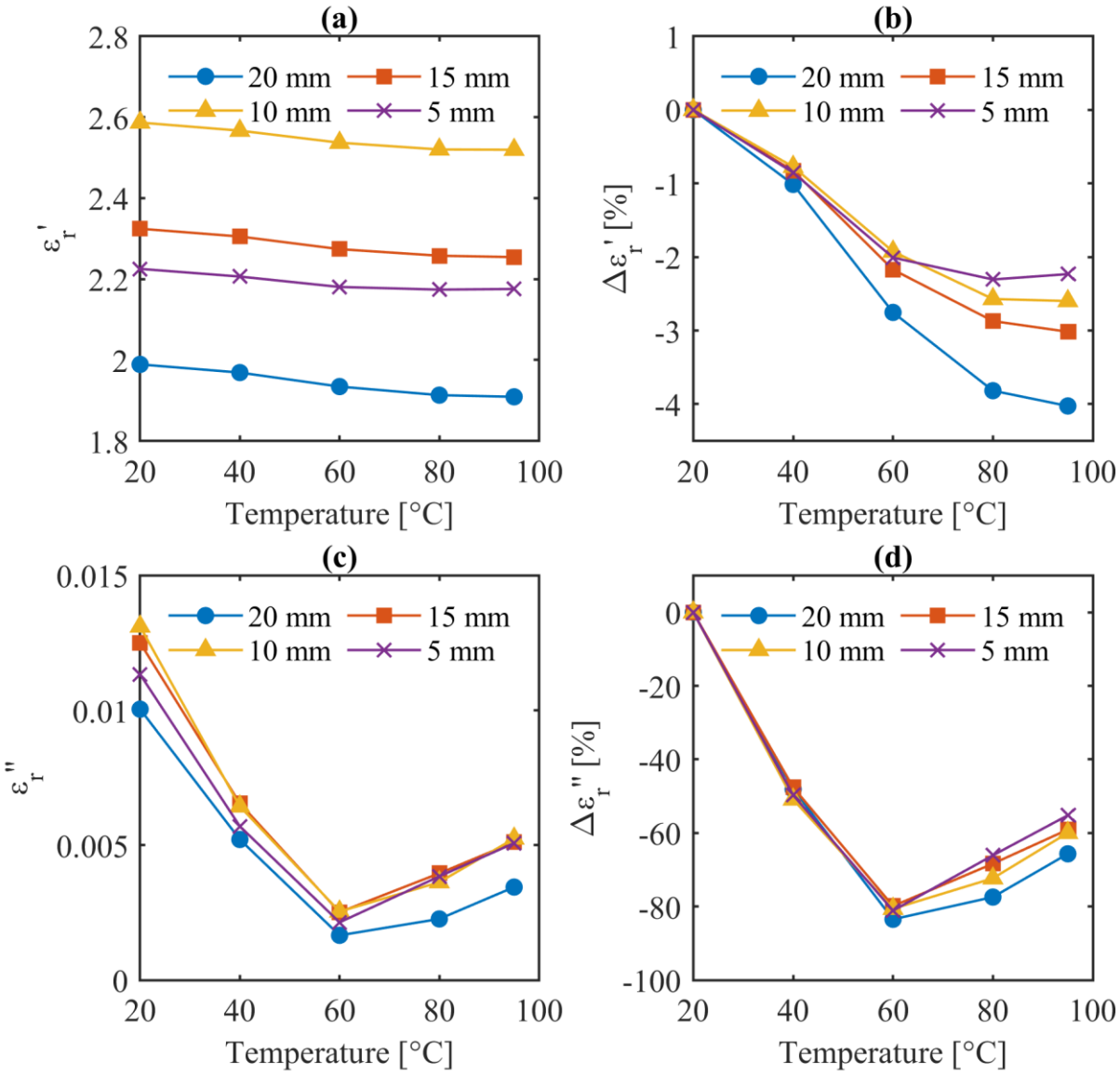

Fig. 3.16 Variation in 10 kHz values of ε_r' and ε_r'' for increasing temperatures (20–95 °C). End-of-setpoint values shown. (a) estimated 10 kHz ε_r', (b) percentage change in estimated 10 kHz ε_r' from 20 °C, (c) estimated 10 kHz ε_r'', and (d) percentage change in estimated 10 kHz ε_r'' from 20 °C. Gel depths are 20 mm (blue, circle), 15 mm (orange, square), 10 mm (yellow, triangle) and 5 mm (purple, cross).

diffusion path length or the thermal mass of the gel itself, as all other factors were identical for the test. The nominal C_p for each gel thickness sample was not identical and ranged from 351.82 pF for the 20 mm sample at 95 °C to 396.58 pF for the 10 mm sample. Although this variance could contribute to the percentage change at 95 °C relative to 20 °C, it is not related to the gel thickness in the same way as the reduction in ε_r'. Additionally, $\Delta\varepsilon_r'$ (and correspondingly ΔC_p) is the only parameter in this testing that shows a distribution similar in nature to the gel thickness. Consequently, the link between gel thickness and $\Delta\varepsilon_r'$ is credited to sample variance, rather than any correlation. From 20–60 °C, both ε_r' and ε_r'' are shown to reduce, but the behaviours differ for the 80–95 °C setpoints. The change in ε_r' begins to plateau, and ε_r'' begins to increase. This inflection point could be due to the humidity spike at the beginning of the 40 °C setpoint, and the inability of the chamber to control 20% RH for the 20 °C setpoint. The relative magnitudes of these changes in relative humidity are minor, indicating that ε_r'' is especially sensitive to variations in the ambient humidity. This will be investigated in the humidity-only testing. It is also worth noting that the trend in the values for ε_r' at low temperatures could also be impacted by the increased humidity at those setpoints, although clearly to a lesser extent. The picture is evidently not perfectly clear for the variation of electrical parameters of the gel in this scenario when temperature is the controlled environmental parameter. Slight changes in the ambient humidity appear to cause significant changes in the electrical parameters when considering the relative scale of the changes in ambient temperature, and the changes in ambient humidity.

Proportionally, the results thus far indicate that the temperature-only condition has a weak impact on the electrical properties of the gel. When proceeding from 95–60 °C, a minor increase in ε_r' is observed ($\overline{\Delta\varepsilon_r'}\{95\,°C \rightarrow 60\,°C\} = +0.76\%$), and in the same temperature interval, a significant reduction in ε_r'' is observed ($\overline{\Delta\varepsilon_r''}\{95\,°C \rightarrow 60\,°C\} = -53.01\%$). From the 60 °C to the 20 °C setpoints, the change in ε_r' continues with the same trend ($\overline{\Delta\varepsilon_r'}\{60\,°C \rightarrow 20\,°C\} = +2.27\%$), but ε_r'' appears to be heavily influenced by the unexpected presence of elevated ambient humidity as shown in Fig. 3.12 and increases significantly ($\overline{\Delta\varepsilon_r''}\{60\,°C \rightarrow 20\,°C\} = +436.54\%$).

3.3.3 Humidity-only Testing

i. Test Procedure

Given the significant impact of the ambient humidity on the electrical properties highlighted by the temperature-only testing, similar tests were repeated for the gel samples in an isothermal environment with varying ambient humidity. Samples were placed inside the environment chamber and connected to the automated measurement system previously described. A frequency sweep was triggered every 30 s, with sweeps performed on each sample in turn, giving an effective measurement period of 120 s. The gel encapsulated IDC samples were held in the dry-out condition (95 °C / 20% RH) for 24 h before commencement of the test, which consisted of stepwise increasing RH setpoints with a fixed ambient temperature throughout. A dwell of 24 h was held at each environmental condition. As in the temperature-only testing, a total of 4 gel-depth samples were investigated, with depths 5 mm, 10 mm, 15 mm, and 20 mm, measured from the top of the IDC sensor boards. A summary of the test conditions and durations is provided in Table 3.4.

TABLE 3.4
SETPOINTS FOR HUMIDITY-ONLY TESTING

Stage	Temperature [°C]	Relative humidity [% RH]	Absolute humidity [$g \cdot m^{-3}$]	Sequential duration [h]
0	95	20	98.402	24
1	30	30	9.177	24
2	30	60	18.355	24
3	30	90	27.532	24

ii. Results

The temperature and RH as measured by the environment chamber over the course of the test are shown in Fig. 3.17. The chamber stabilises at the first setpoint (30 °C / 30% RH) only 40 minutes after the dry-out condition, with humidity varying from 17% to 43% RH in that window. A slight overshoot of about 2% RH the humidity is seen at each change of setpoint, settling after approximately 14 minutes. Consequently, the chamber holds to the test setpoints with only negligible error over the course of the test, so due to the isothermal environment, the changes in the electrical properties of the gel samples are expected to be almost purely due to changes in the ambient humidity. In this test, the impact of temperature has been sufficiently isolated as to not be a confounding factor.

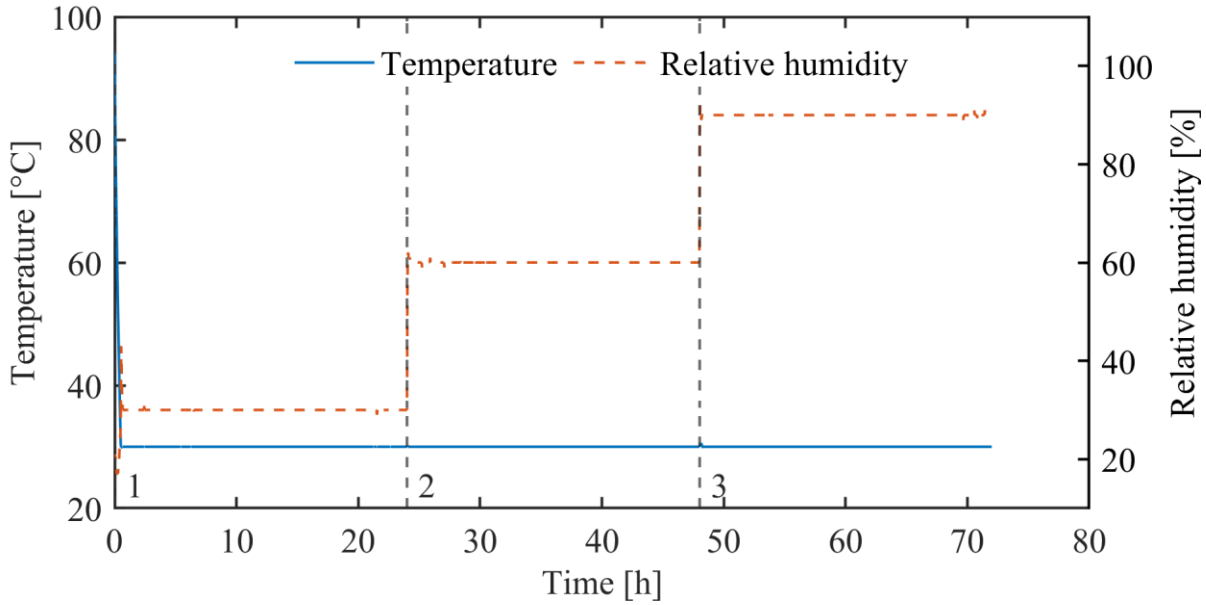

Fig. 3.17 Temperature (blue) and relative humidity (orange, dashed) as measured by the environment chamber over the course of the humidity-only test. Beginning of test stages outlined in Table 3.4 are indicated by the numbered vertical dashed lines. Data not recorded during preconditioning (Stage 0).

As with the temperature-only test, it is difficult to identify changes in the behaviours of the samples over the course of the humidity-only test when considering frequency sweeps. The frequency sweep data for each sample at the end of each setpoint are shown in Fig. 3.18, which includes impedance magnitude and phase, as well as inferred parallel capacitance and resistance. Due to measurement noise at low frequencies, significant error is presumed to be present in the R_p data, causing negative values before an inflection point. In general, increasing the RH applies a slight downshift in the primary resonant frequency for the $|Z|$ data, although measurement error must be considered. This is reinforced by a slight increase in C_p for each sample with increasing RH, as shown in Fig. 3.18(c), although the respective increases appear to be slight. Due to the measurement errors at low and high frequencies as discussed previously, choosing a single frequency allows the nature of changes in the electrical properties of the samples over time to be more clearly demonstrated. In the interest of consistency with previous results, the 10 kHz values for the data are shown in Fig. 3.19. The percentage change in these values from the start of test is shown in Fig. 3.20. Low-frequency noise notwithstanding, a reduction in R_p is observed for increasing RH up to about 100 kHz, with a downshift in the R_p inflection frequency. This implies an increase in the conductivity of the gel due to moisture absorption.

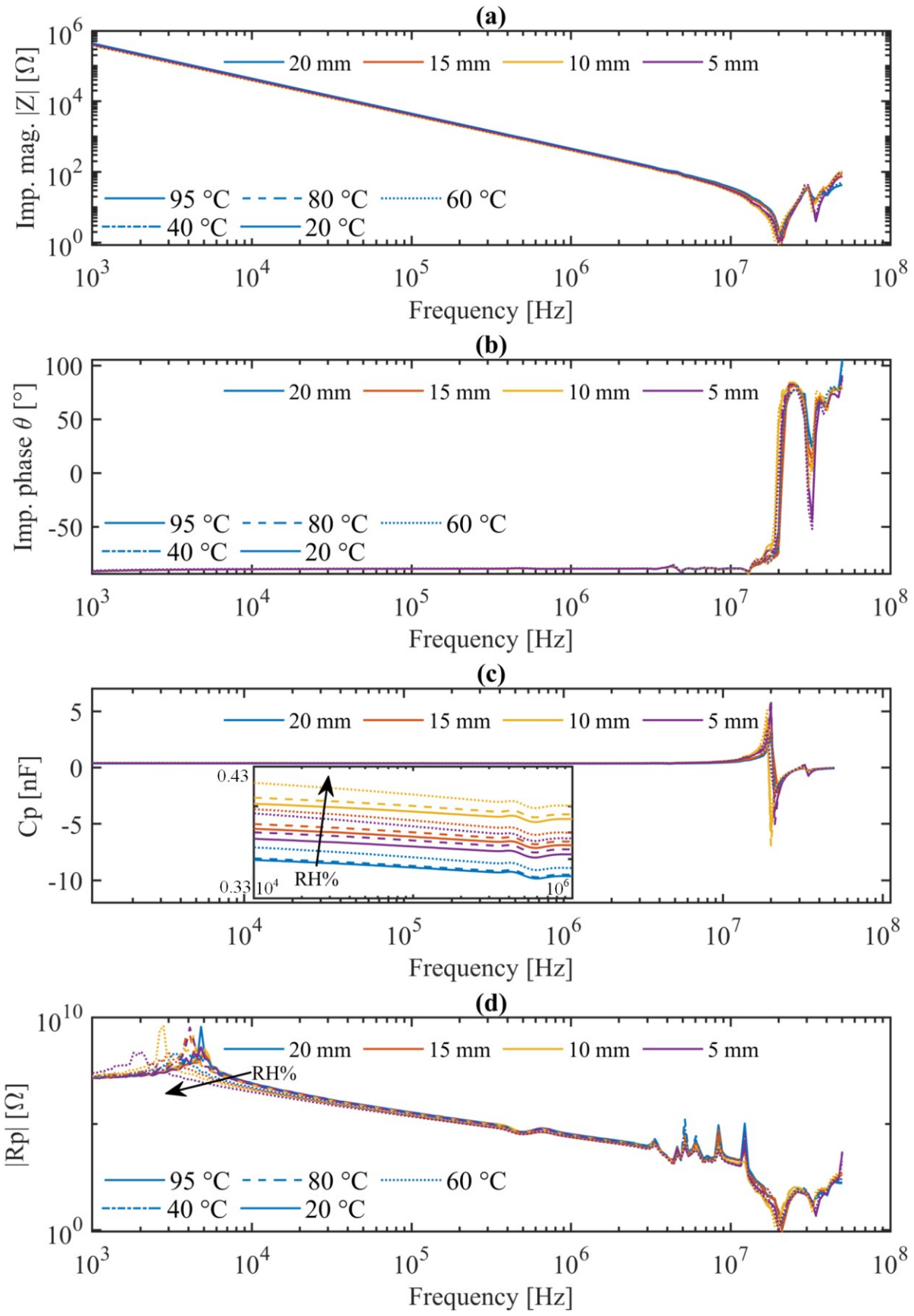

Fig. 3.18 Plots of sample electrical parameters against frequency for individual points in time over the course of the humidity-only testing. (a) impedance magnitude, (b) impedance phase, (c) inferred parallel capacitance, (d) inferred parallel resistance. Sample gel depth represented by plot colour: 20 mm (blue), 15 mm (orange), 10 mm (yellow), 5 mm (purple). Values from end of humidity setpoints.

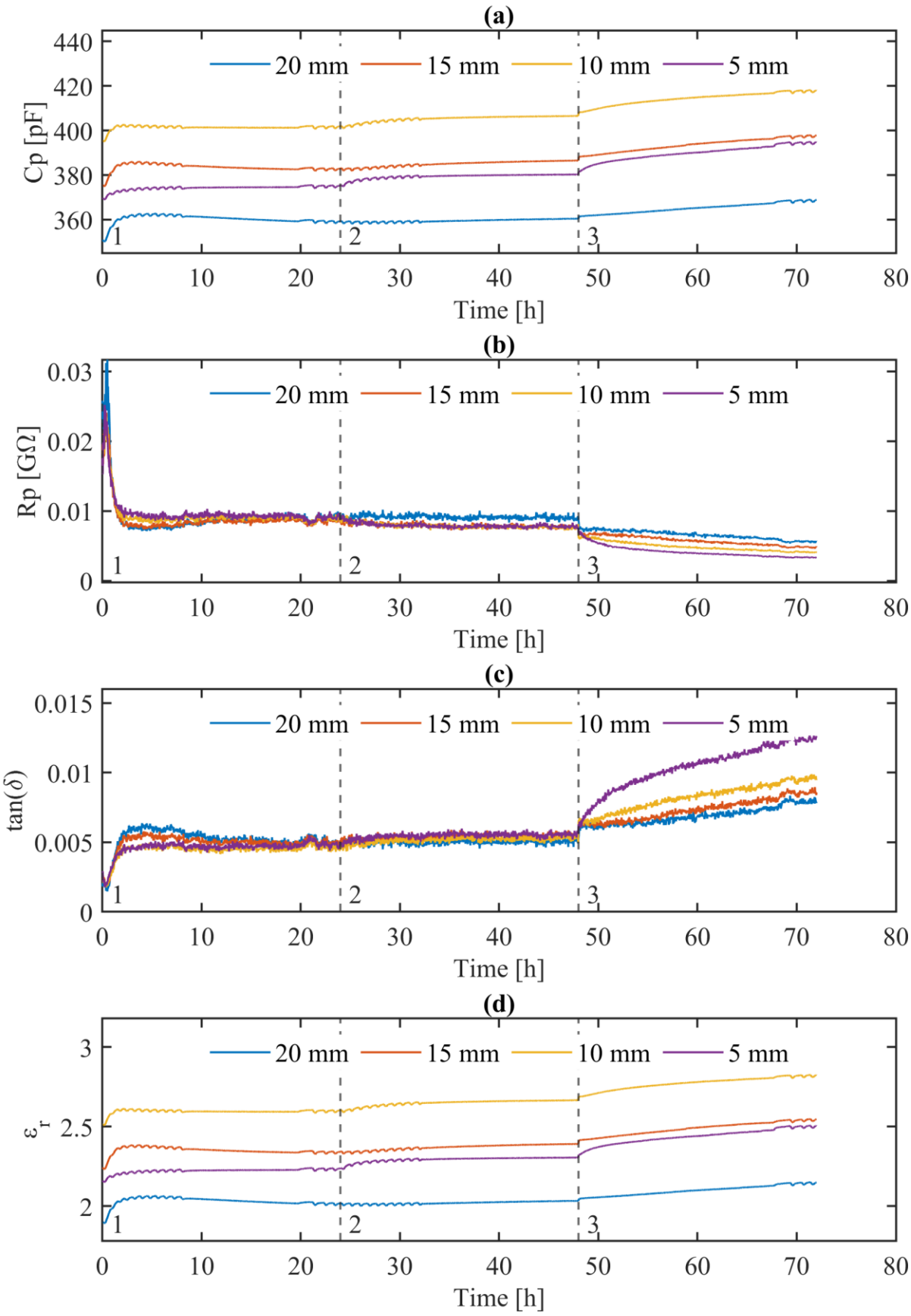

Fig. 3.19 Plots of 10 kHz values recorded over time for the humidity-only testing with gel encapsulated DBC samples. (a) inferred parallel capacitance, (b) inferred parallel resistance, (c) derived $tan(\delta)$, and (d) relative permittivity calculated using (49). Gel depths indicated by trace colour: 20 mm (blue), 15 mm (orange), 10 mm (yellow), and 5 mm (purple). Test stages indicated by vertical dashed lines.

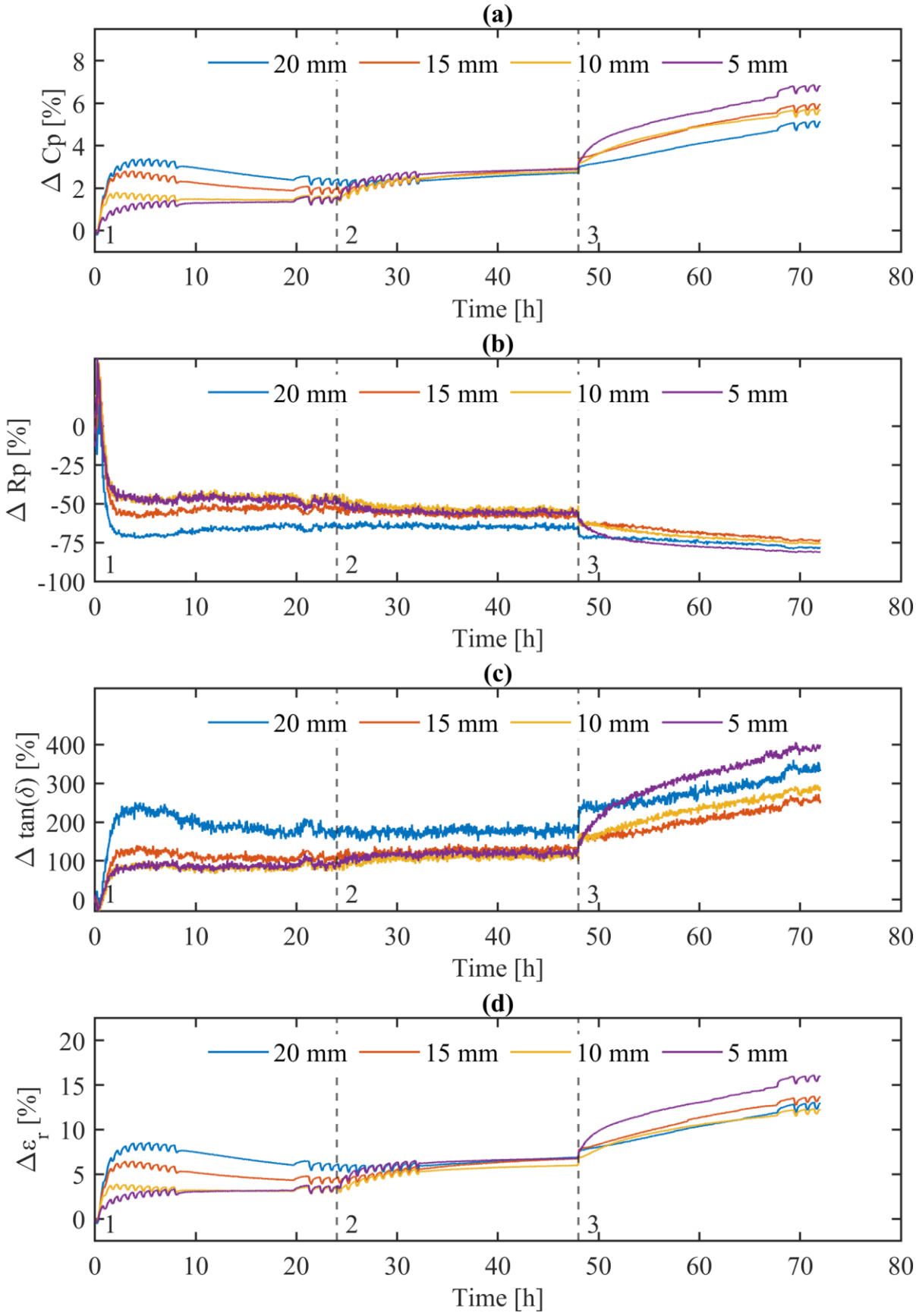

Fig. 3.20 Plots of percentage change in 10 kHz parameters from start-of-test values for the humidity-only testing with gel encapsulated DBC samples. (a) inferred parallel capacitance, (b) inferred parallel resistance, (c) derived $tan(\delta)$, and (d) relative permittivity calculated using (49). Gel depths indicated by trace colour: 20 mm (blue), 15 mm (orange), 10 mm (yellow), and 5 mm (purple). Test stages indicated by vertical dashed lines.

As was visualised for increasing temperature against the real and imaginary portions of the relative permittivities in Fig. 3.16 for the temperature-only test, the same can be done for increasing RH in this humidity-only test. These results are shown in Fig. 3.21. At time t_0, the setpoint for the environment chamber is changed from the dry-out (95 °C / 20% RH) condition to the first test setpoint (30 °C / 30%), causing the chamber to begin reducing the ambient temperature and increasing the ambient humidity. This is followed by an initial steep increase in parameters C_p, ε_r' and $tan(\delta)$, with a steep decrease in R_p as shown by Fig. 3.19 and Fig. 3.20. This short-term change presents an overshoot (undershoot in the case of R_p) in the parameters, which eventually settle as the 30 °C / 30% RH condition is maintained.

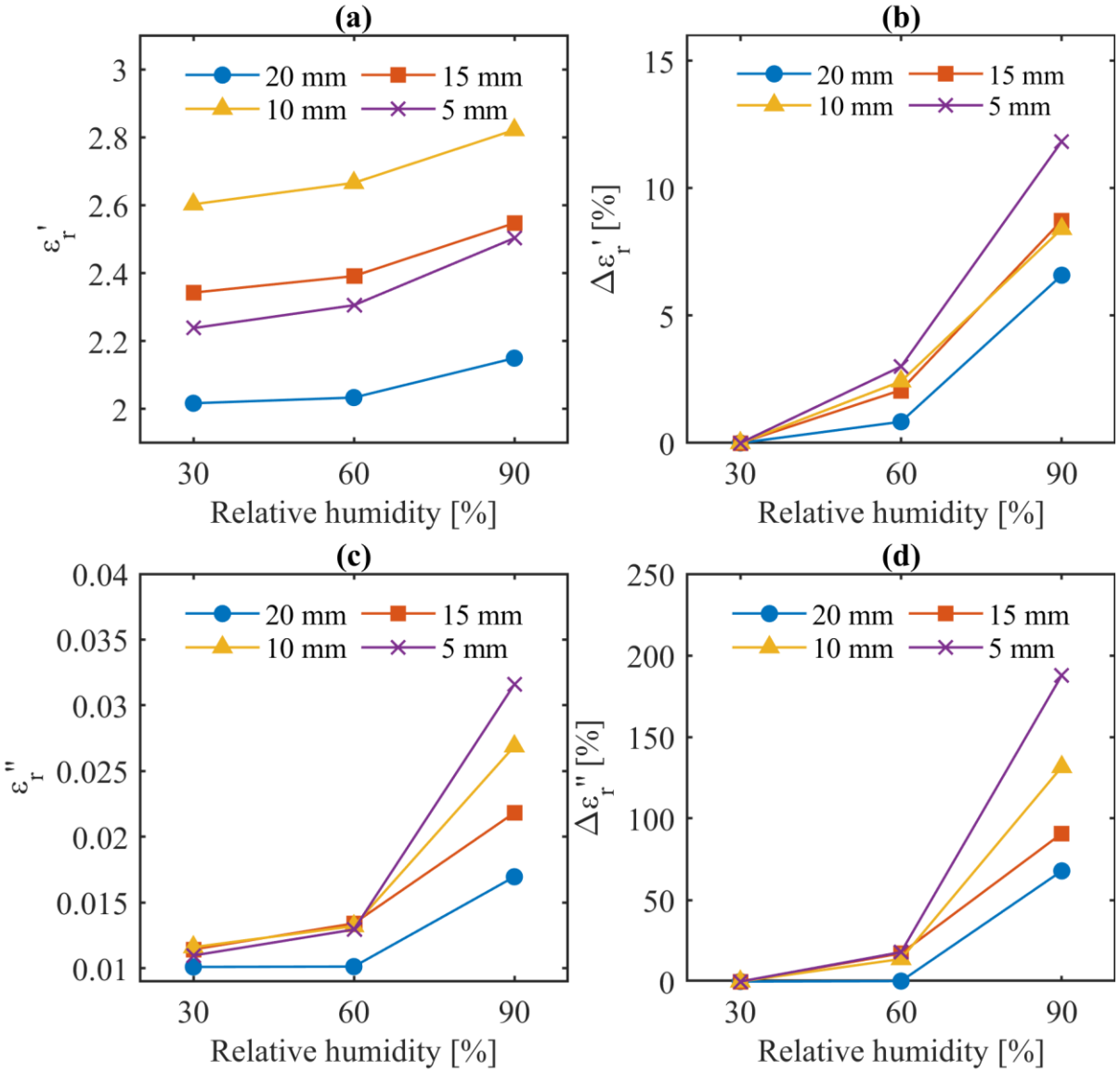

Fig. 3.21 Variation in 10 kHz values of ε_r' and ε_r'' for increasing RH (30–90% RH). End-of-setpoint values shown. (a) estimated 10 kHz ε_r', (b) percentage change in estimated 10 kHz ε_r' from 30% RH, (c) estimated 10 kHz ε_r'', and (d) percentage change in estimated 10 kHz ε_r'' from 30% RH. Gel depths are 20 mm (blue, circle), 15 mm (orange, square), 10 mm (yellow, triangle) and 5 mm (purple, cross).

The overshoot and settling can be explained by a rapid absorption of moisture at the start of test due to several aspects. First, the RH in the chamber overshoots the setpoint by nearly 50%, settling after about 40 minutes. Second, the coefficient of diffusion for most materials is understood to be a function of temperature. In solids the temperature dependence of the coefficient of diffusion is described by the Arrhenius equation, which is applied to moisture absorption in silicone gel in where it is given by (53):

$$D = D_0 \cdot \exp\left(-\frac{E_a}{\mathcal{R} \cdot T}\right) \tag{53}$$

where D is the coefficient of diffusion for the material at the given temperature; D_0 is the pre-exponential factor; E_a is the activation energy for the material; $\mathcal{R}$ is the universal gas constant representing the energy per temperature increment per amount of substance, $\mathcal{R} = 8.314$ J·mol^{-1}·K^{-1}; and T is the temperature.

Although the chamber is cooling down at this time, the sample will still be at a relatively high temperature due to the gel and PTFE mould thermal mass, and cool more slowly than the ambient environment. Consequently, the humidity overshoot happens when the coefficient of diffusion for the gel is high, resulting in rapid absorption. Finally, the chamber reaches its setpoint, and the sample shortly thereafter, so both the ambient humidity is reduced from the overshoot and the coefficient of diffusion for the gel is reduced due to the cooling. This results in desorption of the moisture absorbed during the RH overshoot and settling towards equilibrium at the current temperature and humidity setpoints.

Rapid absorption of moisture into gel-encapsulated PEMs was investigated via simulation in [42].The initial rapid absorption is also observed to be a function of gel thickness, which is logically explained by the relative thermal masses influencing local cooling and consequently the absorption/desorption time constants for the different thickness gel samples. Considering the longer-term impact of increasing ambient humidity, the same absorption trends as the initial overshoot are seen, albeit with a lower rate presumably owing to the coefficient of diffusion for the gel. As Fig. 3.21 shows percentage change from the end of the 30% RH setpoint, it is better placed to understand the longer-term behaviours. The changes in the gel parameters are more pronounced when moving from

60–90% RH than from 30–60% RH. Only ε_r' and ε_r'' are shown in Fig. 3.21 so in the interest of clarity, Table 3.5 presents the percentage changes from the start of test (t_0) to the end of the 90% RH setpoint.

Table 3.6 similarly provides results from the end of the 30% RH setpoint, respective to the end of the 90% RH setpoint. The results in Table 3.5 include the initial rapid absorption and overshoot of the chamber RH, while the results in Table 3.6 attempt to exclude them.

TABLE 3.5
PERCENTAGE INCREASE IN GEL SAMPLE ELECTRICAL PARAMETERS FROM START TO END OF TEST

Sample [mm]	ΔC_p [%]	ΔR_p [%]	$\Delta tan(\delta)$ [%]	$\Delta\varepsilon_r'$ [%]	$\Delta\varepsilon_r''$ [%]
20	5.14	-78.17	335.69	13.00	392.33
15	5.96	-73.53	256.54	13.71	305.41
10	5.65	-75.27	282.70	12.17	329.29
5	6.79	-81.25	399.46	15.94	479.05

TABLE 3.6
PERCENTAGE INCREASE IN PARAMETERS FROM END OF 30% RH SETPOINT TO END OF TEST

Sample [mm]	ΔC_p [%]	ΔR_p [%]	$\Delta tan(\delta)$ [%]	$\Delta\varepsilon_r'$ [%]	$\Delta\varepsilon_r''$ [%]
20	2.70	-38.16	57.47	6.58	67.84
15	3.90	-45.15	75.47	8.73	90.79
10	3.97	-54.98	113.64	8.40	131.60
5	5.15	-63.05	157.38	11.84	187.85

The strong influence of the initial absorption of humidity while the coefficient of diffusion for the gel is high is reflected in the difference between the results presented in the two tables. Nevertheless, individually the tables do not paint the complete picture of the change in the gel's electrical parameters due to moisture absorption for the humidity-only test, and both must be considered together. The results highlight an important consideration for this research, in that the influence of temperature and humidity are linked, and care must be taken if the study of each parameter in isolation is desired. Taken with Fig. 3.21, Table 3.6 shows a clear relation between the thickness of the gel samples and the rate of change of the electrical parameters. Comparing the temperature-only testing and the humidity-only testing, the magnitude of the change in C_p when increasing RH from 30% RH to 90% RH appears to be greater than the influence of reducing the ambient temperature from 95 °C to 20 °C, although the influence of erroneous elevated levels of humidity weakens the results in the latter case. With attempts made to isolate and study the influence of both temperature and humidity in turn painting a relatively unclear picture, further testing was required.

3.3.4 Combined Temperature and Humidity Testing

i. Test Procedure

To characterise the change in the electrical properties of the gel due to moisture absorption in an environment representative of field operation, testing was performed with combined temperature and humidity stresses. Although the work of previous authors indicates that the peak temperature stress in the gel of power modules under operation in converters is about 40 °C when adequate cooling is applied, these measurements are made in the bulk of the gel and far away from the active area of the devices. As with the previous tests for isolated temperature and humidity stress in § 3.3.2 and § 3.3.3, respectively, samples were placed in the environment chamber, connected to the automated measurement system, and held in a dry-out condition of 95 °C / 20% RH for 24 h before commencing testing. The combined T-RH stress (90 °C / 90% RH) was held for 120 h, followed by 12 h periods where first the humidity setpoint was reduced to 30% RH, then the temperature setpoint was reduced to 30 °C. Table 3.7 gives a summary of the intended setpoints for the combined T-RH testing.

TABLE 3.7
SETPOINTS FOR COMBINED TEMPERATURE AND HUMIDITY TESTING

Stage	Temperature [°C]	Relative humidity [% RH]	Absolute humidity [$g \cdot m^{-3}$]	Sequential duration [h]
0	95	20	98.402	24
1	90	90	373.972	120
2	90	30	124.657	12
3	30	30	9.177	12

ii. Results

The temperature and humidity recorded by the environment chamber over the course of the testing are shown in Fig. 3.22. After changing from the preconditioning stage, the environment chamber stabilises at the 90 °C / 90% RH condition after only 20 minutes. Due to a fencepost error in the test profile, the combined T-RH stress was held for 119 h rather than the intended 120 h, but conclusions may nevertheless be drawn for the behaviours up to that point. The remainder of the setpoints are held well with one exception at the start of Stage 3 (as defined in Table 3.7), where the reducing temperature causes a temporary increase in RH peaking at 7%, settling to the Stage 3 setpoints after approximately

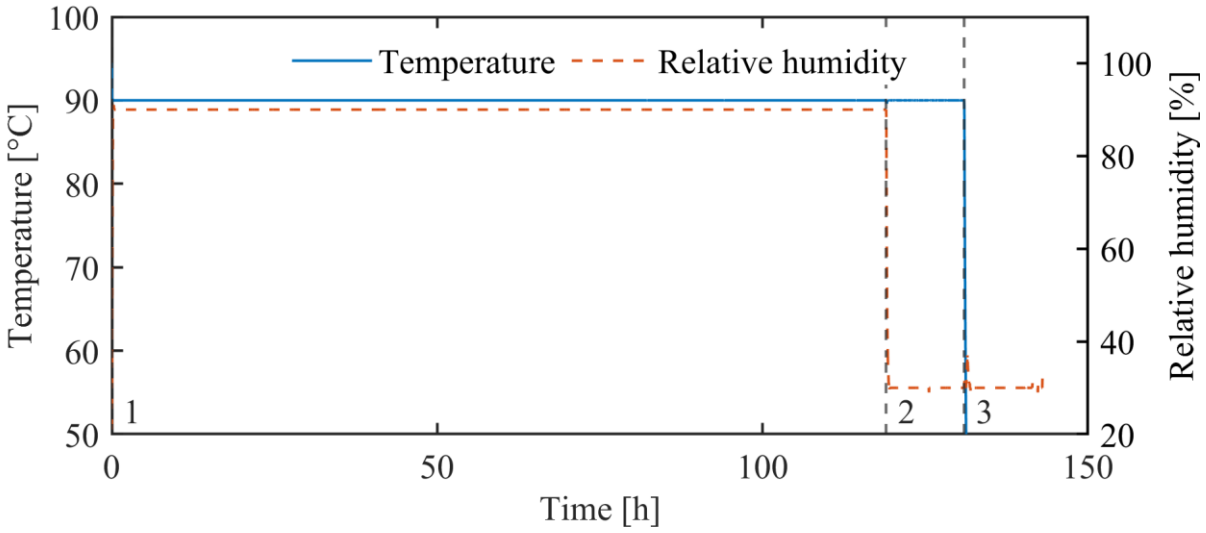

Fig. 3.22 Temperature (blue) and relative humidity (orange, dashed) as measured by the environment chamber over the course of the combined temperature and humidity test. Beginning of test stages outlined in Table 3.7 are indicated by the numbered vertical dashed lines. Data not recorded during preconditioning (Stage 0).

an hour. Fig. 3.23 shows full frequency sweeps (1 kHz – 50 MHz) of impedance magnitude, phase, inferred parallel capacitance and inferred parallel resistance. The instants in time as presented in the plot (t_0–t_3) relate to the start of the test (t_0), the end of the 90 °C / 90% RH setpoint (t_1), the end of the 90 °C / 30% RH setpoint (t_2) and the end of the test (t_3). As before, due to measurement noise and a recorded phase lower than -90° at low frequencies, the absolute value of R_p is shown, where values before the inflection point were recorded as negative. The change from t_0 to t_1 is significant in all parameters shown, with significant reductions in $|Z|$ and R_p, and increases in θ and C_p. The changes appear to be more pronounced at lower frequencies, agreeing with the previous results of Fig. 3.9, indicating the change is due to the absorption of moisture within the samples. With the reduction of the high humidity in the environment ($t_1 \rightarrow t_2$), these parameter changes are mostly recovered, indicating a drying phase in the samples. At t_2, the inflection point peak in R_p is reintroduced, although still downshifted in frequency from the values at t_0, indicating that the dry-out was not fully complete by 12 h. Nevertheless, the relative changes from $t_0 \rightarrow t_1$ and $t_1 \rightarrow t_2$ signify a difference between the absorption and desorption rates, which can be reasonably explained considering that in the absorbing case the moisture must travel nearly the full diffusion path length (up to 20 mm) through the gel until it is close enough to influence the IDC capacitance in a meaningful way. Conversely in the desorbing case, the moisture need only travel a short distance away from the IDC surface until its contribution to the measured capacitance is reduced.

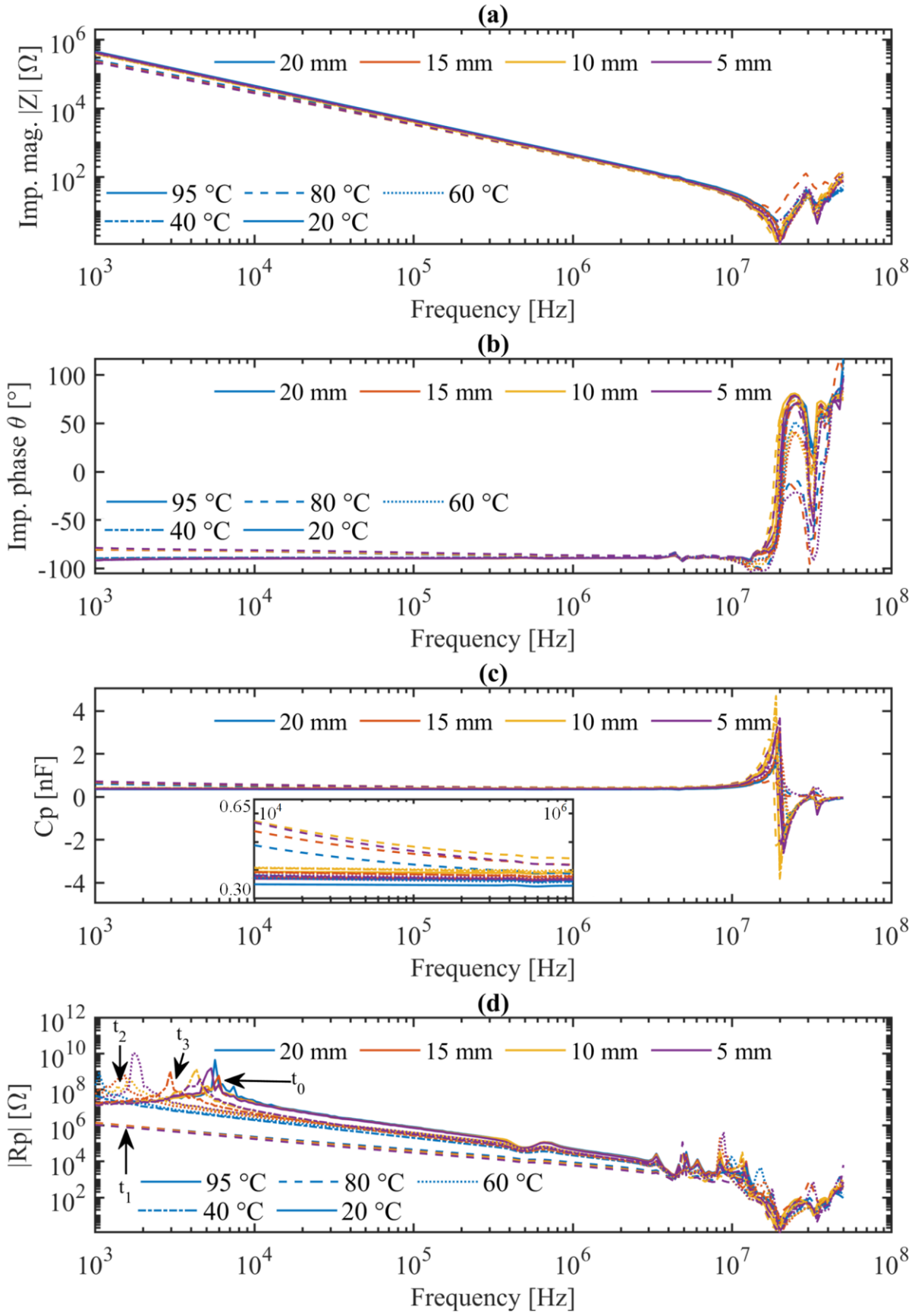

Fig. 3.23 Plots of sample electrical parameters against frequency over the course of the combined T-RH testing. (a) impedance magnitude, (b) impedance phase, (c) inferred parallel capacitance, (d) inferred parallel resistance. Sample gel depth represented by plot colour: 20 mm (blue), 15 mm (orange), 10 mm (yellow), 5 mm (purple). Time instants for measurements relate to start of test (t_0) and end of each successive setpoint (t_1–t_3).

Finally, after the final test setpoint ($t_2 \rightarrow t_3$) wherein the high temperature stress is also reduced, further changes are observed. Generally, C_p approaches the start-of-test values, and the inflection point peak in R_p shifts up in frequency towards the behaviours at t_0. Similar changes occur in $|Z|$ and θ. The 20 mm sample opposes the trend of the other samples in this period, which bears further investigation. As shown in Fig. 3.24, the inferred C_p of each sample over t_0 to t_1 decreases monotonically with frequency. The influence of moisture absorption over time is more prevalent at lower frequencies, where it is shown to significantly increase C_p, similar in behaviour to the previous observations of Fig. 3.9 and Fig. 3.23. The trend is similarly reflected in other parameters. It is not efficient to visualise complete time-frequency data for each permutation of time interval, parameter, and sample. Consequently, and

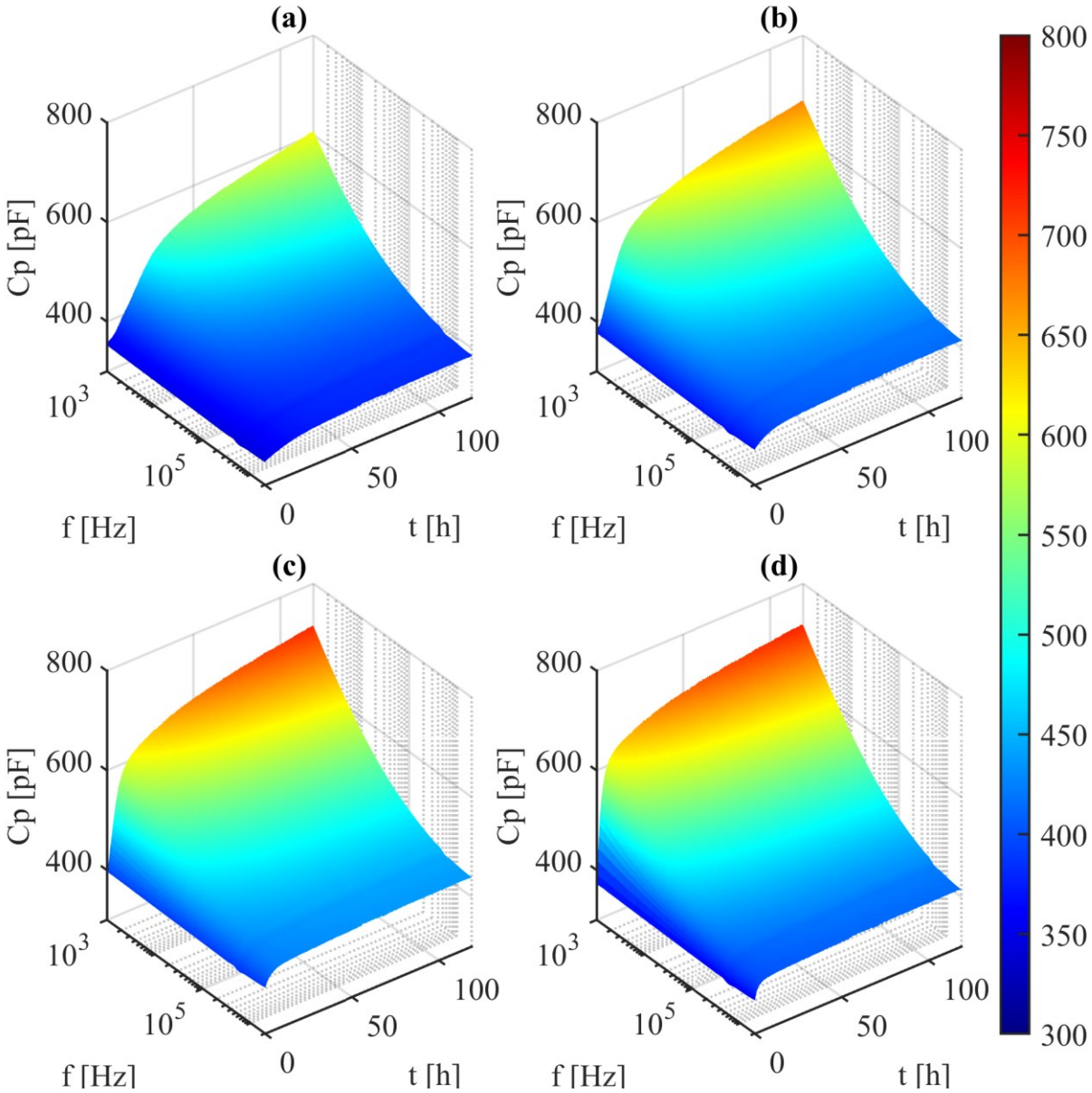

Fig. 3.24 Surface plots of C_p for each sample (a) 20 mm, (b) 15 mm, (c) 10 mm, (d) 5 mm from t_0 to t_1.

for consistency regarding the low-frequency measurement noise, the 10 kHz values of the parameters will be shown against time to investigate the behaviours more closely. The 10 kHz values of parameters C_p, R_p, $tan(\delta)$ and ε_r' are shown in Fig. 3.25 for the t_0–t_1 interval (90 °C / 90% RH), Fig. 3.26 for the t_1–t_2 interval (90 °C / 30% RH), and Fig. 3.27 for the final t_2–t_3 interval (30 °C / 30% RH). The percentage change in the parameters from the start of each interval are shown, to highlight the parameter change solely due to the test environment. This two-stage response agrees well with the Langmuir diffusion model for moisture absorption in silicone gel as previously discussed.

i. Changes in 10kHz values over the interval t_0–t_1 (90 °C / 90% RH / 119 h):

Relevant results for this period are shown in Fig. 3.25. Values C_p, $tan(\delta)$ and ε_r' increase significantly due to moisture absorption over the course of this period, with a commensurate reduction in R_p. At the start of this interval, the temperature is only reduced from the dry-out condition to the setpoint by 5 °C, so the coefficient of diffusion for the gel is not expected to change much over the course of the interval. The initial change in the investigated parameters (up to ~10 h) is related to the gel thickness, most likely owing to the differing diffusion path lengths; with the 5 mm sample showing the fastest response and the 20 mm the slowest. The long-term absorption rate does not appear to be correlated in any meaningful way with the diffusion path length and could instead be attributed to inhomogeneity of the gel encapsulation either due to the manual nature of the preparation or by slight concentrations of absorbed moisture, or slight differences in the IDC boards received from the commercial PCB fabricator. The two-stage growth supports the Langmuir diffusion model. The final percentage changes in the investigated parameters are given in Table 3.8.

TABLE 3.8
PERCENTAGE INCREASE IN INVESTIGATED PARAMETERS AT t_1 WITH RESPECT TO t_0

Sample [mm]	ΔC_p [%]	ΔR_p [%]	$\Delta tan(\delta)$ [%]	$\Delta \varepsilon_r$ [%]
20	39.75	-99.11	7943.53	100.86
15	43.98	-99.00	6850.66	101.36
10	45.68	-99.10	7559.31	98.74
5	54.31	-98.97	6208.53	127.41

ii. Changes in 10kHz values over the interval t_1–t_2 (90 °C / 30% RH / 12 h):

Relevant results for this period are shown in Fig. 3.26. With the removal of the high ambient humidity, the moisture content in the air is decreased. According to Fig. 3.22, the chamber achieves the humidity setpoint after 32 minutes. As the temperature is still the same, the coefficient of diffusion of the gel is not expected to change, and so any parameter change can be attributed purely to the reduction of moisture in the ambient environment. Behaviours similar the previous period are observed, where the initial parameter change is related to the thickness of the gel samples. The 5 mm gel sample responds quickly to the changing environment, whereas the 20 mm sample responds the slowest. The eventual parameter changes by the end of the interval are also ordered inversely to the gel thickness, with the value changes due to moisture absorption almost completely recovered. That the long-term parameter change rates are ordered by thickness is attributed to coincidence rather than any physical mechanism given the relative trajectories of the 15 mm and 10 mm parameter changes.

iii. Changes in 10kHz values over the interval t_2–t_3 (30 °C / 30% RH / 12 h):

Relevant results for this period are shown in Fig. 3.27. This interval sees the temperature setpoint reduced from 90 °C to 30 °C, so samples will begin to cool. At the start, the coefficient of diffusion for the gel is expected to be high, falling over time as it cools. Due to this cooling, the RH setpoint cannot be adequately held, resulting in a slight increase in the ambient humidity, settling after 2 hours. The varied change in the investigated parameters can be described by considering these changes in temperature and humidity. Initially, the parameter change is due to the reducing temperature and the samples desorb moisture. As the humidity in the chamber increases, all but the 5 mm sample begin reabsorbing moisture due to the concentration gradient. Moisture is quickly reabsorbed in the thicker gel samples, as it had not yet desorbed through the thickness of the gel. The long-term dynamics are then attributed to the inability of the cool environment to cause adequate desorption of moisture from the gel. It must be noted that although only a single test run is shown for each of the temperature-only, humidity-only, and combined T-RH tests are shown, additional testing was performed to confirm that the results were repeatable in terms of trends. Due to slight variation between the samples, the absolute values at each gel thickness differed slightly, however.

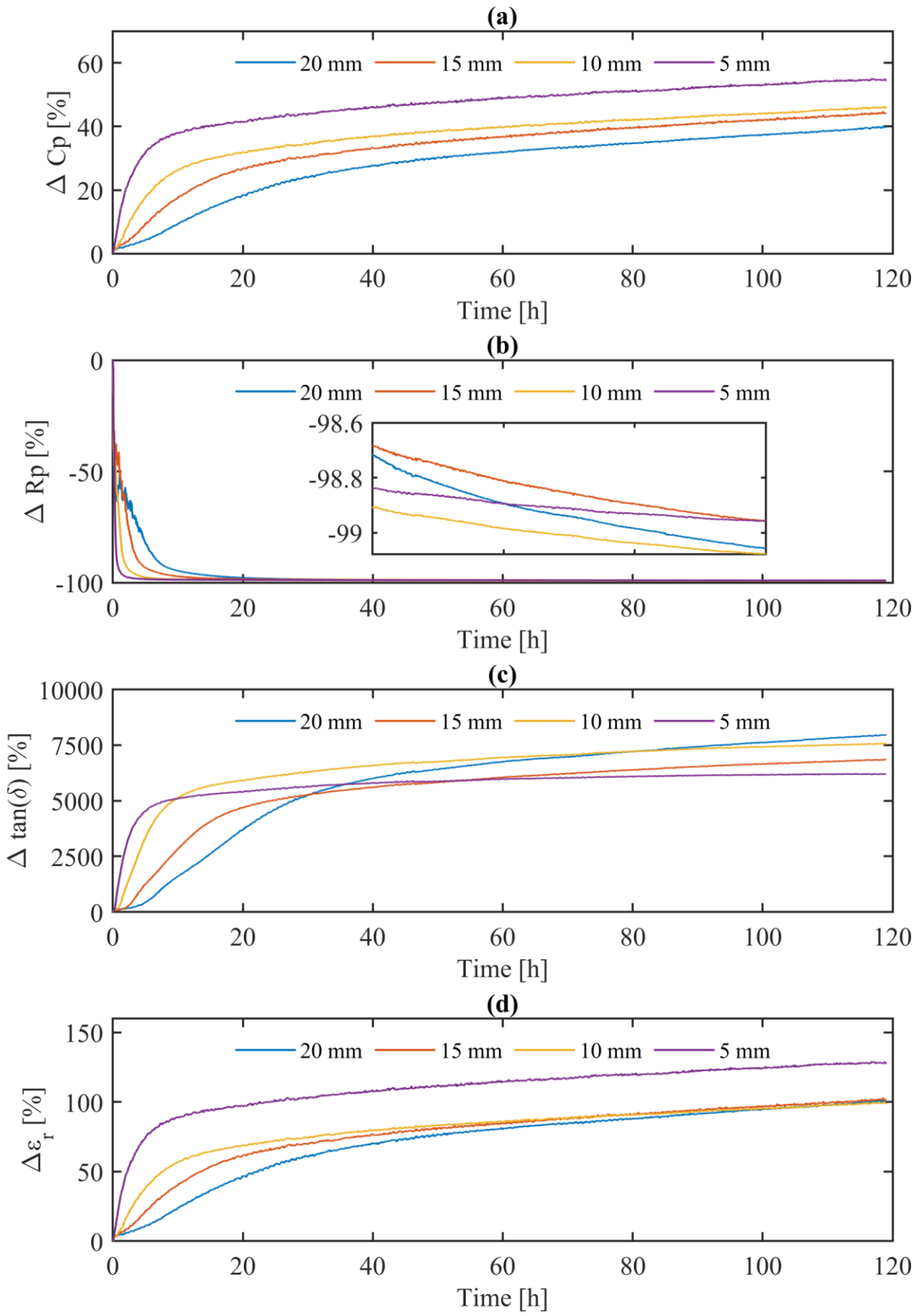

Fig. 3.25 Plots of percentage change in 10 kHz parameters from start-of-interval values (t_0–t_1) for the combined temperature and humidity testing with gel encapsulated DBC samples. (a) inferred parallel capacitance, (b) inferred parallel resistance, (c) derived $tan(\delta)$, and (d) relative permittivity calculated using (49). Gel depths indicated by trace colour: 20 mm (blue), 15 mm (orange), 10 mm (yellow), and 5 mm (purple).

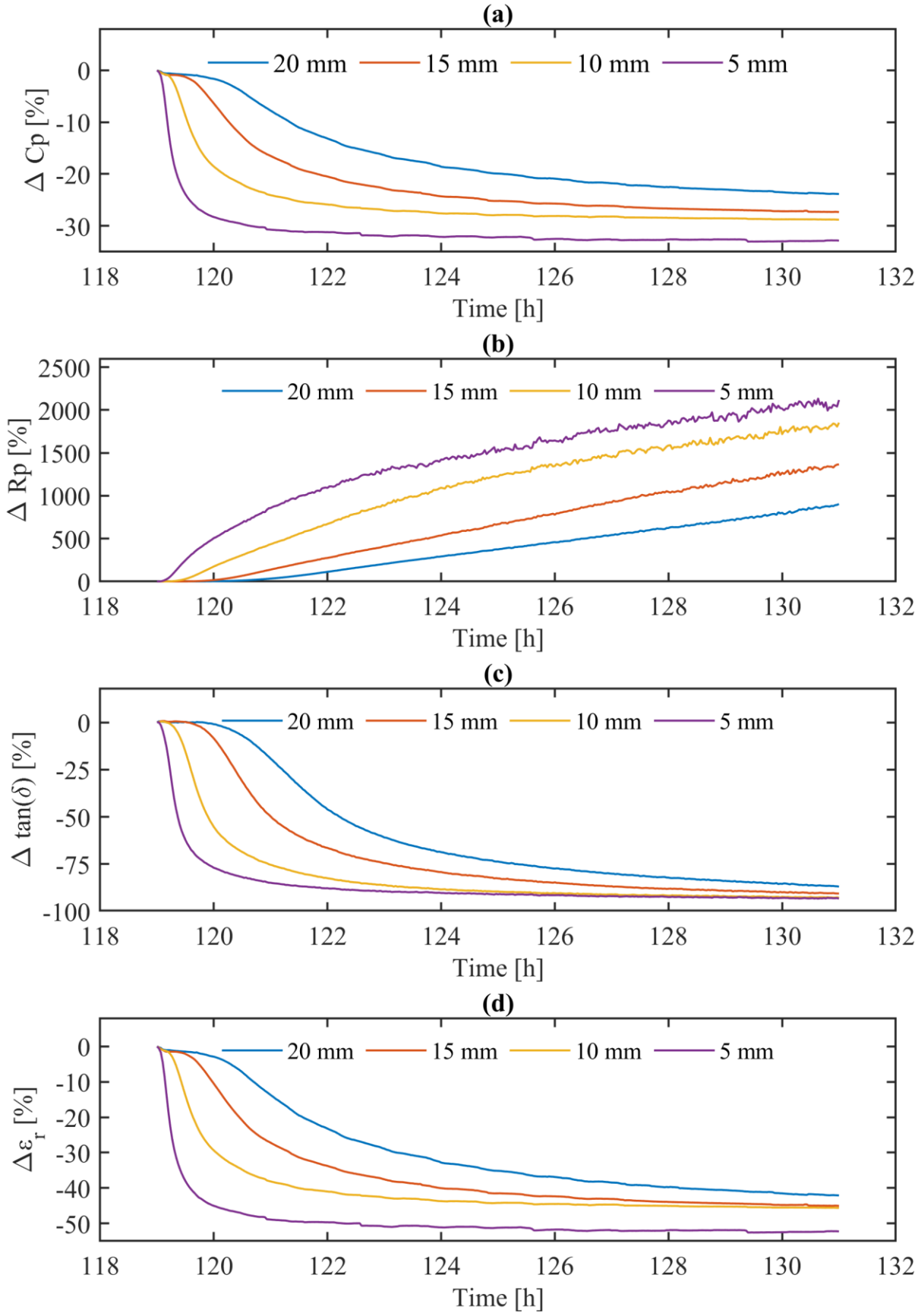

Fig. 3.26 Plots of percentage change in 10 kHz parameters from start-of-interval values (t_1–t_2) for the combined temperature and humidity testing with gel encapsulated DBC samples. (a) inferred parallel capacitance, (b) inferred parallel resistance, (c) derived $tan(\delta)$, and (d) relative permittivity calculated using (49). Gel depths indicated by trace colour: 20 mm (blue), 15 mm (orange), 10 mm (yellow), and 5 mm (purple).

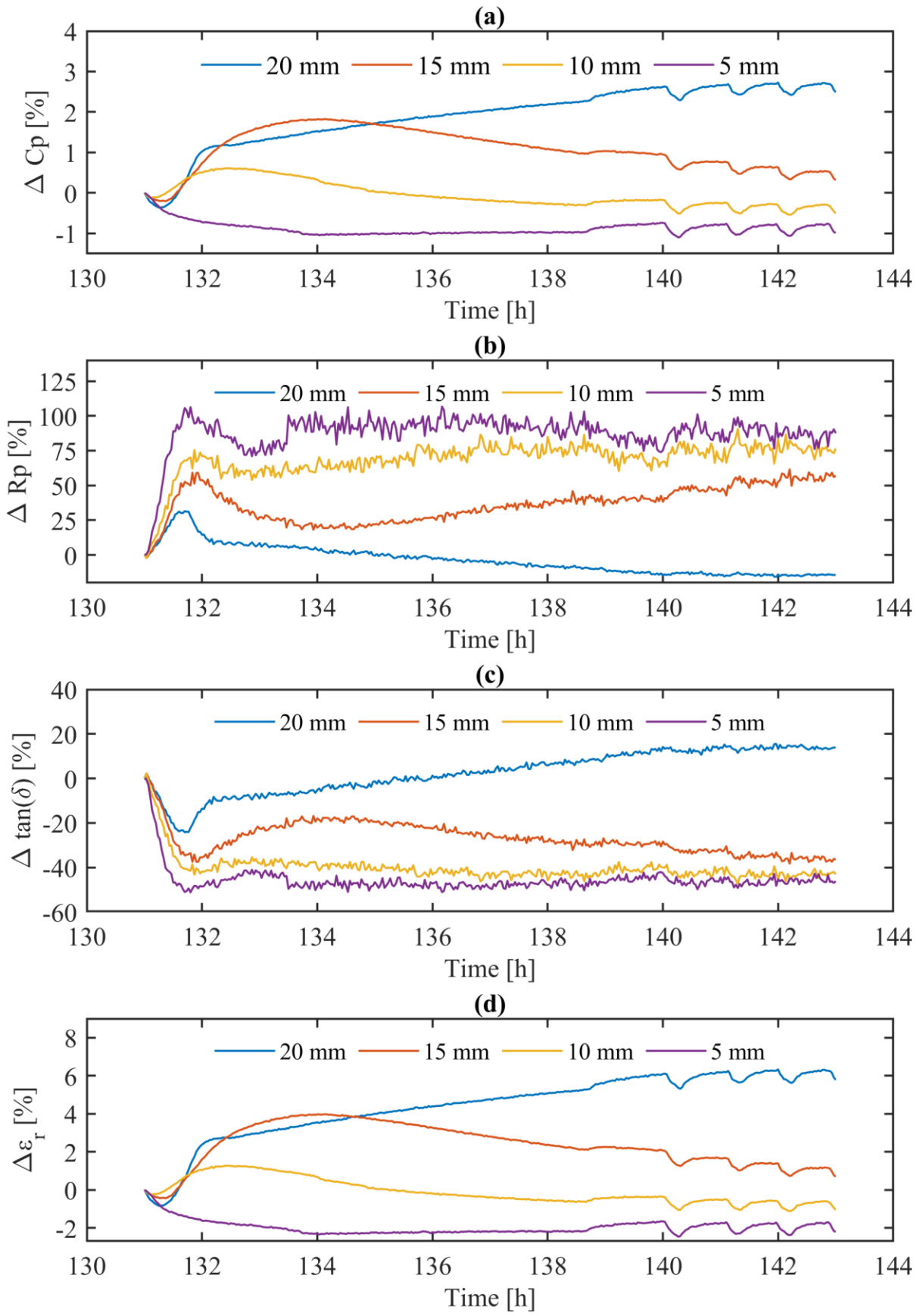

Fig. 3.27 Plots of percentage change in 10 kHz parameters from start-of-interval values (t_2–t_3) for the combined temperature and humidity testing with gel encapsulated DBC samples. (a) inferred parallel capacitance, (b) inferred parallel resistance, (c) derived $tan(\delta)$, and (d) relative permittivity calculated using (49). Gel depths indicated by trace colour: 20 mm (blue), 15 mm (orange), 10 mm (yellow), and 5 mm (purple).

iii. Fits of relative permittivity to Fickian and Langmuir diffusion models

As previously discussed, moisture diffusion into silicone gel can be described by a diffusion process. These are either based on analytical solutions to Fick's laws, determined by the moisture concentration gradient, or by Langmuir diffusion, which builds on the former and includes coefficients for the probability of binding and unbinding of water molecules to the material into which the moisture diffuses. Equations (29) and (34) were used to represent the $\mathcal{L}(t)$ term in (42) to provide fits to the Fickian and Langmuir diffusion models, respectively. These fits used the relative permittivity estimates over the t_0–t_1 interval and are shown in Fig. 3.28 and Fig. 3.29 for the 5 mm and 10 mm samples, respectively. As the thicker samples (15 mm, 20 mm) did not begin to saturate over the course of the test, the fitting results were poor and did not provide parameters indicative of realistic phenomena and are hence not shown. Significantly longer test times would be required to provide sufficient data to achieve fits for the thicker samples. It is observed that the Langmuir model results in a better fit than the purely Fickian model, which helps validate this diffusion model for RTV-2 silicone gels, whereas this has yet only been done for HTV silicone rubbers in the literature. The bonding and debonding coefficients are within an order of magnitude to those shown in literature previously for silicone rubber [90], and the diffusion coefficient closely matches other work for silicone gel [79]. A list of the fitting parameters for each sample with each model are provided in Table 3.9. As steady-state was not outright achieved, the steady-state value of relative permittivity (ε_∞) was left as a fitting parameter. Given these results, it is expected that for gels of a similar thickness and composition to those studied, in the 85 °C / 85% RH environment would have a diffusion coefficient in the range 1×10^{-3}–2×10^{-3} mm^2·s^{-1}, and a steady-state relative permittivity (ε_∞) in the range 5–6.

TABLE 3.9
FITTING RESULTS OF RELATIVE PERMITTIVITY WITH DIFFUSION MODELS

Sample [mm]	Fit model	Fitting parameters				R^2
		α [s^{-1}]	β [s^{-1}]	D [mm^2·s^{-1}]	ε_∞	
5	Fickian	—	—	4.7024×10^{-4}	4.6911	0.81374
5	Langmuir	9.9395×10^{-7}	4.0358×10^{-6}	1.1272×10^{-3}	5.1707	0.99854
10	Fickian	—	—	9.2311×10^{-4}	4.8046	0.93749
10	Langmuir	8.7417×10^{-7}	2.2736×10^{-6}	1.8010×10^{-3}	5.6490	0.99680

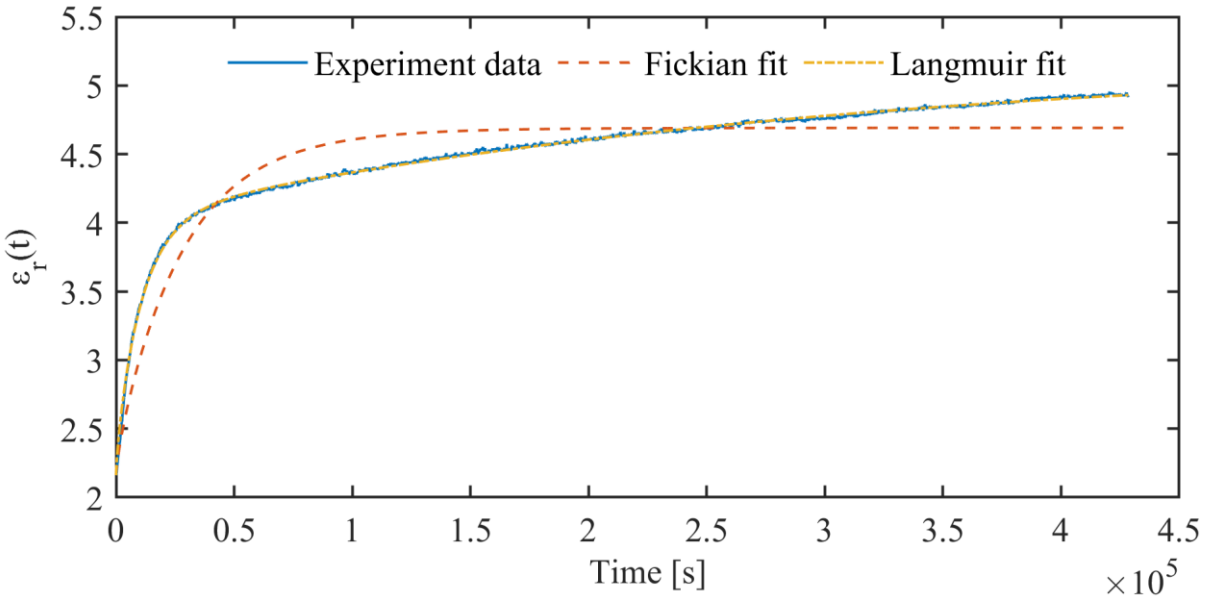

Fig. 3.28 Fitting results for 5 mm gel sample. Experimental data (blue, solid), fit to Fickian diffusion model (orange, dashed), fit to Langmuir diffusion model (yellow, dash-dotted).

Fits using the Fickian model are notably less accurate than the Langmuir model, with a significantly lower R^2 value. The diffusion of moisture into the silicone gel is best represented by the multiple exponential rates present in the Langmuir model, which the Fickian model does not capture. The relative permittivity for the 5 mm and 10 mm samples reached 63.2% of the estimated ε_∞ values according to the fit after only 142 minutes and 224 minutes, respectively, indicating that the gel depth has a significant impact on the time constant of the moisture absorption process.

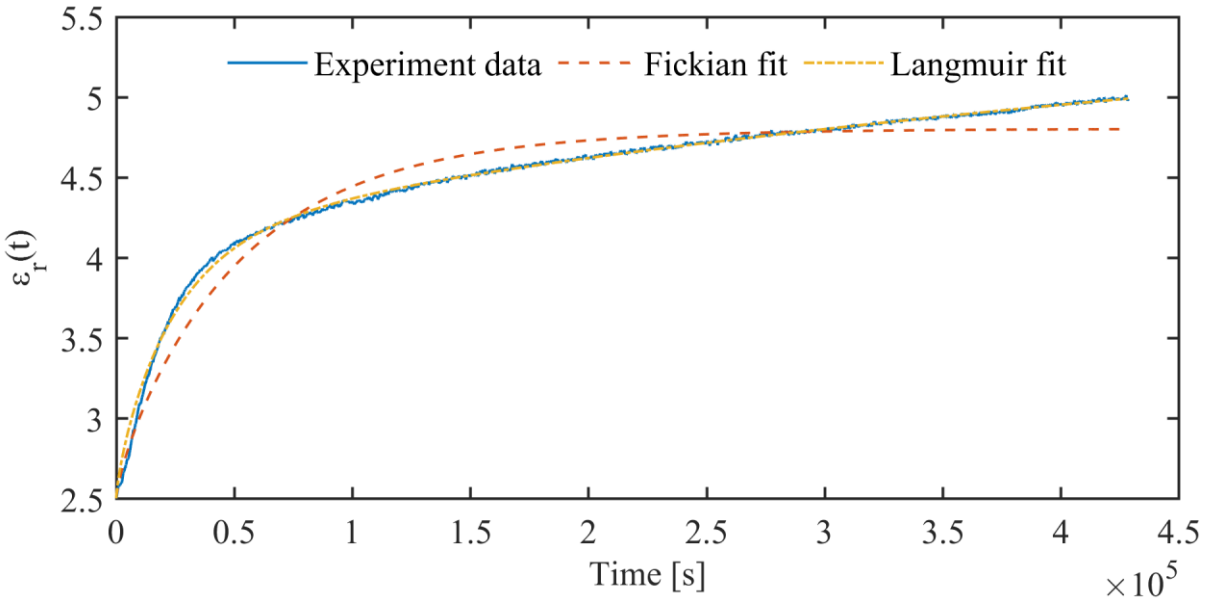

Fig. 3.29 Fitting results for 10 mm gel sample. Experimental data (blue, solid), fit to Fickian diffusion model (orange, dashed), fit to Langmuir diffusion model (yellow, dash-dotted).

A large absolute increase in the relative permittivity is observed for all samples over the course of the test. The end-of-test permittivities are 2.27, 1.99, 2.01, and 2.01 times the start-of-test (dry) permittivities for the 5 mm, 10 mm, 15 mm, and 20 mm samples, respectively. These are greater in extent to the capacitance gain of ATH-filled silicone rubber samples investigated in [90], in which the end-of-test permittivities ranged between 1.38–1.64 times the initial values. The discrepancy between those results and the present research are attributed to the difference between the HTV silicone rubber and RTV-2 silicone gel samples studied, respectively. The permittivity values for each sample obtained by fitting to the Langmuir diffusion model can be used to estimate the relative mass gain ($m(t)/m_\infty$) due to moisture absorption using (43), which are shown in Fig. 3.30. By the end of the test, relative mass gains of 96.49% and 89.51% are observed for the 5 mm and 10 mm samples, respectively. These percentages represent mass gains in terms of the maximum possible gain at 100% but give no information about absolute gains. Gravimetric analyses in the literature show an absolute mass increase of silicone gel samples in similar environmental conditions of 0.07% [42], and for HTV silicone rubber samples of up to 1.29 % [90]. Other research indicates a mass loss mechanism present in silicone gels [79], whereby uncured silicone fluids in gel dissolve into the absorbed moisture. This in turn evaporates, reducing the total mass of the gel component. Consequently, mass gain analysis for such samples is not trivial, requiring balances capable of operation in the harsh environment.

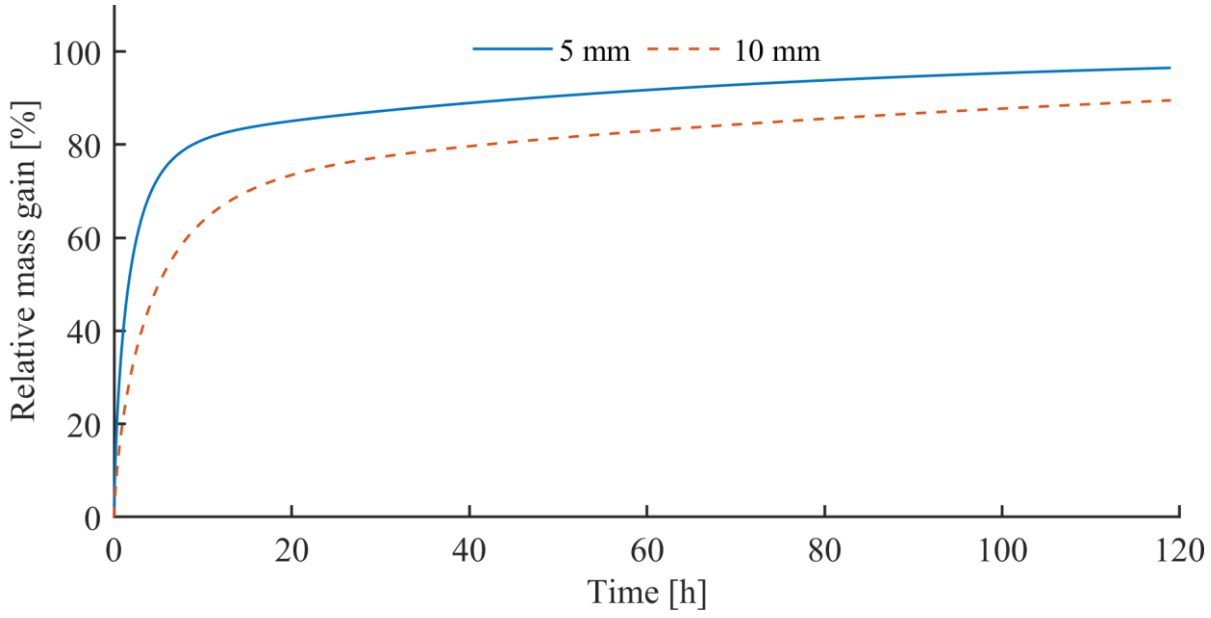

Fig. 3.30 Relative mass gain of 5 mm (blue) and 10 mm (orange, dashed) samples calculated using Langmuir diffusion model.

3.4 Influence of Sample Orientation on Capacitance Increase

In practice, PEMs used in WECS are attached to large heatsinks for active cooling. Though sample orientation is a design choice, there is little evidence in the literature that this choice is ever deemed significant. At 25 °C, the density of water is generally accepted as 997 $kg \cdot m^{-3}$, and per the datasheet provided by Wacker for SilGel 612 [75], the density of the gel when cured is 970 $kg \cdot m^{-3}$. That these densities are dependent on temperature (for which no information is provided in the case of the silicone gel) notwithstanding, water is slightly denser than the gel. It could conceivably pool at the base of the gel at the die attach layer in an upright orientation due to rapid absorption through gaps in the cross-linked network. According to the results of experiments carried out in this chapter, this would cause a significant change in the electrical properties of the dielectric gel. A simple test was performed with setpoints identical to those in § 3.3.4 to investigate whether the orientation of samples plays a role in the moisture absorption dynamics of the gel. This was motivated by the slight difference in the densities of gel and water, the large magnitude of the change in permittivity, and considering that moisture diffusing upwards must overcome the influence of gravity. Two sets of gel samples were prepared, with one mould held in an inverted orientation. A photograph of these samples in situ is shown in Fig. 3.31.

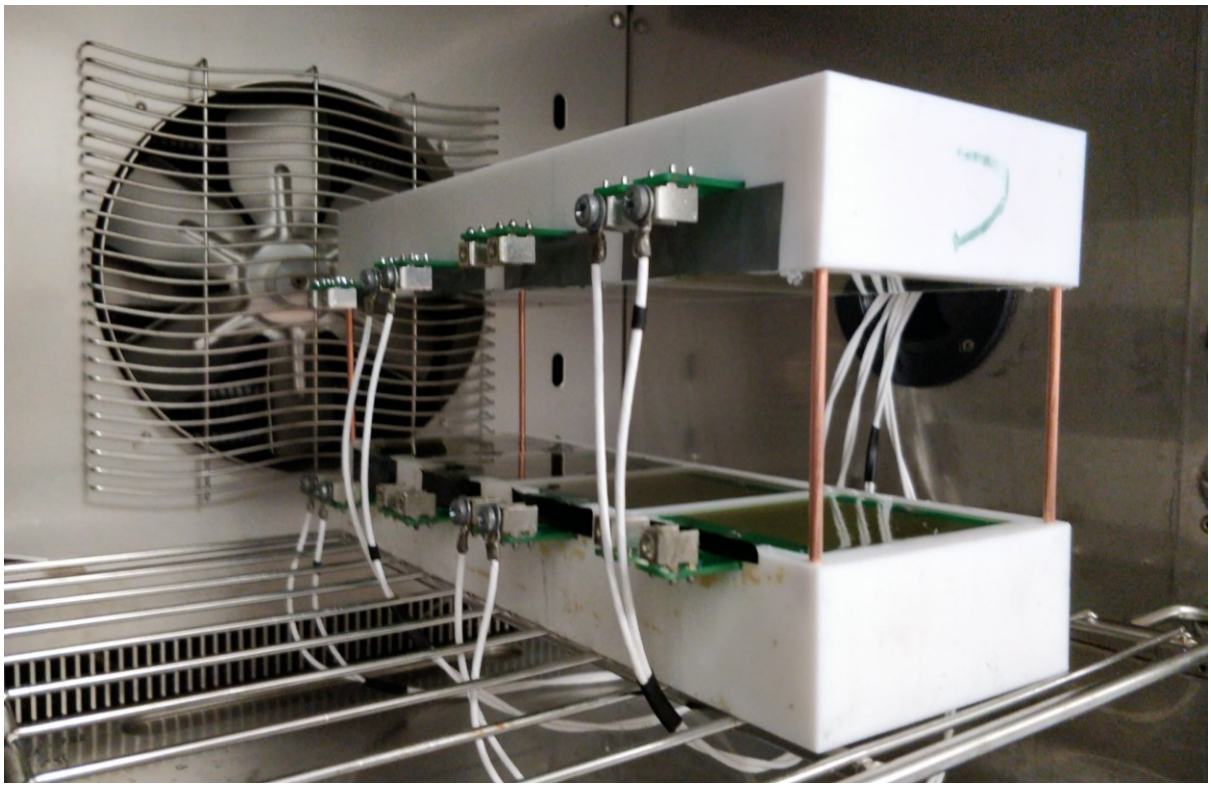

Fig. 3.31 Photograph of samples used in inverted orientation testing.

As the automated measurement system using the Bode-100 VNA only provided 4 channels, only the 10 mm and 20 mm samples of each mould were measured for this test. The humidity in the chamber was not expected to vary significantly due to positioning based on initial commissioning verification testing, so any variation in the measured capacitances was attributed solely due to variation in the moisture absorption dynamics. The derived relative permittivities at 10 kHz over the course of 120 h at 90 °C / 90% RH are shown in Fig. 3.32. Slight variance is observed between the sample relative permittivities at the start of the test, which was consistent throughout the dry-out period. Consequently, and to better highlight the change due to orientation, the percentage increases in permittivities from the start-of-test values are shown in Fig. 3.32(b). The initial permittivity growth rate is greater in the 10 mm samples, irrespective of orientation. The longer-term absorption dynamics appear to be influenced significantly by the mould orientation, with the upright samples gaining permittivity at a greater rate than those in the inverted orientation. Measurement error notwithstanding, a clear difference is observed

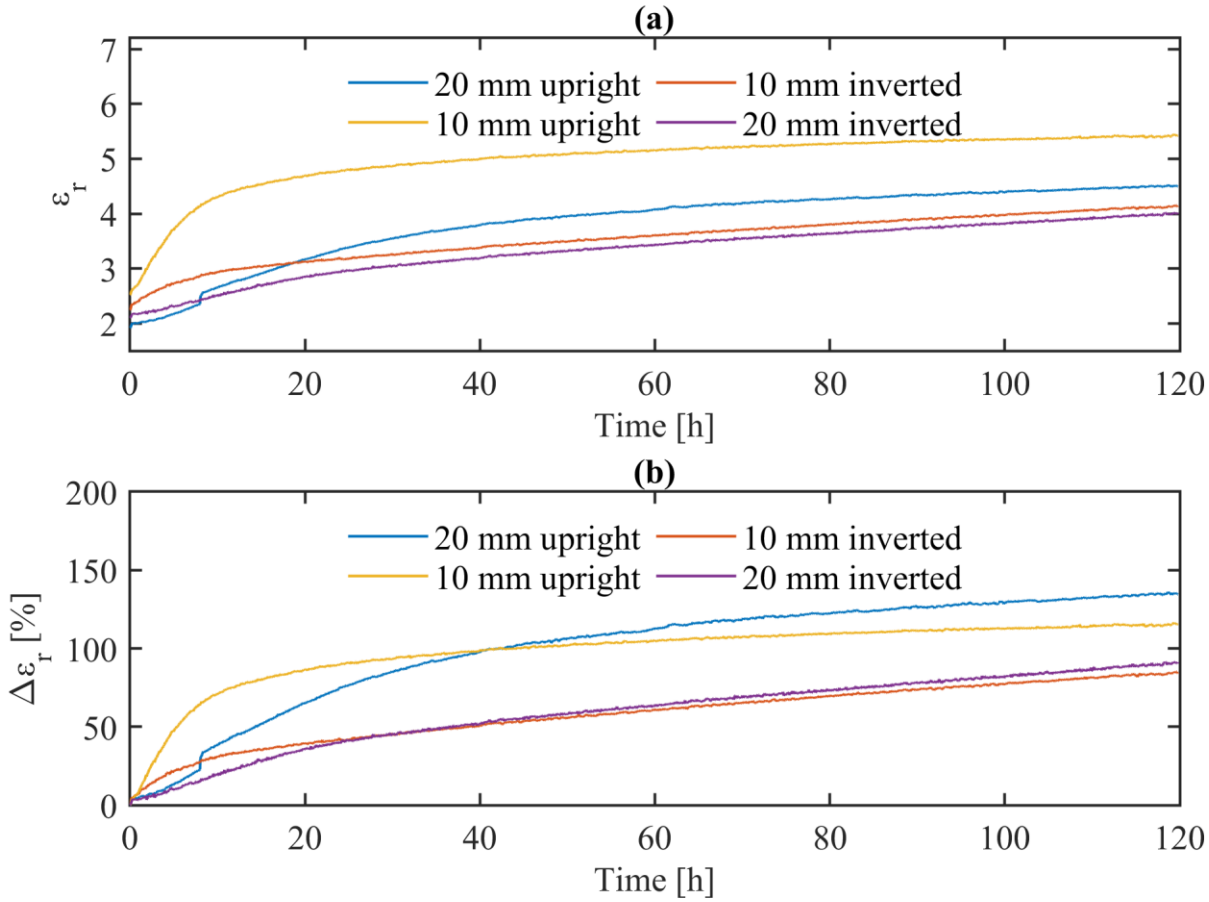

Fig. 3.32 Derived ε_r (10 kHz) of silicone gel samples held at 90 °C / 90% RH, with differing orientations. 20 mm, upright (blue); 10 mm, upright (yellow); 20 mm, inverted (purple); 10 mm, inverted (orange). (a) estimated 10 kHz ε_r based on parallel capacitance measurement, (b) percentage change in 10 kHz relative permittivity from start-of-test values.

between the permittivity increase due to moisture absorption depending on the orientation of the samples. Note that the step in the measurements for the 20 mm upright sample at 8 hours is likely due to a slight unintentional movement of the measurement cabling. This is not expected to influence the outcome of this work in any meaningful way.

It must be noted that only the 10 mm upright sample approached steady-state over the course of the test, with the trajectories for the other samples indicating that steady-state of a similar percentage increase over the starting value would eventually be reached. Consequently, sample orientation should be considered a mitigating factor for moisture absorption only in that the time constant for moisture absorption could be increased. The humidity variation in the control cabinet of a WECS and the inclusive IGBT microclimate is on the order of a single day rather than the multiple days used in this test profile [94]. Consequently, adjustment of module orientation to reduce the rate of moisture absorption could be a powerful tool in the mitigation of humidity-driven performance and lifetime degradation mechanisms for WECS where the use of thicker encapsulation is not permissible due to design constraints.

3.5 Conclusions

In this chapter, the environment-driven change in the electrical properties of a commercial silicone gel commonly used in the encapsulation of HV PEMs was studied. Bespoke IDC sensor boards were used to measure the changes in the electrical properties of the gel in an arrangement representative of the die attach level in PEMs, underneath varying thicknesses of cured silicone gel. In § 3.2.3, impedance measurements of the gel-coated IDC sensors were taken with a Wayne Kerr 6500B impedance analyser and used to parameterise a parallel RC model representative of a lossy dielectric. Complete submersion in water caused a significant increase in the sample low-frequency capacitance, owing to space charge and dipolar turning polarisation processes.

To study the moisture absorption characteristics of the silicone gel encapsulation over time, an automated platform based on a Bode-100 VNA was used to take periodic frequency sweep measurements in the range 1 kHz – 50 MHz. Samples were subjected to a series of tests consisting of

stepwise reductions in temperature with fixed ambient humidity, stepwise increases in ambient humidity with fixed ambient temperature, and combined temperature and humidity stress.

In § 3.3.2, a fixed ambient humidity setpoint of 20% was applied while temperature was reduced from 95–20 °C in 15 h dwell periods. An inflection point is seen in the results from 60–40 °C, due to an unintended spike in ambient humidity. Over the range 95–60 °C, reducing temperature causes a slight increase in C_p, a significant increase in R_p, a significant reduction in $tan(\delta)$ and a slight increase in ε_r'. At lower temperatures, erroneous elevation in ambient humidity causes significant behavioural change in R_p and $tan(\delta)$. A large reduction in R_p and corresponding increase in $tan(\delta)$ is observed. The variation in electrical parameters due to temperature alone was minimal, and even a small variation in ambient humidity can cause significantly greater variation.

In § 3.3.3, a fixed temperature setpoint of 30 °C is applied while the humidity is increased from 30–90% RH, with a dwell of 24 h at each setpoint. At the start of the test, the chamber temperature was reduced from the preconditioning stage setpoint of 95 °C, influencing initial parameter variation at that time. Measured C_p increased rapidly at the onset of the first test condition owing to the reduction in temperature and the increasing RH. As RH increases, a steady increase in C_p is observed. At the start of the test, R_p is reduced sharply, commensurate with increasing $tan(\delta)$. The end-of-setpoint measurements were used to evaluate the impact of ambient humidity on the gel's electrical properties, showing that the parameter changes were mostly dependent on the thickness of the gel. In each case the largest change was seen in the 5 mm sample. From 30-90% RH C_p was increased by 5.15%, R_p reduced by 63.05%, $tan(\delta)$ increased by 157.38%, ε_r' increased by 11.84% and ε_r'' increased by 187.85%. Consequently, the influence of humidity alone is shown to be far greater than temperature alone.

In § 3.3.4, combined temperature and humidity stress was applied to samples: 90 °C / 90% RH for 120 h, the interval t_0–t_1; 90 °C / 30% RH for 12h, the interval t_1–t_2; and 30 °C / 30% RH for 12h, the interval t_2–t_3. In the interval t_0–t_1, initial C_p increase is shown to be linked to encapsulation thickness, with thinner samples increasing more rapidly at the start of the test, and all samples increasing by roughly the same rate after the initial increase. The 10 kHz C_p was shown to increase by 54.31% from

the start to the end of this period. The measured R_p was significantly reduced over this period, by about 99% for each sample. Correspondingly, a substantial increase in $tan(\delta)$ is also observed, increasing by up to 7943.53% for the thickest (20 mm) sample. In the interval t_1–t_2, the changes are largely reversed. Observed changes are proportional to the thickness of the gel samples, with the initial rate of parameter change being the highest for the thinner gel samples. Meanwhile, the longer term changes are attributed only to sample variance. In the following environment (t_2–t_3), complex variations are observed in the measured parameters due to the changing coefficient of diffusion for the gel at the start of this interval. Thicker samples cool more slowly in the reducing temperature environment due to the increased thermal mass and reabsorb moisture due to the chamber's unintentional increase in RH. Thicker gels are determined to be more favourable from a module design standpoint, as with adequate climate control moisture may be inhibited from reaching the die attach layer in meaningful quantities. However, in the case of long durations of sustained elevated temperature and humidity, the increased gel thickness may exacerbate long-term degradation effects due to moisture storage. In this case, dry-out periods are recommended. In operation, a temperature gradient must be consistently maintained such that the module baseplate is higher than the ambient environment. This limits moisture storage in the gel.

A discussion is held to evaluate the applicability of two well-known diffusion models in the case of silicone gel: Fickian and Langmuir types. The Langmuir model is shown to adequately capture the moisture absorption dynamics in terms of relative permittivity increase in the first test interval (t_0–t_1: 90 °C / 90% RH) for the 5 mm and 10 mm samples, supporting the use of this model over simple Fickian diffusion in future work. For the 15 mm and 20 mm samples, the duration of the test was insufficient to provide accurate fits with either diffusion model. Comments on the literature are made to highlight the difficulties of gravimetric analyses for silicone gel samples. A hypothesis of moisture pooling under the gel was proposed and tested with samples in an inverted orientation alongside those held upright. The results indicated that although the inverted orientation reduced the initial rate of moisture absorption, the long-term moisture absorption dynamics were largely unaffected. Consequently, this is useful only in the case of humidity variation in the PEM microclimate on the order of hours, rather than days.

Chapter 4: Short-term Influence of Humid Environment on Performance of IGBT Power Modules

4.1 Introduction

The previous two chapters investigated the change in the electrical properties of the major encapsulant used within PEMs due to moisture absorption in a high humidity environment. A large increase in the relative permittivity measured at the bottom of the gel was observed, which was attributed to the absorption. Sensors placed at the bottom of the silicone gel were used to provide a representative indication of the changing dielectric properties at the die attach level in PEMs. This chapter follows on from the findings of the previous by investigating the impact of moisture absorption by the gel on actual module parasitic capacitances, and the subsequent influence on switching behaviours. Typically, the primary parasitic capacitances of interest to the designer of a power converter are the input capacitance C_{ies}, reverse transfer (or Miller) capacitance C_{res}, and the output capacitance C_{oes}. These are made up mostly of unavoidable factors of the chip structure, but also include parasitic elements due to the layout of the module outside the chip, i.e. the floorplan of the DBC and the requisite wire bonds used to make interconnects in high power modules. The gate-collector capacitance (C_{GC}) of an IGBT is equivalent to C_{res} during the Miller plateau, and has previously been shown to permanently increase due to thermal cycling, highlighting the possibility of dV_{CE}/dt as a TSEP [125]. Given the results of the previous chapter, a natural concept of how this may be influenced by moisture absorption within the dielectric gel arises.

4.1.1 Conceptual Influence of Humidity on Power Module Parasitics

A photograph of a region of a typical commercial IGBT half bridge power module (Infineon FF1000R17IE4) is shown in Fig. 4.1 alongside its circuit diagram representation (Fig. 4.1(b)). Capacitive coupling occurs between many of the packaging elements, arising from the DBC, gel encapsulation and baseplate. As previously demonstrated, moisture absorption within the gel in a high-temperature high-humidity environment significantly influences its electrical properties. This presents as an increase in the gel's relative permittivity, in both the real (ε_r') and imaginary (ε_r'') components. In

a field application, these parameters are better investigated in terms of values more useful to the module and converter designer: capacitance and dielectric loss ($tan(\delta)$), respectively.

The model of the IGBT with parasitics shown in Fig. 2.7 can be extended to include those present in the gel encapsulation portion of the packaging structure, which is shown in Fig. 4.2. Note that the parasitic capacitances related to the capacitive coupling of the conductive elements through the dielectric gel (C_1–C_3) are shown as variable as they will increase due to moisture absorption. A sufficiently high increase in parasitic gel capacitances C_1 and C_2 should cause corresponding increase in Cies, resulting in higher initial gate current i_G, and longer turn-on and turn-off times due to the increased delays. An increase in C_1 may also cause a lengthened Miller plateau due to its coupling with C_{GC} according to (2). A notable increase in C_3 could cause a shift in the output capacitance of the IGBT, C_{oes}, potentially introducing harmful oscillatory effects in the wider context of the converter.

Common-mode parasitic capacitance through the ceramic of the DBC to the baseplate could be considerable in some converter topologies, but as the ceramic is not prone to the absorption of moisture,

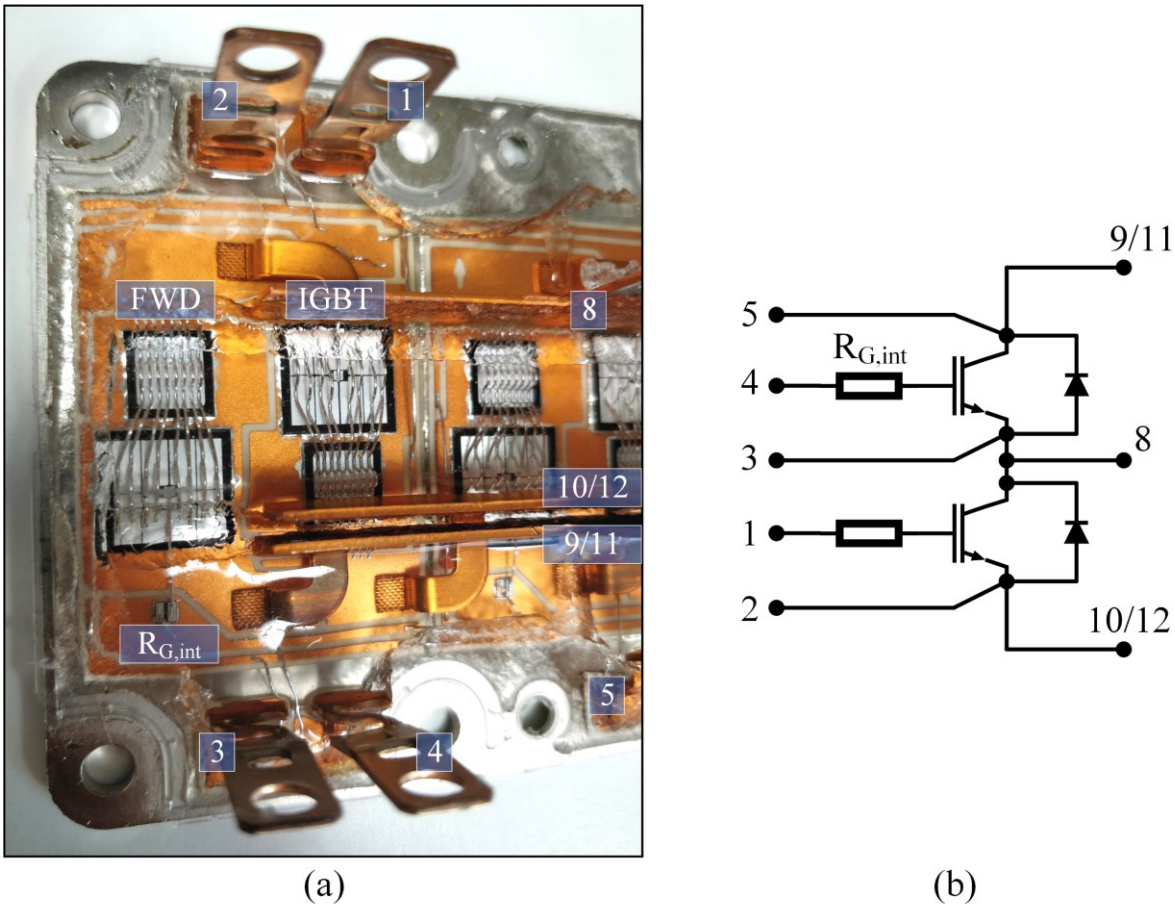

Fig. 4.1 Infineon FF1000R17IE4 IGBT half bridge module. (a) photograph, (b) equivalent circuit diagram.

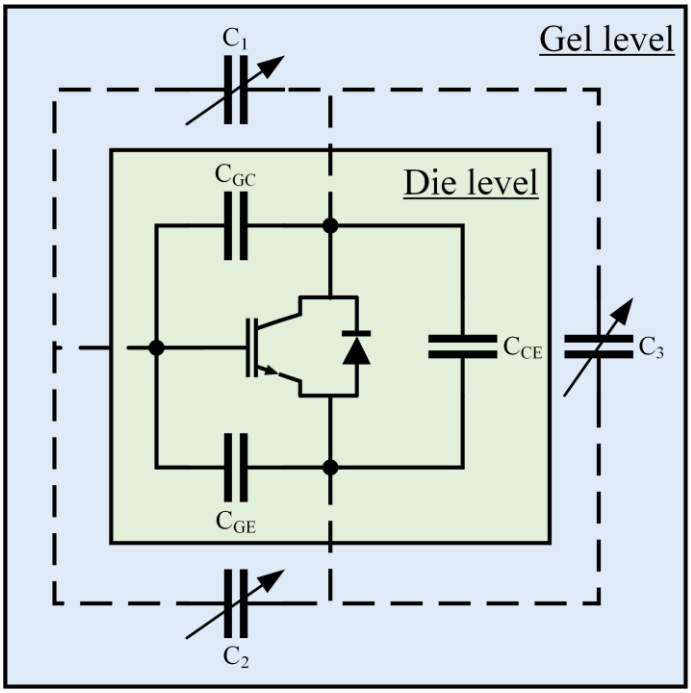

Fig. 4.2 Graphical representation of IGBT parasitic capacitances. Related to the die (green background), related to capacitive coupling through the dielectric gel (blue background).

this was not studied. The trench depth of the FF1000R17IE4 DBC was measured manually at 330 µm, i.e., the thickness of the top copper. The measured trench width was 762 µm, and an approximate effective coupling length between the copper connected to the module's top terminal (9/11, Fig. 4.1(b)) and the top IGBT gate copper was measured at 25 mm. A quick estimation of C_1 using these values for a dry gel permittivity of 2.7 and alumina permittivity of 9.8 with (44)–(48) results in a capacitance (using only one 'digit', i.e., $N = 1$) estimate of just 2.03 pF. When the gel permittivity is increased commensurate to the observations in Chapter 3 to a value of 5, the estimated capacitance for C_1 in this instance is increased to 2.58 pF, a net increase of 0.55 pF. Although this is not expected to cause significant changes to switching behaviours when compared with the datasheet given reverse transfer capacitance of 2.6 nF, the uncertainty in the rough analytical estimate and the presence of many capacitive coupling paths bear further investigation.

4.1.2 Simulation of Module Parasitic Capacitance Change Due to Ambient Humidity

The previous chapters used IDC sensors to observe change in the electrical properties of the dielectric gel due to humidity absorption, which were by necessity designed with a high capacitance in mind. This provided easily measurable quantities, as the sensitivity of the sensor variation to moisture

absorption was increased by increasing its capacitance. In the case of the IDC this was done by increasing the effective length of each digit, and fabricating sensors with many digits. PEMs are designed to limit the package-related parasitic capacitances, as far as is reasonably practicable given other design constraints such as lead inductances and thermal dissipation. Consequently, the magnitude of capacitance variation observed in the previous chapters should far exceed those in actual PEMs. Evaluation of the scale of these changes due to the absorption of humidity within the silicone gel on an actual PEM was performed to evaluate the expected range of capacitance increase due to moisture absorption, which could be later verified with practical measurement. Ansys Q3D Extractor was used to determine the moisture-driven increase in the parasitic capacitances of a typical PEM DBC layout.

The geometry used for simulation is shown in Fig. 4.3, based on physical measurement of one of six DBC rafts in a commercial PEM typically used in power conversion applications. Measurements were taken with digital micrometers. DBC manufacturers generally provide fixed options for geometries, but these were not given in the module datasheet and so the measurements were used. The length (Y) and width (X) were measured at 53 mm and 39 mm, respectively. The thickness (Z) was measured at 990 µm, with equal thicknesses in the top copper, alumina, and bottom copper of 330 µm. The trench width and copper pullbacks were 762 µm and 562 µm, respectively. The pullback was identical for the top and bottom copper. Bond wires were used to connect Out to Emit Top and Bot to Emit Bot,

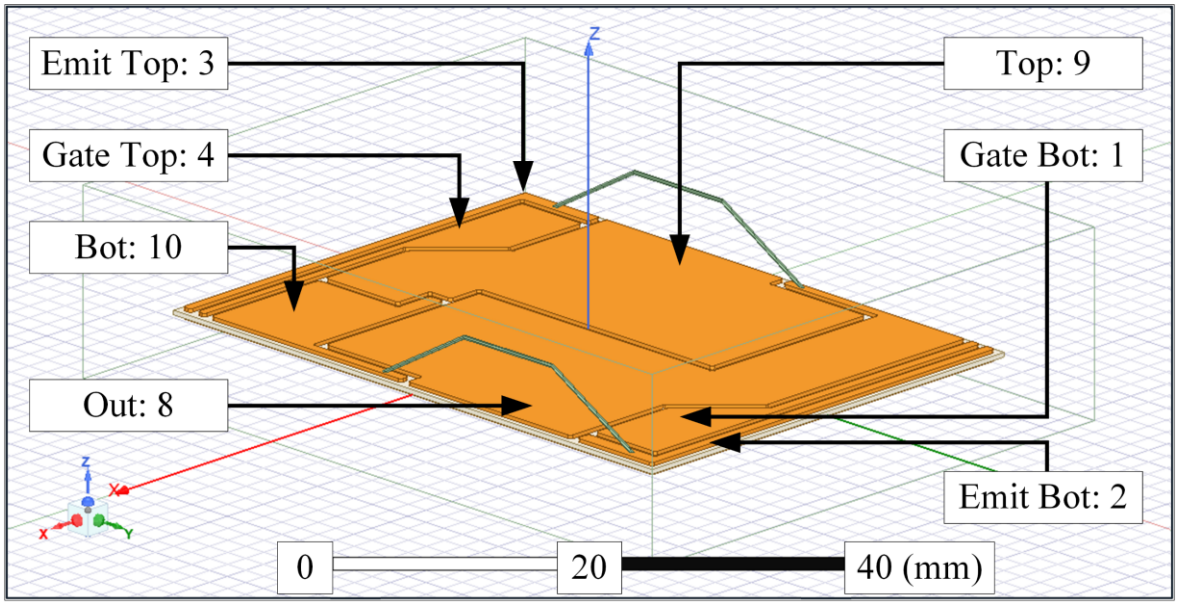

Fig. 4.3 Geometry of single FF1000R17IE4 DBC raft used for parasitic capacitance simulation in Ansys Q3D Extractor. Annotations refer to corresponding terminal indications as shown in Fig. 4.1, 'Top' indicates the upper device in the half bridge configuration, 'Bot' indicates the lower.

representative of the configuration of the real module, providing unbroken nets for the simulation. To aid in computational efficiency and simulation times, only the encapsulated DBC portion of the module was simulated, with no bond wires other than those required. The silicone gel was represented as a cuboid measuring 49 × 63 × 15 mm (X × Y × Z), centred on the origin about the DBC. A spherical vacuum region with radius (r) 100 mm is applied, centred on the origin, to the edge of which a balloon-voltage boundary condition is applied ($V(r = \infty) = 0$).

According to the results shown in Chapter 3, the absorption of moisture within the gel causes two main parameter shifts relevant for the Q3D simulation. This work considers the 5 mm gel depth sample, as absorption to steady-state of this sample was more complete and the scale of the changes are larger than in other samples, giving a better understanding of the worst-case scenario. At 10 kHz, the derived ε_r' of this sample was observed to increase from 2.16 to 4.96 after 120 h in the 85 °C / 85% RH environment. Similarly, the dielectric loss factor $tan(\delta)$ was observed to increase from 0.0026 to 0.1555. The typical values of these parameters at 50 Hz as given by the manufacturer datasheet are 2.7 and 0.001, respectively. The relationship between ε_r' and $tan(\delta)$ is likely not precisely linear, and no cross-correlation study was performed to better identify the relationship as this was deemed out of scope. Consequently, parametric simulations were performed for each combination of the following parameter ranges: $2 \leq \varepsilon_r' \leq 5;\ 0.001 \leq tan(\delta) \leq 0.16$. A total of 32 linearly-spaced points were considered across each range, resulting in a total of 1024 total simulations at which the DBC capacitances were evaluated. No specific boundary conditions or excitations are required for Q3D Extractor, only material definitions. Nevertheless, to aid the simulation in convergence to a representative solution with respect to possible minute fringing effects outside of the silicone gel, a vacuum region was applied as a 100 mm radius sphere, situated at the origin. The origin for this simulation was centred within the centre of the DBC. Results are presented in terms of C_1–C_3 relating to the top and bottom IGBT placements in the half bridge configuration shown in Fig. 4.1. The capacitive couplings C_1–C_3 are taken with respect to the geometries shown in Fig. 4.1 and Fig. 4.3. For the top IGBT, C_1, C_2 and C_3 are taken from the matrix results for: Top (9/11) to Gate Top (4), Out (8) to Gate Top (4), and Top (9/11) to Out (8), respectively. For the bottom IGBT, C_1, C_2 and C_3 are taken

from the matrix results for: Out (8) to Gate Bot (1), Bot (10/12) to Gate Bot (1), and Out (8) to Bot (10/12), respectively. Note that auxiliary collector terminal 5 is not simulated as it exists outside the DBC rafts carrying dies, and that the top and bottom IGBT emitter nets are shorted via bond wire to their respective output terminals, i.e., Emit Top (3) is the same net as Out (8), and Emit Bot (2) is the same net as Bot (10/12). For clarity, a key to these results is provided in Table 4.1, where an 'X' represents a self-capacitance which is not studied, and a 'O' represents a coupling capacitance not trivially related to C_1–C_3 and is not studied in this work.

TABLE 4.1
KEY FOR Q3D CAPACITANCE SIMULATION RESULTS FOR FF1000R17IE4 DBC

	Top	Gate Top	Out	Gate Bot	Bot
Top	X	C_1 Top	C_3 Top	O	O
Gate Top	C_1 Top	X	C_2 Top	O	O
Out	C_3 Top	C_2 Top	X	C_1 Bot	C_3 Bot
Gate Bot	O	O	C_1 Bot	X	C_2 Bot
Bot	O	O	C_3 Bot	C_2 Bot	X

The results shown in Fig. 4.4 highlight a clear relationship between the effective coupling length of the copper elements on the DBC floorplan and the resultant parasitic capacitance, as expected. These results in terms of minimum and maximum capacitance and adjacent copper coupling lengths are shown in Table 4.2. The results of Fig. 4.4 also show a non-monotonic relationship between the DBC parasitic capacitance with increasing $tan(\delta)$. In each case, the maximum capacitance increase is observed to occur at $\varepsilon_r' = 5$ and $tan(\delta) = 0.1036$, rather than at the maximum of $tan(\delta) = 0.16$. In percentage terms, the DBC parasitic capacitances increased on average by 356.24%, although in each case C_2 increased the most, followed by C_1 and then C_3.

TABLE 4.2
SELECT CAPACITANCE RESULTS FROM Q3D SIMULATION OF FF1000R17IE4 DBC

Capacitance ID	Minimum [pF] $\varepsilon_r' = 2$ $tan(\delta) = 0.001$	Maximum [pF] $\varepsilon_r' = 5$ $tan(\delta) = 0.1036$	Increase [%]	Effective adjacent coupling length [mm]
C_1 Top	0.3460	1.6515	377.31	25.16
C_2 Top	0.4938	2.3773	381.43	42.66
C_3 Top	1.4529	6.0698	317.77	57.15
C_1 Bot	0.4940	2.3499	375.69	37.78
C_2 Bot	0.4901	2.3685	383.27	42.66
C_3 Bot	0.9461	3.8030	301.97	25.30

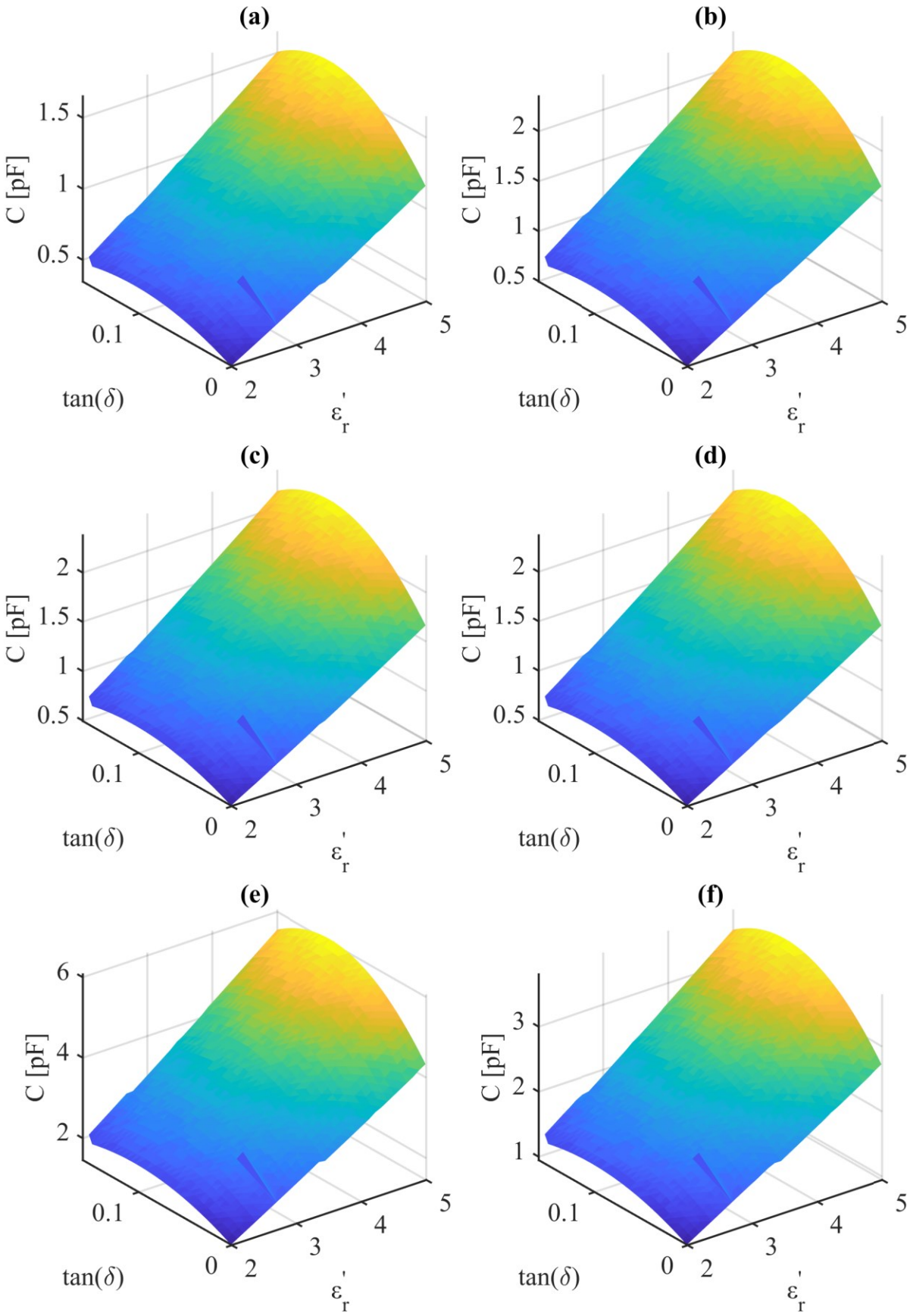

Fig. 4.4 Q3D simulation results on FF1000R17IE4 DBC for capacitance based on sweeps of ε_r' and $tan(\delta)$ in the ranges 2–5 and 0.001–0.16, respectively. Subplots refer to capacitances from DBC top copper couplings as labelled in Table 5.1: (a) C_1 Top, (b) C_1 Bot, (c) C_2 Top, (d) C_2 Bot, (e) C_3 Top, and (f) C_3 Bot.

The values for C_{ies} and C_{res} for the FF1000R17IE4 IGBT module given by the datasheet are 81 nF and 2.6 nF, respectively. No measurement data is provided for C_{oes}. The increase in these parameters related to the DBC parasitic capacitances C_1–C_3 are given by (54)–(56):

$$C_{ies}^{*} = C_{ies} + \Delta C_{ies} = C_{ies} + C_1 + C_2 \tag{54}$$

$$C_{oes}^{*} = C_{oes} + \Delta C_{oes} = C_{oes} + C_1 + C_3 \tag{55}$$

$$C_{res}^{*} = C_{res} + \Delta C_{res} = C_{res} + C_1 \tag{56}$$

where C_{ies}^{*}, C_{oes}^{*}, and C_{res}^{*} are the adjusted values of C_{ies}, C_{oes}, and C_{res}, respectively; and ΔC_{ies}, ΔC_{oes}, and ΔC_{res} are the DBC-related parasitic capacitance at maximum moisture absorption according to Chapter 3 in the 85 °C / 85% RH condition.

Note that the datasheet-given values are stated at 1 MHz, whereas the change in capacitances use the 10 kHz values of ε_r' and $tan(\delta)$, limiting the applicability of this approach. For the top IGBT, the increases in parasitic capacitance due to moisture absorption are estimated as: $\Delta C_{ies} = 4.03\,pF$, $\Delta C_{oes} = 7.72\,pF$, and $\Delta C_{res} = 1.65\,pF$. For the bottom IGBT, the values are: $\Delta C_{ies} = 4.72\,pF$, $\Delta C_{oes} = 6.15\,pF$, and $\Delta C_{res} = 2.35\,pF$.

Taking the largest increase in C_{ies} (4.72 pF for the bottom IGBT), the change in the corresponding datasheet-given die-related capacitance ($C_{ies} = 81\,nF$) is only a roughly 0.006% increase, which can be considered negligible. If the datasheet values are given in terms of the complete module rather than the individual IGBT dies, the increase in capacitance will be larger. The datasheet values provide no information as to test temperature or humidity, but it is likely to be 25 °C, commensurate with other parameters. In that case, as there are six individual DBC rafts in parallel to form the module, the increase in C_{ies} due to moisture absorption in the gel would instead be 28.32 pF or 0.035%, which can still be considered negligible. This simple analysis neglects the complicated nature of capacitive coupling from multiple sources working in tandem, and neglects fully the influence of the capacitance due to coupling through the ceramic to the baseplate, so it should be considered an indication of a possible phenomenon rather than absolute fact.

4.2 IGBT Module Parasitic Capacitance Measurement in High Humidity Environment Under Bias

Although the gel-related parasitic capacitance increase highlighted by simulation in the previous section in the humid condition were but a fraction of the parasitics already present in the module due to the IGBT die itself, the simulation models only a few material properties and does not provide a complete perspective. Additionally, no bias is applied in the case of simulation using Ansys Q3D Extractor, which may have unintended effects given the dynamic nature of the die parasitic capacitances respective to the applied bias, V_{CE}. To query the expected negligible change in module capacitances due to moisture absorption in the silicone gel encapsulation, measurement of C_{ies} of a commercial IGBT module (Infineon FF1000R17IE4) was performed with a fixed 25 V bias. This was done in situ using the measurement circuit described by Fig. 4.5 based on manufacturer guidance [233]. The collector and emitter of the top IGBT in the half bridge module were shorted to isolate the bottom IGBT for measurement. A 2.2 µF capacitor was used to short the collector and emitter of the bottom IGBT to AC signals, across which a bias V_{CE} of 25 V was applied for the duration of the test. A 10 kΩ resistor was placed between the bias and the collector of the IGBT to limit the current during the test. The measurements were performed using a Wayne Kerr 6500B precision impedance analyser, connected between the IGBT gate and emitter. The impedance analyser required no additional isolation from the circuit due to the connection to the insulated gate of the IGBT. The IGBT module was placed inside a programmable benchtop environment chamber, alongside the limiting resistor and AC shorting

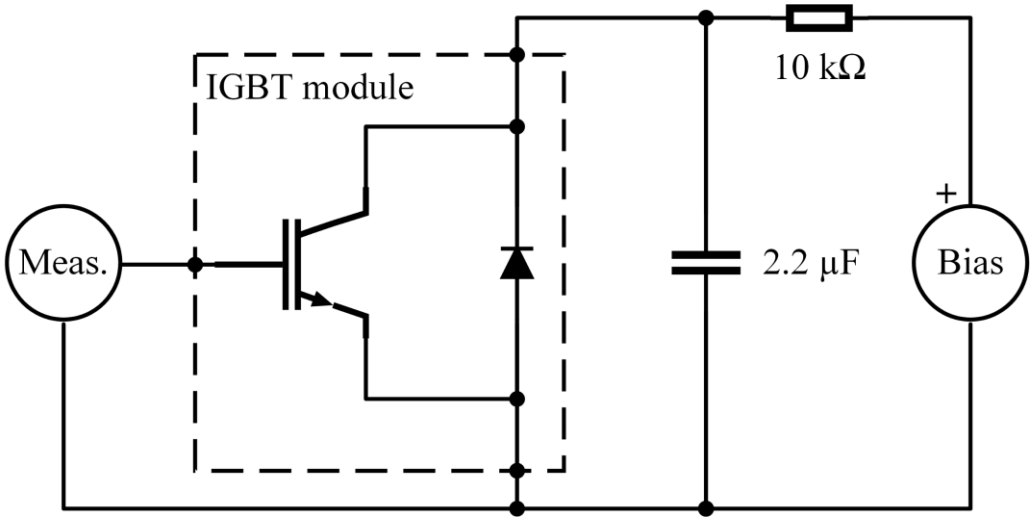

Fig. 4.5 Circuit used for measurement of C_{ies} on FF1000R17IE4 module. Only bottom IGBT is measured, with the top IGBT having its emitter and gate shorted. IGBT module, AC shorting capacitor and current limiting resistor placed inside environment chamber.

capacitor. Connection to the power supply and impedance analyser were made via wire through a sealed foam bung. In this way, the C_{ies} of the IGBT is measured in situ of a controlled environment and under bias. When devices are characterised by manufacturers, they are placed in specialised and well-controlled jigs which make all requisite connections and ensure identical conditions from sample to sample and lot to lot, so the measurement in this case value was expected to deviate from the datasheet even at 25 °C.

To drive off any moisture absorbed in the IGBT housing or in the silicone gel, the setup was held at a controlled environment of 85 °C / 30% RH for 24 h before the start of test. On commencement of the test, the RH setpoint of the chamber was changed to 85% RH. At that time, the DC power supply unit (PSU) was energised, providing a bias V_{CE} of 25 V. Based on previous experience, the chamber was expected to achieve the RH setpoint within 15 minutes. The frequency sweep measurement of C_{ies} was limited to the range 50 kHz – 1.5 MHz due to measurement difficulties at lower and higher frequencies, owing to the dynamic behaviours of the chip capacitances and the parasitic inductances introduced by the necessary cabling. Measurements were taken every 10 minutes for 2 hours, and then every 10 minutes again from hours 3–4. Due to relative lack of variation in the measurement by that time and considering the time scale of changes observed in previous testing, the high-temperature high-humidity environment was held overnight. Another hour of measurements were performed the following day. By the end of this last set of measurements, a total of 26 hours had passed. Fig. 4.6 presents the frequency sweep data at the start of the test (t_0), after 4 hours (t_{240}), and at the end of test at 26 hours in the high-temperature high-humidity environment (t_{1560}). At 50 kHz, the measurements for t_0, t_{240} and t_{1560} were 80.769 nF, 80.782 nF, and 80.782 nF, respectively, an increase of about 13 pF. At higher frequencies, measurement noise outweighs any discernible difference in the measurements.

The increase in C_{ies} for the bottom IGBT taken from simulations in Ansys Q3D, which was performed at 10 kHz, was 4.72 pF, about a third of the practical measurement. Although slight disagreement between practice and simulation are evident, they are within the same order of magnitude relative to the scale of C_{ies} pertaining to the IGBT die itself. The lack of increase in measured C_{ies} from t_{240} to t_{1560} across the full frequency range indicates that the moisture absorbed in the gel had reached

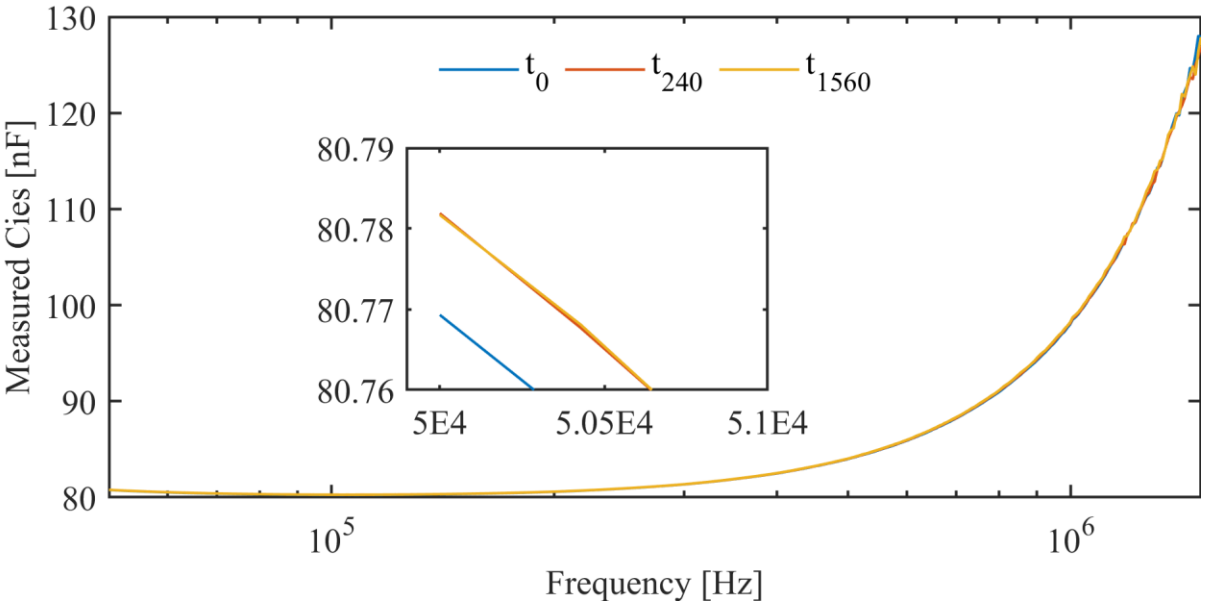

Fig. 4.6 Measured C_{ies} of FF1000R17IE4 after time in 85 °C / 85% RH condition. Measurements performed under 25 V bias. Starting condition is 85 °C / 30% RH. Traces shown are start of test t_0 (blue), after 4 hours t_{240} (orange) and end of test after 26 hours t_{1560} (yellow). Measurements in frequency range 50 kHz – 1.5 MHz. Inset shows range 50–51 kHz.

steady-state by t_{240}. Measurements of C_{res} and C_{oes} were attempted but failed due to the negative influence of the cabling required to hold the DUT in the environment chamber. These parameters are significantly lower in value, pertaining to the IGBT die of the FF1000R17IE4. Consequently, moisture absorption in the gel is expected to cause a larger increase in C_{res} and C_{oes}, when compared with the measured increase in C_{ies}.

4.3 Investigation of Humidity Impact on IGBT Module Switching Parameters via Double Pulse Test

Although the expected increase in module parasitic capacitances due to moisture absorption are small, their influence on the dynamics during operation may be noticeable. Even slight increases in switching losses over time can reduce the useful lifetime of devices, leading to early failures and costly maintenance, made only more costly in the case of OWTs. It is pertinent then, to ascertain whether the switching behaviours of IGBTs in environments representative of the OWT application are influenced by the environment. Specifically, due to moisture absorption in the encapsulating silicone gel.

The prevailing technique for the retrieval of switching behaviours is the DPT, described by IEC 60747-9 Section 6 [234]. In this test, the IGBT is subjected to clamped inductive switching, and the turn-off and turn-on intervals are studied. The typical DPT arrangement is shown in Fig. 4.7. In the case

studied here which is a half bridge module, the top portion of the half bridge provides the FWD, and the bottom portion is the DUT.

Arrangements exist to study the top device rather than the bottom, but this is often more complicated. Consequently, it was determined that to provide an indication of the change in switching behaviours, study of the bottom device was sufficient. The DPT is performed over 3 consecutive time intervals, here named t_1, t_2 and t_3. In the first interval, t_1, the load inductor L is charged to a set load current I_L by switching the DUT on. This current is a test parameter and is determined by the values of the following: the DC PSU voltage, V_{DC}; the size of the load inductor, L; and the length of the first interval, t_1. Interval t_2, also sometimes called t_{break}, has the DUT switched off, and I_L commutates to the FWD. This is the turn-off instant, at which appropriate measurements of the related turn-off parameters are taken under the specified I_L. This interval must be short to minimise power dissipation in the FWD and L, so that the same current flows through the DUT during turn-off and turn-on instants. The final interval is t_3, in which the DUT is again switched on for a set period, which should be long enough for the device to turn on fully. This provides the turn-on instant, allowing measurement of related parameters. The duration of interval t_1 is recommended to be less than 100 µs by industry-provided application notes, to limit self-heating of the device [235].

A graphical overview of the time periods and associated ideal waveforms typical in the DPT is provided in Fig. 4.8. In the literature, I_G is sometimes not investigated during DPT, but due to the potential influence of moisture absorption on C_{ies} the present work chose to include it.

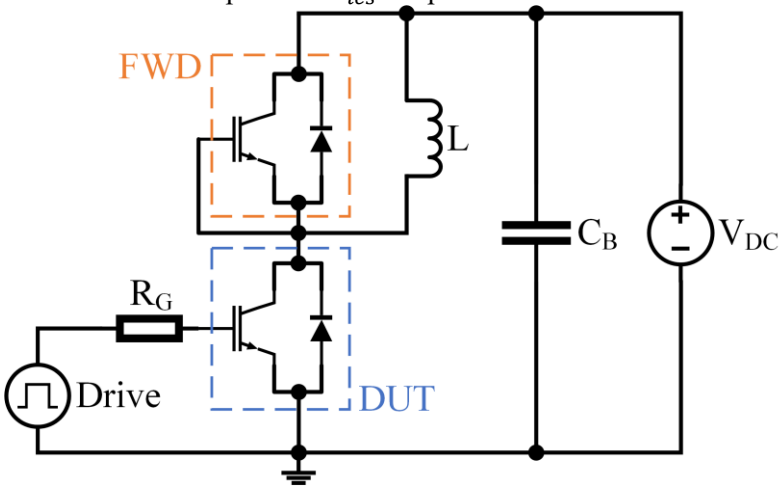

Fig. 4.7 Typical DPT circuit for half bridge IGBT module. Bottom IGBT is taken as the DUT (blue), top diode used as the FWD (orange).

4.3.1 Test Platform

Connection of the DUT to the DPT equipment was made using cabling directed through a sealed foam bung. Similarly, measurements were taken ex situ, and therefore some influence of parasitic inductance and capacitance of the necessary cabling was expected. The DPT test apparatus was designed in accordance with IEC 60747-9 and industry application notes. The first design parameter was to limit self-heating within the device by fixing the duration of each individual DPT to less than 100 µs. The load inductor L is dimensioned according to the Rohde & Schwarz application note and considering that the devices chosen for test are usually operated at $V_{DC} = 1100\,V$ [235]. Dimensioning considers the higher and lower limits for the value of the load inductor. The higher limit of the load inductor is given by (57):

$$L \leq t_1 \cdot \frac{V_{DC}}{I_L} \tag{57}$$

The lower limit of the load inductor considers the current loop during the t_2 interval, where I_L commutates to the FWD. During this time, the current in this loop will decay according to the forward

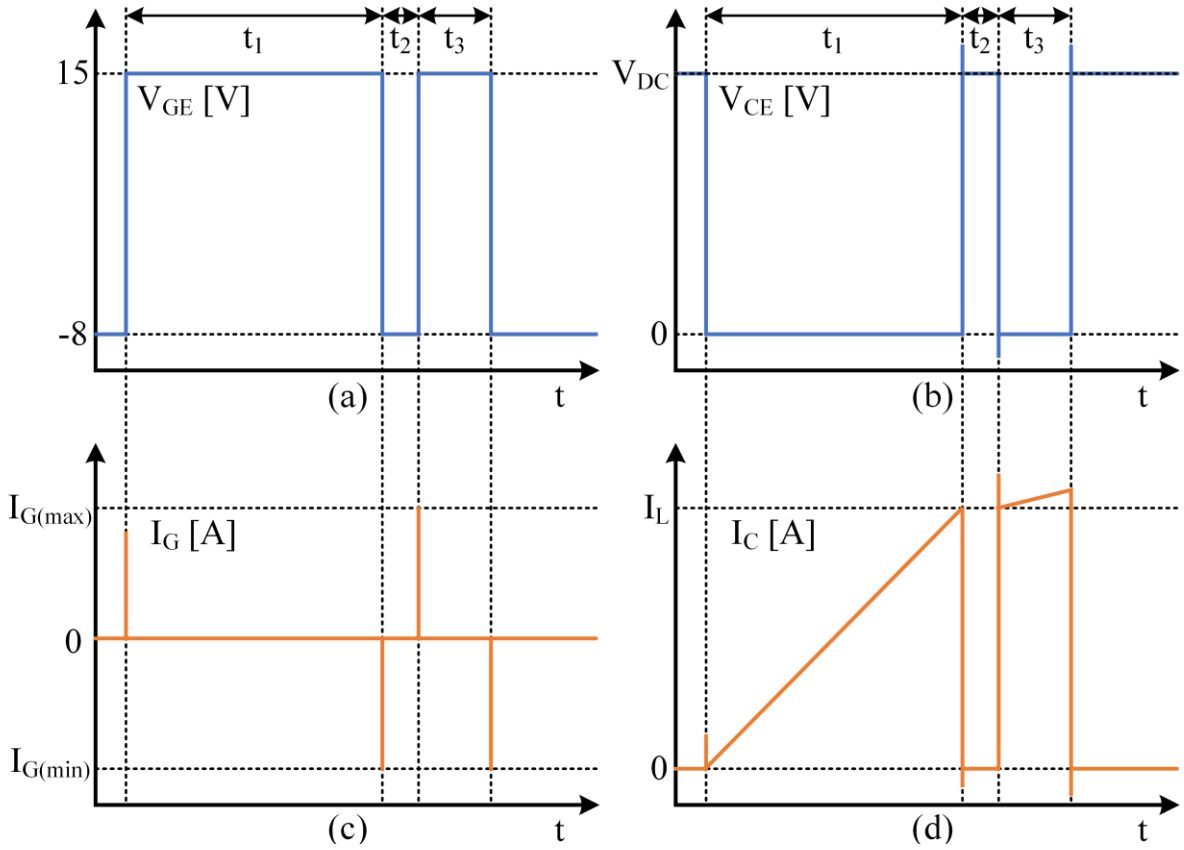

Fig. 4.8 Idealised waveforms for DPT on IGBT. (a) V_{GE}, (b) V_{CE}, (c) I_G, and (d) I_C.

voltage of the clamping diode V_f, and the parasitic resistance of L, R_s. A full derivation of this parameter can be found in the application note, but only the final relationship is required here. It is given by (58):

$$L \geq -\left[R_s \cdot t_2 \cdot \left(\frac{1}{\ln\left(\frac{\Delta I}{I_L + \frac{V_f}{R_s}} + 1\right)}\right)\right] \tag{58}$$

where ΔI is the drop in the circulating current during the interval t_2.

The lowest current rating of the module types studied was 100 A. The voltage rating of all modules chosen was 1.7 kV, although as previously discussed, $V_{DC} = 1100\,V$ was chosen. The stray resistance R_s depended on the length of wire used for the inductor, which was to be hand-wound and air-cored.

To ensure that sufficient current can be provided for the test, a capacitor bank (C_B as shown in Fig. 4.7) is required. This also provides the opportunity to protect the DC PSU from harmful oscillations by using a snappy high-voltage diode. During the test, energy is taken from C_B to provide the desired test current through L. Over the course of the test, a voltage drop will occur on the capacitor as power is dissipated, termed ΔV_{DC}. It is desirable to maintain the DC bus at a constant value over the course of the test, and so ΔV_{DC} is a design parameter that is usually kept low in value relative to that of the DC bus. For $V_{DC} = 1100\,V$, it was determined that a 1% decrease in V_{DC} was tolerable for this work, so $\Delta V_{DC} \leq 11\,V$. The full theoretical derivation of the value of C_B is again provided in the Rohde & Schwarz application note, with the result presented here in (59):

$$C_B \geq \frac{L \cdot I_L^2}{2 \cdot V_{DC} \cdot \Delta V_{DC} - \Delta V_{DC}^2} \tag{59}$$

The air-cored inductor was fabricated by hand according to Lundin's formula for a single-layer circular coil [236], which depends on the 'shape ratio' of the inductor, i.e., its diameter ($2a$) divided by the axial length (b). The handbook formula is given by (60) and (61), depending on the shape ratio:

$$For\ 2a \leq b; \quad L = \frac{\mu_0 n^2 \pi a^2}{b}\left\{f_1\left(\frac{4a^2}{b^2}\right) - \frac{4}{3\pi}\frac{2a}{b}\right\} \tag{60}$$

$$For\ 2a < b; \quad L = \mu_0 n^2 a\left\{\left[ln\left(\frac{8a}{b}\right) - \frac{1}{2}\right] f_1\left(\frac{b^2}{4a^2}\right) + f_2\left(\frac{b^2}{4a^2}\right)\right\} \tag{61}$$

where n is the number of turns of the coil, a is the radius of the coil, b is the axial length of the coil, $f_1(x)$ is given by (62), and $f_1(x)$ is given by (63).

$$f_1(x) \approx \frac{1 + 0.383901x + 0.017108x^2}{1 + 0.258952x}, \quad 0 \leq x \leq 1 \tag{62}$$

$$f_2(x) \approx 0.093842x + 0.002029x^2 - 0.000801x^3, \quad 0 \leq x \leq 1 \tag{63}$$

The plastic bobbin around which L was to be formed provided $2a \leq b$, so (60) was used. The number of turns, was determined by rearranging (60) to give (64):

$$n = \sqrt{\frac{L \cdot b}{\mu_0 \cdot \pi \cdot a^2 \cdot f_f}} \tag{64}$$

where f_f is given by (65):

$$f_f = f_1\left(\frac{4a^2}{b^2}\right) - \frac{4}{3\pi}\frac{2a}{b} \tag{65}$$

After all theoretical dimensioning was complete, C_B was determined to be 600 µF due to availability of bulk capacitors in a suitable form factor and with sufficient voltage rating. The minimum L was determined to be around 4.15 µH. The maximum L was determined to be between 110 µH – 1.1 mH depending on t_1 ($10\ \mu s \leq t_1 \leq 100\ \mu s$). Some inaccuracy was expected in the hand-winding of L, so it was anticipated that the test intervals would require fine-tuning to achieve the desired I_L of 100 A. The fabricated load inductor was measured with an RLC meter at 200 kHz as 154.75 µH, with 1.23 Ω of parasitic resistance. The capacitor (Kemet C44U, 600 µF, 1.3 kV) was similarly measured at 120 Hz as 578.4 µF and 3.3 mΩ. To provide sufficient gate drive signals, a Semikron Skyper 42 LJ R driver core was selected, and placed on an appropriate adapter board created for this work. To protect the DC PSU, a 1.7 kV diode (Wolfspeed C5D05170H) was inserted between it and the C_B connection. A 10 kΩ, 25 W discharge resistor R_{dis} was placed across C_B, which was switched out only for the duration of the test, ensuring that C_B was energised only when required. A NI cRIO was used to control R_{dis} and generate user-defined gate timings which were fed into the driver board, as well as to set the voltage level and number of consecutive tests. To measure V_{GE} with minimal loading and disturbance, a HV fibre-optic isolated voltage probe with BW 60 MHz was used (Teledyne LeCroy HVFO103), connected

to the gate and emitter of the DUT by additional wires to minimise impact on the drive loop. Gate current I_G was measured with a conventional 100 MHz current probe (CP031). A 400 MHz HV differential probe was used to measure V_{CE} (HVD3220), and a 30 MHz Rogowski coil was used to measure the test current I_C (Power Electronic Measurement CWTUM/1/B). All measurement equipment was connected to a Teledyne LeCroy WavePro 404HD 4 GHz BW oscilloscope, set to a sample rate of 10 GS·s^{-1} and configured to trigger on the first gate voltage positive slope at the start of t_1. Channels were deskewed to the HVFO103 using a deskew calibration source (Teledyne LeCroy DCS025). An annotated photograph of the DPT control cabinet equipment is provided in Fig. 4.9.

Before testing, the value of the gate resistor R_G in the driver board was investigated. To be representative of converters used in WECS, it was desirable to keep the value of R_G low. The application guidance for the Skyper 42 LJ R advises 2 Ω. With $R_G < 6.8\ \Omega$, oscillations were observed in each measurement channel during t_3, which could indicate incipient failure of the DUT, or potentially cause spurious switching and invalidate the test. This was attributed to the cabling required to connect to the

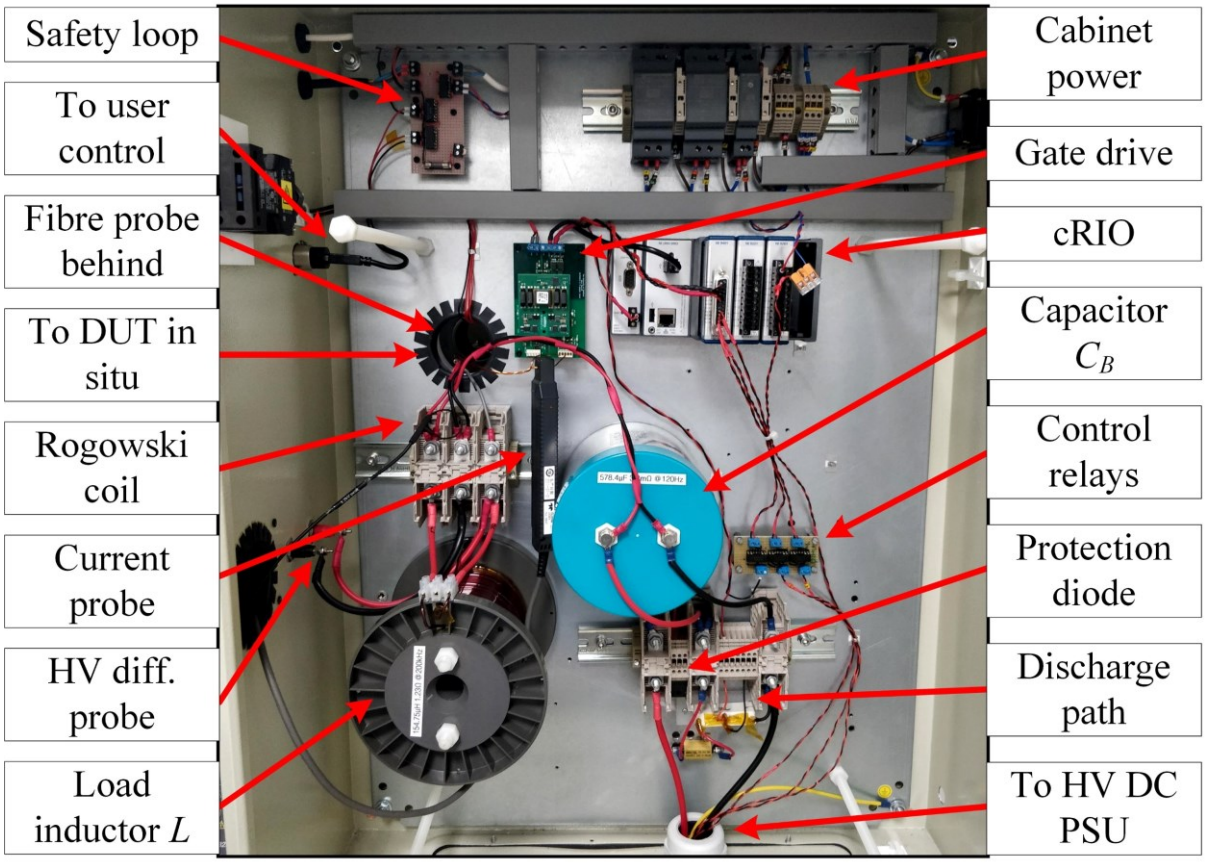

Fig. 4.9 Annotated photograph of control and measurement cabinet for DPT.

DUT in the environment chamber. Fig. 4.10 shows recorded oscillations in V_{ge}. Consequently, R_G was set to 6.8 Ω. For reference, a diagram of the full DPT setup used in this work is given in Fig. 4.11.

4.3.2 Test Procedure

The layout, or floorplan, of the DBC is expected to significantly influence coupling paths between copper elements and could cause significant changes in the increase in the parasitic capacitances. As a result, this work chose to investigate 3 module types from different manufacturers, which are outlined in Table 4.3. Modules were placed inside the environment chamber and dried out at 85 °C / 30% RH for 24 h before commencement of the tests, with single module being the DUT of each test run. Just

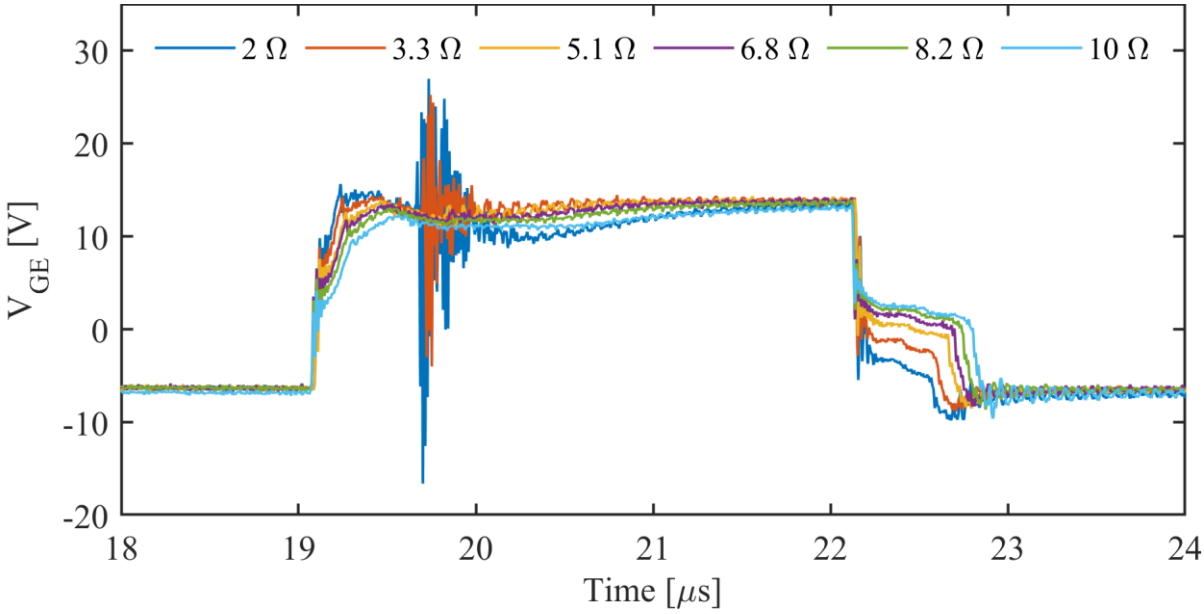

Fig. 4.10 Influence of value of R_G on V_{GE} oscillations recorded during DPT platform commissioning.

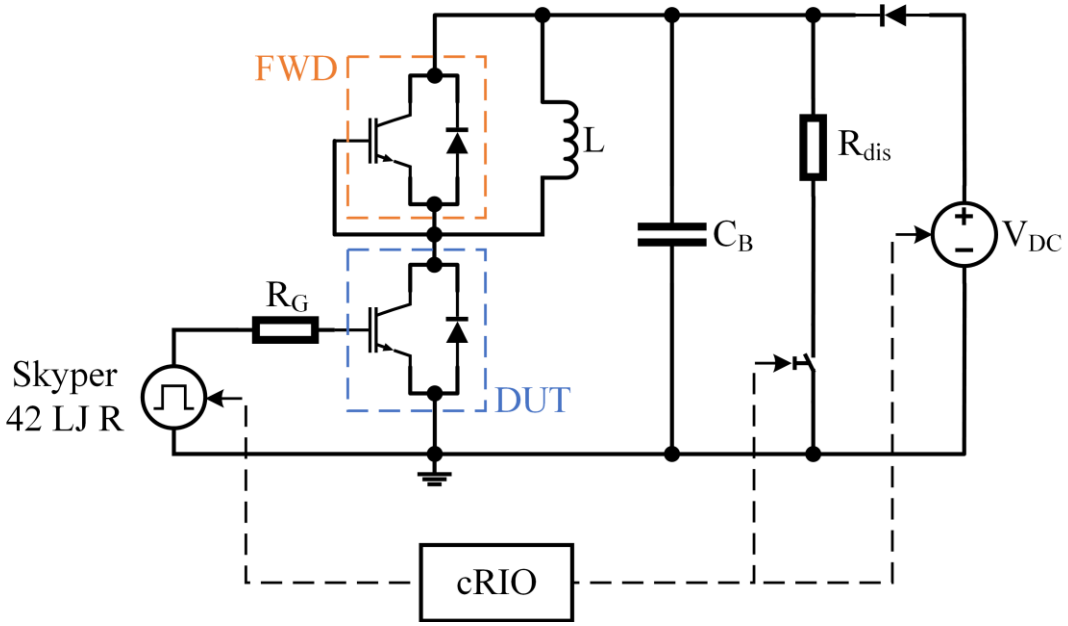

Fig. 4.11 Circuit diagram of major components of DPT test platform used in this research.

before testing, C_B was charged to the desired V_{DC}. A slight overshoot of V_{DC} during this period was present due to the lack of feedback control for the DC PSU, which settled to the desired value after approximately 30 tests. Consequently, the first 30 DPT were discarded from each test run to ensure that the overshoot was not reflected in the results. Tests were performed at a rate of 1 every 10 seconds for a duration of 3 hours, not including the discarded tests. At the start of the test clock, the chamber setpoint was changed from 30% RH to 85% RH, with the environment inside expected to stabilise after roughly 20 minutes, based on previous experience.

Test parameters are fully outlined in Table 4.4. Timing intervals were determined through trial and error to give the desired I_{test} and allow full turn-on and turn-off. Module type C has a higher gate charge than the other modules (10 µC vs. 800 nC), so it required longer intervals. Additionally, significant V_{CE} oscillations were present during testing of group C, resulting in several catastrophic failures. Consequently, the level of the DC bus was reduced.

TABLE 4.3
IGBT HALF BRIDGE MODULES TESTED IN THIS WORK

Module ID	Manufacturer	Part number	Voltage rating [V]	Current rating [A]
A	Semikron	SKM100GB17E4	1700	100
B	Star Power	GD100HFX170C1S	1700	100
C	Infineon	FF1000R17IE4	1700	1000

TABLE 4.4
PARAMETERS USED FOR DPT

Parameter	Module		
	A	B	C
Pulse count	1080	1080	1080
Test rate [min^{-1}]	6	6	6
Total test duration [h]	3	3	3
Test voltage, V_{DC} [V]	1100	1100	250
Test current, I_{test} [A]	100	100	82
t_1 [µs]	14	14	50
t_2 [µs]	3	3	40
t_3 [µs]	5	5	40

4.4 Results

4.4.1 Switching Characteristics

i. Definitions

A total of 20 switching-related characteristics were investigated in this research, including those typically presented in manufacturer datasheets. A full list is given in Table 4.5, alongside the definitions used.

TABLE 4.5
SWITCHING CHARACTERISTICS INVESTIGATED BY DPT

Turn off		Turn on	
Characteristic	Definition	Characteristic	Definition
$t_{d(off)}$	90% V_{GE} to 10% V_{CE}	dV_{CE}/dt	Slew rate of V_{CE} at turn off[4]
t_f	90%–10% I_C	$t_{d(on)}$	10% V_{GE} to 10% V_{CE}
t_{off}	$t_{d(off)} + t_f$	t_r	10%–90% I_C
E_{off}	$\int V_{CE} \cdot I_C \cdot dt$; 10% V_{CE} + 4 µs	t_{on}	$t_{d(on)} + t_r$
t_{GP}	Miller plateau width[1]	E_{on}	$\int V_{CE} \cdot I_C \cdot dt$; 10% I_C to 5% V_{CE}
$I_{G(off,pk)}$	Minimum value of I_G	I_{RRM}	Peak reverse recovery current[5]
$dI_{G(off)}/dt$	10%–90% slew rate of I_G	$I_{G(on,pk)}$	Maximum value of I_G
$Q_{G(off)}$	$\lvert\int I_G \cdot dt\rvert$ during turn off	$dI_{G(on)}/dt$	10%–90% slew rate of I_G
$V_{GE(off)}$	Lower state of V_{GE} histogram[2]	$Q_{G(on)}$	$\lvert\int I_G \cdot dt\rvert$ during turn on
V_{GEP}	V_{GE} in Miller plateau[3]	$V_{GE(on)}$	Higher state of V_{GE} histogram[3]

Notes: 1, Measured using distance between peaks in time derivative of V_{GE} during off transient following the approach of [57]; 2, determined from peaks of histogram of V_{GE} data in a window centred on off or on transient; 3, determined from peak of histogram of V_{GE} data in small window at off transient; 4, using slew rate of V_{CE} during turn-off in a similar manner to [125], given C_{GC} dependency; 5, calculated by subtracting peak value of I_C during turn-off from that at during turn-on.

ii. Initial Investigations in Fixed Conditions on Group A

Initial testing was performed on 3 modules in group A to ascertain which investigated characteristics change in a meaningful way due to moisture absorption. Modules placed inside a controlled environment chamber were held at 85 °C / 30% RH for 24 h before being subjected to 100 tests, with a repetition rate of 10 s. The chamber setpoint was changed to 85 °C / 85% RH and held for another 24 h, and then 100 more tests were performed. Notable changes were observed only in the characteristics relating to I_G: $I_{G(pk)}$, dI_G/dt, and Q_G. These initial results are shown in Fig. 4.12.

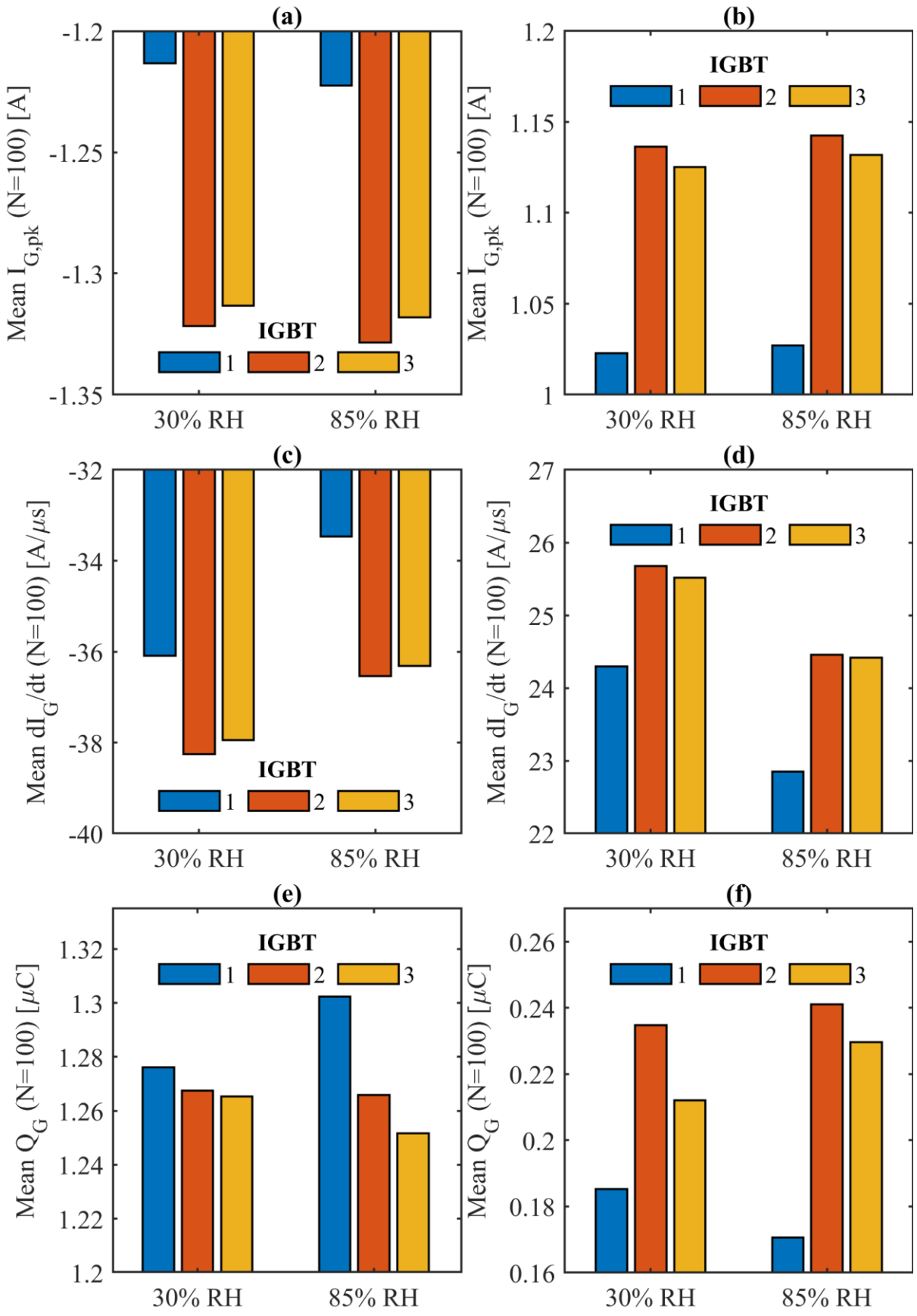

Fig. 4.12 Select switching characteristics from DPT on 3 modules of type A (SKM100GB17E4) after 24h in each of 2 environmental conditions: 85 °C / 30% RH and 85 °C / 85% RH. Results presented as means of 100 DPT runs. (a) $I_{G(off,pk)}$, (b) $I_{G(on,pk)}$, (c) $dI_{G(off)}/dt$, (d) $dI_{G(on)}/dt$, (e) $Q_{G(off)}$, and (f) $Q_{G(on)}$.

Although clear changes in the gate current related characteristics are demonstrated in Fig. 4.12, they are not consistent between modules of the same type (A). The recorded I_G during both turn on and turn off was lower for IGBT1 than it was for IGBT2 & IGBT3, though an increase in this parameter due to the high-humidity environment is observed for all samples. The humid environment appears to cause a reduction in the magnitude of dI_G/dt for all samples, which could be a result of an increase in C_{ies} due to moisture absorption within the gel. Sample behaviours again differ from IGBT1 to IGBT2 & IGBT3 for Q_G, where during turn off sample IGBT1 displays an increase in the humid environment and the others a slight decrease, with the reverse being true at the turn on interval. These preliminary investigations give a clear indication of a change in the switching behaviours of the IGBTs tested, but the nature of those changes is not consistent. Consequently, further testing required careful examination of these parameters.

iii. DPT Parameter Change Over Time in High-humidity Conditions – Module Type A

Typical DPT waveforms as recorded during testing of module type A are shown in Fig. 4.13. Oscillations are present during the start of the turn-off and turn-on intervals in V_{GE} and I_G, which are attributed to the length of cabling required to send drive current into the DUT in the environment chamber. To mitigate these oscillations, a 10 kΩ resistor is placed between gate and emitter of the DUT, at the terminal side. Additionally, V_{GE} is not held at precisely the output voltage of the driver board of +15/-8 V, and is attenuated to +13.7/-7.7 V, presumably due to the remote coupling of the driver and IGBT. A typical scenario is a closely-coupled arrangement of driver and IGBT, which was not possible here due to the anticipated negative influence of the harsh environment on the driver board. A study of just the IGBT behaviours was the focus of this research, with the study of an included driver left for future work. Nevertheless, the DUT is driven to completely off and on as required. The measurement noise present in most other recorded parameters is present in I_C due to the BW of the Rogowski coil used, relative to the other measurement equipment. Although $V_{CE(on)}$ is commonly used as a TSEP and used in CM works in the literature, the measurement performed in this research was not sensitive enough to precisely evaluate the influence of the humid environment. Evaluation of $V_{CE(on)}$ as a humidity sensitive electric parameter (HSEP) is therefore planned for future work.

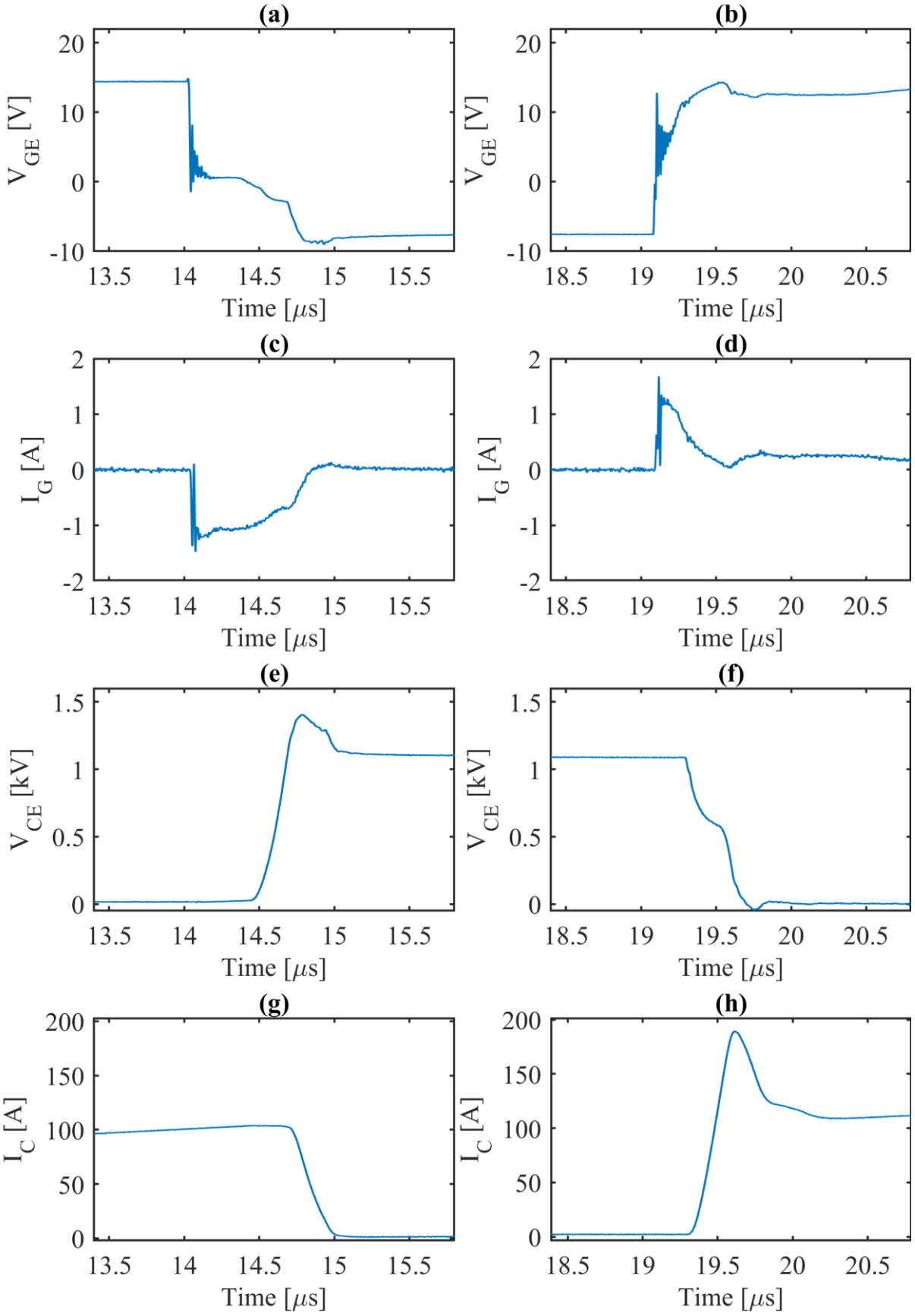

Fig. 4.13 Typical waveforms of DPT of module type A. Records taken at start of test clock (t_0) when humidity setpoint is changed from 30% to 85% RH. Records scaled in time axis to better display turn-off and turn-on intervals. (a) $V_{GE(off)}$, (b) $V_{GE(on)}$, (c) $I_{G(off)}$, (d) $I_{G(on)}$, (e) $V_{CE(off)}$, (f) $V_{CE(on)}$, (g) $I_{C(off)}$, and (h) $I_{C(on)}$.

The initial results highlighted a change in the gate current related parameters, which are shown for DPT over time in the harsh environment on module type A in Fig. 4.14. Here, only a slight increase in $Q_{G(off)}$ is observed at the start of the test, which is within the range of the noise in the measurement. No other gate current related characteristic displays any trend over time in 85 °C / 85% RH.

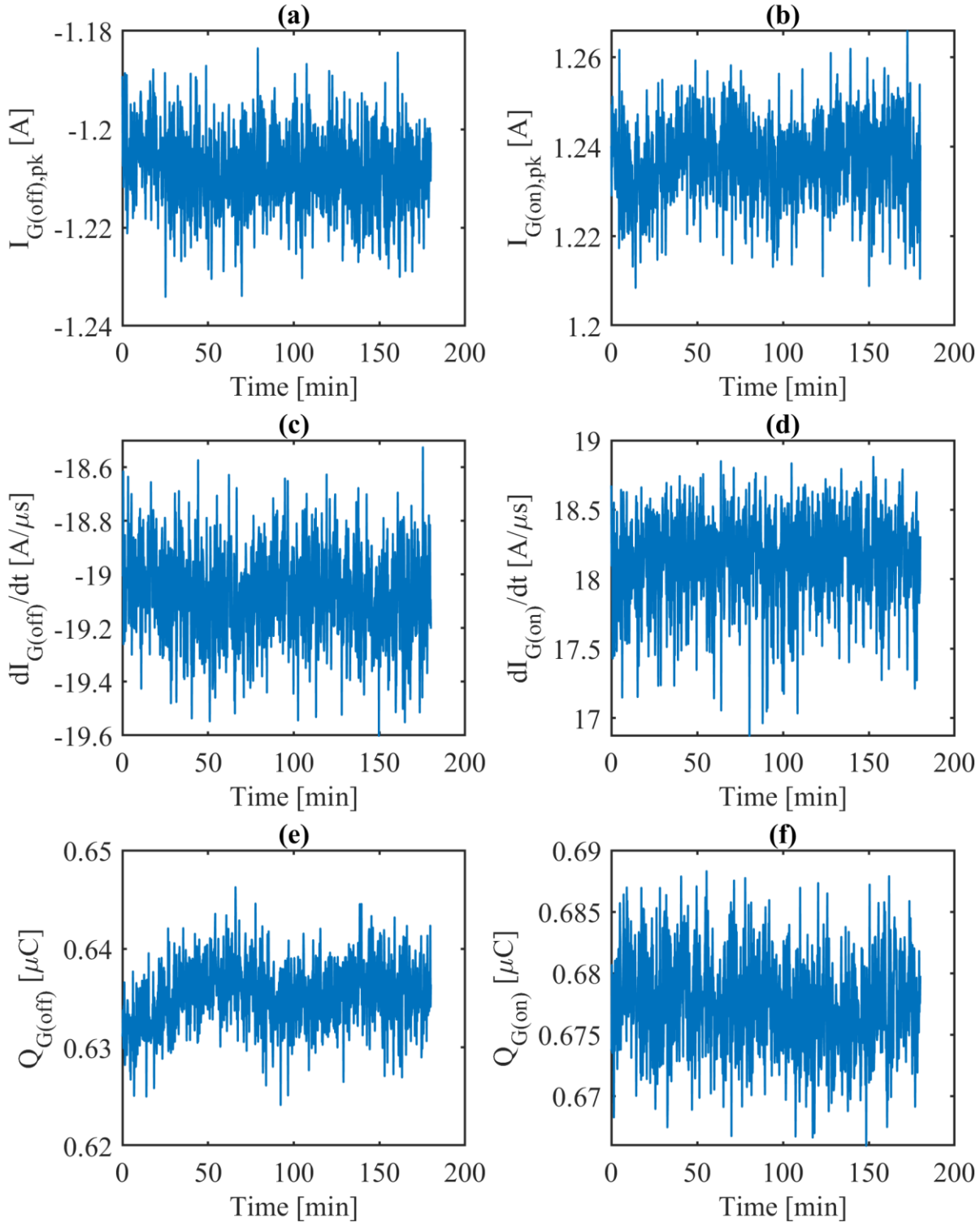

Fig. 4.14 Gate current related characteristics from DPT on module type A over time in 85 °C / 85% RH condition. (a) $I_{G(off,pk)}$, (b) $I_{G(on,pk)}$, (c) $dI_{G(off)}/dt$, (d) $dI_{G(on)}/dt$, (e) $Q_{G(off)}$, and (f) $Q_{G(on)}$.

Previous work in § 4.1 and § 4.2 indicates a potential increase in C_{GC}, which could lengthen the Miller plateau according to (2), although its influence is expected to be limited. Miller plateau width t_{GP} and voltage V_{GEP} for DPT on module type A are shown in Fig. 4.15. No appreciable change is observed over time for V_{GEP} other than a decrease in the mean value from 0.575 V to 0.56 V at approximately 83 min, which is attributed to noise within the estimation method. However, t_{GP} exhibits a decrease over time, until around 1 h. Though this change appears to relate to the moisture absorption in the gel given the results shown in Chapter 3, it is not commensurate with the expectation of a slight increase, rather than decrease. This change is then attributed to a different phenomenon, which will be discussed in § 4.4.2.

The switching parameters typically given in module manufacturer datasheets were also investigated, and these results are presented in a similar manner to the previous in Fig. 4.16. The only discernible change in any of the switching characteristics as presented is in $t_{d(off)}$, which shows an initial decrease outside of the range of the measurement noise, up until about 1 h of the test. A decrease in this parameter is not commensurate with the expectation of that if any change were to occur due to the absorption of moisture, an increase in time delays would be the result.

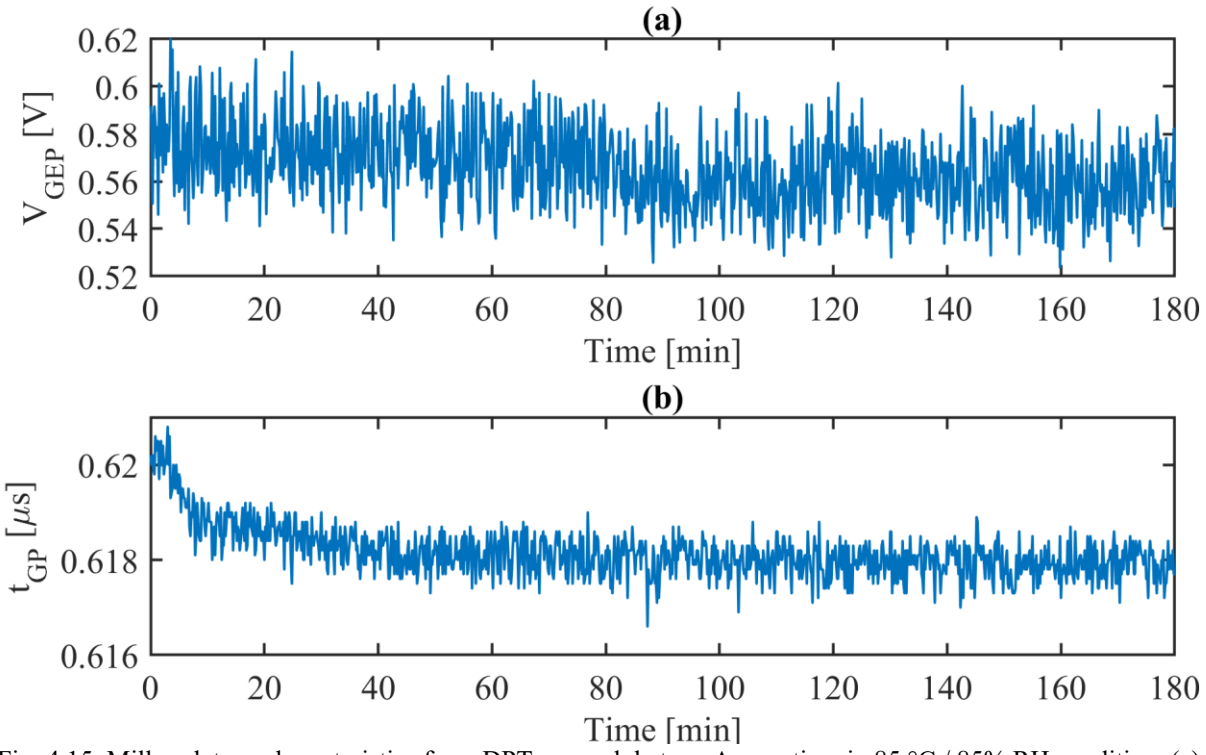

Fig. 4.15 Miller plateau characteristics from DPT on module type A over time in 85 °C / 85% RH condition. (a) Miller plateau voltage V_{GEP}, (b) Miller plateau width t_{GP}.

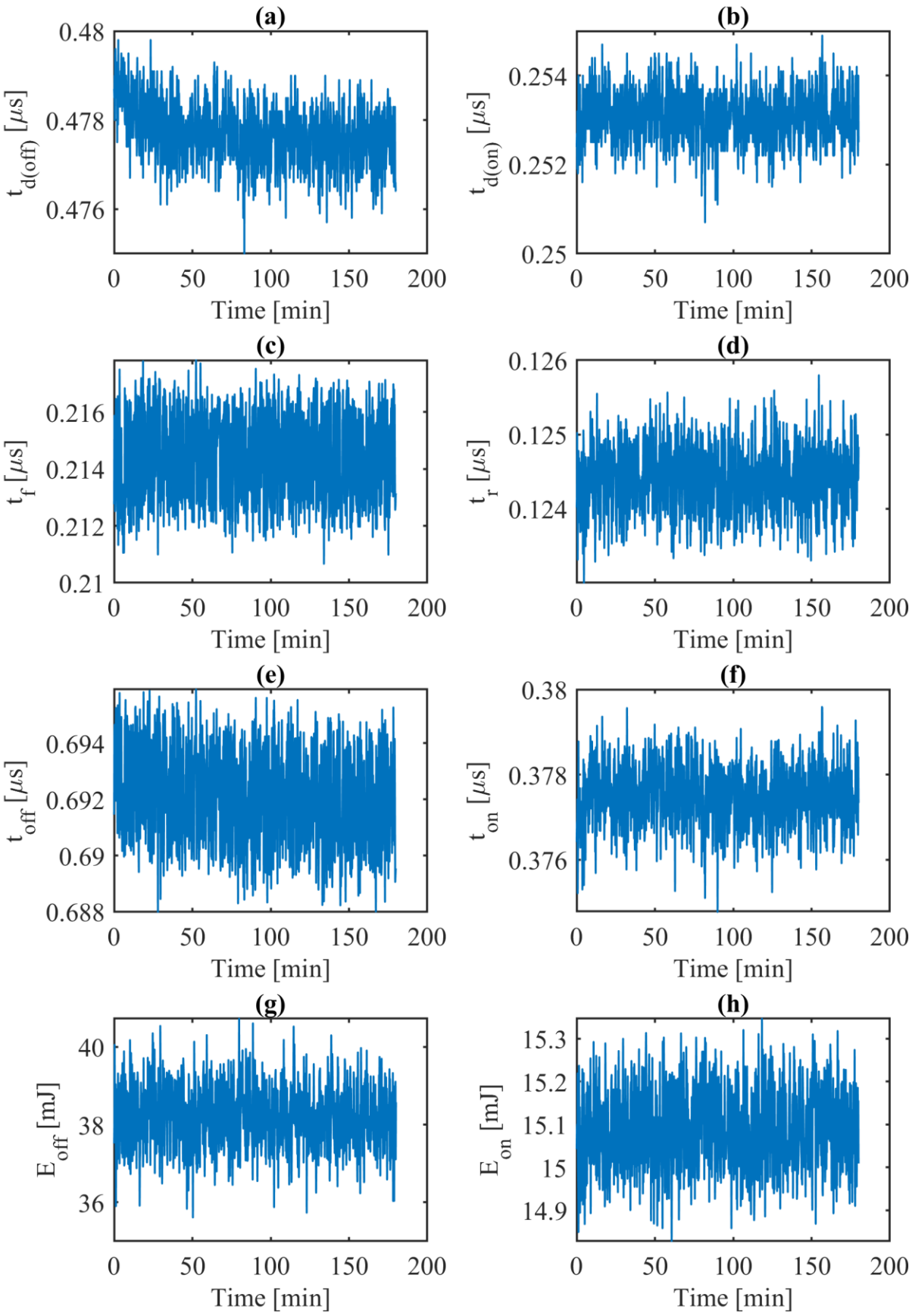

Fig. 4.16 Switching characteristics from DPT on module type A over time in 85 °C / 85% RH condition. (a) $t_{d(off)}$, (b) $t_{d(on)}$, (c) t_f, (d) t_r, (e) t_{off}, (f) t_{on}, (g) E_{off}, and (h) E_{on}.

During DPT testing of module type A some slight oscillation in V_{DC} was observed, owing to the open-loop control of the DC PSU and the heating-cooling cycle of the air conditioning in the laboratory. To ameliorate this issue the trolley containing the DC PSU was enclosed containing a large thermal mass, consisting of high-density concrete blocks. This achieved limited attenuation of the oscillatory behaviour in V_{DC}. Without the thermal stability mitigation, the variation in V_{DC} was ±2 V (results for module type A). With mitigation, ±0.5 V was observed (results for module types B and C).

iv. DPT Parameter Change Over Time in High-humidity Conditions – Module Type B

The waveforms recorded from DPT on module type B at the commencement of the test are shown in Fig. 4.17. Module B exhibits slight differences to module A when subjected to the DPT, such as increased V_{GE} oscillation, a reduced Miller plateau dip in V_{GE} and I_G, and a higher I_{RRM}. However, the behaviours are similar enough that the same interval times and test conditions were applied to DPT on module type B.

Fig. 4.18 shows the gate current related switching characteristics over time in the high-humidity environment derived from DPT on module type B. A significant amount of noise was originally present in these estimations due to the oscillatory behaviour of V_{GE} and I_G at the steepest parts of the switching intervals. The oscillatory behaviour was generally also inconsistent, where sometimes the first peak in the oscillation was either attenuated or increased relative to the following peaks. This caused the time-based thresholding procedure used to estimate the characteristics to 'bounce' between several peaks. In the data presented here, this issue is slightly ameliorated using Savitzky-Golay filtering of order 1 with a window of 301 samples (30.1 ns at 10 GS·s^{-1}). The fact must then be acknowledged that to smooth the waveforms such that the issue is eliminated entirely would naturally obfuscate any small changes in behaviours due to moisture absorption, and so the window is kept small. This scenario is worst in module type B, for which the filtering is applied to V_{GE} and I_G, but present in all modules tested to some extent. The noise is a result of oscillations introduced by the unavoidable presence of additional parasitics in the cabling required to connect to the DUT in situ, combined with the placement of the HVFO at the driver side rather than device side. Consequently, the filtered data for module type B are presented with the acknowledged caveat.

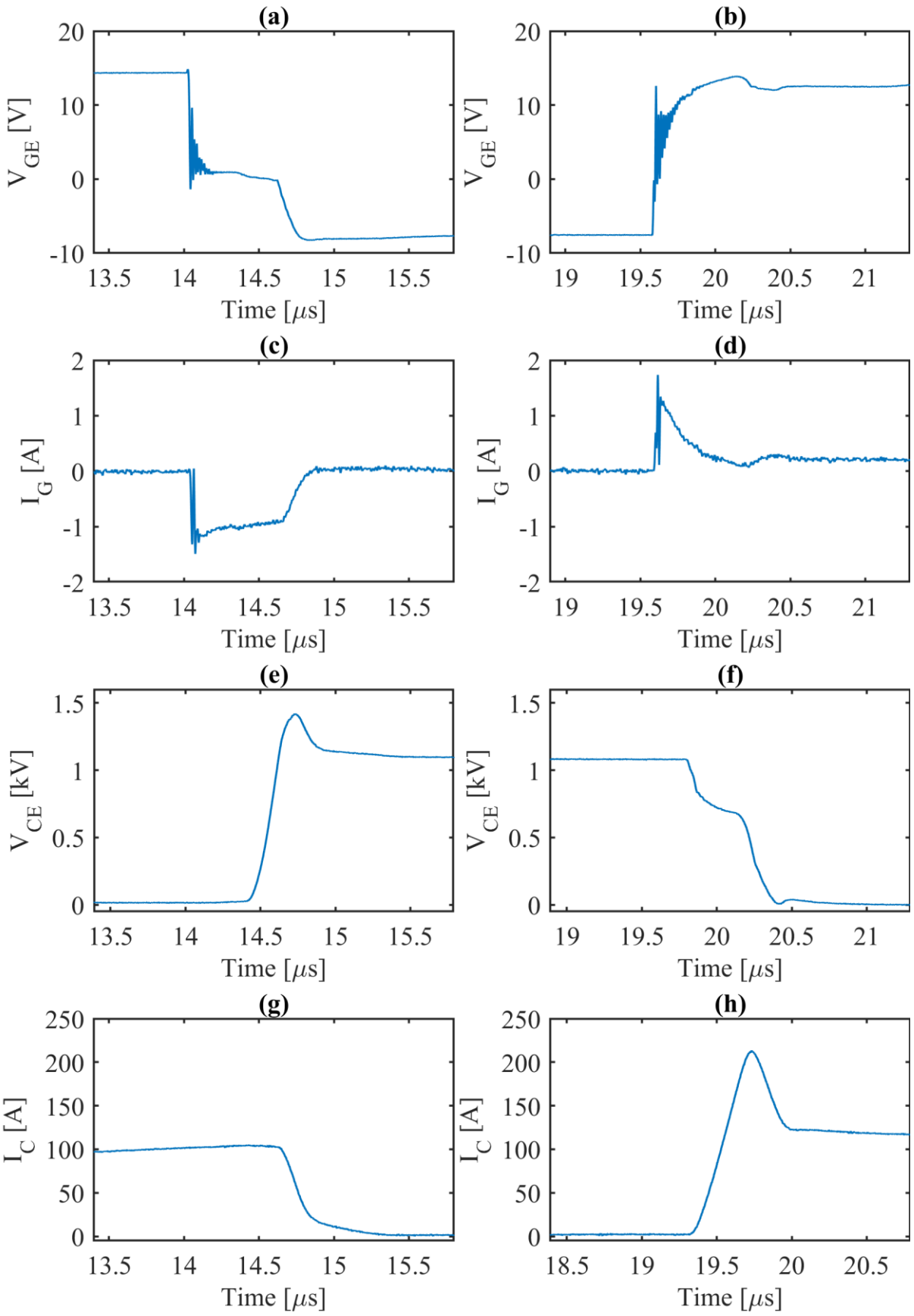

Fig. 4.17 Typical waveforms of DPT of module type B. Records taken at start of test clock (t_0) when humidity setpoint is changed from 30% to 85% RH. Records scaled in time axis to better display turn-off and turn-on intervals. (a) $V_{GE(off)}$, (b) $V_{GE(on)}$, (c) $I_{G(off)}$, (d) $I_{G(on)}$, (e) $V_{CE(off)}$, (f) $V_{CE(on)}$, (g) $I_{C(off)}$, and (h) $I_{C(on)}$.

For module type B, the gate current related parameters of Fig. 4.18 show only two behaviours worth noting. The first is the underlying oscillation that can be seen in the mean of the data, which is attributed to the aforementioned V_{CE} variation. Secondly, a minor increase in both $Q_{G(off)}$ and $Q_{G(on)}$ over time is observed. The increases are just 0.89% (6.5 nC) and 1.29% (8.4 nC) in the local means of $Q_{G(off)}$

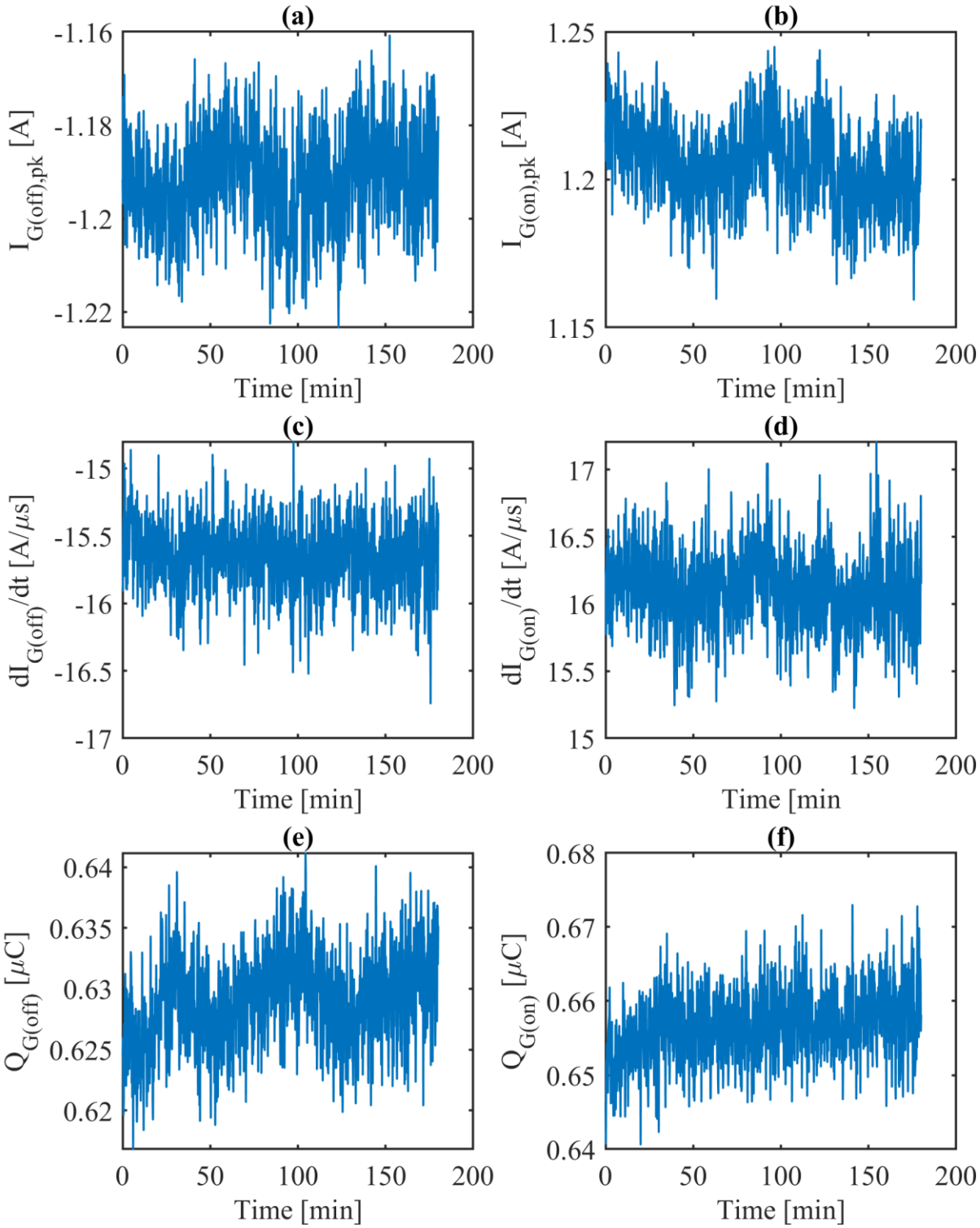

Fig. 4.18 Gate current related characteristics from DPT on module type B over time in 85 °C / 85% RH condition. (a) $I_{G(off,pk)}$, (b) $I_{G(on,pk)}$, (c) $dI_{G(off)}/dt$, (d) $dI_{G(on)}/dt$, (e) $Q_{G(off)}$, and (f) $Q_{G(on)}$.

and $Q_{G(on)}$, respectively. In absolute terms, each of these increases are less than half the magnitude of the noise in the signal, respectively, and must therefore be declared to be negligible. Similar behaviour is observed for $I_{G(on,pk)}$, which is similarly negligible.

The recorded Miller plateau related characteristics are shown in Fig. 4.19. As previously mentioned, the oscillations present significantly limited the accuracy of any estimated parameters pertaining to or derived from the V_{GE} data. Therefore, the filtered data are also shown alongside a moving mean (window 20 min), to attempt to better understand the underlying trends, if any. Although a slight increase in both V_{GEP} and t_{GP} over time could be interpreted from the means, they cannot be easily attributed to any specific phenomenon. As with module type A, the traditional switching parameters as given in the module datasheets are presented for module type B in Fig. 4.20. Slight increases over time are observed in the local means of several of the presented parameters: $t_{d(off)}$, $t_{d(on)}$, t_{on} and E_{on}. However, these are slight in magnitude with respect to the noise in the respective signals, and so again must be concluded to be negligible. Consequently, no change in module type B switching characteristics observed over time in the 85 °C / 85% RH environment.

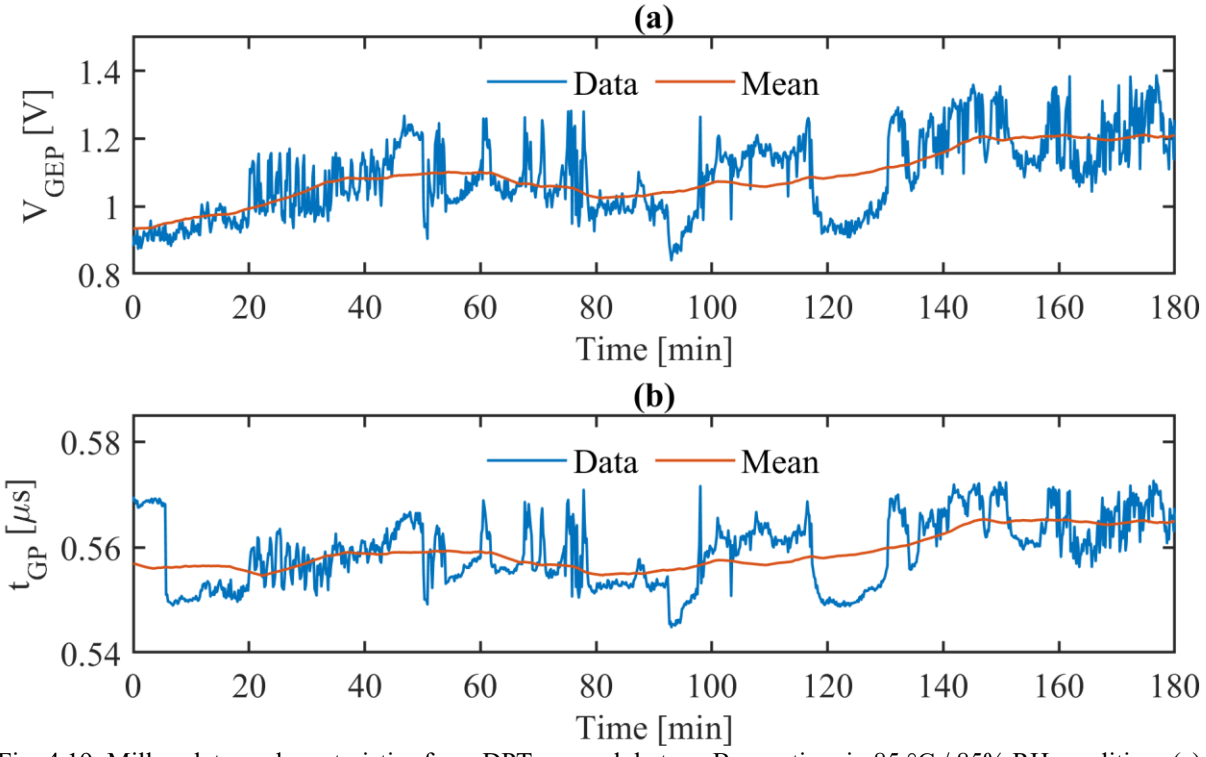

Fig. 4.19 Miller plateau characteristics from DPT on module type B over time in 85 °C / 85% RH condition. (a) Miller plateau voltage V_{GEP}, (b) Miller plateau width t_{GP}. Data in blue, moving mean ($N = 200$) in orange.

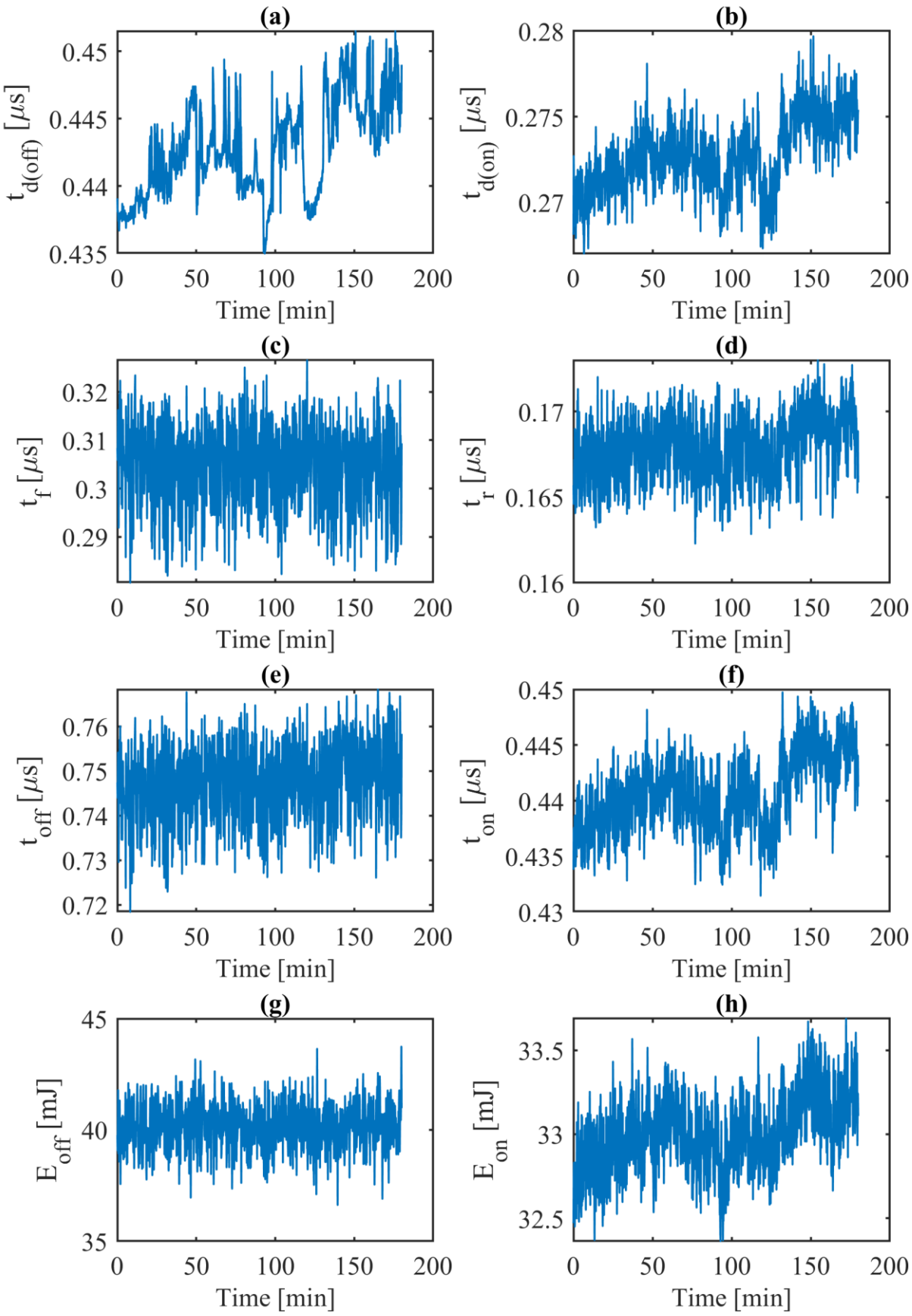

Fig. 4.20 Switching characteristics from DPT on module type B over time in 85 °C / 85% RH condition. (a) $t_{d(off)}$, (b) $t_{d(on)}$, (c) t_f, (d) t_r, (e) t_{off}, (f) t_{on}, (g) E_{off}, and (h) E_{on}.

v. DPT Parameter Change Over Time in High-humidity Conditions – Module Type C

For module type C, having a significantly higher gate charge due to the paralleling of multiple IGBTs within the package, the test intervals are increased to allow complete turn-off and turn-on. The datasheet-given gate charges are 800 nC, 940 nC and 10 µC for module types A, B, and C, respectively. The gate charges of module types B and C are both stated in the datasheets at a condition of $V_{GE} = -15 \ldots +15\,V$, whereas module type A is stated at $V_{GE} = -8 \ldots +15\,V$. The recorded waveforms from DPT on module type C at the commencement of the test are shown in Fig. 4.21. Note that V_{DC} is reduced to 250 V for this test in the interest of safety due to unavoidable harmful oscillatory behaviours at higher voltages. Consequently, the switching parameters estimated here by DPT are not comparable to those given in the module datasheet. The previously observed oscillatory behaviour of V_{GE} is present for module type C also, although due to the increased switching times relative to module types A and B, the portion of the waveform including oscillation is reduced. In the case of I_G, which saw similar behaviours at the steep switching edge for module types A and B, the oscillations are obfuscated due to the scale of the time axis, but still present. A larger V_{CE} undershoot is present at the turn-on interval for module types B (−71 V) and C (−69 V) compared to module type A (−47 V), which could influence switching parameters that are derived from it, such as $t_{d(on)}$, t_{on} and E_{on}.

The change over time in the high-humidity environment in the switching characteristics immediately derived from the gate current are shown in Fig. 4.22. The peak gate current, $I_{G(pk)}$, for module type C is higher than the other module types due to the increased input capacitance and hence gate charge, but no changes are observed to occur over time in the harsh environment. This is also true of the other characteristics: dI_G/dt and Q_G. The characteristics related to the Miller plateau are shown in Fig. 4.23. The observed V_{GEP} is significantly higher for module type C (~4.05 V) compared to module types A (~0.62 V) and B (~0.89 V), which could be attributed to the reduced V_{DC}, reduced I_C, or increased Q_G. Nevertheless, these results are not intended as a comparison between module types but are intended to provide an indication of parameter shift over time in the harsh environment.

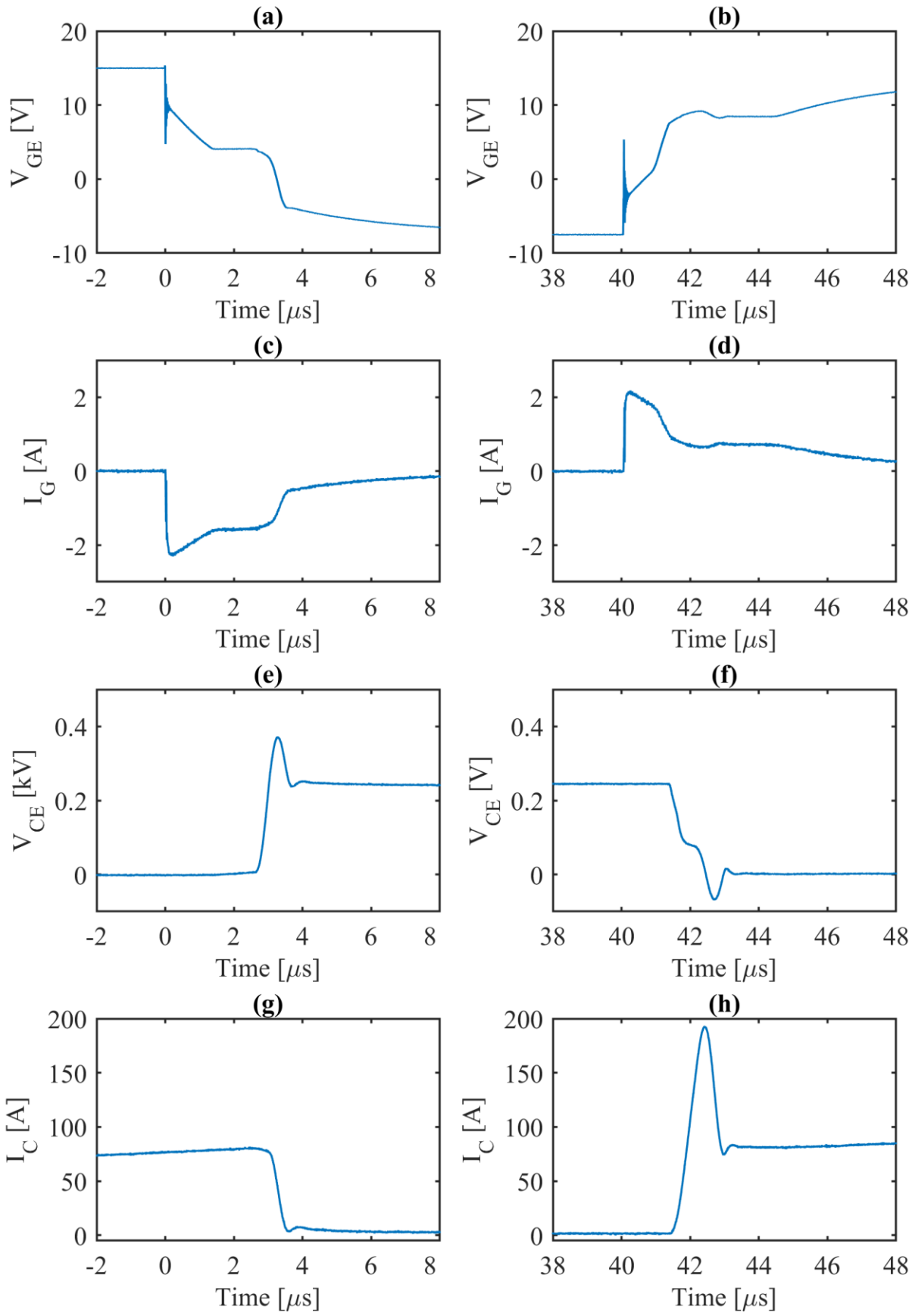

Fig. 4.21 Typical waveforms of DPT of module type C. Records taken at start of test clock (t_0) when humidity setpoint is changed from 30% to 85% RH. Records scaled in time axis to better display turn-off and turn-on intervals. (a) $V_{GE(off)}$, (b) $V_{GE(on)}$, (c) $I_{G(off)}$, (d) $I_{G(on)}$, (e) $V_{CE(off)}$, (f) $V_{CE(on)}$, (g) $I_{C(off)}$, and (h) $I_{C(on)}$.

As was the case for the gate current related characteristics, there are no discernible changes observed in the Miller plateau characteristics V_{GEP} and t_{GP} which can be reasonably attributed to the absorption of moisture within the silicone gel. A slight inflection point is present at about 60 min for V_{GEP}, where

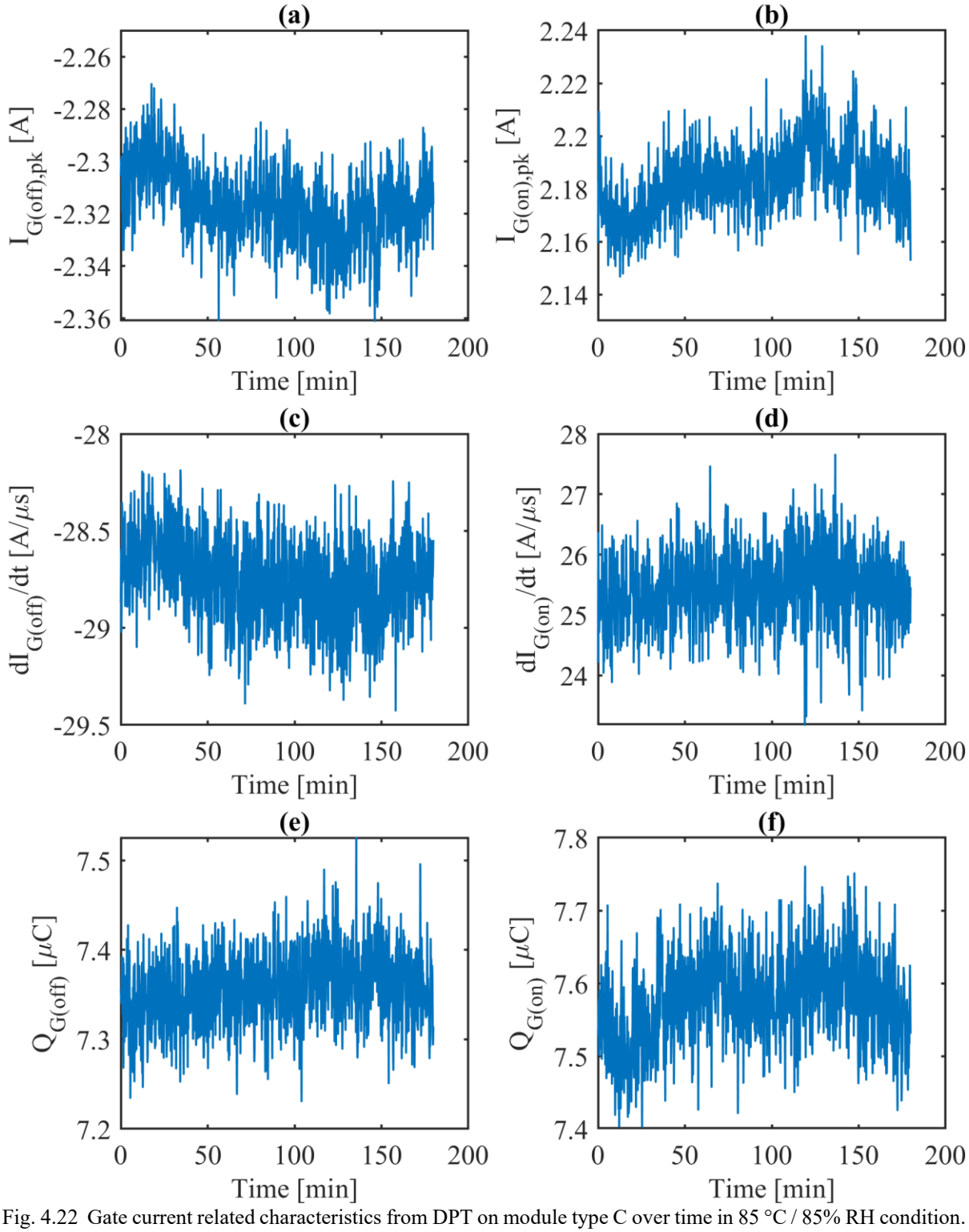

Fig. 4.22 Gate current related characteristics from DPT on module type C over time in 85 °C / 85% RH condition. (a) $I_{G(off,pk)}$, (b) $I_{G(on,pk)}$, (c) $dI_{G(off)}/dt$, (d) $dI_{G(on)}/dt$, (e) $Q_{G(off)}$, and (f) $Q_{G(on)}$.

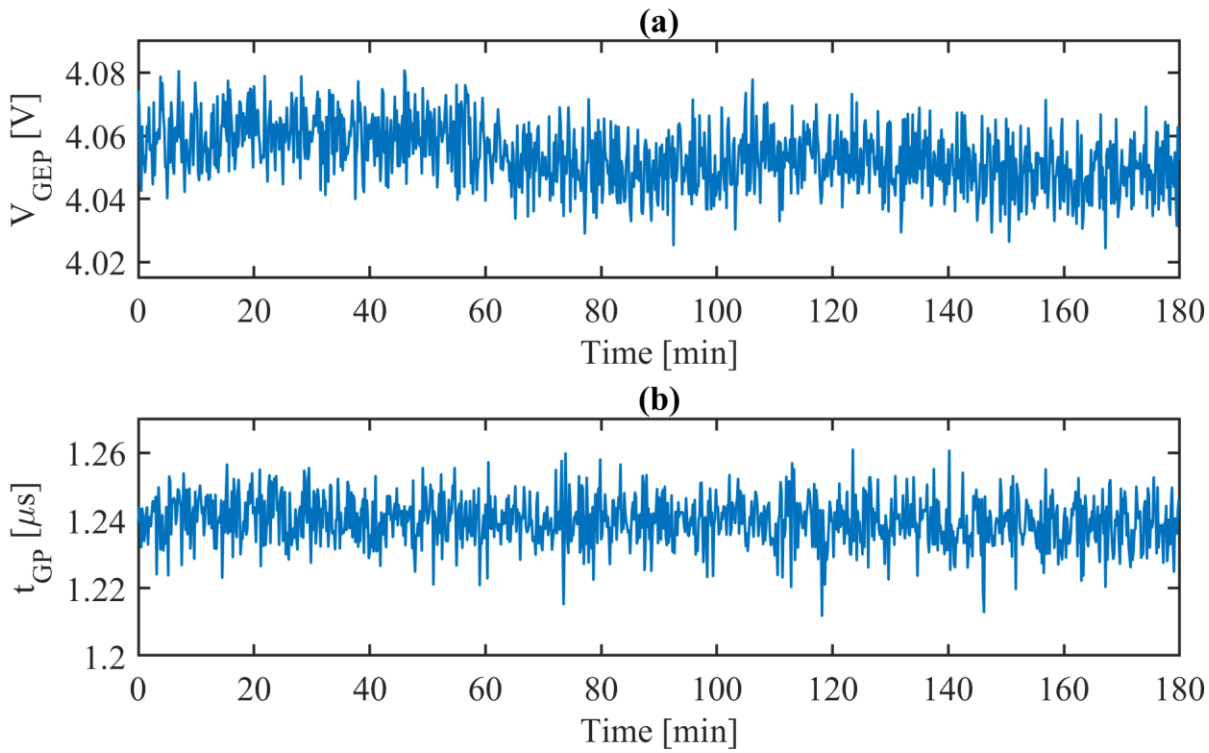

Fig. 4.23 Miller plateau characteristics from DPT on module type C over time in 85 °C / 85% RH condition. (a) Miller plateau voltage V_{GEP}, (b) Miller plateau width t_{GP}.

the local mean is reduced by roughly 10 mV, but this is not commensurate with expectations concerning the absorption of moisture. For t_{GP}, almost no deviation in the local mean is observed.

The traditional switching parameters typically found in module datasheets are presented for module type C in Fig. 4.24. The first observation is the reduction in $t_{d(off)}$, which initially appears to be correlated to the increase in capacitance or relative permittivity caused by moisture absorption in the gel discussed in Chapter 3. Although this change is indeed attributed to moisture absorption in the gel, the reduction in $t_{d(on)}$ does not agree with the expectation of increased capacitance causing increased switching delays. This is discussed in the next section for all module types. Secondly, a significant amount of noise is present in the slew characteristics t_f and t_r. This is attributed to the 'peak bouncing' phenomenon previously discussed for module type B and is not expected to be a result of moisture absorption. The oscillation in V_{DC} is strongly reflected in E_{on}, where the measured 0.5 V fluctuation results in a 50 µJ disturbance in this parameter. The trends over time in the harsh environment for the remaining characteristics appear to remain constant, and consequently no influence of moisture on the switching characteristics can be stated.

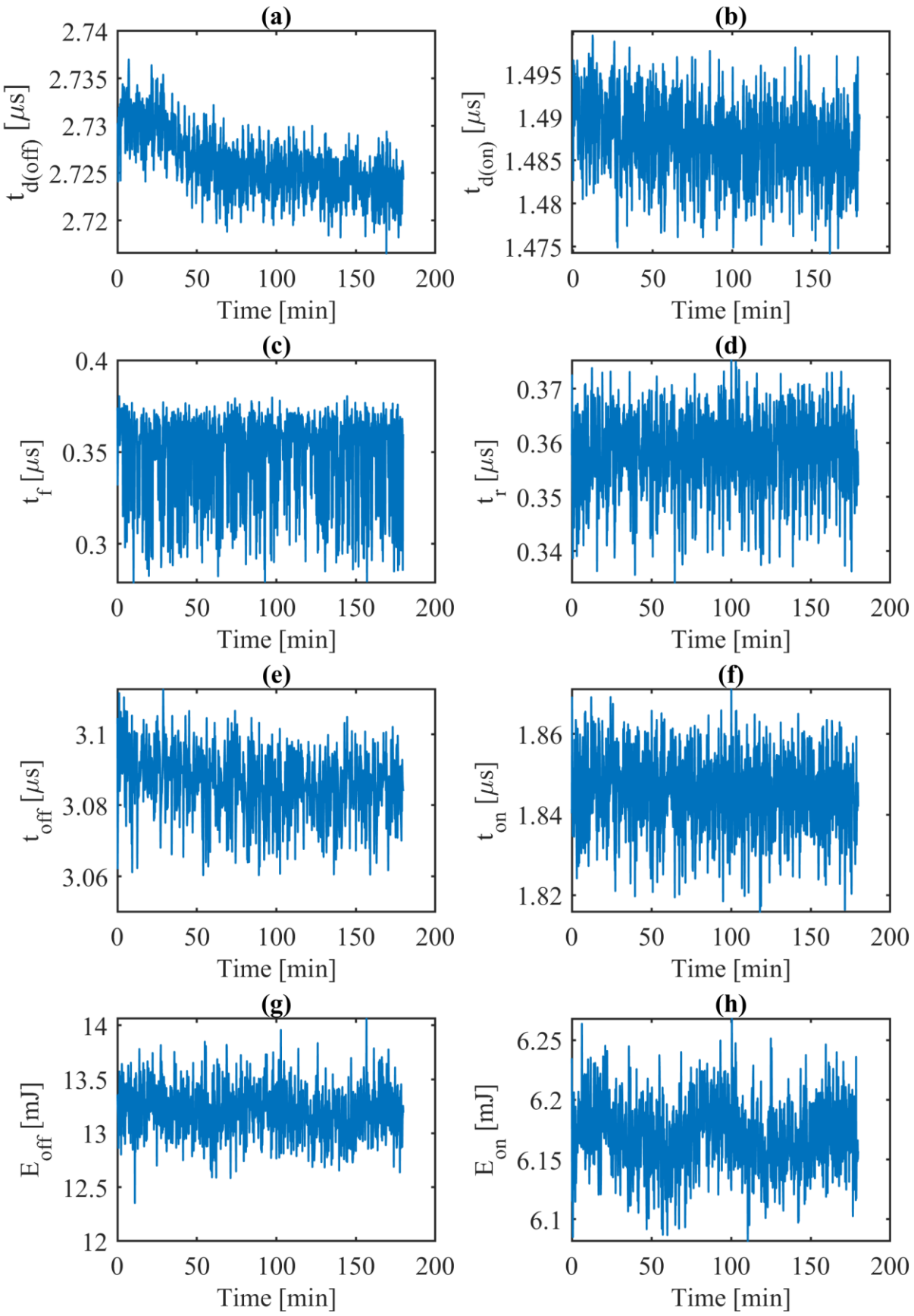

Fig. 4.24 Switching characteristics from DPT on module type C over time in 85 °C / 85% RH condition. (a) $t_{d(off)}$, (b) $t_{d(on)}$, (c) t_f, (d) t_r, (e) t_{off}, (f) t_{on}, (g) E_{off}, and (h) E_{on}.

4.4.2 Gate-Emitter Voltage Oscillation

In the previous DPT results, several of the measured switching characteristics displayed a change that could be attributed to moisture absorption in the gel, but with a trend in opposition to expectations. It was initially anticipated due to the results presented in Chapter 3, which showed that the dielectric gel increased in capacitance due to absorbed moisture, that if any parameters were to shift, it would be the increase in switching times and delays. Module type A exhibited slight reductions in t_{GP}, $t_{d(off)}$, and t_{off} as shown in Fig. 4.14(b), Fig. 4.16(a), and Fig. 4.16(e), respectively. Similarly, module type C showed a reduction in $t_{d(off)}$ over time in the harsh environment, as seen in Fig. 4.24(a). Module type B is expected to display similar trends, but this cannot be confirmed due to noise and inaccuracy in the characteristic estimation methods due to oscillatory behaviours. Consequently, a commonality between these characteristics was sought, to aid in investigation. The characteristics t_{GP}, $t_{d(off)}$, and t_{off} are defined in Table 4.5, where it is acknowledged that each depends on the behaviour of the measured V_{GE}. An inspection of the V_{GE} waveforms from the DPT on each module type revealed a significant increase in the oscillatory behaviour at the steepest portion directly at the instant of turn-off and turn-on over time in the harsh environment. These are presented for each module type in Fig. 4.25 for both switching intervals, showing the first and last records of each DPT, i.e., t_0 and t_{1080} (min). For each module type tested, the oscillatory behaviour of V_{GE} is exacerbated due to the absorption of moisture. For module type A, the range of the first period of the oscillation in the turn-off interval increases from 9.73 V to 15.34 V (+57.66%). For module type B this increase is from 11.03 V to 14.95 V (+35.45%), and for module type C it is from 8.12 V to 12.66 V (+55.91%). In each instance, the frequency of the oscillation is slightly reduced. For the turn-on interval the increases are most pronounced on the second period of the oscillation. The increases are: 7.27 V to 8.90 V (+22.42%), 8.67V to 10.23 V (+17.99%), and 7.05 V to 8.89 V (+26.10%), for module types A, B, and C, respectively. The power spectra for each of the results shown in Fig. 4.25 are presented in Fig. 4.26, where the downshift in oscillation frequency is easily observed. For module type A, the oscillation frequency at turn-off is reduced from 62.99 MHz to 51.06 MHz at turn-off, increasing in power from −3.08 dB to 4.25 dB. For module type B at turn-off, the values are 61.86 MHz to 53.40 MHz and

−0.33 dB to 4.31 dB, and for module type C they are 62.00 MHz to 52.11 MHz and −5.94 dB to 1.76 dB. At turn on, the V_{GE} oscillation for module type A downshifts in frequency from 62.61 MHz to 51.74 MHz and increases in power from 4.70 dB to 5.41 dB. For module type B these values are 61.20 MHz to 54.32 MHz and 6.65 dB to 7.59 dB, and for module type C they are 61.81 MHz to 53.12 MHz and 3.09 dB to 4.59 dB. In the interest of clarity, these values are restated in Table 4.6.

TABLE 4.6
INFLUENCE OF HARSH ENVIRONMENT ON V_{GE} OSCILLATION METRICS

Module	Edge	Instant	Oscillation range [V]	Oscillation frequency [MHz]	Oscillation spectral power [dBm]
A	Turn-off	t_0	9.73	62.99	−3.08
A	Turn-off	t_{1080}	15.34	51.06	4.25
A	Turn-on	t_0	7.27	62.61	4.70
A	Turn-on	t_{1080}	8.90	51.74	5.41
B	Turn-off	t_0	11.03	61.86	−0.33
B	Turn-off	t_{1080}	14.95	53.40	4.31
B	Turn-on	t_0	8.67	61.20	6.65
B	Turn-on	t_{1080}	10.23	54.32	7.59
C	Turn-off	t_0	8.12	62.00	−5.94
C	Turn-off	t_{1080}	12.66	52.11	1.76
C	Turn-on	t_0	7.05	61.81	3.09
C	Turn-on	t_{1080}	8.89	53.12	4.59

The increase in oscillation voltage range is highest for module type A at turn-off, and lowest for module type B at turn-on, although these were very similar modules in terms of construction, IGBT generation and DBC layout. In general, across module types, the turn-off oscillation exhibited a higher frequency at turn-off at the start of the test, than at turn-on, but at the end of the test the oscillation frequency was higher at the turn-on interval. On average, the frequency of oscillation was reduced by approximately 10.1 MHz at turn-off and by 8.8 MHz at turn-on. The spectral power of the oscillation varies significantly between module types and switching interval and so is not suitable for comparative analysis. Nevertheless, the harsh condition increased the power of the oscillation spectrum in every case. These changes are commensurate with the anticipated increase in module parasitic capacitances due to moisture absorption in the gel over time in the high-humidity environment, and so can be confidently attributed to that cause.

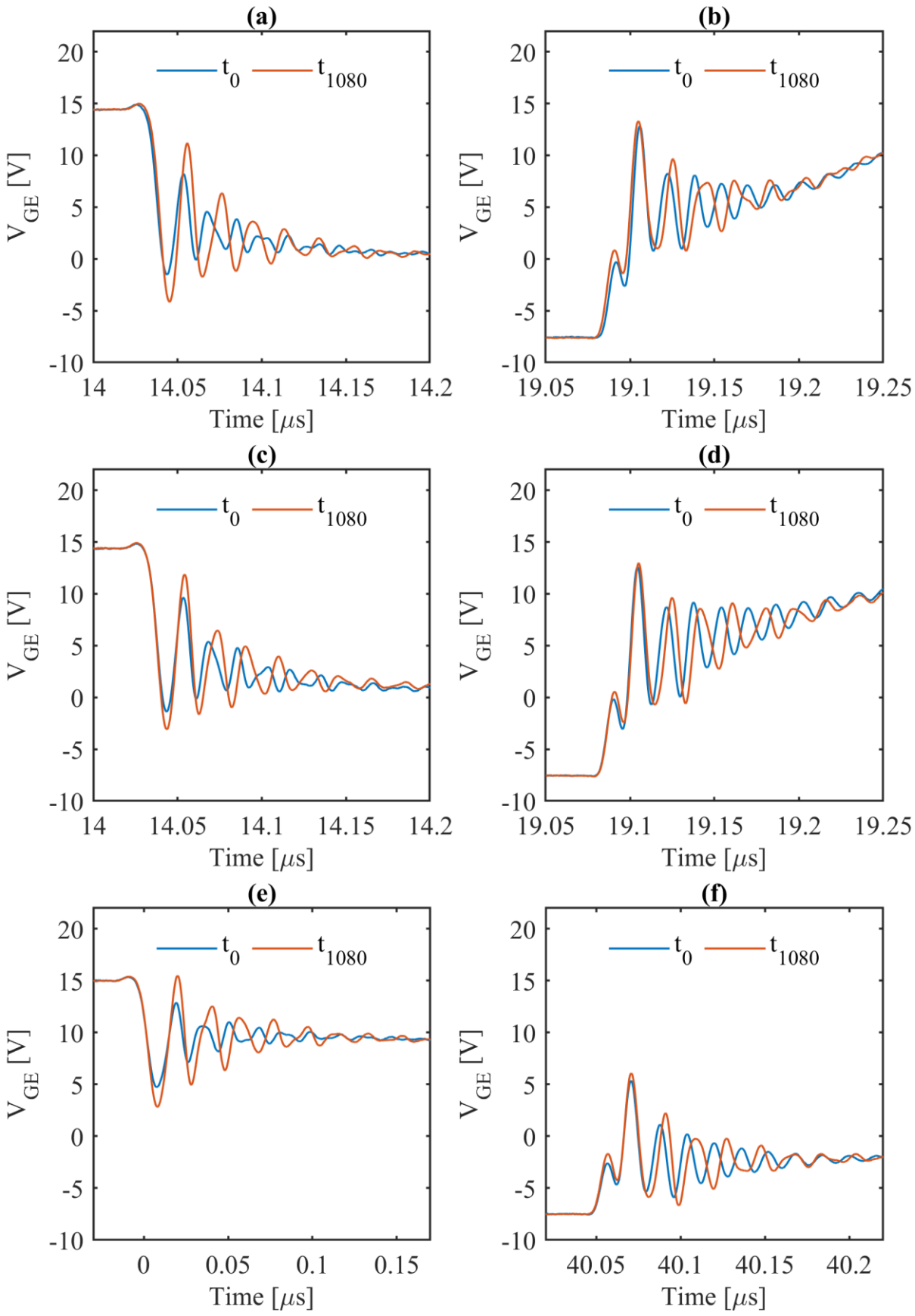

Fig. 4.25 Oscillations in V_{GE} at the start of each switching interval. (a) turn-off, module type A; (b) turn-on, module type A; (c) turn-off, module type B; (d) turn-on, module type B; (e) turn-off, module type C; (d) turn-on, module type C. Time domain shown.

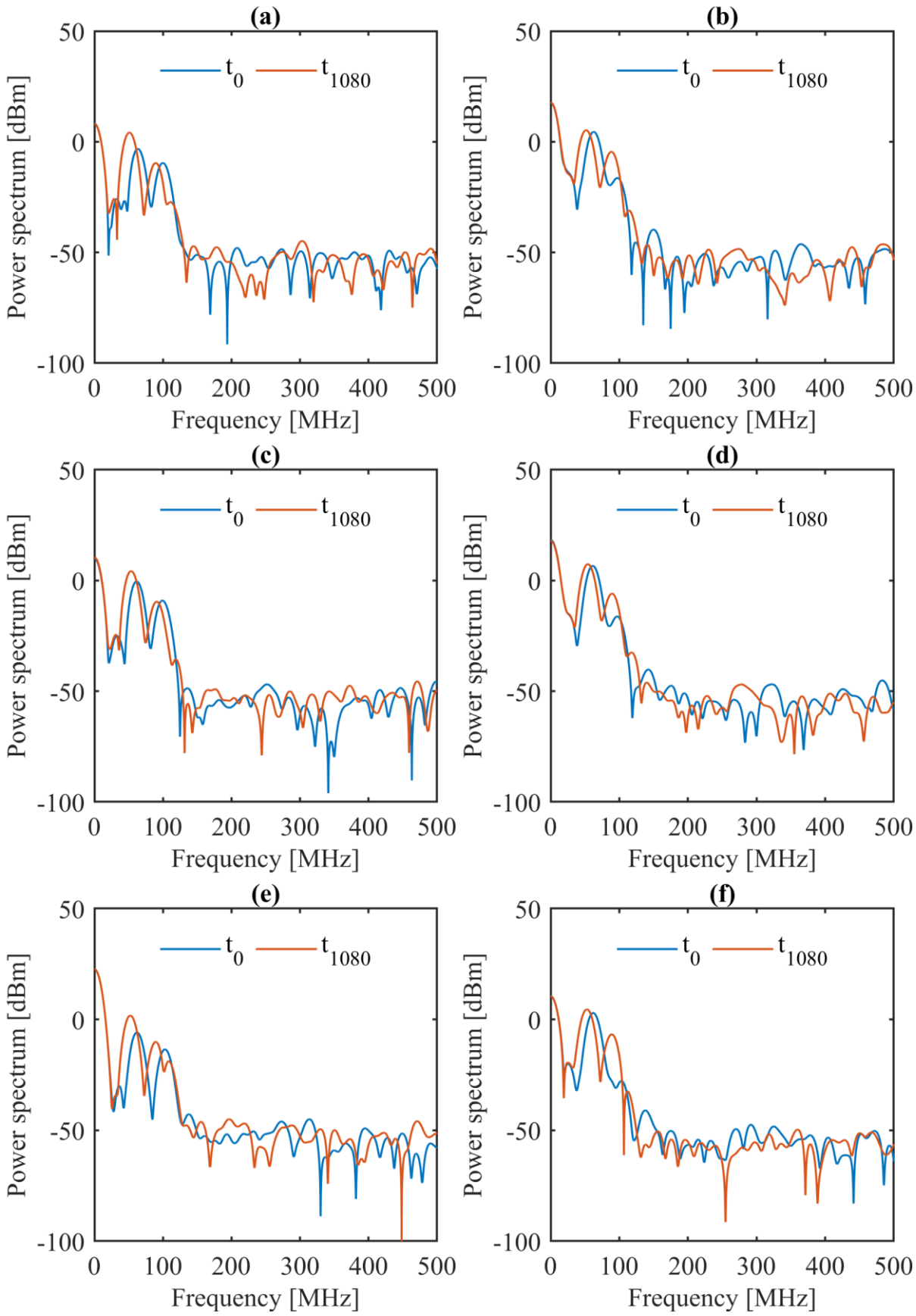

Fig. 4.26 Power spectra for V_{GE} at the start of each switching interval (0–500 MHz). (a) turn-off, module type A; (b) turn-on, module type A; (c) turn-off, module type B; (d) turn-on, module type B; (e) turn-off, module type C; (d) turn-on, module type C.

4.5 Conclusions

Motivated by the observations of relative permittivity growth in silicone gel due to moisture absorption in the previous chapter, the influence of this parameter increase on the performance of HV-IGBTs was studied. This was first performed in representative simulations of the gel and DBC structure using Ansys Q3D extractor, where it was found that the gel-DBC capacitances which conceivably existed in parallel with the IGBT die capacitances increased by up to 380%. However, the absolute value of the gel-DBC capacitances at steady-state by moisture absorption was slight compared to the die capacitances, potentially only a 2.27% increase in C_{ies} for the IGBT module overall. Measurements of C_{ies} of a module held in a high-temperature high-humidity environment and under 25 V bias were performed to verify the simulation findings. At 50 kHz, which was the lowest frequency investigated, C_{ies} was observed to increase by only roughly 13 pF, which could plausibly be considered negligible to the module C_{ies} of 81 nF.

To confirm the negligible influence of the slightly increased capacitance on the performance of operating modules, a series of DPTs were performed, for which a bespoke test platform was created. Tests were carried out every 10 seconds over the course of 3 hours, with the environment chamber setpoint changing from 85 °C / 30% RH to 85 °C / 85% RH at the start of testing. A total of 3 types of modules from different manufacturers were tested, all with a 1.7 kV maximum voltage rating, representative of IGBT modules typically used in OWT installations. Investigation of 20 switching parameters revealed no clear changing behaviours that could confidently be attributed to moisture absorption by the modules. Careful inspection of the oscillations of the V_{GE} waveforms for each module revealed only that the added gel capacitance exacerbated ringing, reducing its frequency, and increasing its power relative to the rest of the signal.

This chapter shows that in the short term, the overall performance of IGBTs is not expected to change due to operation in a high-humidity environment. There are potential implications for EMC and spurious switching if V_{GE} oscillations are not adequately controlled, but the influence of moisture here is limited. Increased operational confidence for these conditions is nevertheless a worthwhile finding and could help alleviate design constraints for IGBT-based converters used in OWTs.

Chapter 5: Partial Discharge Characteristics of Gel Encapsulated Power Module Substrates Under High Humidity

5.1 Introduction

The previous chapter investigated the short-term influence of high ambient humidity on power module parasitics and switching parameters. This chapter follows on from those results by investigating the degradation-causing phenomenon of PD on power module substrates encapsulated in silicone gel, when subjected to a high-humidity environment representative of field operation for OWT applications. A diagram illustrating this concept for a representative insulation system with a microvoid is provided in Fig. 5.1. The void and insulation can be modelled as capacitances with values determined by the insulating material dielectric properties. The voltage across the void (V_v) is determined by the capacitive voltage divider of the insulation (C_1 & C_2) and void (C_v), which is in parallel with the bulk capacitance of the insulation (C_b). An increase in the insulation capacitance due to moisture absorption increases the voltage across the void for a fixed external potential applied to the system. As shown in the capacitive voltage divider model of Fig. 5.1, an increase of C_1 and C_2 will result in increased voltage drop across C_v. The void has a breakdown strength determined by its gaseous composition, so an increase in voltage across it could cause a localised breakdown, i.e. PD. This chapter will investigate whether PD characteristics are indeed influenced by moisture absorption of gel encapsulated power module substrates in high humidity conditions as suggested by the simplified model of Fig. 5.1.

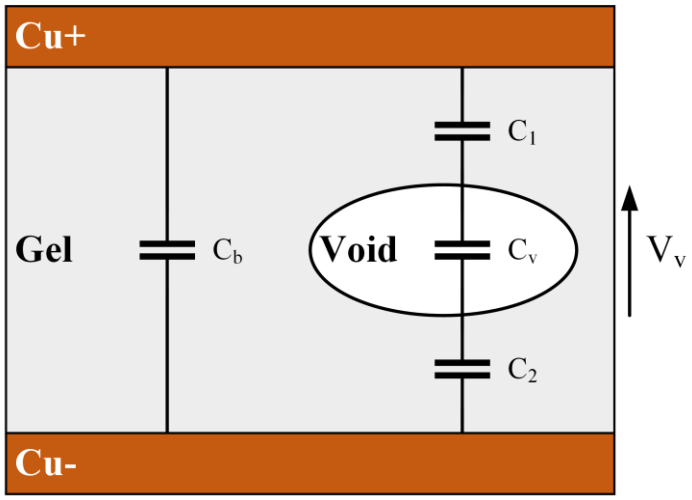

Fig. 5.1 Diagram of model capacitances for an insulation system with inclusive void.

5.1.1 Modelling of PD

A useful first step in understanding the dynamics of PD behaviours is the well-known Paschen's Law, which describes the breakdown voltage of gases held between two parallel electrodes as a function of pressure and the electrode distance. This can give an indication of the opportunity of PD to occur in air-filled microvoids or cracks within power module insulation systems at a combination of electric field stress, ambient pressure, and conductor separation. It is given by (66), assuming that the electric field is homogeneous and there are free electrons already at the cathode, i.e., Townsend's breakdown criterion is met [237]:

$$V_{BD} = \frac{B \cdot p \cdot d}{\ln[A \cdot p \cdot d / ln(1 + 1/\gamma)]} \quad [V] \quad (66)$$

where V_{BD} is the breakdown voltage, p is the gas pressure, d is the electrode separation distance, and γ is the Townsend secondary ionisation coefficient. Constants A and B for a given gas relate to the saturation ionisation of the gas and the excitation and ionisation energies thereof.

A typical Paschen curve for air is shown in Fig. 5.2 using coefficients from [237]. It is commonly acknowledged that the minimum breakdown voltage of air at a pressure of one atmosphere is 327 V, with an approximate electrode separation of 7.5 µm. Changing the separation distance or the pressure naturally influences the breakdown voltage, which means that applications with tight volume

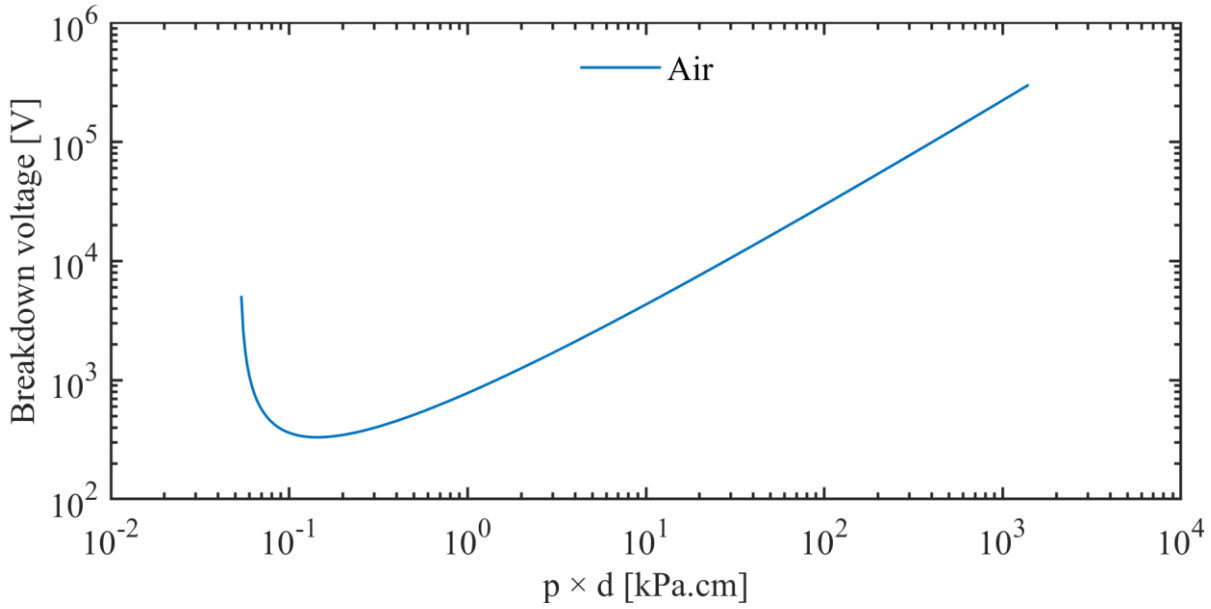

Fig. 5.2 Typical Paschen curve for air at sea level using (66) and values from [237].

constraints, or situations where the ambient air pressure is reduced pose an increasing risk of breakdown. This is a significant concern especially for aerospace applications, which is demonstrated well in [238]. From the perspective of power modules, the impact of Paschen's Law can be seen in research investigating varying the trench distance of DBC samples, showing that increasing this distance increases the PDIV of the samples tested [201].

One mechanism for PD-driven degradation of silicone gel insulation theorised in the literature is that of DEA [238], whereby incoming free low-energy electrons attach to molecules and cause them to fragment. This is adequately described by (67):

$$AB + e^{-} \rightarrow A + B^{-} \; or \; A^{-} + B \tag{67}$$

The energy required to break a molecular bond is called the bond dissociation energy. Typical bond energies for the bonds present in silicone gel are provided in Table 5.1.

TABLE 5.1
TYPICAL BOND DISSOCIATION ENERGIES IN SILICONE GEL

Bond	Bond dissociation energy [kJ·mol^{-1}]	Bond dissociation energy [eV]	Source
C–O	345	3.58	[239]
C–H	386	4	[238]
Si–O	460	4.77	[239]

PD events can be modelled as a low-energy plasma using an electron energy distribution function (EEDF) and can be approximated with techniques such as the Druyvesteyn distribution function, which is given by (68) [238]. The Druyvesteyn EEDF relates the energy of a population of electrons (w) in a low energy plasma to the population's mean energy level ($\langle w \rangle$):

$$f(w) = 1.23 \cdot \left(\frac{w}{\langle w \rangle^3}\right)^{\frac{1}{2}} \exp\left(-0.55 \cdot \left(\frac{w}{\langle w \rangle}\right)^2\right) \quad [eV^{-1}] \tag{68}$$

Fig. 5.3 shows the Druyvesteyn EEDFs for populations with mean energy levels of 1–9 eV, highlighting the regions where these populations have sufficient energy to cause DEA of the bonds presented in Table 5.1. For EEDFs with low mean electron energies, there are still portions of the populations with energy sufficient to cause damage to the chemical structure of silicone gel.

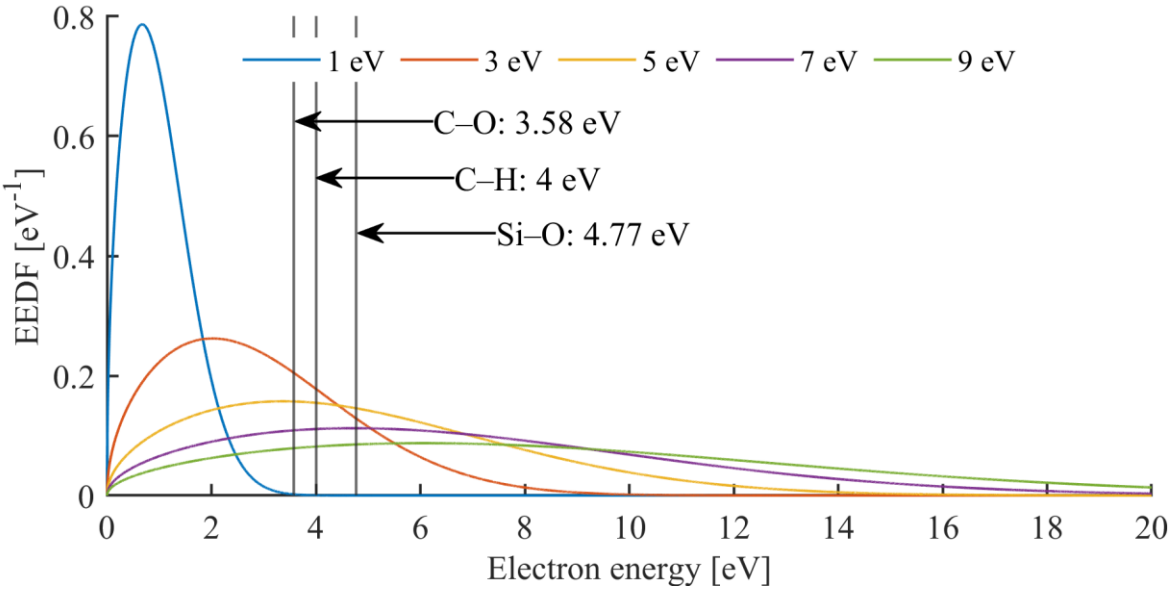

Fig. 5.3 Druyvesteyn EEDFs for mean electron population energies in the range 1–9 eV. Vertical lines represent bond dissociation energies for bonds within silicone gel: C–O at 3.58 eV, C–H at 4 eV, and Si–O at 4.77 eV.

In some research, empirical formulae for the estimation of PDIV are presented, but in each case, these are particular to the morphology of the sample, the environmental condition, the test stimulus, and the specific controlled parameters for the test. There is no single unified expression for the estimation of PDIV. An approximate expression for the field strength required to incept PD (E_i) in a void in insulation is provided in [238] based on much older work [240], it is given by (69):

$$E_i = 25.2 \cdot p\left(1 + \frac{8.6}{\sqrt{pl}}\right) \quad [V \cdot m^{-1}] \quad (69)$$

where p and l relate to the gas pressure inside the void and the void diameter, respectively.

However, accurate estimation of the gas pressure and diameter of voids or defects within power modules is not trivial, and besides there may be many such defects with varying geometries present in a single power module [241]. For gel encapsulated DBC substrate samples, the impact of pulse width and rise time of fast positive square impulses are discussed in [201], where it is shown that for pulses of certain width (~300 µs), the influence of increasing rise time is dominant in the reduction of PDIV. For pulses longer than this, the pulse width was the dominant factor, and the authors proposed an empirical relation of PDIV and these factors, which is given by (70):

$$V_{PDIV} = \frac{A_\alpha}{t_w^{B_\alpha} + C_\alpha} t_r + C_\beta t_w^{B_\beta} + A_\beta \quad [V] \quad (70)$$

where t_r and t_w are the rise time and pulse width, respectively; constants A_α, B_α and C_α are fitting parameters related to the curve slope; and A_β, B_β and C_β are fitting parameters relating to the intercept.

The authors note this relation is validated only for rise times of 100–200 ns, and pulse widths of 20–800 µs, which limits its use in wider contexts. Additionally, how this relation might vary with regards to temperature, humidity, pressure, and void geometries is not known. The multivariate and stochastic nature of PD must consider these factors and more: such as the geometry of the insulation system; the breakdown strengths of the constituent materials and their state of cure and cross-linking in the case of gels; and other environmental factors relating to the presence of ionic contaminants. Naturally, this system is nearly impossible to describe. It is of no surprise then that PD research gives no general quantitative prediction for PDIV encompassing these factors and must rely on specific narrow-scope experimentation.

PD behaviours are dominated by the electric field strength in the power module, which concentrates around the triple interface. Finite element analysis (FEA) investigations correlating the E-field strength in simulations to PDIV measured in experiments were performed in [160]. The maximum electric field strength was strongly correlated with PDIV in a linear fashion, with a reduction of 3–4 kV·mm^{-1} field strength indicating an increase by ~1 kV in the PDIV for the studied geometry. This was based on a previous work which explored the difficulties with electric field simulations, aimed at identifying measurement points considering the numerical singularity effects of varying mesh sizes for the simulation geometry and the locality to sharp interfaces [242]. Electric field simulations are performed in other works [72], [210], [212], [213], [243] to optimise the field strength for varying material and geometrical variations, providing increased ruggedness to PD. A thorough approach towards modelling of PD for FEA is presented in [244] where simulations of surface charge density on the surface of the DBC trench side wall are used to enhance PDIV by varying the trench distance. This procedure avoided using electrical field strength due to its sensitivity to variations in the simulation mesh size, or singularity effects at complex material interfaces such as the triple interface.

5.1.2 Partial Discharge Testing Standards

This work identified several IEC standards outlining test methods for PD which are currently available and exist to guide users of HV equipment including power modules in qualification and routine testing. Most PD research related to power modules to date is in some way based on one or more of these standards, and most commercial test equipment aims to implement the configuration, measurement, and reporting procedures detailed therein. The scope and limits of the most recent implementations of these standards are discussed below.

i. IEC 60270 – High Voltage Test Techniques. Partial Discharge Measurements.

The current version of this standard was introduced in 2000 and received amendment in 2015 [198]. The stability date for the current version of this standard given by the IEC is 2024, so it is likely to see further changes soon. Its scope is limited to PD occurring in electrical systems caused by AC voltages up to 400 Hz, or by an applied DC voltage. A PD measurement system for testing with AC stimuli described by this standard generally consists of the following: the sample to be tested; a coupling capacitor (or secondary test object similar to the first) that exhibits sufficiently low levels of PD; a HV supply which introduces sufficiently low background noise; requisite connections; and an impedance or filter system which is able to reduce background noise. The standard proposes several PD measurement circuits using coupling devices, wideband sensors, or narrow-band sensors. The primary metric for PD described is the measured apparent charge, normally represented in picocoulombs (pC), though other metrics such as the stimulus voltage and phase, the discharge current and power, and the radio disturbance voltage are also described.

Being limited to ≤400 Hz AC or an applied DC test stimulus makes this standard unsuitable for use in modern power converter or power module testing and is more applicable to insulation systems used for electrical machines, or HV cabling. Additionally, no guidance is given as to the correct configuration of a PD test concerning power modules as this is out of scope for the standard. The approaches outlined are useful in power module reliability research as a good foundation, but other standards that build on IEC 60270 are more suitable, which are discussed below.

ii. IEC 61287 – Railway Applications. Power Converters Installed on Board Rolling Stock.

This work is concerned with Part 1 of this standard: *Characteristics and test methods* [197]. Part 2 provides additional technical information to the first part and is of little use for PD research. The standard is recent as of 2014, and stable until 2027. It is concerned primarily with power converters, subassemblies, and components to be used in railway applications, but is applicable to other industries where these systems are used. Section 4.5.2.2.2 of the standard outlines the PD test, referring to IEC 60270. Section 4.5.3.7 outlines the routine dielectric test, which should provide assurances of good quality insulation of converter components. Section 4.5.3.8 describes the routine insulation resistance test, also used for qualification. A combination of type tests and routine tests are described from the converter level down to the semiconductor device and drive assemblies to allow for correct qualification and servicing for power converters used in railway applications. The description of PD measurement is limited, although it is commonly accepted that the configuration for the PD test on power modules is the same as that of the dielectric test: the test voltage is applied between the terminals of the device connected together, and the housing (i.e. baseplate). The AC test voltage (50 or 60 Hz AC) of $1.5 \cdot U_m/\sqrt{2}$ is applied, where U_m is the highest recurring peak voltage across the insulation. The test voltage is ramped up to this value over 10 s and is maintained for 1 minute. This is termed the electrical pre-stress period in relevant research. After this time, the voltage is reduced to $1.1 \cdot U_m/\sqrt{2}$, again over 10 s, and is held for 30 s. PD activity is recorded during this time to evaluate the insulation of the component or subassembly. The test voltage is then ramped down to zero over the course of 10 s. This standard highlights a tolerable PD apparent charge limit of up to 10 pC for individual components, and up to 50 pC for converter subassemblies. Though the recommendation of test configuration and the holistic overview of electrical testing for power converter subassemblies and individual components is of use to modern power module research, there are still some limitations as with IEC 60270, namely the test stimulus. The waveforms applied to power modules in field operation is not like that outlined in the standard. Consequently, a difference in PD behaviours witnessed in the qualification procedures, or the routine testing here outlined, and the behaviours exhibited during field operation are expected.

iii. IEC TS 61934 – Electrical Insulating Materials and Systems. Electrical Measurement of Partial Discharges (PD) Under Short Rise Time and Repetitive Voltage Impulses.

This standard [199] is more applicable to power modules than the previous in that the stresses outlined within are closer to those witnessed in the field operation of power converters, though much of this standard is an extension of IEC 60270, which is included as a normative reference. In scope, the standard outlines typical applications as any electrical insulation systems (EIS) driven by power electronics and subjected to the repetitive voltage impulses caused by such. Additional terms describing the behaviours of PD related to repetitive impulses are introduced in this standard such as the repeat PDIV (RPDIV), defined as the minimum peak-to-peak voltage at which PD occurs on more, than 5 in 10 voltage impulses, respectively. The repeat PDEV (RPDEV) is similarly described as the maximum for less than 5 in 10. Ultra-wide band (UWB) detection combined with a high-pass filter (HPF) having a sufficiently high cutoff frequency is put forth in this standard as the primary PD measurement technique, as it avoids measurement of the current induced in the sample by the test voltage. Additionally, narrow-band approaches are recommended using ultra-high frequency (UHF) sensors. The UHF band is defined by the International Telecommunication Union (ITU) as 300 MHz to 3 GHz. Though the standard outlines procedures for both inductive and capacitive test objects, it is the latter that is of interest to power module reliability researchers. The main PD detection devices are outlined in Section 5.2: a coupling capacitor with a multipole filter, a high-frequency current transformer (HFCT) and filter, and electromagnetic couplers. The standard provides guidance as to the use of these equipment for the purposes of PD detection, including recommended test circuits, calibration of detection systems, and the quantities to be reported.

Although this technical specification is far more relevant to PD testing of power modules under representative electrical stress, it makes no reference to standard setpoints for environmental conditions. It is understood that these should be chosen based on the application, and with the guidance of application-specific standards if available. Additionally, for the configuration of the power module to be tested there is little information provided as the standard refers to the test sample in a more

generalised sense. The reader is then left to consider alternative standards which provide guidance as to the configuration such as the previously discussed IEC 61287.

5.2 Fabrication of Test Samples

The samples used in this work were fabricated using DBC rafts harvested from 1.7 kV IGBT half-bridge modules (Infineon FF1000R17IE4) representative of those used in OWTs. This allowed for the creation of samples as close as possible to those used in field operation. A photograph of one of the power modules chosen for this research is provided in Fig. 5.4(a).

5.2.1 Sample Preparation

To remove the individual DBC rafts from the IGBT module, the polyamide housing was first removed by unscrewing it from the baseplate, levering the IGBT terminals to a vertical orientation, and carefully lifting the housing free. The busbars were then cut off carefully, followed by careful manual removal of most of the silicone gel using plastic tools and fine-bristled brushes to ensure the surface of the copper was not damaged. Further removal of silicone gel was performed after soaking the module in IPA solution, which allowed for most of the gel to be removed without damage to the device. Removal of the original silicone gel was necessary as its composition was unknown, and not provided by the manufacturer. A photograph showing one DBC raft attached to the module baseplate at this stage is provided in Fig. 5.4(b). Although solutions targeted at silicone gel removal such as Dow Corning

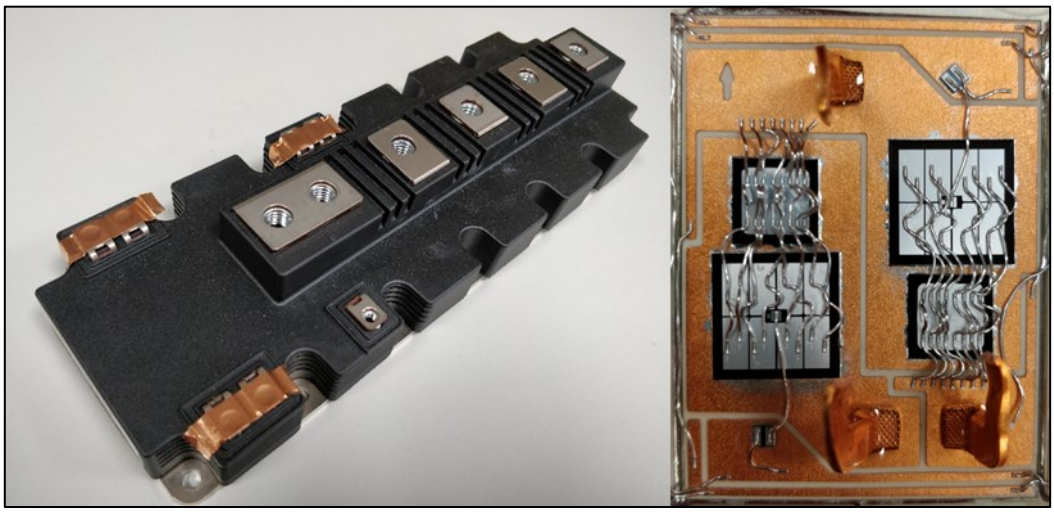

(a) (b)

Fig. 5.4 Infineon FF1000R17IE4 half-bridge IGBT power module used in this research. Rated 1.7 kV, 1 kA. (a) complete module newly procured, (b) single DBC raft attached to module baseplate after removal of busbars and silicone gel.

DOWSIL DS-2025 exist, these are corrosive and so their use was avoided. The bond wires were then cut and carefully removed so that the individual DBC rafts could be desoldered from the baseplate using a hot plate. The IGBT and diode dies were likewise desoldered from the rafts. A thorough repeat cleaning process using IPA solution, the fine-bristled brushes and light abrasion was then performed to remove the remaining portion of the busbars, any residual surface solder, oxidation of the copper surface from the desoldering process, and the lingering silicone gel.

After an initial qualification process, which is outlined below, and once clean and dry, cross-linked polyethylene (XLPE) insulated leads were soldered to the rafts. To mimic field operation and to simplify the test parameter space, the edge and back copper of the rafts were bonded using quick-drying silver paste (Electrodag 1415) which was carefully painted on using a small brush. This coating is designed for high conductivity electromagnetic interference (EMI) shielding applications and provided sufficient coverage on the ceramic to give a low impedance short to the back copper. The thin coating was deemed to be the least invasive bonding option and was not expected to influence the electric fields local to the regions of interest as it was far from the stressed trench or ceramic. Copper or aluminium conductive adhesive tapes were avoided as the behaviour of the adhesive when subjected to a high humidity environment was an unknown. Furthermore, a solder bridge was not used as it could not cover the trench gap between the top copper atop the ceramic, and bond wires could not be used to attach the top and back copper elements. This configuration allowed stressing of both the lateral trench between top copper elements, and the ceramic in the vertical direction between the top and back copper. Such a configuration was suggested by [98].

The rafts were then placed into acrylonitrile butadiene styrene (ABS) potting boxes and affixed with a small quantity of cyanoacrylate (CA) glue. Fresh silicone gel was then mixed and degassed in clean lab glassware. Per manufacturer guidelines [75], the gel was mixed in a 1A:1B ratio and degassed under vacuum (approximately 30 mBar) for 10 minutes. A small quantity of the gel was then poured into the moulds, to a thickness a little more than the height of the substrate, and the sample was then degassed again for 10 minutes. Finally, the target gel thickness of 3 mm above the substrate was achieved with another pour and degas process. The two-stage venting process was recommended by power module

manufacturers to allow for better degassing of the critical region around the substrate surface and triple interface. Per manufacturer guidelines, the samples were then placed in the environment chamber at 85 °C / 30% RH and normal ambient pressure to cure overnight. The elevated temperature allows for a greater degree of crosslinking, and the low humidity ensures little moisture intrusion during the curing process, which was desirable as the subject of the study was the impact of moisture absorption. The gel used for this work was again Wacker SilGel 612, an RTV-2 silicone rubber, with a breakdown voltage measured by other authors of 32.5 $kV \cdot mm^{-1}$ [76], and is recommended by its manufacturer for the potting of power electronics. Once fully cured, samples were allowed to cool and were subjected to additional qualification using HV to rule out early failing samples. The samples were then stored in a dust-free environment until testing. A photograph of a fully prepared sample is provided in Fig. 5.5.

5.2.2 Sample Qualification

Qualification of the samples before testing ensured that any likely early failures would be removed from the dataset. Removal of the silicone gel was verified using scanning electron microscopy (SEM) imaging and energy dispersive X-ray spectroscopy (EDS) mapping. EDS mapping is an elemental analysis imaging technique wherein a high energy electron beam is directed at a target sample, which displace core electrons (i.e., those not in an outer shell) from an atom. This leaves behind a hole which an electron in a higher energy shell then fills, generating characteristic X-rays unique to the element as it relaxes. The characteristic X-ray energy is then used to determine the distribution of elemental components on the sample surface. SEM images of a small region on a sample at 80x magnification

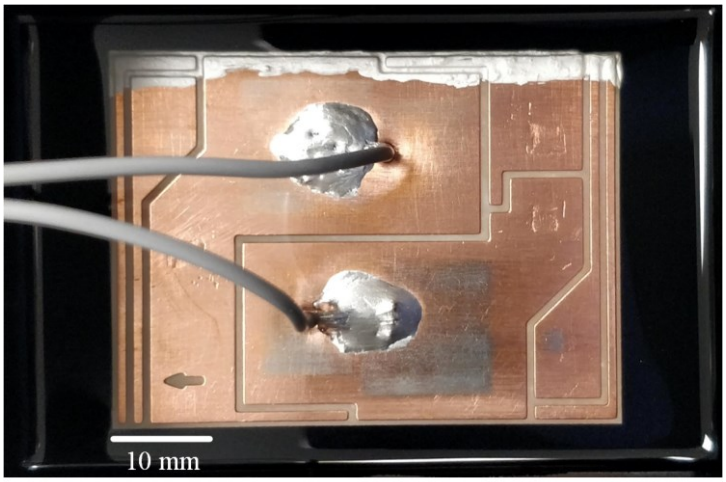

Fig. 5.5 Fully prepared DBC sample consisting of DBC harvested from commercial module, freshly cured silicone gel, XLPE insulated test leads, and silver paste.

before and after cleaning are shown in Fig. 5.6, taken using a Hitachi TM3030Plus microscope. A significant quantity of the silicone gel was removed by the cleaning process, but in Fig. 5.6(b), defects in the copper can be seen at the triple interface. It is not possible that these were caused by the cleaning procedure, and so these defects were attributed to the etching process from the manufacturer. The SEM imaging shows a smooth top copper surface, with only slight rounding-off of the top edges of the copper, which was not expected to influence the electric field about the triple interface during testing.

The EDS mappings for Si on the previous SEM images before and after cleaning are shown in Fig. 5.7, using a Quantax 70 EDS system attached to the SEM. Si was chosen as a tracer element to evaluate the presence of the silicone gel, as one of its major constituents. The imaging time was limited to 120 s due to limited resource availability. Detection of Si is represented in blue, and so the reader is directed to any available online or colour version of this thesis. Note that the EDS mapping is a relative measure based on the user-configured element targets, and that for clarity only Si is shown here. The mappings further highlight in a qualitative manner that most of the silicone gel is removed by the cleaning process. For a quantitative representation of the presence of the silicone gel before and after cleaning, the EDS results are reported in Fig. 5.8 as intensity, i.e., counts per second (cps) per electron-volt (eV) of the characteristic X-ray energy against electron beam energy. These traces are recreated from the EDS results generated by the imaging equipment. Peaks in the data at specific electron beam energies are used to determine visible elemental content. For this sample, the cleaning process reduced the visible Si-Kα from 28.93 $cps \cdot eV^{-1}$ to 1.05 $cps \cdot eV^{-1}$, as more of the copper surface is exposed due to this removal, the intensity for copper is significantly increased. These results, in combination with the qualitative analysis of the SEM and EDS mappings, are indicative of a successful cleaning procedure. Consequently, the gel-encapsulated DBC samples were deemed suitable for use in testing.

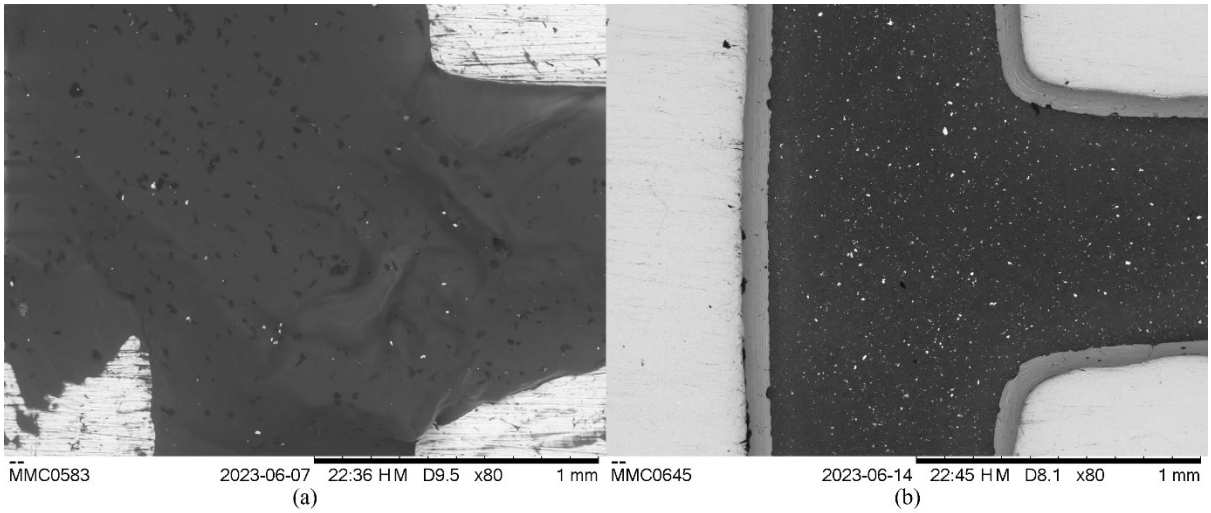

Fig. 5.6 SEM images of a region on a DBC sample: (a) before, and (b) after cleaning process. Images taken using a Hitachi TM3030Plus tabletop microscope at x80 magnification.

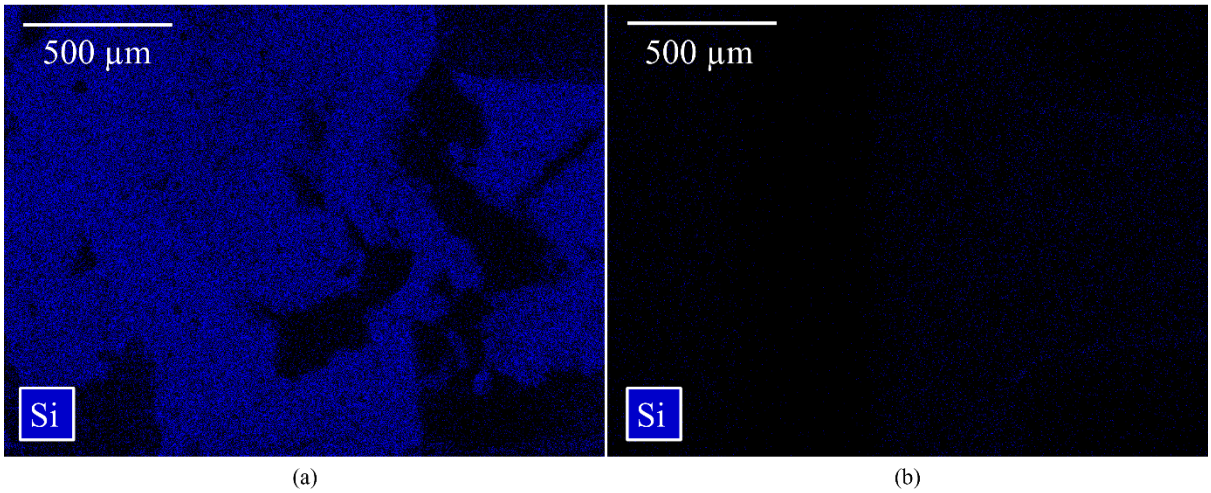

Fig. 5.7 EDS mapping performed on SEM images of a region on a DBC sample: (a) before, and (b) after cleaning process. Mapping results show only detected silicon (Si) for clarity. Taken with Quantax 70 EDS.

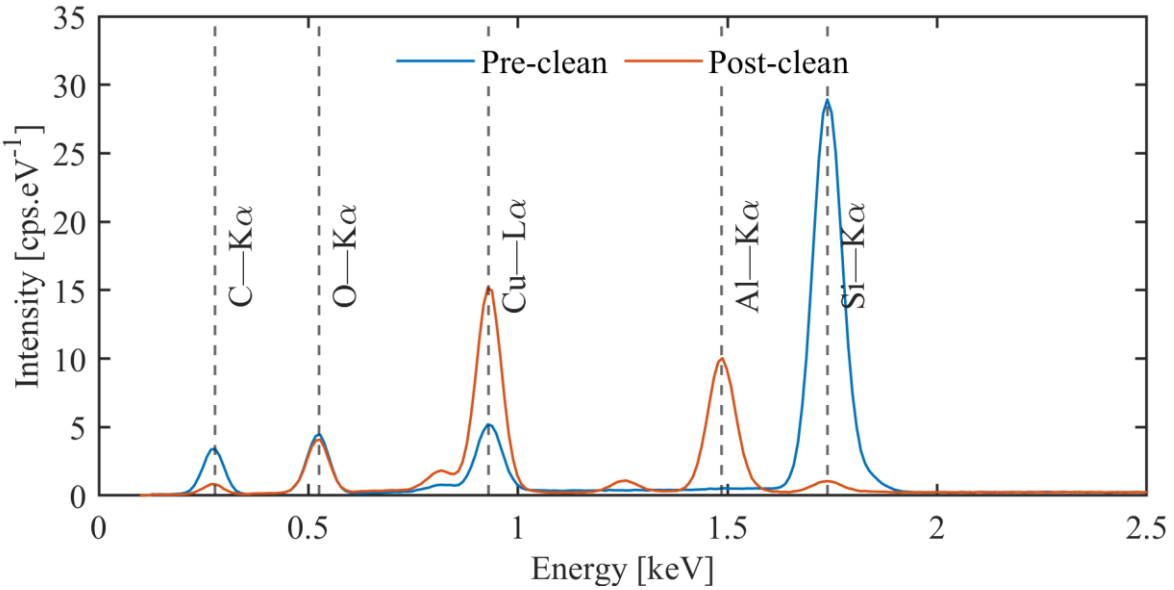

Fig. 5.8 EDS results of a region on a DBC sample before and after cleaning process. Dashed vertical lines show characteristic energies for target elements. Lα and Kα refer to electron relaxation from M to L shells and L to K shells in Siegbahn notation, respectively.

The isolation voltage (V_{isol}) of power modules is used to indicate the quality of its insulation, usually quoted as a duration of time at a given AC voltage. This is also known as an AC withstand (ACW), dielectric withstand, or high potential (Hi-Pot) test. The standard configuration for this test is to short the module terminals and apply the test voltage between the terminals and the baseplate. A graphical representation of this setup is shown in Fig. 5.9. As the samples designed for this work contain no active devices, and hence have a structure dissimilar to that traditionally used in ACW testing, it was determined that insulation resistance (IR) testing was more suitable and would also provide measurements that could aid interpretation of PD results if there was a large disparity in PD behaviours across the sample set. Section 4.5.3.8 of standard IEC 61287-1 outlines a routine insulation test to be performed on power converter subassemblies and components, stating that for rated insulation voltages exceeding 1 kV, the IR should be greater than 1 $k\Omega \cdot V^{-1}$. As the FF1000R17IE4 modules have a rated V_{isol} of 4 kV_{RMS} (f = 50 Hz, t = 60 s), the IR should be greater than 4 MΩ for qualification purposes. IR testing was performed using a Kikusui TOS9031 electrical safety tester at 2 kV. The measured IR values for the 6 samples prepared for testing are shown in Fig. 5.10. Sample 1 was a premature failure due to electrical breakdown during IR testing, and all other samples far exceeded the 4 MΩ threshold. A measurement could not be obtained for Sample 4 as the reading was over range, and notably Sample 6 had an IR reading an order of magnitude less than the others. After all the qualification steps, a total of 5 test samples were qualified for use in PD testing.

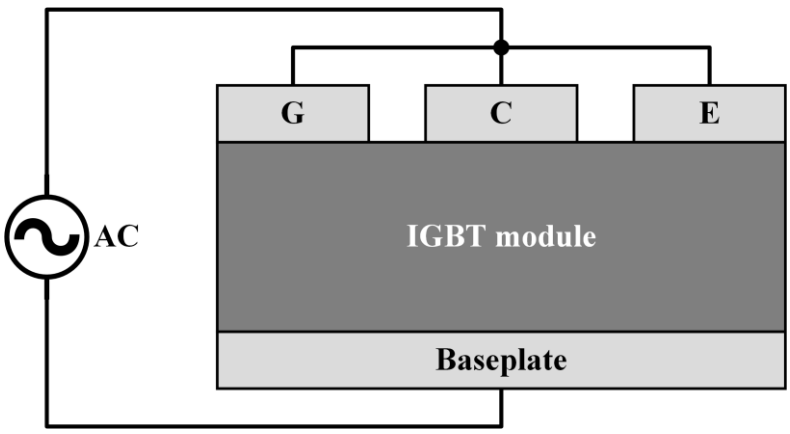

Fig. 5.9 Typical configuration for AC withstand test. This is also the configuration for insulation resistance testing, and per IEC 61287, PD qualification testing for power modules.

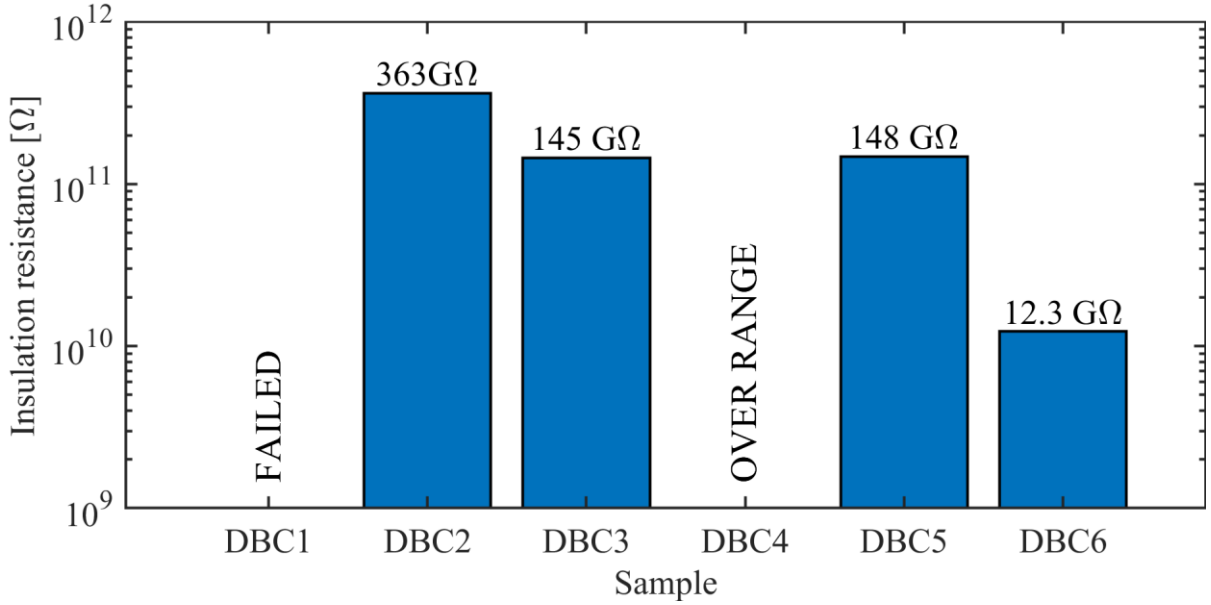

Fig. 5.10 Insulation resistance qualification test results for DBC samples 1–6. Sample DBC1 failed during testing, and no value is presented for sample DBC4 as the reading was over range.

Due to the varied behaviours of IR readings for the samples, additional impedance analysis was performed using a Bode-100 VNA. Fig. 5.11 shows these impedance results in room conditions as a bode plot, revealing negligible difference between the sample impedances.

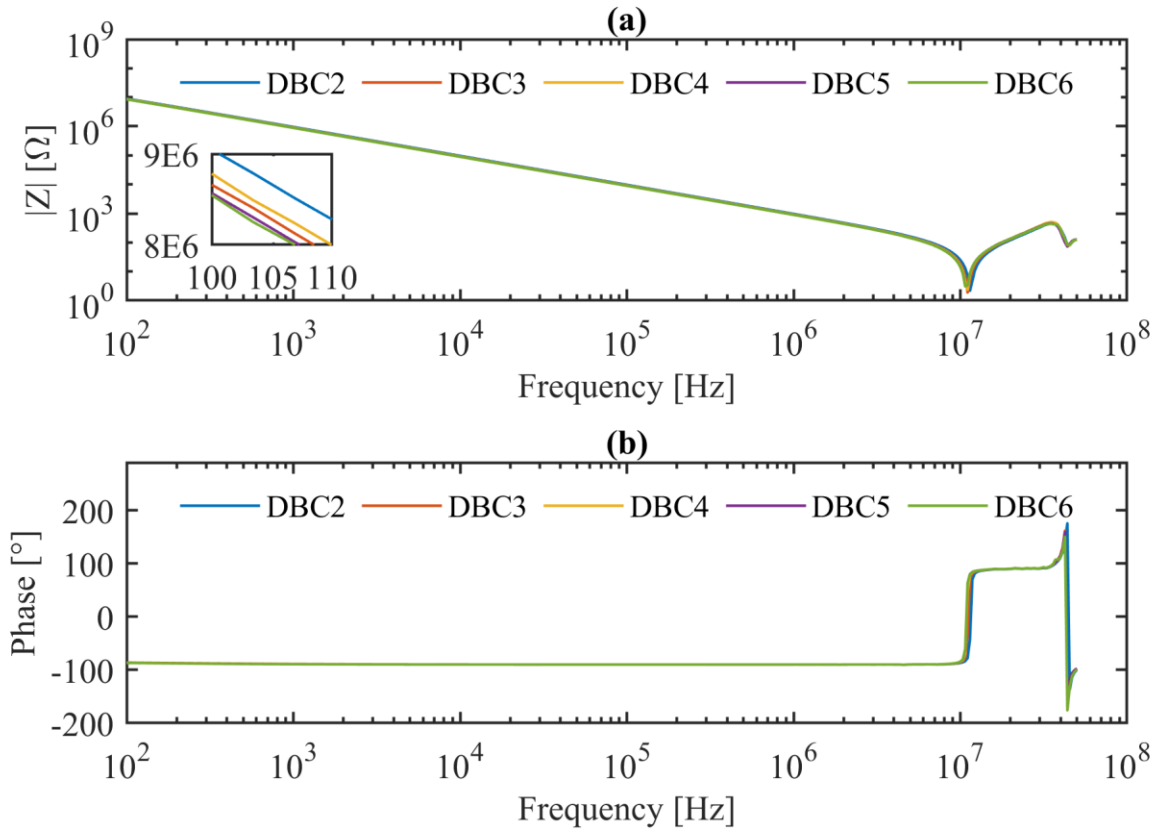

Fig. 5.11 Bode plot of impedance magnitude (a) and phase (b) for DBC samples.

5.3 Development of Bespoke Partial Discharge Test Platform Using a Silicon-Carbide Push-pull Switch

5.3.1 Test Platform

In the literature, it has been shown that PD characteristics are highly dependent on the test stimulus. The waveform applied has a significant impact on the techniques that can be used for PD detection, the reportable parameters, and the environments that may be used for testing. Although much of PD research for power modules uses phase-resolved PD (PRPD) analysis techniques, these use AC stimulus. Traditional qualification tests also use AC stimulus. However, the transients seen within an operating power module are not AC; they are either a fixed DC bias when in blocking mode, or steep square-like pulses. The square pulses can be either unipolar or bipolar depending on the application. This work chooses to investigate the PD characteristics of gel-encapsulated power module substrates under unipolar square pulses due to practical limitations at the high voltage range.

Initially, a commercial surge tester with PD testing capability (Schleich MTC2) was trialled for use in this work, but on capacitive samples at high surge voltages the equipment exhibited PD internally. Consequently, a bespoke PD test platform was designed and built for this work, with a SiC push-pull switch as the main active element. A circuit diagram of the main components in the test apparatus is shown in Fig. 5.12. The push-pull switch was obtained from Behlke Power Electronics GmbH (HTS 81-15-SiC-GSM) and is rated for HV operation up to 8 kV per switch, and capable of 150 A peak load current. This device can switch at 100 MHz with steep voltage gradients during turn on and turn off. It is controlled using a National Instruments (NI) Compact RIO (cRIO) 9063 with appropriate C-series voltage output modules (NI 9401, NI 9263). The cRIO was not capable of driving the control side of the switch module directly, so an interface board of optocouplers (Broadcom ACPL-W484-000E) was used. A Glassman 20 kV EQ series HV DC PSU is used as a source for the testing, controlled via the cRIO by applying 0–10 V to the back of the unit, corresponding to 0–20 kV from the PSU. The output current of the HV DC PSU is limited to only 60 mA, which was not sufficient for the generation of PD within test samples, so a 68 nF (6 kV) polypropylene (PP) film capacitor was connected in parallel to

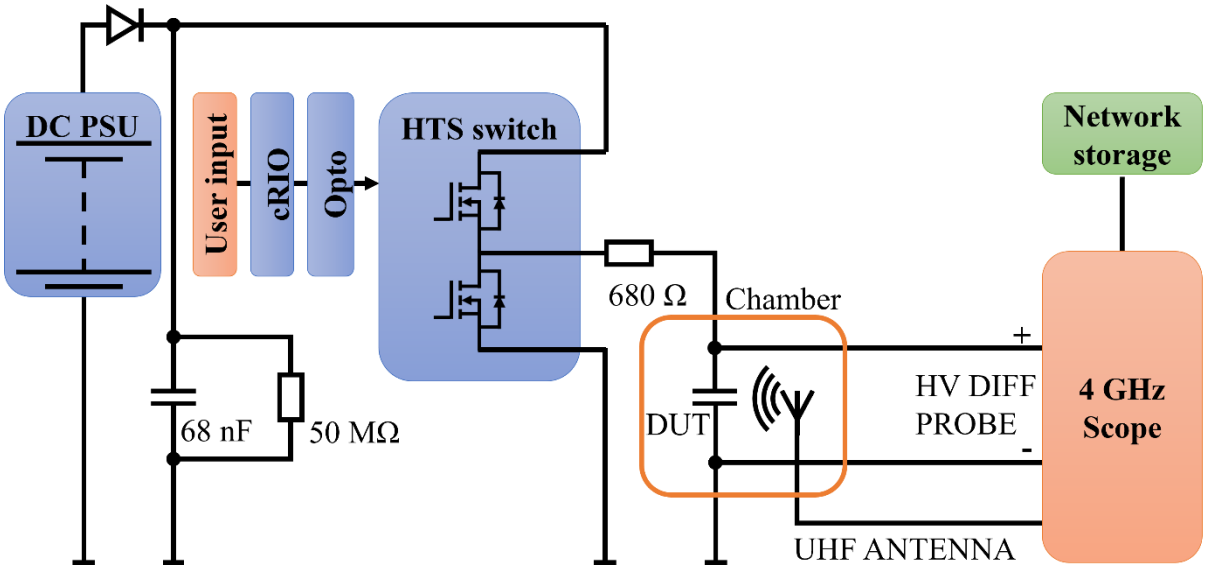

Fig. 5.12 Diagram of major components in bespoke PD test platform.

the HV output and charged prior to each test. To avoid harmful transients caused by the necessary cabling, a 680 Ω power resistor (FPA100 680R J, 100 W, $L < 50$ nH) was placed in series with the output to limit overshoot of the test pulses. For safety considerations, the DC PSU was protected by a fast Schottky diode (Wolfspeed C5D05170H: 1.7 kV, 5 A), and a high-value bleed resistor (50 MΩ) was connected across the boost capacitor. These elements were placed on a single interface PCB for convenience. To provide the high temperature high humidity ambient environment, an Espec SH-662 benchtop climate chamber was used, in which samples were placed for the duration of testing. The XLPE cabling from the samples was fed through a cable port in the side of the environment chamber and sealed with a foam stopper. A HV active differential probe (Pico technology TA044) was used to record the test pulses. To perform measurement as close as possible to the samples, this work used the Schleich potted monopole antenna (SPMA) that was previously discussed, which was placed inside the environment chamber to maximise the signal-to-noise ratio (SNR) of PD events considering outside noise sources from the laboratory and office environment. To maintain safe working practices, the control and HV components were placed inside an interlocked control cabinet. The environment chamber door was also interlocked, and additional safety relays were put in place to ensure that the DC PSU de-energised safely should any interlock open. The environment chamber provided several alarm relays which close if the temperature inside exceeds the setpoint by a fixed value, and for other faults,

which was connected to the safety loop also. A labelled photograph of the control cabinet and the major components is provided in Fig. 5.13.

Test pulses and ensuant UHF EMI in the sample were recorded using the SPMA connected to a BW oscilloscope (Teledyne LeCroy WavePro 404HD, 4 GHz BW, 20 GS·s^{-1}) via RG316 coaxial cable. The sample rate used in these experiments was 10 GS·s^{-1}, and data was saved directly to network storage via an ethernet connection.

Fig. 5.14 shows typical time and frequency domain behaviour of a sample subjected to a 50 µs pulse of 4.8 kV amplitude, both PD EMI and commutation EMI are displayed. The stimulus dV/dt for this test was approximately 14.88 kV/µs. The PD event was observed in the middle of the test pulse, when no other excitations were present, and the commutation EMI was observed during the rising edge of the test pulse and with no PD activity. In this manner, the spectrum of the commutation EMI is attributed purely to commutation and contains no PD spectral information. The strength of the residual commutation EMI near DC is still very large after filtering, and there is spectral power in higher frequency ranges up to 900 MHz. This range overlaps the PD EMI spectrum in the range 450–900 MHz, but the broad power spectrum of the PD EMI provides opportunity for PD detection, providing its strength is greater than that of the residual commutation noise.

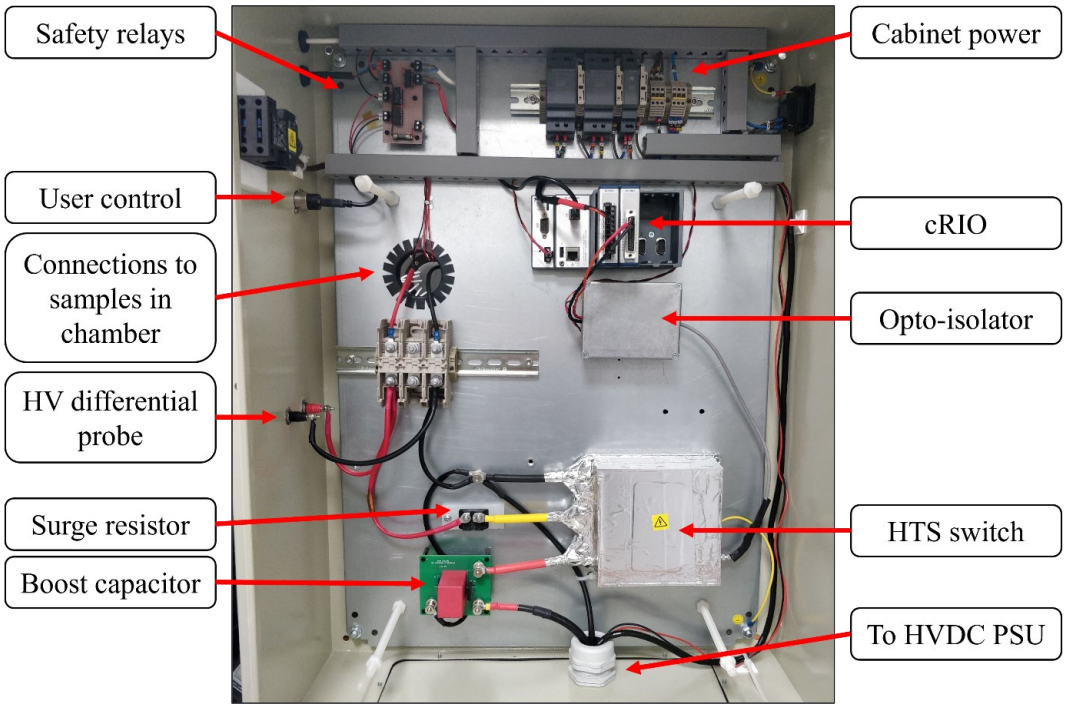

Fig. 5.13 Annotated photograph of control cabinet for PD test platform.

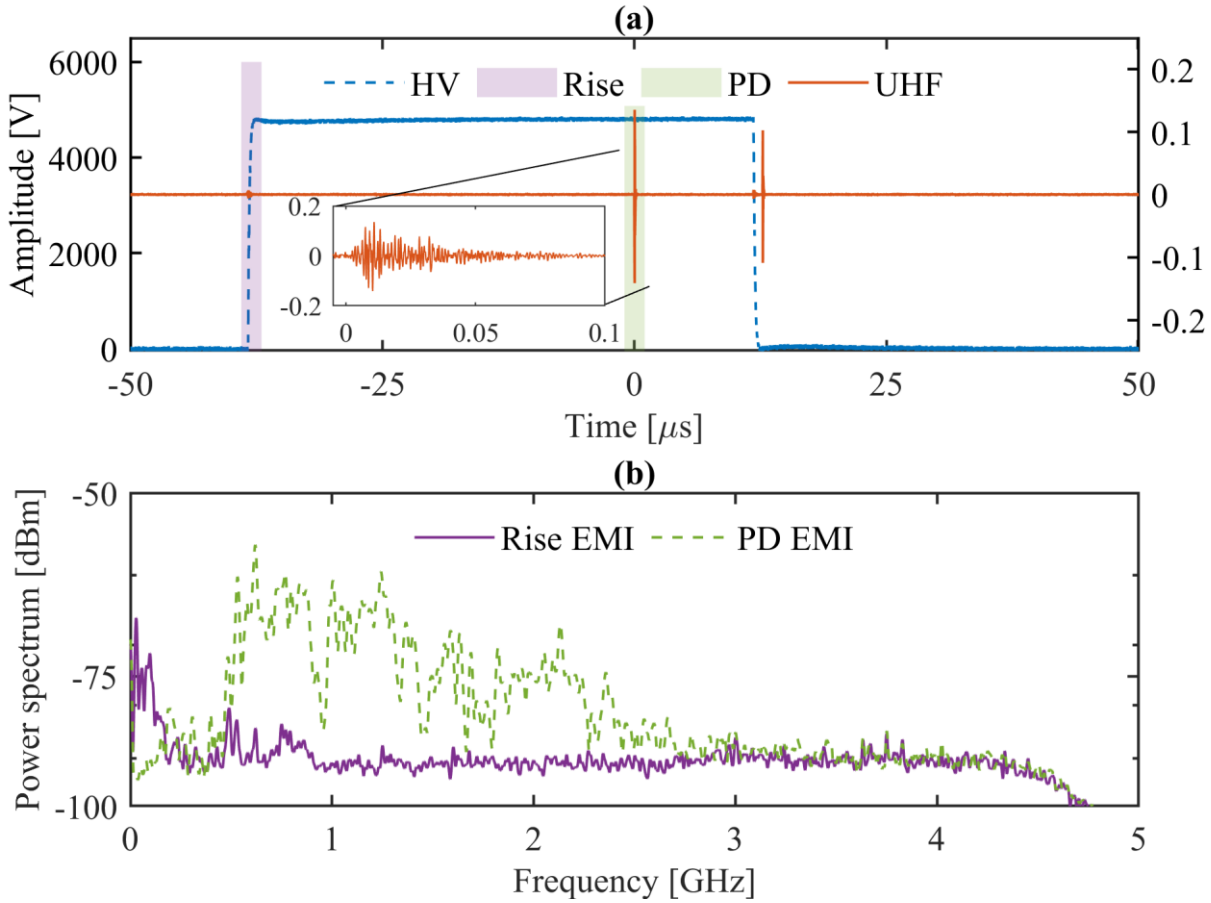

Fig. 5.14 Typical time (a) and frequency (b) characteristics of PD generated by a HV square pulse. Power spectra taken from windows centred on regions of interest. Test pulse shown is 4.8 kV amplitude at 50 µs width. Rise and fall times of HV pulse are approximately 260 ns.

5.3.2 Qualification of Potted Monopole Antenna

The SPMA was used as a basis comparison for PD detection antennas in previous work [245], [246]. Nevertheless, its narrow sensitivity does not perfectly suit the recommended flat wideband response in the range 0.3–3 GHz as recommended by IEC 61934, so additional validation of this antenna was performed to confirm its PD detection capability for this work. A wideband log periodic antenna (LPA) was obtained and used as a benchmark, a photograph of which is provided in Fig. 5.15. Though its large

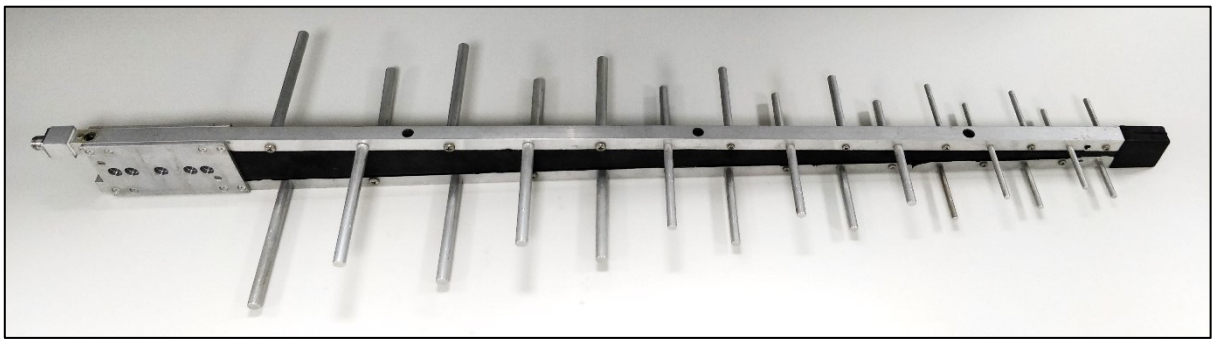

Fig. 5.15 Log periodic antenna (LPA) used as a benchmark to evaluate Schleich potted monopole antenna (SPMA).

size (~1.5 m in length) and susceptibility to outside noise sources ruled out the use of the LPA for long-duration testing, comparison was made to its performance in PD detection in the short term to qualify the SPMA for use.

First, the S11 reflection coefficients of the SPMA and LPA were measured using a Siglent spectrum and vector network analyser (SVA) (SVA1015X; 9 kHz to 1.5 GHz). The measured S11 characteristics of the SPMA and LPA are shown in Fig. 5.16. The LPA is more sensitive in general to the frequency range investigated, so it was expected that it would outperform the SPMA in this antenna qualification work regarding the detection of EMI resulting from PD events.

This validation continued with PD tests on gel encapsulated DBC samples under AC stimulus using a Kikusui TOS9301 electrical safety tester as a voltage source. A photograph of the tester is given in Fig. 5.17, and typical time and frequency domain data for a typical AC validation test are shown in Fig. 5.18. Signals are sampled at 20 $GS \cdot s^{-1}$, and both antennas are filtered with Crystek 7^{th} order Butterworth HPFs with a cutoff frequency of 700 MHz (CHPFL-0700) in line with the recommendations for UHF measurement of PD outlined in IEC 60270 and considering the spectra of PD observed in Fig. 5.14. For this test, the SPMA outperforms the LPA contrary to expectations, owing to signal power in the range 1.75–3.3 GHz. The SPMA responds faster due to its proximity to the discharges, which would allow for better estimation of PD time lag, and more accurate resolution of PD events in time or with phase. Additionally, the SPMA records with greater amplitude a secondary event at 220 ns. As PD dynamics can vary depending on the applied stimulus, additional tests under unipolar square wave stimulus were performed.

Typical time and frequency domain characteristics of the SPMA and the LPA are shown in Fig. 5.19 for the positive square wave stress, and here the LPA is observed to outperform the SPMA as expected. However, the SPMA still showed clear separation of the commutation EMI and background noise with the PD EMI. Based on these results, the SPMA was determined to operate with sufficient SNR to provide adequate detection of PD in this work and was used for all testing.

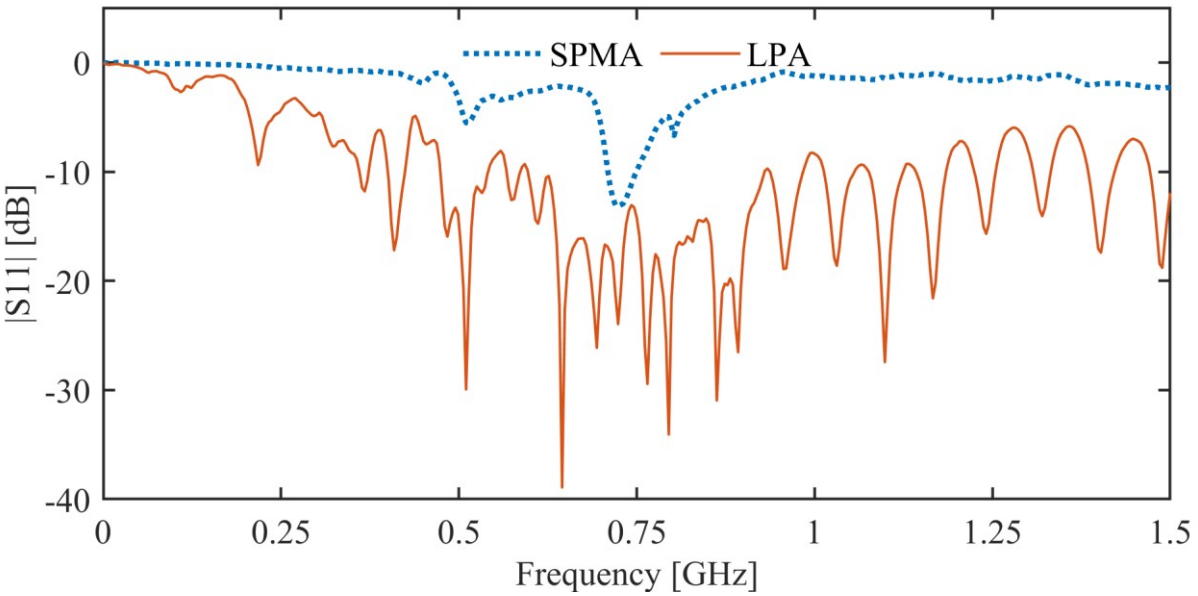

Fig. 5.16 Measured reflection coefficients (S11) of SPMA (blue, dotted) and LPA (orange, solid).

The presence of moist air within the environment chamber could attenuate signal strength based on the conclusions of [247], so this was investigated for the SPMA used in PD test system. For this, the tracking generator (TG) of the Siglent 1015X SVA was used to generate radio frequency (RF) emissions using a commercial whip antenna as an RF source, sweeping over the range 9 kHz to 1.5 GHz at a signal strength of 0 dBm. The distance between the RF source and SPMA was kept close to the planned test configuration involving the samples.

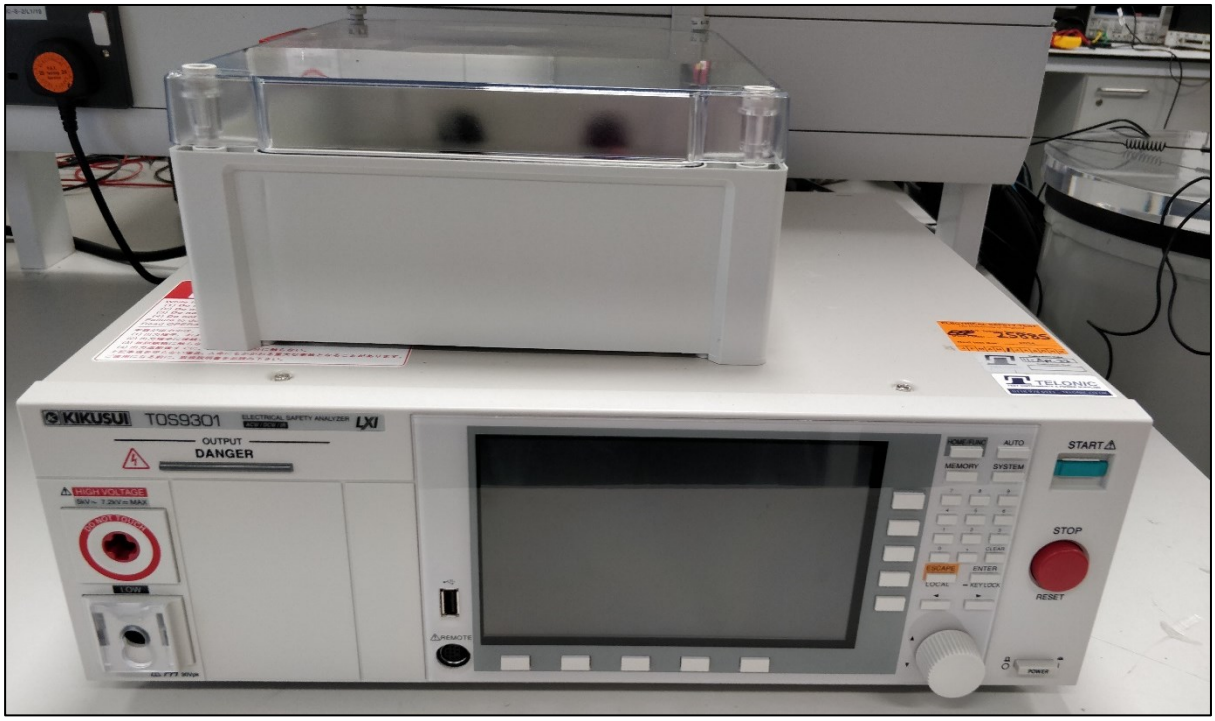

Fig. 5.17 Photograph of Kikusui TOS9301 electrical safety tester used for the generation of PD under 50 Hz AC stimulus.

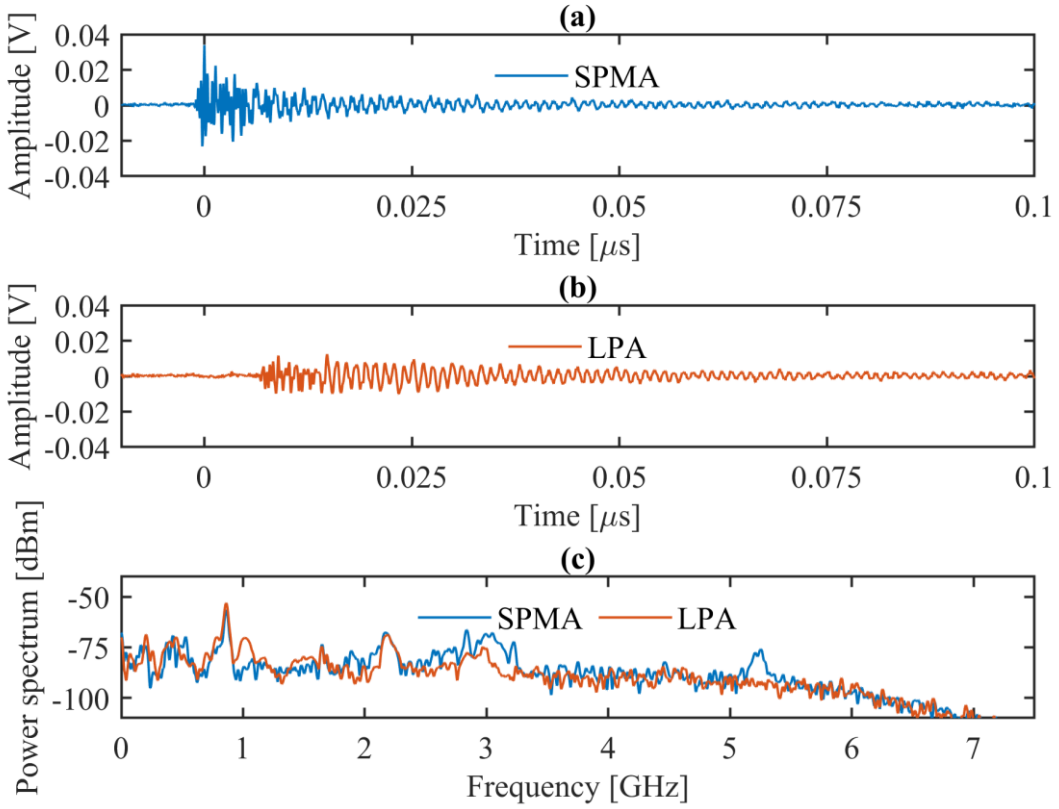

Fig. 5.18 Time (a) & (b), and frequency (c) characteristics of PD measured with SPMA (a, blue) and LPA (b, orange) under HV AC. HV AC stimulus not shown. Sample rate 20 GS·s^{-1}.

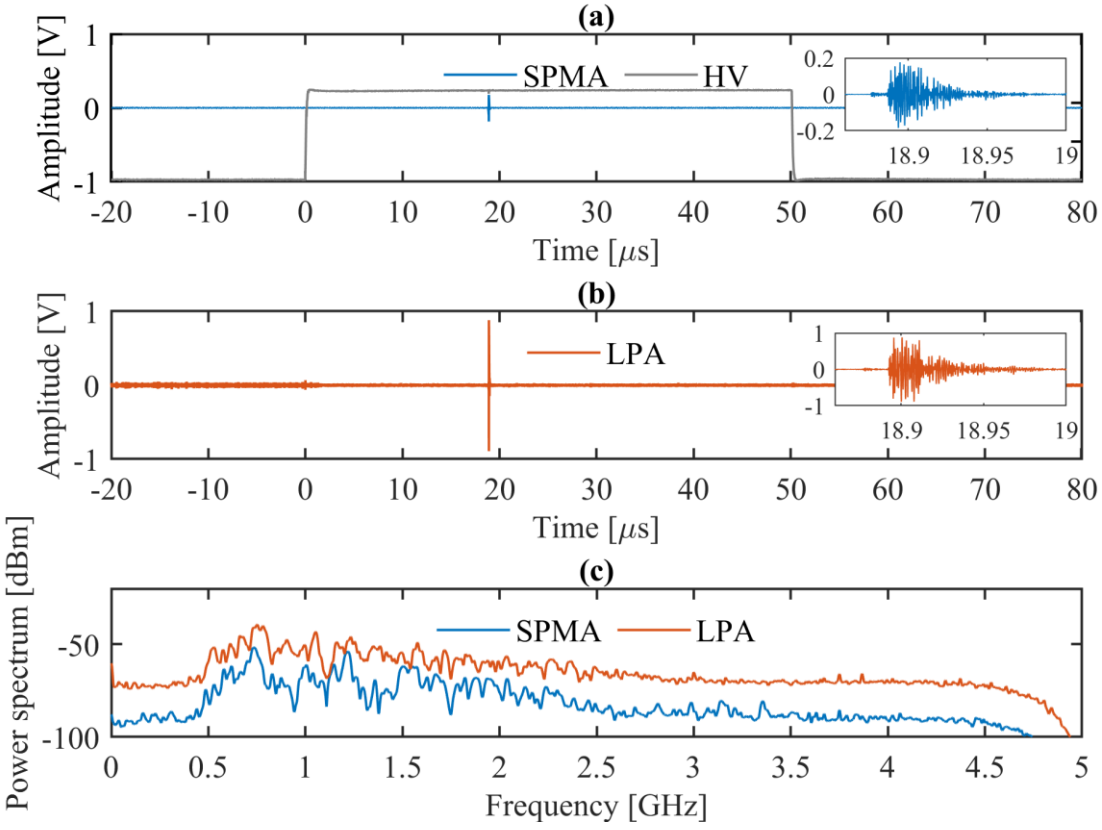

Fig. 5.19 Time (a) & (b) and frequency (c) characteristics of PD measured with SPMA (a, blue) and LPA (b, orange) under HV DC. HV DC stimulus shown in grey in (a), pulse width 50 µs. Sample rate 20 GS·s^{-1}.

With this configuration, the EMI measured by the SPMA depend on the configuration of the TG, the characteristics of each antenna, and their separation. Fig. 5.20 shows the response of the SPMA to the TG output through the whip antenna. As the attenuation over the range is negligible in most places and even improved at about 520 MHz and 860 MHz, the attenuation due to humidity was determined to be no relevant factor for testing.

5.4 Partial Discharge Testing of Gel-encapsulated DBC Samples

5.4.1 General Test Procedure

Fast slew rates of up to 23 $kV \cdot \mu s^{-1}$ are generated by the test platform, which causes considerable high-frequency EMI at the rising and falling edges of the test pulse. To combat this, the recommendation in IEC 60270 and IEC 61934 is to use a HPF with a cutoff sufficient to attenuate the commutation EMI such that the PD EMI can be recorded. In this work, the previously discussed 7^{th} order Butterworth HPF was again used.

Samples were placed centrally inside the environment chamber, allowing the SPMA to be placed closely underneath. The samples were raised from the metal racking in the chamber by a polypropylene (PP) spacing block 20 mm in thickness. Connection to the samples was made via the XLPE insulated leads, which were passed through the cable port. This was then sealed with a foam bung. Care was taken to separate the test leads to avoid spurious readings from potential PD between conductors, though only

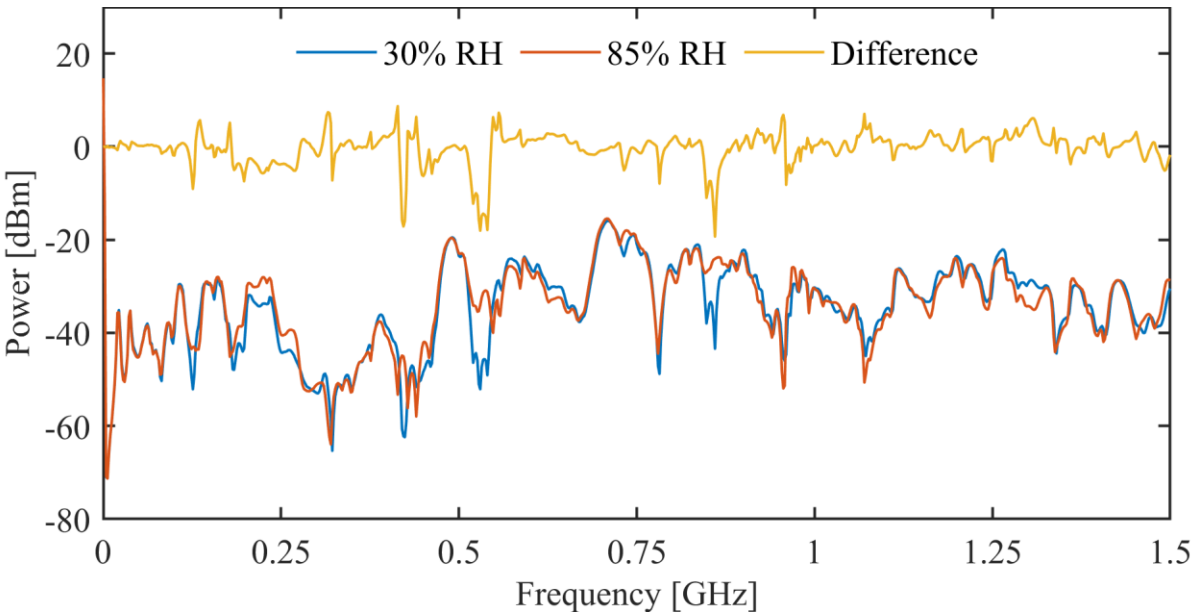

Fig. 5.20 Attenuation of TG signal received by SPMA due to humidity.

one sample was energised at a time, and the leads were themselves rated for 6 kV operation. To ensure that there was no possibility for the test signals to couple directly with the antenna or its cabling, the SPMA was connected via RG316 coaxial cable and fed through the foam door guard rather than the cable port. To ensure the samples started at a dry state, a forced dry out condition of 85 °C / 30% RH was held for 24 hours before each set of tests. This work makes comparison of PD behaviours at a fixed high temperature (85 °C) with two humidity conditions: low (30% RH) and high (85% RH). Fig. 5.21 shows the qualified DBC samples in situ of the environment chamber.

Two types of PD testing were performed. The first was to evaluate the PDIV of the samples, comparing values obtained in high humidity to those in low humidity. The second was designed to investigate low amplitude PD events that occurred randomly during the previous test. Proper detection of these weaker discharges was not trivial, so the testing was based around a PD event counting procedure over a set number of test pulses. The tests are better explained at the start of each relevant section: § 5.4.2 and § 5.4.4 for strong and weak discharge testing, respectively.

5.4.2 Influence of Environmental Conditions on Partial Discharge Activity

To determine the variation of sample PDIV with humidity, samples were first held at the dry out condition for 24 hours to ensure that no appreciable amount of moisture was absorbed in the sample at

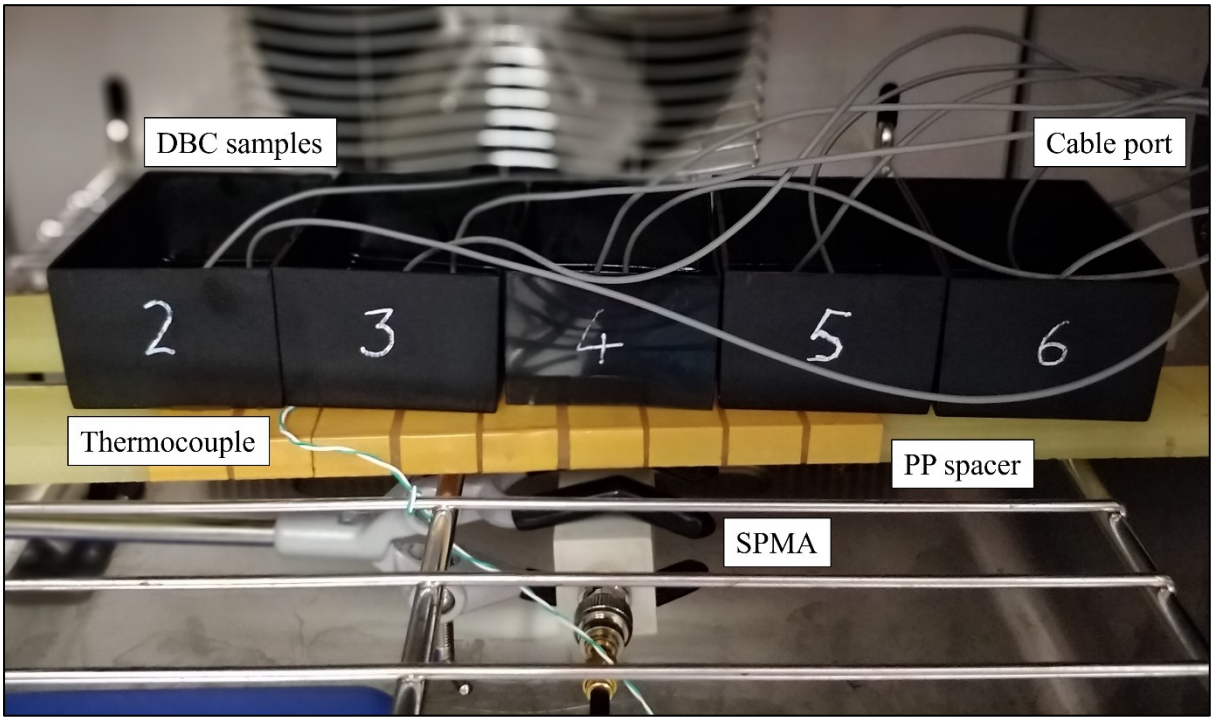

Fig. 5.21 DBC samples in situ of environment chamber.

the start of testing. The test conditions used were intended to highlight the initial variation in PDIV with increasing ambient humidity (i.e., increased moisture content in the gel), further change in PDIV for a dwell at high humidity, and then whether any changes in the PDIV were recoverable by removing the high humidity environment. These conditions are summarised by Table 5.2.

Starting from a test voltage of 1 kV, samples were subjected to a train of 5 10 kHz pulses at 50% duty cycle for the purposes of generating PD. The supply was increased by 50 V increments after each pulse train until PD activity was recorded. This was repeated 5 times per sample. The previously discussed IEC standards advise a threshold of at least twice the noise floor for detection purposes. Residual commutation EMI during testing had an amplitude of about 13 mVpp and given the unavoidable measurement of intermittent outside noise influences, the threshold was set to 100 mV for this experiment. It is possible that a lower threshold would provide a slightly altered view of the PDIV behaviours, but the work chose to eliminate the possibility of false positives. The impact of humidity on the PD should be observable irrespective of the threshold, as increasing test voltages is understood to increase discharge magnitudes, which should apply to both environmental conditions.

TABLE 5.2
SUMMARY OF TEST CONDITIONS FOR THE DETERMINATION OF PDIV

Condition	Temperature [°C]	Humidity [% RH]	Step time [h]	Cumulative test time [h]
1: RH30-24h	85	30	24	24
2: RH85-24h	85	85	24	48
3: RH85-48h	85	85	24	72
4: RH30-24h	85	30	24	96

i. Determination of PD Inception Voltage

In this work, the PDIV is determined to be the voltage applied to the sample during the high region of the test pulse. This was done to simplify the view of the results given there were minor oscillations during the rising and falling edges due to the cabling required by the setup, and the presence of PD after the falling edge of the test pulse. As more than one PD event may be witnessed in a single test, the results presented in this section refer only to the first PD event in each test, we name this the primary PD (PPD) for clarity. Discharges other than the PPD are called secondary PD (SPD) events, and these are explored in the next subsection.

It is typical in electrical breakdown and reliability research to interpret failure data using the two parameter Weibull distribution function. This work regards a PD event to be a localised failure of the insulation in part, and hence the Weibull approach is warranted. The standard form of the Weibull cumulative distribution function (CDF) is given in (71).

$$F(x) = \begin{cases} 0 & for\ x < 0 \\ 1 - \exp\left[-\left(\frac{x}{\beta}\right)^{\alpha}\right] & for\ x \geq 0 \end{cases} \tag{71}$$

where α and β are the Weibull shape and scale parameters, respectively. The scale parameter represents the 63.2% probability of an event, and the shape parameter indicates the dispersion of the data.

When $\alpha = 1$, the Weibull CDF is equal to the exponential distribution. The Weibull plot linearises the CDF by change of variables and plotting $ln\big(-ln\big(1 - F(x)\big)\big)$ against $ln(x)$. If the data fit well to a straight line, they match the Weibull distribution.

The strong PD data for PDIV determination tests across all samples at each successive condition are shown using a Weibull plot in Fig. 5.22. A general shift to the left indicates a reduction in PDIV due to the presence of humidity, but this is limited in extent. The impact of each successive condition is not easy to interpret from the Weibull plot as the changes are minor compared to the full spread of the data.

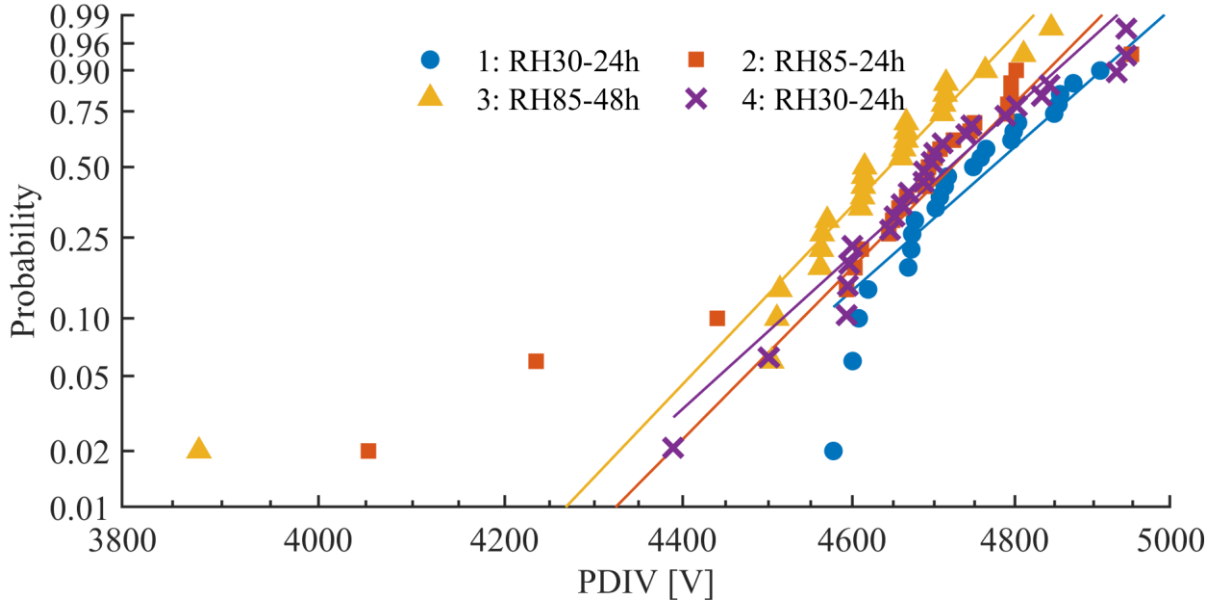

Fig. 5.22 Two-parameter Weibull distribution plots of PDIV tests for strong PD at each subsequent environmental condition: 30% RH / 24 h (●); 85% RH / 24 h (■); 85% RH / 48 h (▲); 30% RH / 24 h (×).

In this case, the tenth percentile (B10) value is chosen to elucidate the changes. The B10 values are shown in Table 5.3 alongside shape and scale parameters at each condition.

TABLE 5.3
SUMMARY OF WEIBULL STATISTICS FOR PDIV

Condition	Shape [α]	Scale [β]	B10 PDIV [V]
1: RH30-24h	33.53	4829	4562
2: RH85-24h	29.12	4757	4540
3: RH85-48h	42.27	4676	4473
4: RH30-24h	37.57	4770	4517

All B10 PDIV values are well above the V_{isol} rating for the original Infineon power module (50 Hz AC, 4 kV_{RMS}, t = 1 min). Increasing the humidity (Condition 2: RH85-24h) caused a slight reduction in B10 PDIV of the samples in general, which worsened over time (Condition 3: RH85-48h). Though the influence is negligible over the 24h period, removal of the high-humidity environment (Condition 4: RH30-24h) ceased the decline in sample PDIV. The total decrease in B10 PDIV for a 48 h dwell in 85% RH was only about 1.95%. The decrease in the scale parameter (β) is about 3.17%.

The Weibull plot does not capture all useful statistics, and it is difficult to determine the spread of the PD data or the influence of humidity using that approach. A box chart presents another view of the PDIV testing and is shown in Fig. 5.23. From this it is observed that although there are more outliers in the high-humidity condition, but the behaviour remains the same in that the influence of humidity on

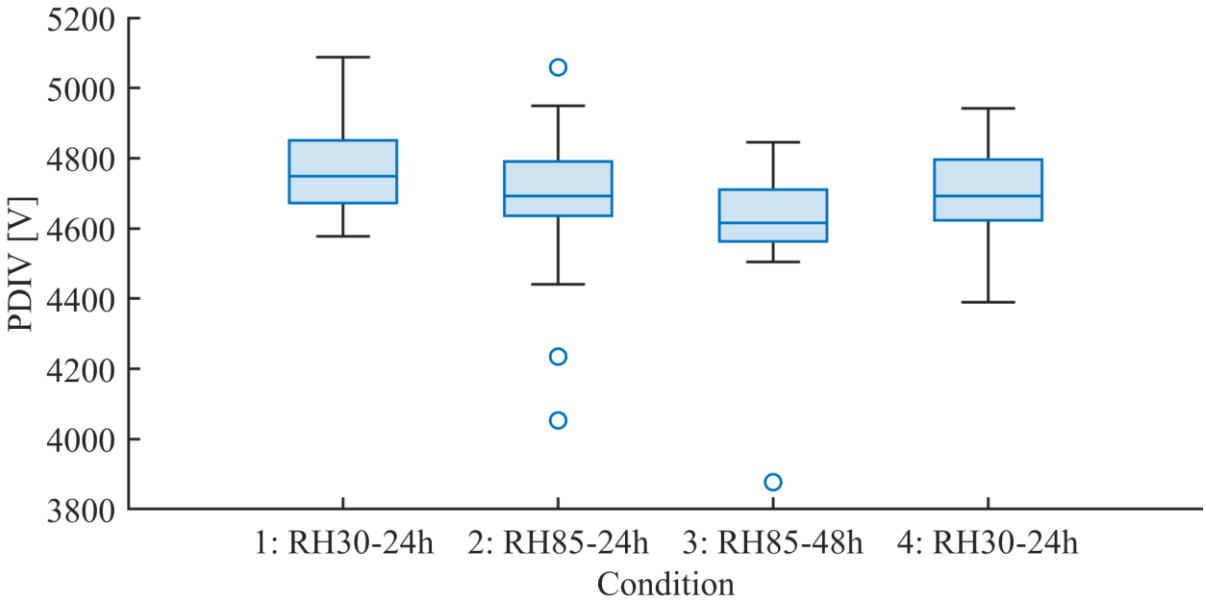

Fig. 5.23 Box chart of PDIV results at each subsequent environmental condition.

the sample PDIV is minor, with the median PDIV value decreasing by only about 2.8%. The interquartile range of the data is less in the humid environment, which combined with the increased quantity of far outliers indicates several events demonstrating exceptionally low PDIV. This was similarly observed for PD on power module substrates ages in a humid environment [98]. To investigate whether the change in PDIV or the presence of outliers is due to variance in the samples, the data can be represented as a grouped scatter for each condition, which is shown in Fig. 5.24. It is evident that the shift in PDIV applies similarly to all samples, and that several samples provided outliers. Consequently, it was determined that sample variance was not the dominating factor for the presence of outliers.

Interestingly, although sample DBC6 had an IR rating during qualification an order of magnitude lower than other samples as demonstrated in Fig. 5.10, the PDIV does not seem to be influenced in any major way corresponding to this result. A decrease in PD amplitude has been reported previously for PD testing in a high temperature environment with high ambient humidity, although this was shown for solid insulation rather than gel [191]. It was proposed that the discharge could be quenched in high humidity due to DEA to water molecules. Taking this into consideration, it is pertinent to investigate PD amplitudes in the PDIV determination testing. These results are discussed in the next subsection.

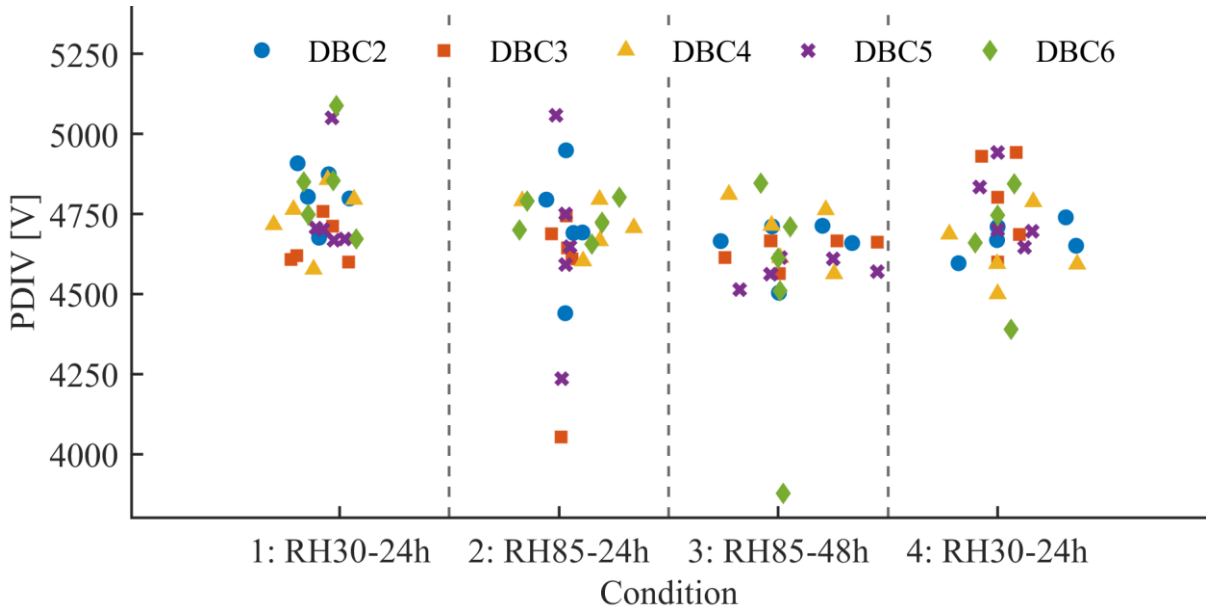

Fig. 5.24 PDIV results per sample in each successive environmental condition.

ii. Time-Resolved PD Study

When testing under AC stimulus, it is common to interpret PD test results using PRPD analysis, where a heat map of PD intensity (in pC) is shown relative to the test voltage phase angle. The pattern of the PRPD plot generally provides information about the type of defect in an insulation system, whether it be protrusions, electrochemical migration (ECM) or the presence of voids, but the patterns are specific to the system being tested and requires significant experience for reliable pattern trend recognition. In test setups using square-shaped pulse excitation of the sample, PRPD is not strictly suitable, so the discharges are resolved in time rather than phase – time-resolved PD (TRPD) analysis. The time at which a PD event occurs relative to the test pulse is the PD time lag. This work uses the 10% value of the test pulse plateau as a baseline for time lag estimations, i.e., $t(V_{10\%}) = 0$. For increasing test voltage and increasing slew rates, the PDIV should be reached sooner, but due to the stochastic nature of PD, a discharge may not always occur at the exact time the PDIV is reached. PD requires the local electric field to meet the breakdown criterion established previously using Paschen's law, but also that an initial electron is present to begin the process of avalanche via impact ionisation. In the literature, this is assumed to always be true given the readily available free electrons stimulated by field or thermionic emission, with the barrier to field emission reducing for higher temperatures, but nevertheless many PD events do not occur with the rising or falling edge of the test pulse.

A greater amplitude discharge correlates with a greater degree of damage to the insulation, and standards based PRPD qualification techniques per IEC 61287 usually use a 10 pC tolerable limit at the module level, though this can be lower for the individual DBC raft level. It is not possible to investigate displaced charge under unipolar square wave excitation, but UHF EMI amplitude has been linked to increasing discharge quantity before in other work [248]. Therefore, this work associates a higher measured UHF amplitude of a PD event with a larger displaced charge, and hence a greater degree of damage to the insulation system.

A TRPD plot of the PD data recorded during PDIV determination testing is shown in Fig. 5.25, where PPD and SPD are presented separately (Fig. 5.25(a) and Fig. 5.25(b), respectively). PPD appear to be reduced in magnitude initially with an increase in the ambient humidity but return to a wider

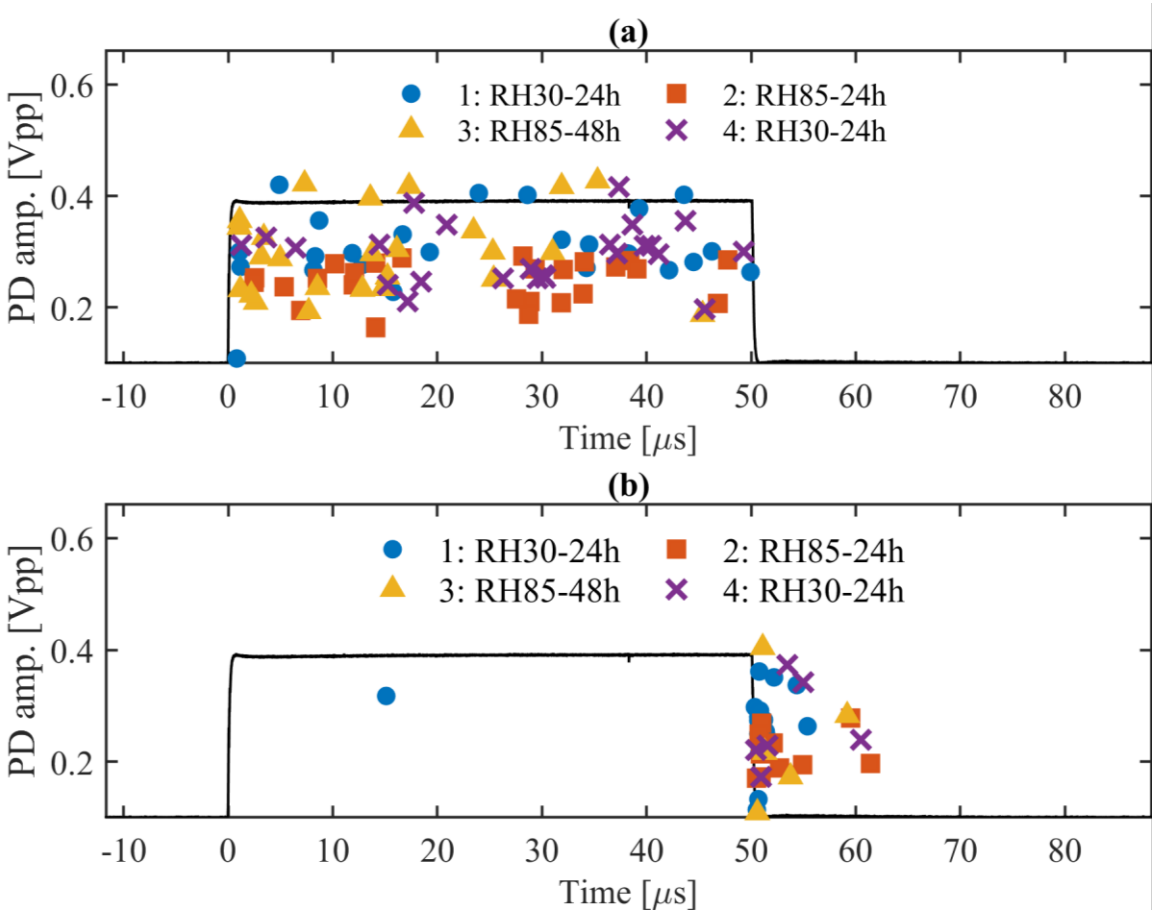

Fig. 5.25 TRPD graphs of (a) PPD and (b) SPD recorded during PDIV determination testing under positive square wave stimulus.

spread for a continued dwell in the high humidity environment. This is true of SPD also, though the lesser quantity of the PD events makes it difficult to argue a case for statistical significance. PPD are spread out across the test pulse with no general concentration in time, which does not appear to change for the successive environmental conditions. The SPD are more concentrated, occurring overwhelmingly at or after the falling edge of the test pulse.

The distribution of the PPD data is not like that of some other research [249], where previous TRPD for silicone gel or DBC samples under positive square wave voltages highlighted a clear concentration of PD events around the rising and falling edges of the square pulse, although this work made no distinction between PPD and SPD. The distribution of PPD events in this work are more like the results presented in [200] for similar samples, albeit the samples in that work were subjected to high temperature stress alone. In that work it was shown that SPD exhibit lower discharge magnitudes than PPD, but that for DBC samples subjected to high temperature stress their distribution with regards to

the test impulse is generally unaffected. The PPD and SPD data shown in Fig. 5.25 support the lesser amplitude of SPD over PPD, though these tests were performed in an isothermal environment of 85 °C.

Two theories for this slight decrease of PD amplitude in humidity are found in the literature. The first is the previously discussed quenching of discharges caused by DEA to water molecules during the PD process [191]. The second relates to ratio of the relative permittivities of the ceramic and the encapsulant, demonstrated for a DBC with a smooth transition from copper to ceramic [214]. In this work it is shown that by varying the permittivity of the encapsulation to be more similar to that of the ceramic in the substrate, the peak electric field strength about the triple interface can be reduced. The optimal ratio $\varepsilon_{encapsulant}/\varepsilon_{ceramic}$ for their smooth transition model is 1.3. Applying the same approach for the traditional model did not converge on a solution for the present research, and gave results like those shown in [242]. As discussed theoretically in Chapter 2 and demonstrated experimentally in Chapter 3, the absorption of moisture by silicone gel changes its relative permittivity. The relative permittivity of the gel was shown to increase from 2.16 to 4.96 in the 5 mm sample. The relative permittivity of Al_2O_3 ceramic is accepted to be about 9.8, and accordingly the strength of the electric field about the triple interface is expected to reduce for the absorption of humidity by the gel. Electric field strength about the triple interface is correlated to PRPD measurement in [160], where it is demonstrated that the peak value of the electric field is an important factor in determining PDIV. The PDIV for the PPD was discussed in the previous subsection, showing only a minor reduction in PDIV in the high humidity environment. From the results presented in [160], [214], the impact of absorbed humidity by the sample should be to increase the PDIV and reduce the PD amplitude, however this is not the case. The PPD and SPD results both show a slight reduction in amplitude due to the absorption of moisture, and the PPD results show a minor decrease in PDIV. As the trends presented do not match similar works in the literature, additional investigations were performed.

5.4.3 Classification of PD by UHF Amplitude

For the PDIV determination testing, a 100 mVpp threshold was set based on the residual commutation EMI and outside noise sources. As the amplitude of PD events past this threshold concentrated at an even higher amplitude (~260 mVpp), the threshold was determined to be sufficient

for the detection of this category of PD. However, the results showed several low amplitude events that did not meet this threshold, with some low amplitude events having amplitude at or below the level of the residual commutation EMI. This led to the suspicion of another PD mechanism relating to a different portion of the insulation than for the stronger discharges. In this work, these are named strong and weak PD due to their magnitudes. The two strengths of PD are shown clearly in Fig. 5.26.

As the hardware HPF left considerable residual commutation EMI, the data were filtered again with a steep software HPF having the same cutoff frequency (700 MHz), to reinforce the cutoff attenuation. The measurement and filtering arrangement is shown in Fig. 5.27. This resulted in a decrease of the residual commutation EMI from ~13.13 mVpp to ~5.26 mVpp, so the new threshold for detection was reduced to 10 mVpp in line with the recommendations outlined in the standards. The noise floor was reduced from ~5.77 mVpp to ~5.12 mVpp, evidencing that the residual commutation EMI was almost entirely attenuated. This allowed for a holistic view of all PD events witnessed during PDIV determination testing. A TRPD graph of the holistic interpreted PD recorded during the PDIV determination testing is shown in Fig. 5.28, using the reduced threshold of 10 mVpp. The data suggest two distinct groups of PD amplitudes. There are only a small number of the weak PD results compared to the strong PD, so considering the low PDIV outlier results discussed in § 5.4.2, it is possible these two results are related. This could indicate that a lower PDIV relates to a lower PD amplitude for these

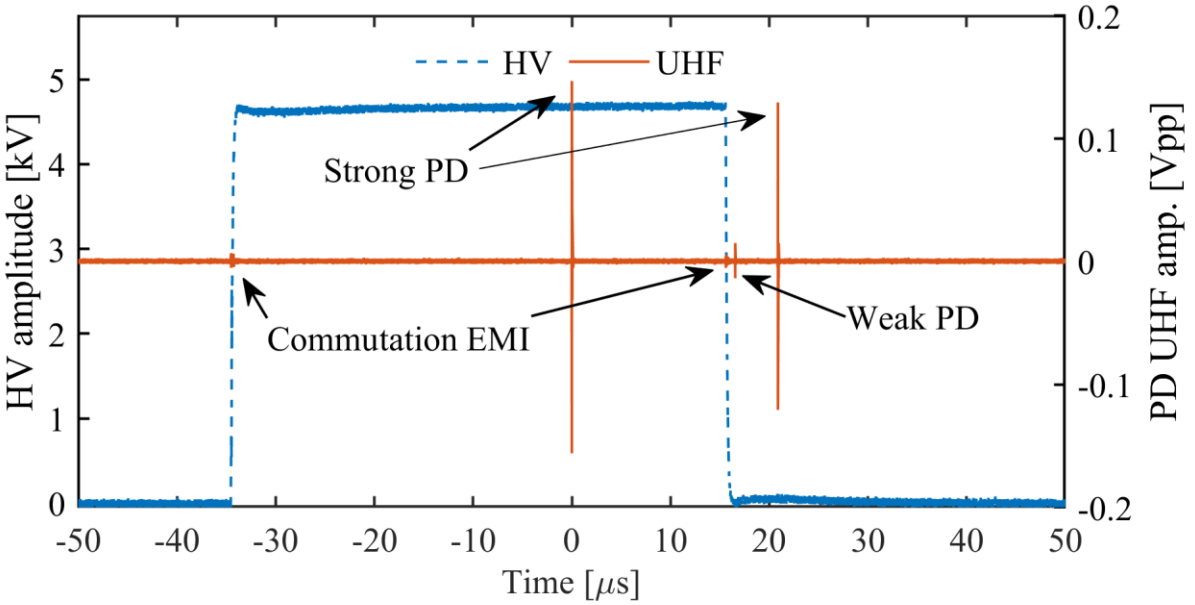

Fig. 5.26 Typical time domain record of a PD test showing the distinction between strong and weak PD magnitudes. Strong PD consists of primary PD (PPD) and secondary PD (SPD).

samples. This is investigated in Fig. 5.29, where PD amplitude is shown against PDIV. This shows that the strength disparity in the discharges is not purely related to the voltage of the test impulse, and that

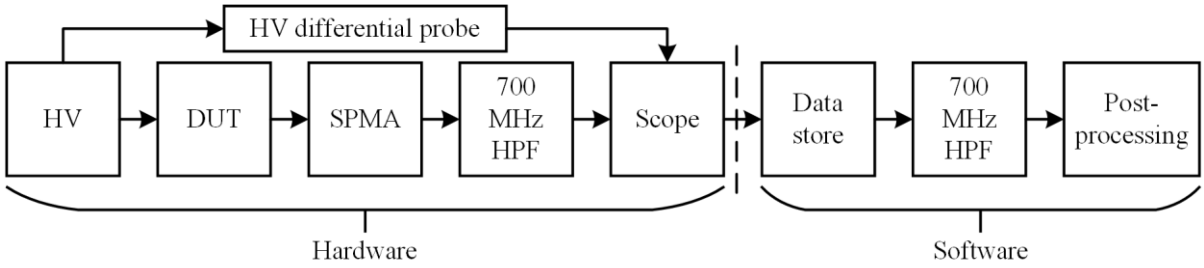

Fig. 5.27 Block diagram showing arrangement of measurement and filtering chain in hardware and software domains for PD testing.

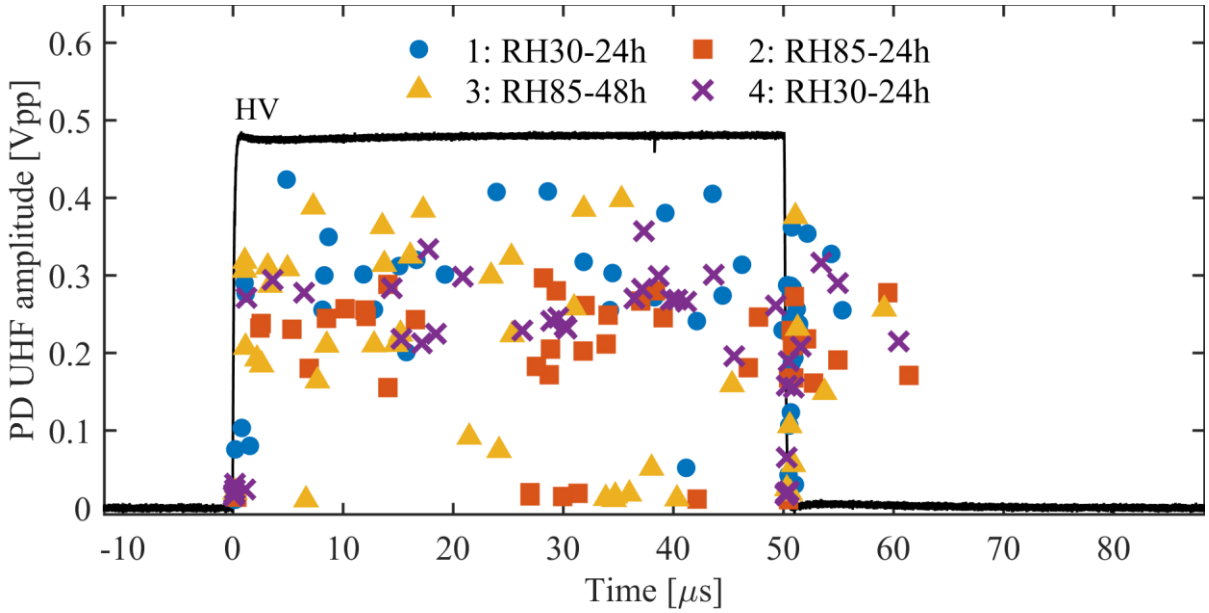

Fig. 5.28 TRPD graph of holistic PD data recorded during PDIV determination testing.

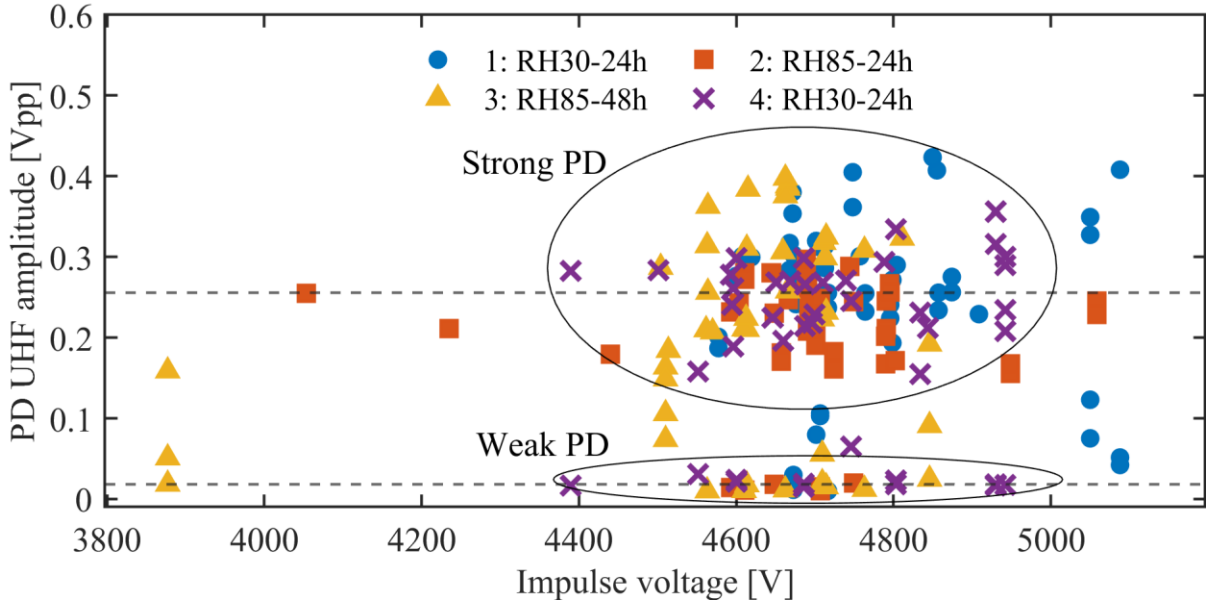

Fig. 5.29 PD amplitude against test impulse voltage for holistic PD data recorded during PDIV determination testing. Ellipses highlight concentrations of strong PD and weak PD, with dashed lines representing their respective median amplitudes.

the two observed groupings are not impacted by the impulse voltage. The two groups have median amplitudes of ~257.41 mVpp and ~27.65 mVpp, relating to strong and weak discharges, respectively. The nature of these groupings is attributed to the physical location of PD on the substrate and is discussed further in § 5.6. In this work, the categorisation by amplitude is such that strong PD are those with amplitudes above 100 mVpp, and weak PD are those below.

5.4.4 Impact of Ambient Humidity on Weak PD

i. Weak PD Count Procedure

The weak PD witnessed during PDIV determination testing occurred with a high degree of randomness and exhibited in many instances a similar power spectrum to the commutation EMI after the software reinforced HPF. Obfuscation of the PD in the frequency domain was then likely, meaning that for weak PD occurring near the rising edge, the traditional filtering approach was not suitable. Fig. 5.30 shows a test which highlights the obfuscating behaviours. Though additional software filtering proved effective in some cases for the detection of weak PD as in the previous section, it was not suitable

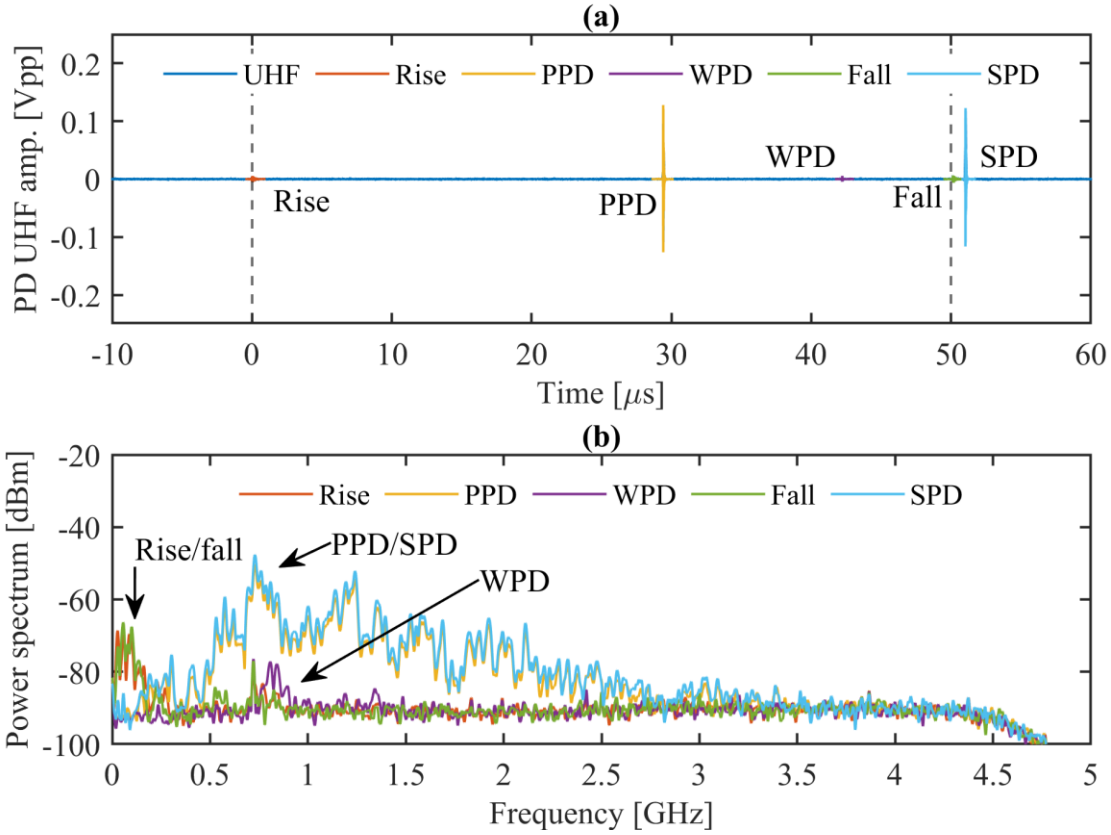

Fig. 5.30 Time (a) and frequency (b) domain records for a PD test performed during PDIV determination testing. The rising and falling edges of the test impulse coincide with the dashed vertical lines. Distinction is made between the strong PD (PPD/SPD) and weak PD (WPD).

for all PD events due to slight variance in the spectral content for PD across samples. Additionally, outside noise sources were not eliminated completely by the environment chamber, so the detection accuracy was also subject to outside influence. Time-frequency, multiresolution, and convolutional neural network based techniques have proved effective in cases in the literature [250], [251], [252], [253], where separation of the background noise and PD signal is not trivial. Attempts for this work involving the use of similar techniques, including wavelet transforms, inspection of the Hilbert spectrum using the Hilbert-Huang transform (HHT), and many others were performed to no avail and were often computationally expensive, and so an alternate approach was sought. The primary barriers to accuracy in this regard were the presence of a high number of false positives, and the inability of a single technique to adequately highlight PD across the wide spread of amplitudes and lags in the dataset.

A large dataset was gathered with the aim of a statistics-based approach toward PD detection. To ascertain whether the weak PD occurred alone or always alongside strong PD, testing was performed using single pulses at fixed voltages with a lower amplitude than in the PDIV determination testing. Fixed voltage levels from 3500–4000 V, below the mean PDIV of samples in either environmental condition, were investigated in fixed increments of 100 V. A total of 100 tests were performed per combination of sample, condition, and test voltage. The environment chamber did not perfectly isolate the SPMA from outside noise sources, so common or constant background noise sources were attenuated during the post-processing with software band stop filters (BSF). Care was taken in the choosing of the cut off frequencies of these filters as several external noise sources overlapped PD in the frequency domain, and aggressive attenuation of the noise would reduce power of the PD events in the signal. The attenuation bands used were as follows: 725–945 MHz, 1680–1790 MHz, and 2385–2500 MHz. Fig. 5.31 shows a test with several of these noise sources present before (Fig. 5.31(a)) and after (Fig. 5.31(b)) filtering. The 2.44 GHz noise source clearly originates from Wi-Fi communications, but the origins of the other noise sources could not be reliably identified. This additional filtering step alone was not sufficient for the purposes of detection of the weak PD as although the external noise sources were attenuated, there was still the possibility of overlap in the time domain of the PD and commutation EMI signals. Consequently, additional processing using a mean of moving

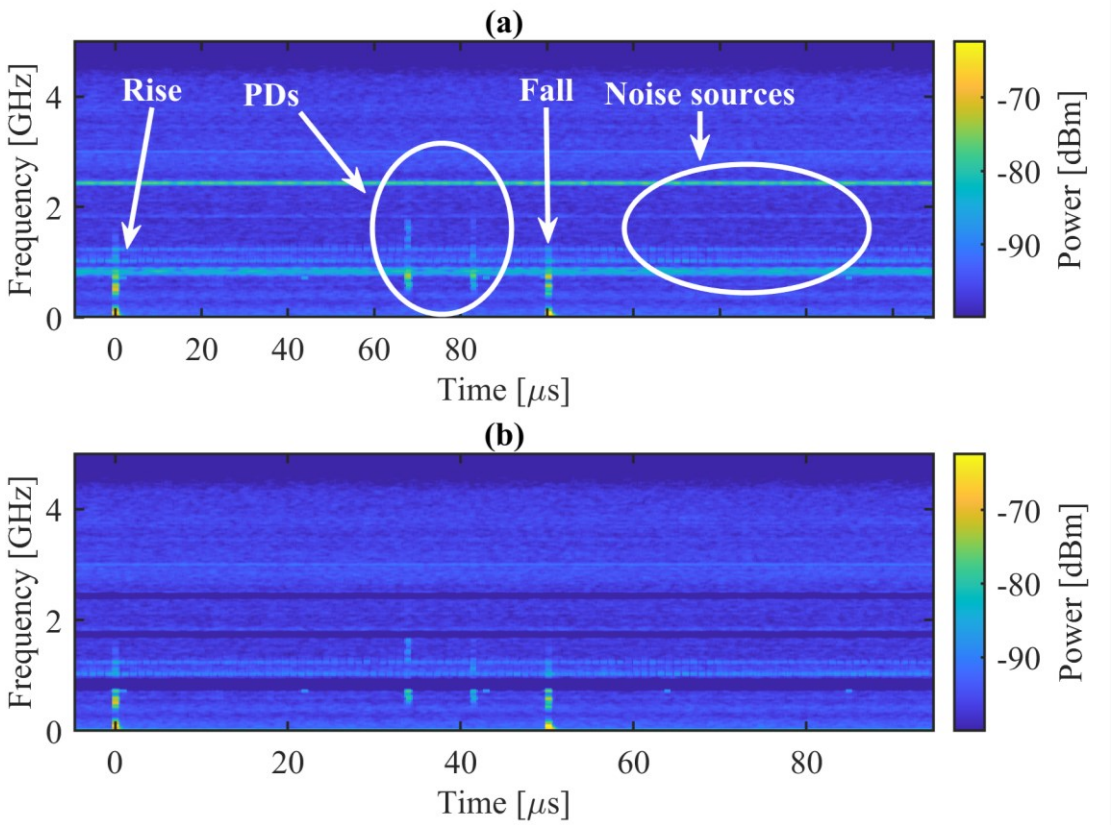

Fig. 5.31 Power spectrum of a typical PD test for weak PD highlighting external noise sources. (a) before additional band stop filtering, (b) after.

standard deviation (MMSD) approach based on the work of [254] was performed, which is outlined below. The core intent behind the procedure takes advantage of the fact that PD is stochastic in nature and that this behaviour is dissimilar to the much more deterministic commutation events, which have only negligible difference from test to test.

With a large dataset sufficient to provide a mean within which the contribution of PD is negligible, the commutation EMI without the influence of PD can be easily estimated. The difference between this commutation-only record and individual records from testing would highlight PD events. This resulted in a procedure that was both computationally lightweight and robust to the identified noise sources, which was favourable for the large dataset gathered in testing. The MMSD procedure for weak PD detection is illustrated through records at each major step in Fig. 5.32, and consisted of the following steps, performed for each sample in each condition and at each test voltage (60 datasets total):

1. Record UHF data from 100 PD tests, this is the dataset.
2. Apply band stop filters to each record in the dataset.
3. Calculate the moving standard deviation of each filtered record.
4. Calculate the mean of all moving standard deviations within the dataset.

5. For each record in the dataset:
    a. Align the filtered record's moving standard deviation with the mean moving standard deviation using cross correlation.
    b. Subtract the aligned mean moving standard deviation from the current filtered record's moving standard deviation.
    c. Smooth the result using a moving mean.
    d. Threshold the result to identify PD.

For the weak PD counting procedure, a window of 200 samples (20 ns at 10 GS·s^{-1}) was used for the moving standard deviation and moving mean operations, and the threshold was set to 200 µV based on trial and error. As a single PD event consisted of many sample points above the threshold, events were

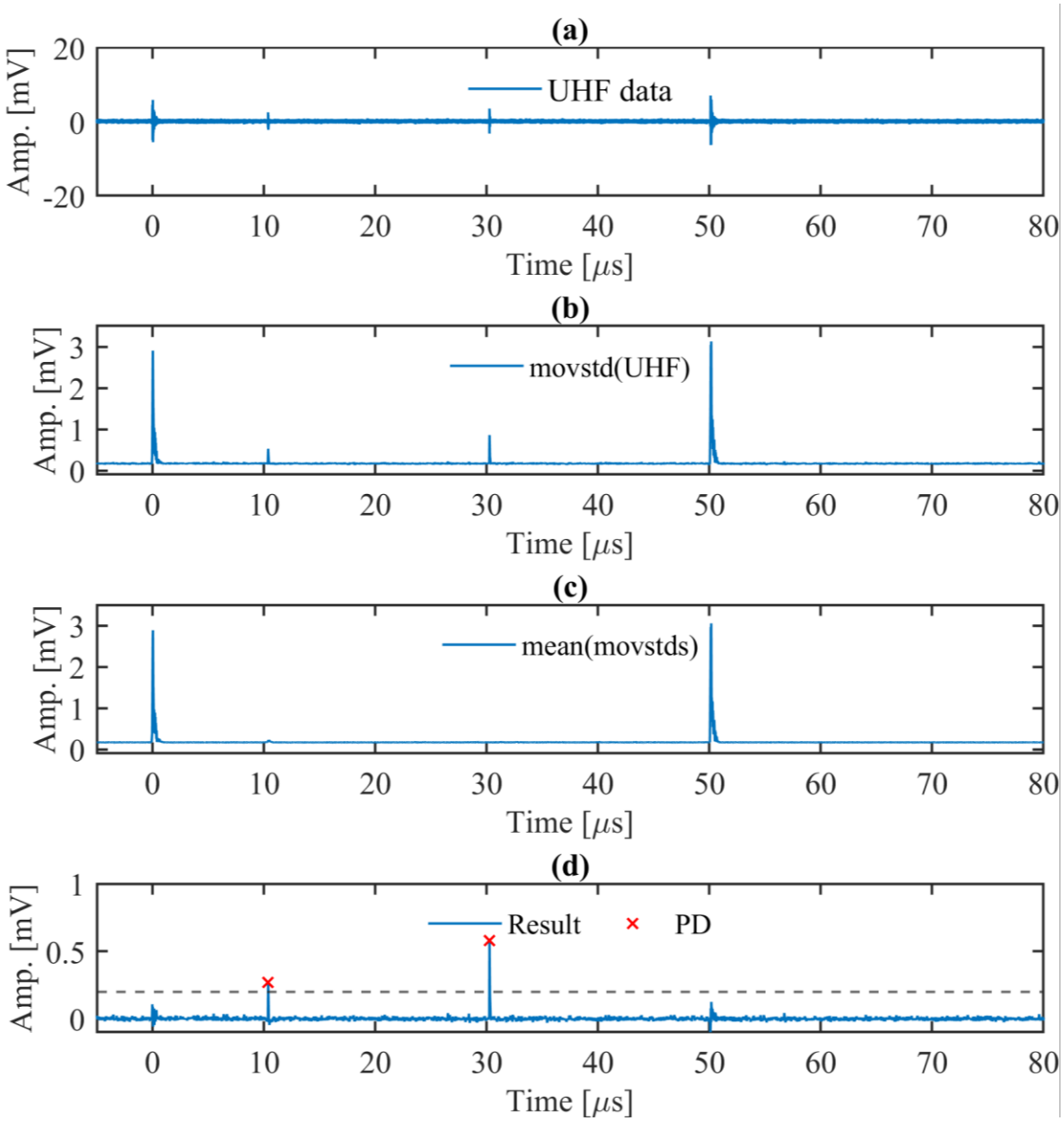

Fig. 5.32 Post processing procedure for detection of weak PD. (a) UHF data after hardware high pass filtering, (b) moving standard deviation of UHF record after additional band pass filtering, (c) mean of all moving standard deviations in dataset ($N = 100$), (d) result after subtracting mean from current trace, with PD.

counted using a neighbourhood grouping scheme based on a 100 ns window. Datapoints exceeding the detection threshold inside the window attributed to the same PD event. The maximum width of the window was consequently a function of the 'width' of the PD event, with the initial window width of 100 ns chosen corresponding to observations of the spread of many PD events observed in the results. Several locations on the sample may exhibit PD at similar times, which would cause overlap of their EMI. Measurement via UHF is not suitable to distinguish between these events based on their location. Such approaches have been shown to work in [178], [179], but the development of such a system was determined to be out of scope for this work.

As with the PDIV determination tests previously performed, samples were held in a dry-out condition for 24 hours before testing. Due to the considerable number of tests, only two setpoints were chosen for comparison: low humidity (30% RH) and high humidity (85% RH), with testing performed for each condition after a dwell of 24 hours. The temperature in the chamber was held at 85 °C for the duration of testing, to eliminate its influence on the observed phenomena. These setpoints are commensurate with the first two test conditions of the PDIV determination testing.

ii. Influence of Humidity on Weak PD Count

The results of the weak PD count testing are provided in Fig. 5.33, which also shows the count per test. Tests in the humid condition exhibited a significantly increased PD count over the dry condition,

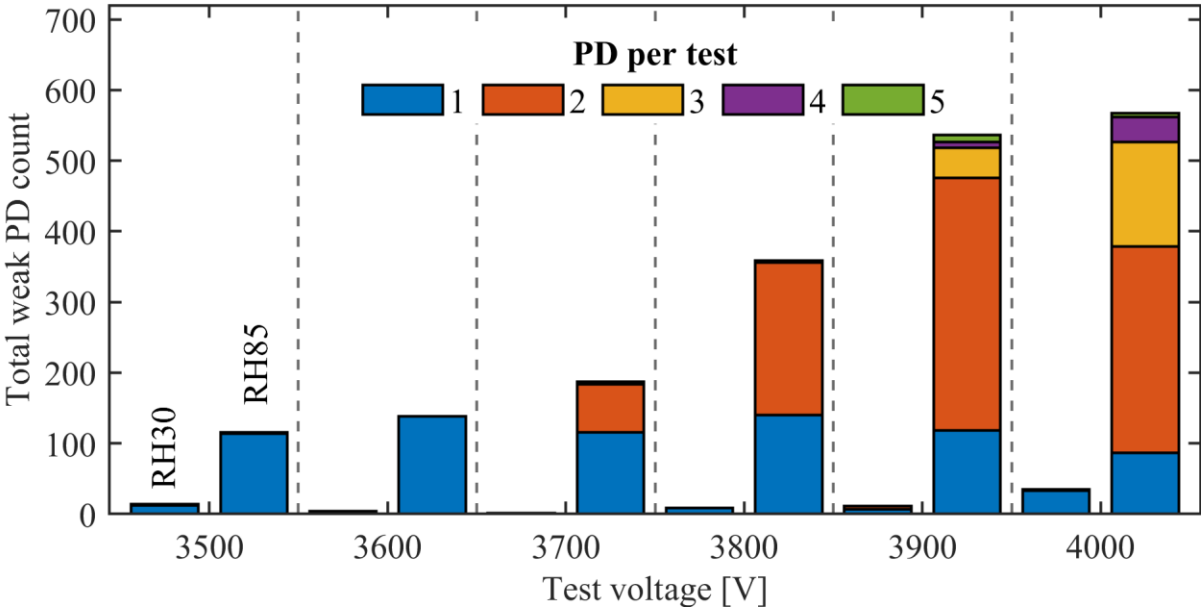

Fig. 5.33 Stacked bar chart of total weak PD count at each voltage. Left in groups is dry (30% RH) condition, right in groups is humid (85% RH) condition. Stacks inside bars represent counts of weak PD within each test.

implying that for weak PD the behaviour is strongly influenced by the absorption of moisture. This is different to the behaviours witnessed for strong PD, in which humidity showed only a minor impact. However, the two tests were not entirely alike in procedure and so a strict comparison is not possible at present. Although PDIV for the weak PD category cannot be strictly determined with the approach used, weak PD occurs at lower test voltages and thus must have a lower PDIV than strong PD. Weibull statistics for weak PD cannot be given due to the fixed voltages. The influence of increasing test voltage for weak PD is to increase the overall PD count, as expected, but also to increase the quantity of PD events for a single test pulse. In the dry case a single PD event was the most common across all test voltages, whereas the humid case saw increasing quantity of PD events per test, indicating a more damaging PD regime based on the previous discussion of DEA.

iii. TRPD of Weak PD in High Humidity

TRPD analysis of the weak PD results was possible by using the PD time lag in the MMSD technique to find the corresponding PD amplitude in the recorded UHF waveform. It must be acknowledged that for PD occurring at the commutation intervals, the amplitude estimated by this technique may erroneously correspond to the commutation EMI at about 15 mVpp, which could not be avoided. Nevertheless, there are sufficient quantities of PD outside of this amplitude to evaluate the general trends. These results are shown in Fig. 5.34. The humid case presents a higher quantity of higher-amplitude PD events, which agrees with work from other authors on solid insulation in [255], but the trend there is not well established. The increased number of higher-amplitude events in the humid condition over the dry is attributed to the overall quantity of events in each condition, rather than a phenomenological link between moisture and discharge amplitude. This is shown by the presence of higher-amplitude events in both conditions. In both test conditions, weaker PD events were more common. The higher amplitude PD events in the humid case concentrate around the centre of the test pulse (~25 μs). In the dry condition the distribution of PD events in time agrees with much of the literature and concentrates around the commutation intervals (0 μs and 50 μs, in Fig. 5.34(a), respectively). However, with the increase in humidity the distribution is more spread out generally, and trends more towards the rising edge and the centre of the test pulse (Fig. 5.34(b)).

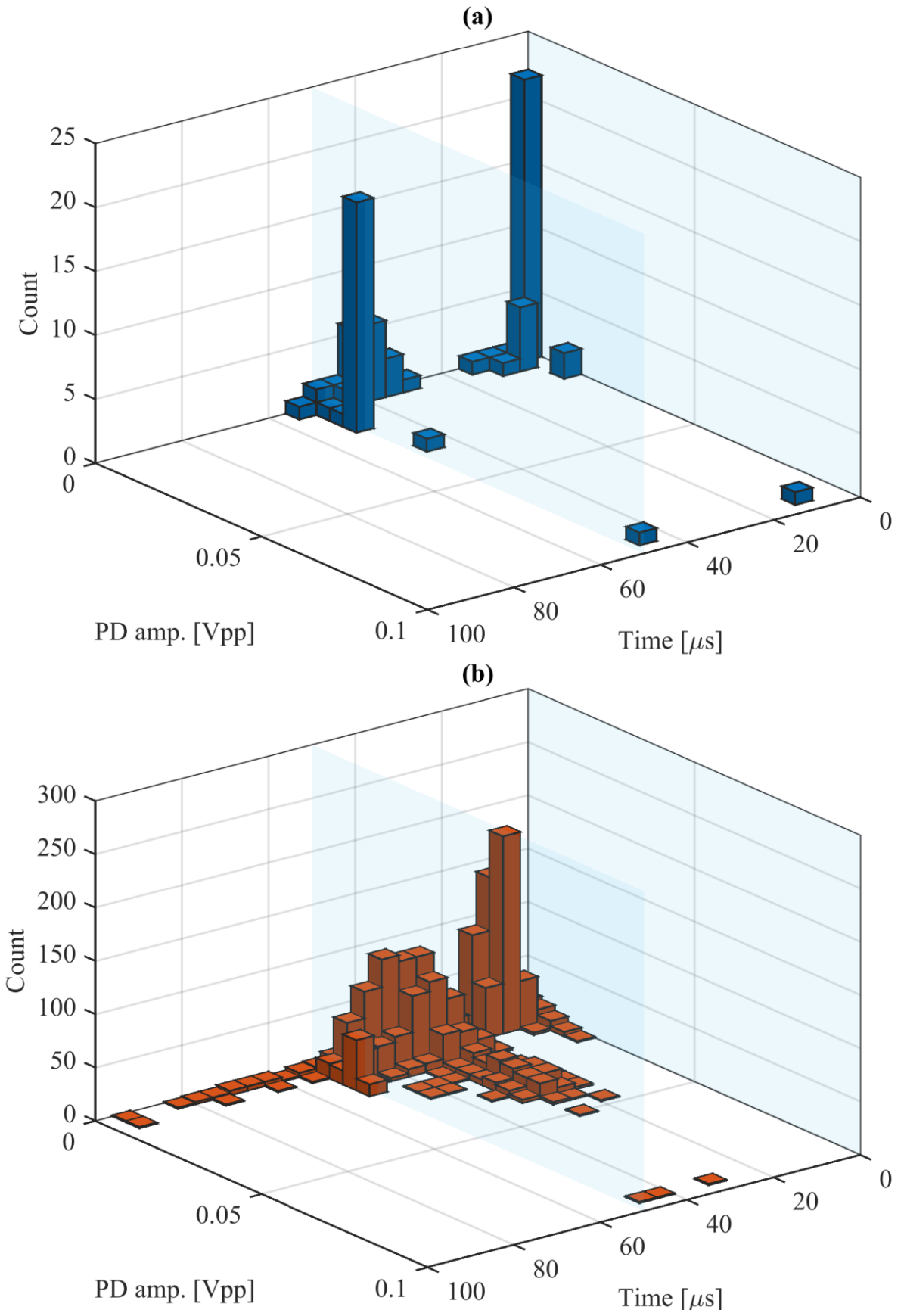

Fig. 5.34 Bivariate histograms of weak PD count against UHF amplitude and time lag of PD events. (a) 30% RH case, and (b) 85% RH case. The commutation events are denoted by translucent blue panes at 0 µs (rising edge) and 50 µs (falling edge).

When PD occurs, electron avalanche causes the buildup of space charges on the boundary of the gaseous void, with a field in opposite polarity to the external field. The samples in this work were subjected to unipolar positive square wave stress, so an accumulation of space charges is possible if the decay time of the space charges is longer than the pulse repetition rate (0.1 s^{-1}). This could result in an inflating PDIV over the course of testing, as the space charges oppose the applied field. For a fixed applied voltage, this effect would be evidenced by a reducing PD count for successive test pulses. Fig. 5.35 shows the number of samples in each test above the PD detection threshold over the course of the 100 test pulses in each condition. From this, no reduction in PD activity for continued testing is observed. Consequently, it must be concluded that the time delay between the test pulses was sufficient for the recombination of space charges in these experiments.

5.5 Electrostatic Simulation of DBC Geometries with Various Flaws

As shown in [160], the peak value of the electric field local to the triple interface in simulations of power module substrates can be used to infer the susceptibility of a sample to PD, with a higher peak electric field corresponding to a lower PDIV. Consequently, an enhancement of the local electric field about the triple interface causes a weakness in the insulation, reducing the PDIV at that point, and leading to early failures due to increased degradation. The field is enhanced by defects or flaws within the system. Pitting in the copper at the triple interface or trench side wall, which may be introduced

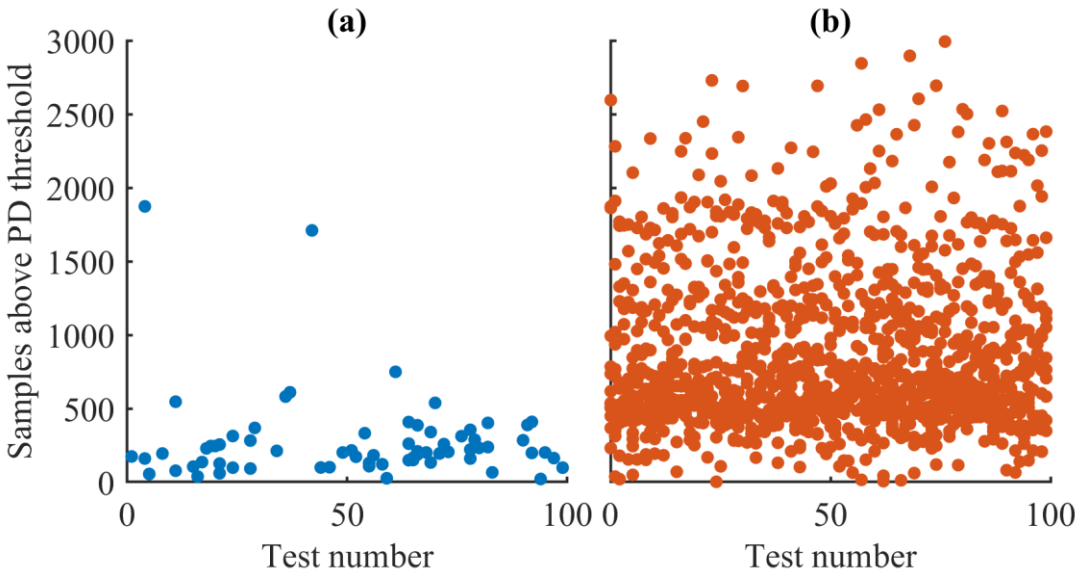

Fig. 5.35 Count of samples above the PD detection threshold against consecutive test number. (a) dry condition (30% RH), (b) humid condition (85% RH).

during the wet-etch, other manufacturing processes, or ECM, could cause local protrusions which enhance the electric field. Field enhancement is also likely to occur due to any dendritic growth. Some examples of these defects in the DBC substrate of a power module are shown in Fig. 5.36, obtained using SEM. Fig. 5.36(a) also shows the grain structure of the Al_2O_3 ceramic, with the individual grains ranging in major diameter from 2–7 µm.

Due to the sintering process and the shape of the grains, pores are possible within the thickness of the ceramic. It is possible for PD to occur within these voids in the ceramic [256]. If surface defects are not fully evacuated of air during the degassing process, an air-filled void may be present at any of these nucleation sites. Should moisture infiltrate the system via diffusion through the silicone gel, it may become bound at several locations: inside the volume of the gel within the un-cured silicone fluid amidst the strongly crosslinked regions, adsorbed as a film at the ceramic or copper surfaces due to poor adhesion with the silicone gel, or mixed into the air-filled voids if present. If moisture is present at the copper surfaces or the die attach layer in a power module and subjected to electrical and thermal stress, corrosion will occur in the metallisation over time. This can lead to increased thermal stress due to increased metallisation resistance and increased local electric field due to roughened metallisation surfaces. Microfractures in the grain structure of the ceramic may also be present due to thermomechanical stresses over the module's lifetime, and in severe cases even delamination of the ceramic and copper [257].

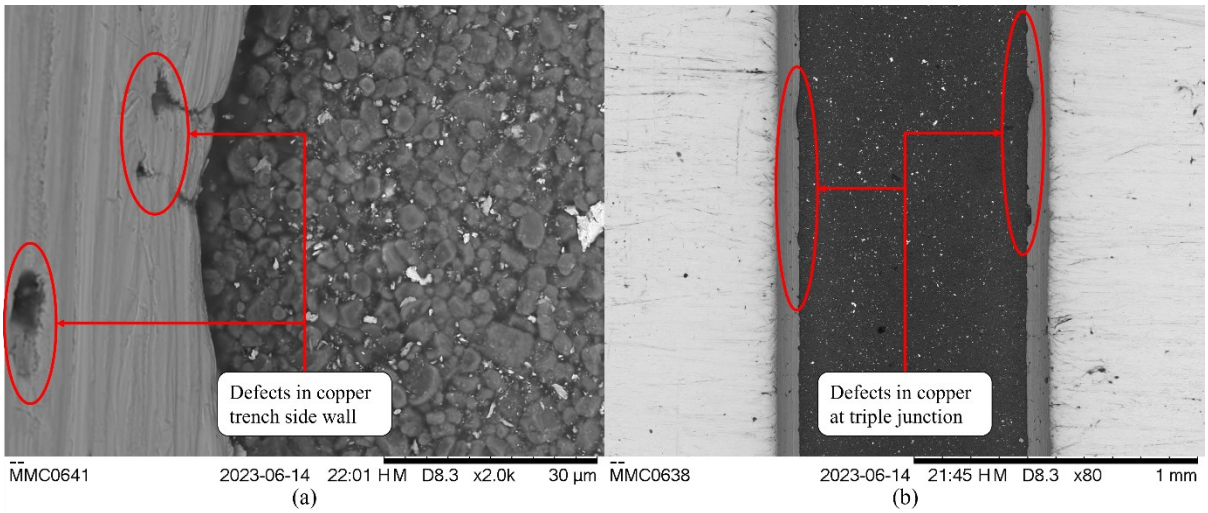

Fig. 5.36 Defects observed on DBC rafts taken from a commercial IGBT half-bridge module. (a) defects in copper side wall within the lateral trench, x2.0k magnification, (b) defects observed at the interface of copper and ceramic at the triple interface, x80 magnification.

To contextualise the previous results shed light on the probable causes of the difference between the identified PD categories, the electric field of representative DBC geometries inclusive of flaws is simulated in electrostatic conditions. The system geometry is changed to mimic the flaws previously discussed, with changes in the resulting electric field used to indicate behaviours of the samples in the experiment. Sample geometries are based on measurements with digital micrometers and SEM imaging of DBCs taken from a commercial power module. To reduce computational complexity and allow clearer interpretation of results, the simulations are limited to two-dimensional solutions. Measurement lines L1, L2 and L3 are chosen based on the recommendations in [98], [242], to investigate the electric field strength across the lateral trench, in the ceramic near the triple interface at the trench, and in the ceramic near the triple interface on the outer edge, respectively. The authors of [242] highlight possible inaccuracies due to mesh size variation or numerical singularities at the material interfaces and recommend measurement nodes at locations far away from these areas. Due to the geometry of the samples in the present work, such points are difficult to choose in a systematic manner, and so comparison will be made only of the measurement lines L1–L3.

For this simulation work, the following cases were considered:

a) DBC with no flaw included.

b) Air-filled void in the silicone gel at the triple interface.

c) Air-filled void in the ceramic under the triple interface.

The materials used were those available in the ANSYS Material Library except the gel, which was implemented based on the manufacturer provided datasheet [75]. To model the dry and humid cases for the simulation, the gel permittivity was adjusted based on the measurements in the combined temperature and humidity condition performed in Chapter 3. The permittivities are as follows: $\varepsilon_{r,gel(dry)} = 2.7$, $\varepsilon_{r,gel(humid)} = 4.96$, assuming steady-state. This investigation chose to not adjust the bulk conductivity of the gel due to the noise present in measurements of the parallel resistance R_p in Chapter 3. To facilitate quick and accurate simulations, a meshing strategy based on [214] was used, which is demonstrated in Fig. 5.37. A circular vacuum region with radius (r) 100 mm is applied, centred on the origin, to the edge of which a balloon-voltage boundary condition is applied ($V(r = \infty) = 0$).

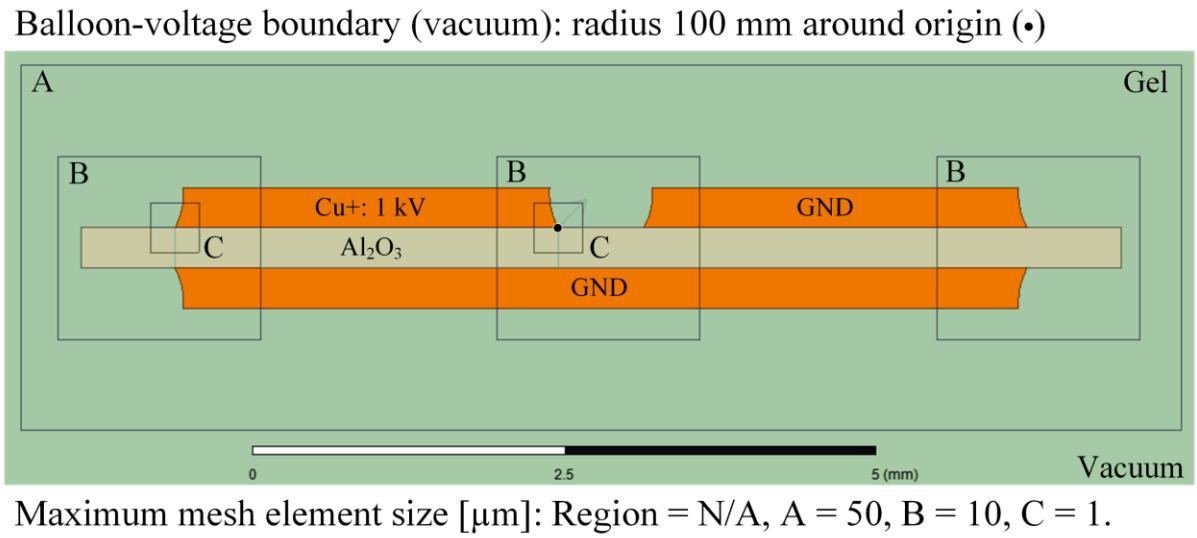

Fig. 5.37 Meshing strategy applied for electrostatic simulation of DBC samples.

The geometries used in these simulations are shown in Fig. 5.38. The air-filled void for case b) was circular, and its diameter was determined by the lack of visible bubbles at the end of the degassing process for samples discussed in § 5.2 at 30 mBar. It is generally acknowledged the human eye can see objects down to about 100 µm in length, which was taken as the maximum spherical diameter of the void. Boyle's law was used to adjust the volume of the sphere once returned to standard pressure, resulting in a diameter of 30 µm for the air-filled void at the triple interface. The void in case c) was

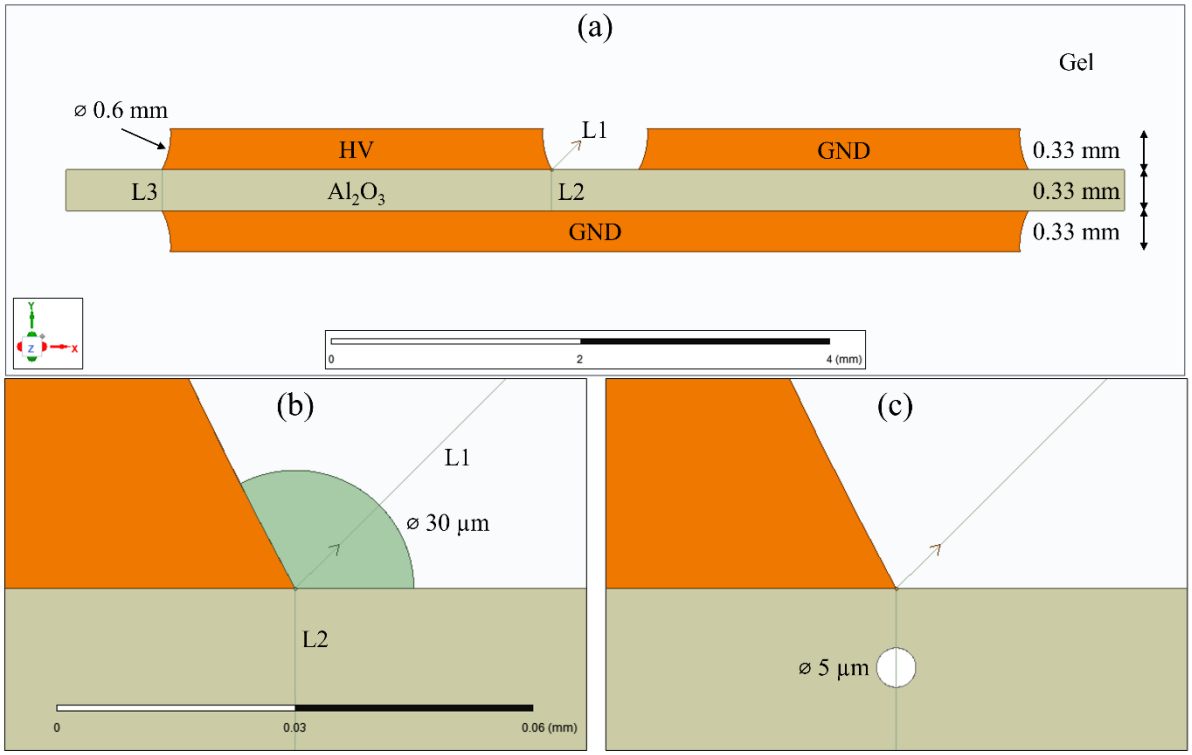

Fig. 5.38 DBC geometries used in electrostatic simulations. (a) whole DBC with no flaw, (b) air-filled void in the gel at the triple interface, (c) air-filled void in the ceramic under the triple interface.

sized to 5 μm in diameter based on SEM imaging of the grain structure of a DBC sample, considering the limitation of mesh sizing in the simulation, and based on the imaging of voids (albeit in AlN) in [258]. The measurement lines L1 and L2 start from the triple interface which is placed at the origin and proceed outward 0.33 mm in accordance with the measured ceramic thickness. L1 proceeds at a 45° angle to the ceramic and L2 proceeds downwards at -90°. The measurement line L3 is similarly placed at the very edge of the triple interface at the exterior metallisation edge of the DBC. As the relationship between the electric field strength and the applied excitation is linear as discussed in [242], a level of 1 kV is used as a representative case. This is applied to the upper-left metallisation only, and the remaining copper elements are held at 0 V in accordance with the testing performed in the previous sections. The field strength along the measurement lines L1–L3 in each condition are shown in Fig. 5.39. In every case, the field strength along each measurement line was reduced in the humid condition over the dry, with a larger reduction closer to the triple interface. According to [160], this would indicate an increase in PDIV due to the absorption of humidity. This is not in agreement with the experimental results showing a slight decrease in PDIV, but does bear similarities to other electrostatic simulation work showing that the field strength can be reduced by adjusting the permittivity of the encapsulation [72], [208], [214]. The slight reduction in measured PD magnitude does support the simulation results. With the inclusion of an air-filled void at the triple interface the field strength there is increased, followed by a steep reduction over a short distance at the void-gel interface. The inclusion of a ceramic void shows both a steep increase and the steep decrease in field strength, as the measurement line passes through both sides of the void. It is possible that these steep gradients indicate increasing potential difference across the void or at the void boundary, which is changed the most in the case of the air-filled void in the gel. Nevertheless, whether in the gel or the ceramic, the presence of a void enhances the local electric field nearby to the triple interface compared to the no-flaw case, which supports the common understanding that defects in the insulation structure increase the likelihood of PD events. It is clear that electrostatic simulation alone is not sufficient to explain both the slightly reduced PDIV for strong PD, and significantly increased PD count for weak PD, and so alternative phenomenological explanations must be sought. These are explored in conceptual terms based on trends in the data and similarly observed phenomena in the literature in § 5.6.

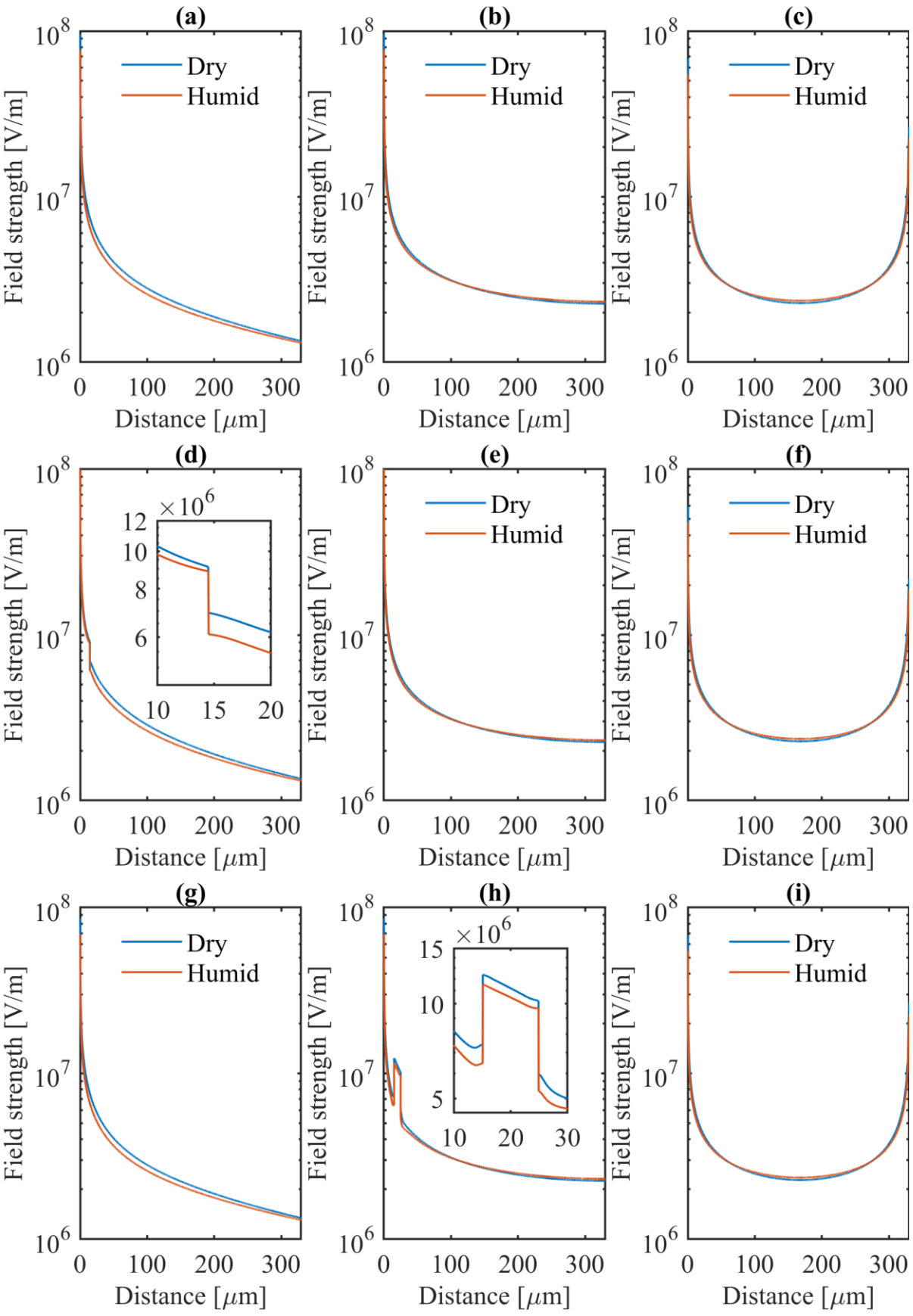

Fig. 5.39 Electric field strengths from electrostatic simulation of DBC geometries with: (a)–(c) no flaw; (d)–(f) an air-filled void in the gel at the triple interface, and; an air-filled void in the ceramic under the triple interface (g)–(i). Measurements are taken along lines L1 (a, d, g), L2 (b, e, h), and L3 (c, f, i) as indicated in Fig. 5.37.

To better show the concentration of the electric field in the voids and influence of moisture absorption at the triple interface outside of the measurement lines, plots of the field strength for each simulation geometry in each condition are shown in Fig. 5.40. The colour bar is adjusted to demonstrate the changes more clearly. The steep change in field strength at the void boundaries is clear, though the accuracy of simulation techniques at such interfaces is questionable.

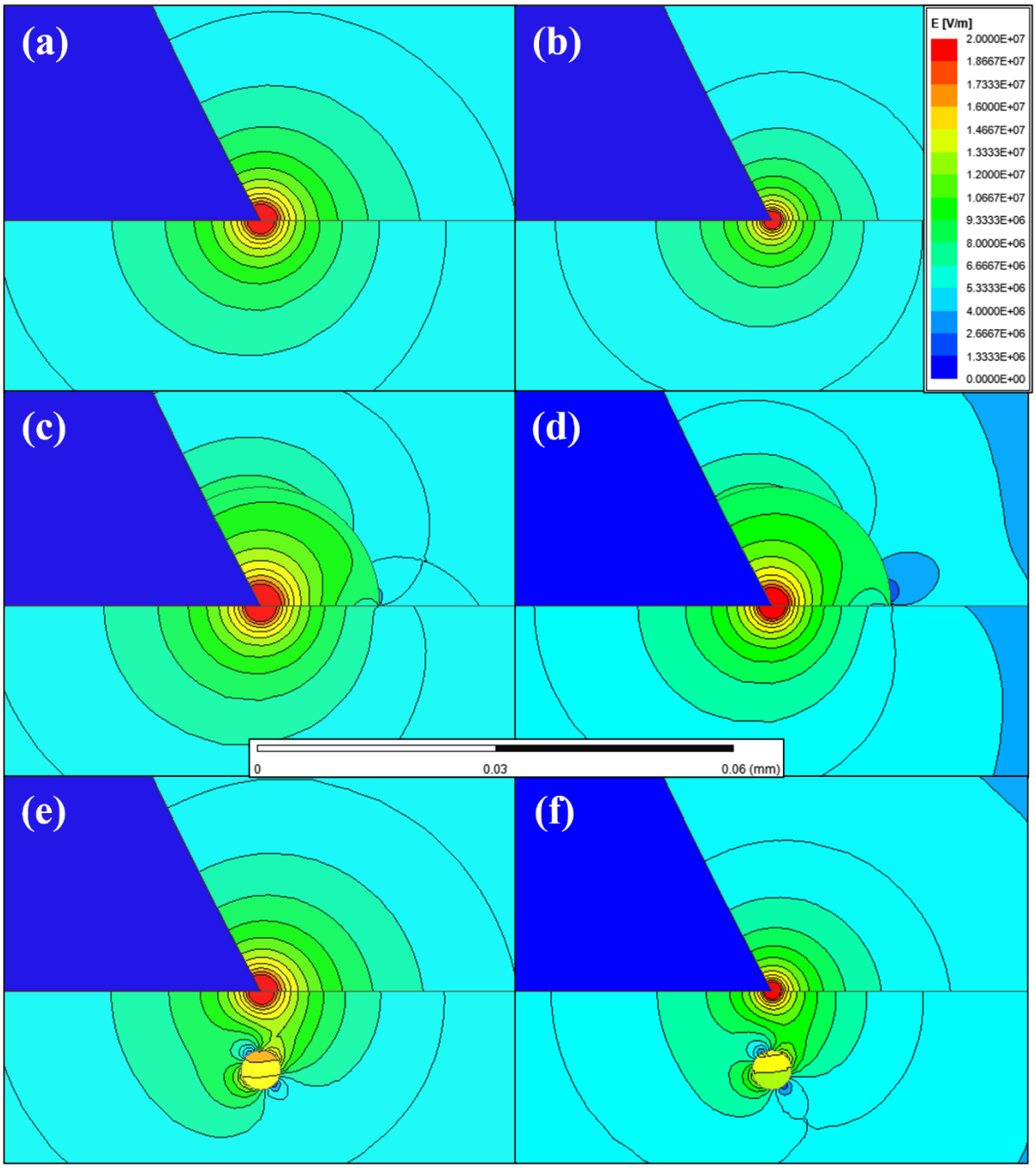

Fig. 5.40 Electric field plots of electrostatic simulations of DBC geometries with various defects in dry (a, c, e) and humid (b, d, f) conditions. (a, b) no flaw, (c, d) air-filled void in gel at triple interface, (e, f) air-filled void in ceramic beneath triple interface. Colour bar adjusted to show electric field concentration more clearly given influence of mesh size.

5.6 Conceptual Origin of PD Related to Amplitude Classification

PD in power modules occurs most often at the triple interface where the ceramic, copper, and gel meet. This arises due to the strength of the electric field in this region due to the geometry of the substrate, which is enhanced by flaws such as copper protrusions, delamination, cracking, or the presence of unfilled voids. PD has been demonstrated before in the literature in a wide range of materials, but concerning power modules it has been identified to occur within the gel and the ceramic of the substrate, or both. The local electric field at the triple interface has components across the lateral trench and through the ceramic, and so both materials are stressed. These regions may each contain air-filled voids: the ceramic through its porous construction, and the gel either through incomplete degassing or by the absorption of moisture which may be vaporised [201]. The experiments performed in this Chapter showed two distinct amplitudes of PD, so it is pertinent to attempt to attribute these groupings to logical origin sites on the DBC sample.

i. Strong PD Origin

Due to the relative lack of variation of strong PD behaviours when compared with weak PD with respect to the high humidity environment, the strong PD group is likely to be attributed to a physical region on the sample where the influence of humidity is limited. In Chapter 3, it has been established that the silicone gel absorbs moisture and that this changes its electrical properties considerably. Therefore, the strong PD group cannot be attributed to the gel. There is no evidence in the literature that even porous ceramic such as the studied Al_2O_3 absorbs moisture in any meaningful way in the conditions investigated. Consequently, the strong PDs observed in this work are most likely ascribed to internal cavities within the ceramic. PDs inside ceramic substrates have been investigated before [188]. It is generally accepted that the probability of PDs within the ceramic is quite low, as most of the literature investigates only those PDs that occur at the triple interface within air filled cavities [201], [205], [259], [260], or spontaneously cavitated voids at nucleation sites at the triple interface. Due to the high field stress, PDs within the ceramic are likely to still occur near to the triple interface. The slight reduction in PD amplitude can be sufficiently explained by the results of the electrostatic simulations in the previous section. Considering only those electrical parameters used in electrostatic

simulation (relative permittivity and bulk conductivity), the electric field strength is expected to reduce slightly for the absorption of moisture by the gel. This is true whether there is no flaw present, an air-filled void in the gel, or an air-filled void in the ceramic. This results in PD of a reduced amplitude owing to the reduced potential difference across the void compared to the dry case. The absorption of humidity in the gel is not known to change the electrical characteristics of the ceramic in any other way, and its influence is therefore likely limited to the reduction of the field strength.

The time lag of strong PD is not influenced in any significant manner by the increased environmental humidity, occurring mainly in the centre, and falling edge of the test pulse. This distribution is in line with some TRPD results in the literature focused on DBC samples [200]. The fact that the PDs do not occur at the rising edge, which is more commonly observed in the literature, could be explained by considering the capacitive divider model illustrated in Fig. 5.41, and modelling the parallel resistances of the system. In this resistive-capacitive divider, the voltage across the void, v_v, can be expressed in terms of the: resistance of the ceramic, R_c; capacitance of the ceramic, C_c; resistance of the void, R_v; capacitance of the void, C_v; and the applied voltage v_{DC} as in (72):

$$v_v = v_{DC}\frac{R_v}{R_c + R_v} + v_{DC}\left(\frac{C_c}{C_c + C_v} - \frac{R_v}{R_c + R_v}\right)\exp\left(-\frac{t}{\tau}\right) \quad [V] \quad (72)$$

where τ is the system time constant given by (73):

$$\tau = (C_c + C_v)\cdot\frac{R_c R_v}{R_c + R_v} \quad [s] \quad (73)$$

The bulk resistance and capacitance (R_b and C_b, respectively) of the ceramic can be neglected from this perspective. Due to the high slew rate during the rising edge, the voltage across the void in the ceramic during this portion of the test pulse corresponds with the ratio of the ceramic capacitance to the total capacitance. During the test voltage plateau, the system progresses to a charging regime determined by the system resistances. Additionally, the time constant is expected to be dominated by the resistance of the ceramic as it is much larger in size than a void. Consequently, the field strength within the void may not exceed its local breakdown strength until well into the test pulse. The absorption of humidity should not change these system parameters in any meaningful way, which could in part

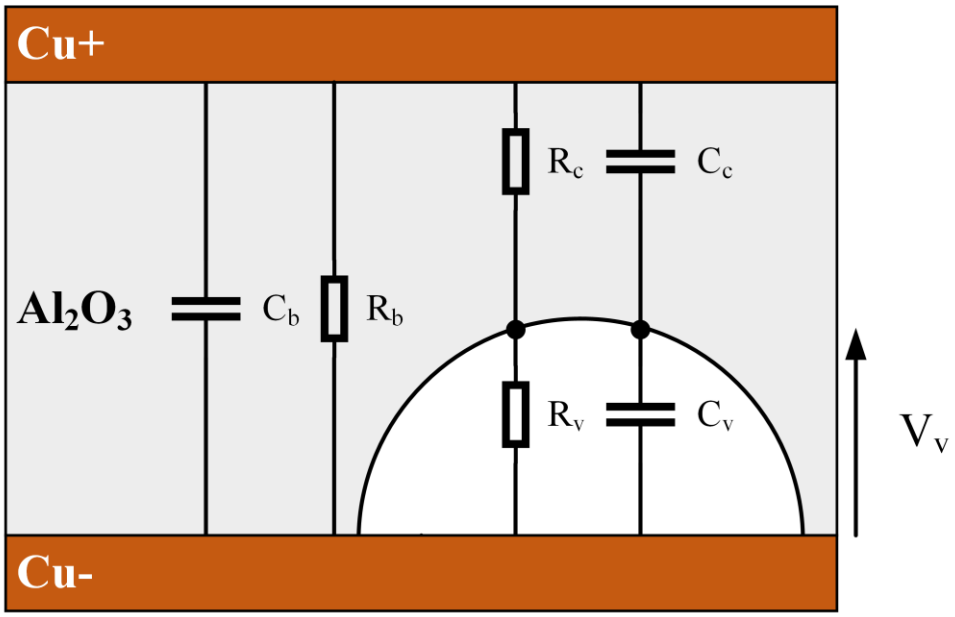

Fig. 5.41 Resistive-capacitive divider model for ceramic insulation in the DBC with an air-filled void.

explain the relative lack of variation of strong PD with humidity. The behaviours of strong PD events can be mapped to the electric fields within the insulation under positive square wave stress by considering the experimental results. This is illustrated diagrammatically in Fig. 5.42 which separates the applied test voltage into 4 intervals: (i), the rising edge; (ii), the voltage plateau until PD; (iii), the voltage plateau after PD; and (iv), the falling edge of the test pulse. This concept is based on a combination of phenomenological explanations for PD processes found in the literature [201], [249], [261], [262]. During (i), no discharges are observed and so either the electric field within the void ($E_{v,pd}$) must not have exceeded its critical value (E_{crit}), or the stochastic time delay for the appearance of an initial electron to begin avalanche has not yet passed. The electric field within the void increases corresponding to the increasing applied electric field ($E_{applied}$) with the rate being dominated by the ratio of the insulation system capacitances. In this region, the actual field within the void is the same as that which would be in the void should no PD occur ($E_{v,no}$), which is superimposed on the void during the entire process: $E_{v,pd(i)} = E_{v,no(i)}$. During the voltage plateau (ii), the field within the void continues to increase towards its DC value, determined by the ratio of the system resistances. According to the experimental results for strong PD this region contains the PPD, so this is where the field within the void exceeds the critical value ($E_{v,pd(ii)} > E_{crit}$) and electron avalanche occurs. Electrons are accelerated to the opposing boundary of the void, leaving behind a net positive charge – in this way, a

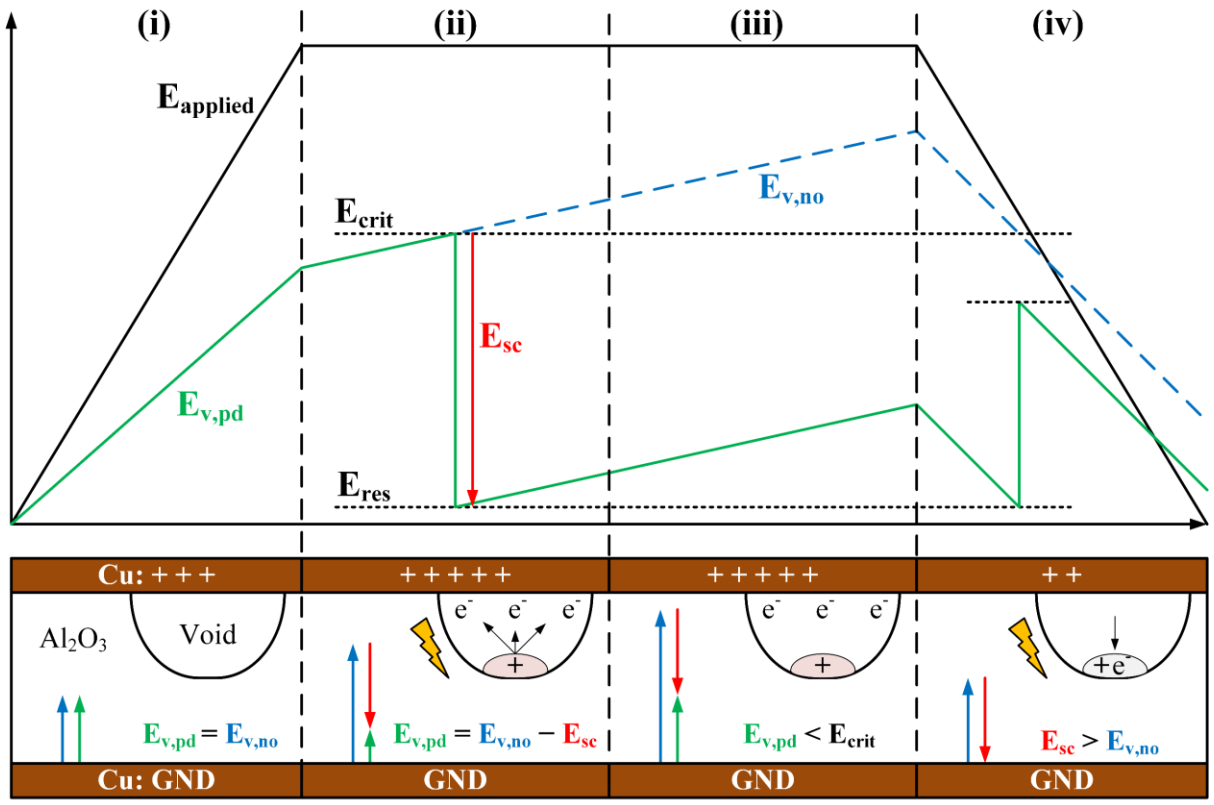

Fig. 5.42 Conceptual mechanism of PD resolved with test pulse, corresponding to experimental results for strong PD during PDIV determination testing.

space charge is developed across the void (E_{sc}) in opposite polarity to the applied field. At the instant PD occurs, the field in the void is reduced to some residual value [262], which can be considered to be negligible: $E_{v,pd(ii)} = E_{res} = E_{v,no(ii)} - E_{sc}$. During the remainder of the voltage plateau (iii), the space charges are sufficient to keep the field within the void below the critical value and so PD does not occur ($E_{v,pd(iii)} < E_{crit}$) [261]. Finally, the test voltage falls during the last region (iv), and at some point, either during the falling edge or shortly thereafter, the portion of the applied field that exists across the void is no longer sufficient to halt the space charges from recombining ($E_{sc} > E_{v,no(iv)}$), and SPD occurs. The SPD has a lower magnitude than the PPD [200], which in this case could be caused by small losses in the space charges. In the strong PD case, it is most common to see a single PPD followed by a single SPD than any other combination of these events, and so the space charges remaining after initial recombination cause no further PD events of note. A similar concept for falling-edge PD is presented in [263], where the field across the void inverts polarity as the excitation voltage falls to zero, due to the presence of space charges. However, this would correspond to discharges after the excitation voltage has reached zero, which is not generally observed in the present results.

ii. Weak PD Origin

In the dry case, the weak PD are primarily concentrated around the rising and falling edges of the test pulse (Fig. 5.34 (a)), in line with much of the current research on power module substrates in gel encapsulation [249], [261]. The count per 100 tests at each fixed voltage is low when compared with the humid case (Fig. 5.33), indicating that the probable PDIV of samples is about 3500 V or slightly lower. In the humid case, many PDs are counted even at 3500 V, indicating the true PDIV of these samples for weak PD in high humidity is much lower than in the dry environment. Across all test voltages the number of PDs counted was significantly higher in the humid case than the dry case, with the count increasing with increasing test voltage as expected. Consequently, the results highlight the clear influence of increased ambient humidity on the weak PD behaviours and are hence attributed to a physical region on the sample where the absorption of moisture is probable. The electrical characteristics of the silicone gel are known to be strongly influenced by ambient humidity, and this was previously linked to absorption processes by fitting the increase in relative permittivity of the gel to well-known diffusion models in Chapter 3. With this observation and considering the focus of most of the PD research in the literature, the weak PD category must be attributed to the gel at the triple interface. The depth of the gel for the investigated samples was 3 mm from the surface of the DBC, and the gel's electrical properties are expected to have changed significantly due to moisture absorption over the 24 hour periods investigated, based on previous experimentation and similar work in the literature [42]. The cause of PD count increase in the humid case is not trivial to explain and may be a combination of several processes:

i. It is known that over a long enough period, the insulation quality of the gel is reduced due to degradation by hydrolysis of the siloxane bonds and hence a reduction in the degree of crosslinking [79]. This results in a critical field in the gel that is reduced in the humid condition over the dry, which indicated by the void charging dynamics proposed in (72) could result in PD that occurs more rapidly and more often during a single test pulse. The duration of the high humidity environment is not long enough in this work to cause any significant degradation via this mechanism.

ii. The insulation quality of the gel may be negatively impacted by PD due to the DEA process, which can occur at even low energies [238], although the effect is implied in the literature to be limited.

iii. The presence of space charges due to a discharge event is less of an inhibitor to PD recurrence in the humid case due to the increased conductivity of the void boundary, i.e., the gel. The lifetime of space charges in this instance may be very small compared to those trapped within the solid ceramic insulation. Additionally, it is understood that the expansion of a microgas void during PD causes the gel insulation to compress with a corresponding force opposing the space charge separation [201], which could aid in space charge decay rate.

iv. Humid air is lighter than dry air. The primary composition of dry air is about 78% nitrogen in the form of N_2, 21% oxygen in the form of O_2, and a mixture of other gases with content less than 1% each. The molar masses are 28 g/mol and 32 g/mol for nitrogen and oxygen molecules in air, respectively. Humid air contains a higher degree of water molecules (H_2O, with mass approximately 18 g/mol) for the same gas volume, which are lighter and displace the heavier oxygen and nitrogen molecules. A reduction in air density is understood to reduce the breakdown voltage for parallel conductors in a homogeneous field according to Paschen's law. As the dry air of the void in the gel is diffused with water molecules, it is possible that their influence is to reduce the critical electric field of the void. This assumes that the displaced nitrogen and oxygen are accommodated into the remainder of the silicone gel structure.

v. The Townsend secondary ionisation coefficient (γ) forms a significant part of the breakdown voltage of gases under Paschen's law according to (66). Previous research has shown an increase in γ due to moisture adsorption on a conductive surface [264], which may also be the case at the triple interface in a high humidity environment. The influence of the increase in γ is illustrated in Fig. 5.43, using values from [237] with $\gamma = 7 \times 10^{-3}$ for the dry case to give the widely accepted minimum breakdown voltage in dry air of 327 V, and using the high humidity (85% RH) value $\gamma = 5 \times 10^{-2}$ presented in [264]. The impact is a clear reduction in the breakdown voltage which is more notable over the small values for $p \times d$.

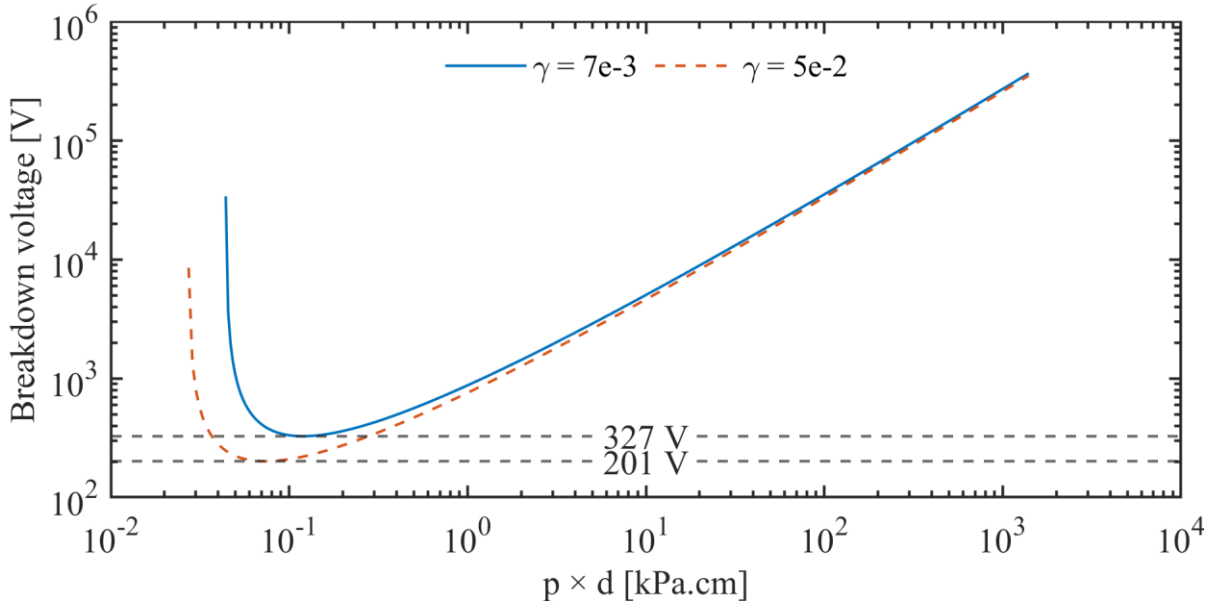

Fig. 5.43 Paschen's curves using values from [237], with $\gamma = 7 \times 10^{-3}$ for the dry case and $\gamma = 5 \times 10^{-2}$ for the humid case at 85% RH [264].

With the above considerations, a gradual understanding of the TRPD results shown in Fig. 5.34 is gained. Humidity demonstrably increases the rate at which weak PD recurs during a single voltage pulse, and there are indications of a reduced PDIV also. The time-alignment of weak PD events spreads out across the test pulse in the high humidity environment, while occurring mainly at commutation edges in the dry case.

5.7 Conclusions

This chapter has highlighted a significant weakness in traditional standards-based qualification of power modules which connect all terminals of a module together and apply electrical stress between there and the baseplate. This provides only sufficient stress for the vertical insulating elements, primarily the ceramic portion of the substrate. The gradual degradation of the silicone gel due to laterally occurring PD within the trench could result in early failures. If traditional qualification tests are used for modules intended for use in WECS, especially in OWT applications, those with significant weakness to electrical stress in the lateral direction may be erroneously qualified for use.

Through PDIV determination testing of gel encapsulated DBC substrates taken from a commercial power module, two groups of PD events were discovered, and were categorised as strong PD and weak PD owing to their relative amplitudes in the UHF measurement. The characteristics of strong PD changed little with an increase in the ambient humidity and are attributed to voids within the ceramic

about the triple interface. The weak PD were not trivial to detect and required the gathering of a larger dataset at fixed test voltages, with postprocessing techniques used to count the occurrence of PD within the test pulses. The count of PD was increased significantly in the humid environment over the dry, and consequently the weak PD category is consequently attributed to air-filled voids within the gel at the triple interface.

The strong PD primarily result due to voids or microfractures in the ceramic, which may appear due to improper installation or thermal stresses. These should easily be identified via routine testing and qualification processes already recommended by the standards. The weak PD are not trivial to detect, and in any case may not be generated with sufficient quantity or amplitude under traditional qualification test stress for adequate detection. Due to DEA-driven degradation of the silicone gel, the weak PD category is expected to cause significant irreparable reduction in insulation quality about the triple interface and is exacerbated by the absorption of humidity due to the increased PD count.

The current trend of PD mitigation within power modules is based on reduction of the electric field local to the triple interface, either by varying the geometry or by adding filler components to the silicone gel in some way. These approaches must also sufficiently manage the negative impact of moisture absorption into the power module, as it has been shown that the electric field local to the triple interface is only part of the picture concerning PD. There is yet little consideration given towards this aspect in the literature, which highlights this topic as the focus of future research. Additionally, from the perspective of power module OEMs, there is a clear need for the development and implementation of better standards for the evaluation of power module substrates which take into account environments and voltage stresses representative of field operation.

Chapter 6: Conclusions and Future Work

6.1 Influence of High Humidity Environment on Electrical Properties of Silicone Gel Encapsulant

This chapter investigated the change due to ambient environment in the electrical properties of silicone gel encapsulation material. Experiments subjected cured gel samples to a variety of environmental stresses with varying temperature-only, humidity-only, and combined temperature and humidity conditions. IDC sensors placed beneath freshly cured silicone gel were used to evaluate the influence of moisture absorption on the parameters of a lossy dielectric model. For high temperature stress alone, the parameters changed by only a small amount. During this test, the presence of erroneous humidity increases revealed the strong temperature sensitivity of the coefficient of diffusion for the gel, which likely reduces the reliability of the results. This was backed up by the humidity-only testing, which held a fixed ambient temperature and increased the ambient humidity in a stepwise fashion. The maximum parameter increases in the end of setpoint values from 30% to 90% RH were greater than those observed in the temperature-only testing. The combined temperature and humidity stress testing showed by far the most growth in the measured parameters. The initial increase rate appeared strongly correlated with the gel thickness, with the expected steady-state values less so. The test followed on with dry-out stages, removing first the high-humidity stress and then the high-temperature stress, showing that these parameter changes are likely fully recoverable, but may be limited in cooler environments due to moisture storage in thicker gels. The loss factor measurements were based on parallel resistance estimated from the impedance measurement, and likely suffered from inaccuracy due to the low source level of the VNA used. The large magnitude of sample resistance change due to moisture absorption was also a likely confounding factor. Relative permittivity results were discussed in the context of common diffusion models for the 5 mm and 10 mm thickness samples, showing that the gel studied (Wacker SilGel 612) behaved in a non-Fickian manner, which could be adequately modelled by the Langmuir diffusion model. Though this has been observed in HTV silicone rubbers, this is the first evaluation of diffusion in silicone gel using the Langmuir model. Additionally, the orientation of samples representative of PEMs is shown to influence moisture absorption dynamics, highlighting a potential for improvements in humidity-robust converter designs.

6.2 Investigations on IGBT Performance in High Humidity Environment

Whereas most humidity-related research on PEMs is concerned with only lifetime measures and accelerated stress testing, this chapter aimed to ascertain the influence of humid environments on switching performance. This was motivated by the strong influence of humidity on the electrical properties of the primary encapsulant observed during the previous chapter. The input capacitance of a HV-IGBT half bridge module was measured under 25 V bias in situ of a high-humidity environment, showing only a ~13 pF increase (+0.016%) after 26 h of harsh environment storage. This was greater than estimations based on simulations of a representative geometry performed in Ansys Q3D Extractor (+4.72 pF in C_{ies} of bottom IGBT). The switching performances of three types of HV-IGBT half bridge modules were evaluated using a bespoke DPT setup. The limited C_{ies} increases due to moisture absorption in the gel with respect to the chip input capacitance, or influence of moisture otherwise, was observed to have no noticeable impact in the switching performances. However, a notable increase in V_{GE} oscillation was observed, which raises concerns about spurious switching and EMC.

6.3 Partial Discharge Characteristics of Gel-encapsulated DBC samples in High Humidity Environment

Building on the previous experimental chapters, this chapter aimed to help answer the question of module reliability through PD testing. DBC substrates were taken from PEMs typical of those chosen for converters in OWTs, and subjected to a rigorous cleaning process which was verified by SEM-EDS analysis. Fresh silicone gel was cured over top of these substrates to provide samples for PD testing. Samples were connected to the HV source in an atypical fashion compared to recommendations in current standards, which have been discussed as insufficient to represent field operation in the literature. In this testing, the configuration was such that the electrical stress was across both the lateral trench in the top copper and through the ceramic, while in the standards the recommendation is to bond all top conductors to HV and test only through the ceramic. These experiments subjected the samples to HV pulses representative of hard switching in the OWT converter application in a high-temperature high-humidity environment (85 °C / 85% RH), and studied the characteristics of the ensuing PD. PDIV, which is the main metric of PD-ruggedness, was initially observed to vary little due to the absorption

of moisture within the gel. However, several low-amplitude discharges were observed during the PDIV determination testing, prompting further investigation. A statistics-based test was devised using a MMSD approach with a large test count to separate weak discharges from commutation and background noise. The characteristics of this weak category of PD were shown to be strongly influenced by humidity. Both the PD count over 100 tests and repetition rate within a single test were significantly increased by harsh environment and increasing test voltage. No strong PD events were observed during investigation of the weak PD, indicating that the weak PD had a lower PDIV than strong PD. This highlights a reliability concern as even low-amplitude PD could degrade the insulation quality of the gel through the DEA process. Due to the different behaviours of the two PD categories with respect to the high humidity environment, they are attributed to different locations on the substrate. The strong PD are hardly changed by humidity, and hence should occur in a location where its influence is limited. They are consequently attributed to microvoids or cracks within the ceramic portion of the DBC. The weak PD varied very strongly with the ambient humidity level and hence likely arise from a location where moisture has a large influence. They are attributed to the triple interface of the DBC and gel, likely within air- or moisture-filled voids. Air-filled voids could also be spontaneously generated due to the PD process. Phenomenological explanations using the trends in the results with respect to TRPD and discharge amplitude are used to validate the attribution of discharge categories to their respective conceptual origins.

6.4 Duration of Experiment Design and Implementation

Reliability-oriented testing of PEMs and their constituent materials is a time intensive process. Not only must test rigs and experimental procedures designed to meet requirements laid out in standards be conceived and fabricated, but the test samples must also be prepared. Due to the nature of reliability testing when degradation and test-to-failure is required, the tests themselves can take a considerable amount of time to be performed. An estimate of the time taken for the experimental work carried out and presented in this thesis is stated in Table 6.1, providing future research a platform for continued work. Note that during the early stages of the research especially, a substantial amount of time was dedicated to literature survey, administrative tasks, and managing the influence of COVID-19.

TABLE 6.1
ESTIMATE OF TIME TAKEN IN THE UNDERTAKING OF THIS RESEARCH

Chapter	Task	Time taken [months]
3	Preliminary investigations	1
3	Sample design	½
3	Sample fabrication	½
3	Experiment rig setup	2
3	Experiment	6
4	Experiment rig setup	3
4	Experiment	8
5	Sample fabrication	4
5	Experiment rig setup	4
5	Experiment	10

Note that Table 6.1 is not an exhaustive list of all work undertaken in the pursuit of this research.

6.5 Future Work

6.5.1 Furthering the Understanding of Moisture Influence on Silicone Gel Insulation Systems with Respect to Electrical Parameters

In this thesis, no consideration is given to the presence of additional passivation measures within PEMs, such as polyimide films or glass coatings around the field-stop and guard ring regions of the semiconductor die. These films are generally thin compared to the gel coating, and hence their impact on the capacitance at the die attach layer should be limited. Nevertheless, their inclusion in such analyses is a required next step in the full understanding of the humidity-varying electrical properties of the insulation structure.

The electrical property most salient to insulation system health is its breakdown voltage. This was not thoroughly investigated in this thesis, and so a complete characterisation of how this varies with respect to a high-humidity environment should be performed. Since the gel capacitance has been shown to increase in this work, the moisture level at the die attach layer may be monitored as in [156], [223], [229]. This would give an indication of breakdown voltage such that active snubbers or control strategies may be devised to limit overvoltages with the potential of breakdown in the humid environment.

WTs may cease operation for long periods of time due to lack of demand or fault isolation. Additionally, during the commissioning phase, the storage of converter components in the high-humidity environment is not unlikely. Consequently, modules may be forced to operate after a long

period of moisture absorption. This thesis provided the beginnings of investigations into the dry-out capabilities of silicone gel, such that changes in its electrical properties may be recovered. A more sophisticated analysis is expected to reduce the rapid failure of devices after long downtimes.

This thesis chose Wacker SilGel 612 as a representative for silicone gels as a whole, to limit test dimensions. Though RTV-2 silicone gels are mostly alike in makeup, a comparison of gels from different manufacturers will aid module and converter designers with respect to humidity-robustness. Similar approaches are outlined in [78], which presents a characterisation methodology for gel dielectric properties. Additionally, the influence of fillers or filled trench coatings such as $BaTiO_3$ or ATH on the die attach layer electrical properties is not investigated. These, or other, coatings are likely to be used in future HV PEM designs [213], [214], [257], [265], but their influence with respect to moisture is not yet rigorously characterised, and is a potential avenue for future work.

6.5.2 Stronger Definition of Degradation of Power Module Switching Performance Due to Ambient Moisture

Although consideration is given to the combined stress of switching and high humidity environment in the literature [149], [150], these approaches focus on device lifetime (N_f). No characterisation of the altered switching performance of devices due to humidity-driven degradation has yet been performed. A combination of DPT and H3TRB testing could reveal opportunities for intelligent gate-drive controls which are able to prolong device lifetimes and increase overall system reliability. In conjunction with this, precise measurements of electrical parameters such as $V_{GE(th)}$ and $V_{CE(on)}$ ought to be included in the search of HSEPS. In this way control schemes can be devised to maintain a negative humidity gradient from the ambient to die attach layer, avoiding moisture condensation condition.

This work chose to isolate the module and drive, placing only modules within the environment chamber for testing. This allowed a clearer interpretation of the results as any changes were strictly due to the influence of moisture on the module but did cause difficulties due to the parasitics introduced by requisite cabling. A close-coupled module and drive arrangement is much more typical of field operation and is a logical iteration of the research. Degradation of components of the gate drive and associated circuitry could be monitored in the harsh environment, and evaluation of conformal coatings

for the driver could be investigated. The results of DPT on modules in high-humidity environment showed an increase in the oscillation of V_{GE}. Though slight, this increase could potentially reduce headroom in already tight design constraints, and so should be more thoroughly researched.

The scope of this thesis was limited to environments with varying temperature and humidity only, but in field operation of OWTs there is also the presence of contaminant species in sea air. As corrosion is exacerbated by these contaminants, their inclusion in this research is important and provides an opportunity for future research. This could include periods of storage in a contaminated environment with varying durations, and confirmation of the migration of the ionic species through the gel to the die attach layer by techniques such as Fourier transform infrared spectrometry or SEM-EDS. A logical humidity mitigation measure may be the application of hermetic sealant for power modules, which could be performed as a production step by the OEM or as part of the installation on site. Any additional measure brings additional costs, and so a comparative feasibility analysis of this approach with the implementation of improved passivation techniques is warranted.

6.5.3 Rigorous Characterisation of Moisture Influence on PD Characteristics for Substrates and PEMs

The results of PD testing on gel-encapsulated DBC substrates in this thesis highlight two distinct categories of PD, categorised by their amplitude. Those above 100 mVpp in the UHF measurement are named strong PD, and those below are named weak PD. Phenomenological explanations are used in conjunction with trends in the data to argue the attribution of these categories to either the ceramic portion of the DBC or the triple interface, respectively. This work requires experimental validation of these attributions, which could be performed with bespoke samples allowing only one or the other of the supposed PD origin sites. Optical measurements could also be included to further verify the PD locations, although imaging devices capable of operating properly in the high-humidity environment are not generally available and so this will require additional care to be taken in the design of the experiment.

PD is a damaging phenomenon, reducing insulation quality and hence device lifetimes. If the attribution of the two supposed categories of PD to their conceptual origin sites can be verified, then

their influence on device lifetimes should be evaluated. This testing would also require the inclusion of a comparison between PD-driven degradation in both the dry and humid conditions. Leakage current and breakdown voltage of the insulation are expected to be the primary metrics representing insulation quality in this future work. The emerging trend of PD mitigation techniques has two main approaches: variation of the substrate geometry, or of the trench coating material. An approach seeing much success is the application of fillers in the gel such as ATH or $BaTiO_3$, or the application of field-dependent conductivity or permittivity (FDC, FDP) coatings about the triple interface, which could include SiC as a filling agent. These approaches are not yet characterised from a PD perspective when subjected to the high humidity environment, which is a clear opportunity for additional research.

This thesis researched only substrate samples with the DBC structure, using Al_2O_3 ceramics. Other substrate technologies such as AMB, or utilising AlN or Si_3N_4 ceramic are commercially available and should be tested in a similar manner with respect to the presence of ambient humidity. This could provide additional tools for humidity-robust converter designs, and in the long term form part of the solution facilitating the shift to a net-zero emissions economy.

References

[1] United Nations Department of Economic and Social Affairs, “World Population Prospects 2022 - Summary of Results,” New York, USA, 2022.

[2] International Energy Agency (IEA), International Renewable Energy Agency (IRENA), United Nations Statistics Division (UNSD), World Bank Group (WB), and World Health Organisation (WHO), “Tracking SDG7: The energy progress report (2019),” Washington DC, 2019. [Online]. Available: https://www.irena.org/newsroom/pressreleases/2019/May/More-People-Have-Access-to-Electricity-Than-Ever-Before

[3] International Energy Agency (IEA), “Electricity 2024,” Paris, 2024. [Online]. Available: https://www.iea.org/reports/electricity-2024

[4] V. Smil, *Energy Transitions: Global and National Perspectives*, 2nd ed. Praeger, 2016.

[5] M. Höök and X. Tang, “Depletion of fossil fuels and anthropogenic climate change—A review,” *Energy Policy*, vol. 52, pp. 797–809, 2013, doi: 10.1016/j.enpol.2012.10.046.

[6] K. A. Dahl, M. F. Fitzpatrick, and E. Spanger-siegfried, “Sea level rise drives increased tidal flooding frequency at tide gauges along the U.S. East and Gulf Coasts: Projections for 2030 and 2045,” *PLoS One*, vol. 12, no. 2, pp. e0170949–e0170949, 2017, doi: 10.1371/journal.pone.0170949.

[7] J. A. Duran-encalada, A. Paucar-caceres, E. R. Bandala, and G. H. Wright, “The impact of global climate change on water quantity and quality: A system dynamics approach to the US–Mexican transborder region,” *Eur. J. Oper. Res.*, vol. 256, no. 2, pp. 567–581, 2017, doi: 10.1016/j.ejor.2016.06.016.

[8] X. Li, Y. Li, and G. Li, “A scientometric review of the research on the impacts of climate change on water quality during 1998-2018,” *Env. Sci Pollut Res Int*, vol. 27, no. 13, pp. 14322–14341, 2020, doi: 10.1007/s11356-020-08176-7.

[9] H. Kong, J. C. L. Chan, and K. S. Liu, “Global Warming and Western North Pacific Typhoon Activity from an Observational Perspective,” *J. Clim.*, vol. 17, no. 23, pp. 4590–4602, 2004, doi: 10.1175/3240.1.

[10] Y. Malhi, J. T. Roberts, R. A. Betts, T. J. Killeen, W. Li, and C. A. Nobre, “Climate Change, Deforestation, and the Fate of the Amazon,” *Science (80-.).*, vol. 319, no. 5860, pp. 169–172, 2008, doi: 10.1126/science.1146961.

[11] United Nations, “Paris agreement,” 2015.

[12] C. Figueres, “3 Years To Safeguard Climate 2017,” 2020.

[13] International Energy Agency (IEA), “World Energy Outlook 2023,” Paris, 2023.

[14] J. Moore and N. Bullard, “BNEF Executive Factbook,” 2021. [Online]. Available: https://data.bloomberglp.com/promo/sites/12/678001-BNEF_2020-04-22-ExecutiveFactbook.pdf?link=cta-text

[15] S. Rahmstorf and A. Levermann, “2020 The Climate Turning Point,” Potsdam, 2020.

[16] Agora Energiewende and Ember, “The European Power Sector in 2020: Up-to-Date Analysis on the Electricity Transition,” 2020. [Online]. Available: www.sandbag.org.uk%0Awww.agora-energiewende.de

[17] U.S. Energy Information Administration, “Electric Power Monthly, February 2021,” 2021.

[18] U.S. Energy Information Administration, “Annual Energy Review 2011,” 2012.

[19] International Energy Agency, “Global Energy Review 2020,” 2020. doi: 10.1787/a60abbf2-en.

[20] Energy Dashboard, “Energy Dashboard - Historical.” Accessed: May 02, 2024. [Online]. Available: https://www.energydashboard.co.uk/historical

[21] UK Department for Energy Security and Net Zero, “National Statistics - Energy Trends March 2024,” London, 2024. [Online]. Available: https://www.gov.uk/government/statistics/energy-trends-section-6-renewables

[22] UK Department for Business and Trade, “Offshore Wind,” 2024. [Online]. Available: https://www.great.gov.uk/international/content/investment/sectors/offshore-wind/

[23] S. Yang, A. Bryant, P. Mawby, D. Xiang, L. Ran, and P. Tavner, “An Industry-Based Survey of Reliability in Power Electronic Converters,” *IEEE Trans. Ind. Appl.*, vol. 47, no. 3, pp. 1441–1451, May 2011, doi: 10.1109/TIA.2011.2124436.

[24] K. Fischer *et al.*, “Reliability of Power Converters in Wind Turbines: Exploratory Analysis of Failure and Operating Data From a Worldwide Turbine Fleet,” *IEEE Trans. Power Electron.*, vol. 34, no. 7, pp. 6332–6344, 2019, doi: 10.1109/TPEL.2018.2875005.

[25] K. Fischer, M. Steffes, K. Pelka, B. Tegtmeier, and M. Dörenkämper, “Humidity in Power Converters of Wind Turbines—Field Conditions and Their Relation with Failures,” *Energies*, vol. 14, no. 7. 2021. doi: 10.3390/en14071919.

[26] K. Pelka and K. Fischer, “Field-data-based reliability analysis of power converters in wind turbines: Assessing the effect of explanatory variables,” *Wind Energy*, vol. 26, no. 3, pp. 310–324, Mar. 2023, doi: https://doi.org/10.1002/we.2800.

[27] O. Alkul, D. Syed, and S. Demirbas, “A Review of Wind Energy Conversion Systems,” in *2022 10th International Conference on Smart Grid (icSmartGrid)*, 2022, pp. 72–77. doi: 10.1109/icSmartGrid55722.2022.9848755.

[28] C. J. Oppedahl and M. E. Tarduno, “Wind Energy Conversion,” in *Harvard Environmental Law Review*, 1st ed., Cambridge, Massachusetts: Harvard Law School, 1981, pp. 431–450. doi: 10.1201/9781315374192.

[29] J. Fadil, Soedibyo, and M. Ashari, “Performance comparison of vertical axis and horizontal axis wind turbines to get optimum power output,” in *2017 15th International Conference on Quality in Research (QiR) : International Symposium on Electrical and Computer Engineering*, 2017, pp. 429–433. doi: 10.1109/QIR.2017.8168524.

[30] A. A. Salem, A. H. K. Alaboudy, and H. A. Gabbar, “Realization of MPPT of PMSG-Based Wind Turbines Using New MPPT Indices,” in *2019 IEEE 7th International Conference on Smart Energy Grid Engineering (SEGE)*, 2019, pp. 315–320. doi: 10.1109/SEGE.2019.8859935.

[31] General Electric (GE), “World’s most powerful offshore wind platform: Haliade-X.” Accessed: Jun. 20, 2021. [Online]. Available: https://www.ge.com/renewableenergy/wind-energy/offshore-wind/haliade-x-offshore-turbine

[32] Dogger Bank Wind Farm, “GE’s Haliade-X 14MW turbine to debut at Dogger Bank C - Press Release.” Accessed: Jun. 20, 2021. [Online]. Available: https://doggerbank.com/press-releases/ges-haliade-x-14mw-turbine-to-debut-at-dogger-bank-c/

[33] Vestas, “Vestas V236-15.0 MW™.” Accessed: May 09, 2024. [Online]. Available: https://www.vestas.com/en/products/offshore/V236-15MW

[34] SKF Wind News, “The world’s most powerful wind turbine – Mingyang’s MySE 22MW.” Accessed: May 09, 2024. [Online]. Available: https://windfarmmanagement.skf.com/the-worlds-most-powerful-wind-turbine/

[35] N. Nguyen, S. Almasabi, and J. Mitra, “Capacity Credit Evaluation of Wind Farm Considering Impact of Turbine Hub Level,” in *2019 North American Power Symposium (NAPS)*, 2019, pp. 1–6. doi: 10.1109/NAPS46351.2019.9000310.

[36] F. Blaabjerg, K. Ma, and D. Zhou, “Power electronics and reliability in renewable energy systems,” *ISIE*. IEEE, pp. 19–30, 2012. doi: 10.1109/ISIE.2012.6237053.

[37] V. Yaramasu, B. Wu, P. C. Sen, S. Kouro, and M. Narimani, “High-power wind energy conversion systems: State-of-the-art and emerging technologies,” *Proc. IEEE*, vol. 103, no. 5, pp. 740–788, 2015, doi: 10.1109/JPROC.2014.2378692.

[38] A. Mansouri, A. El Magri, R. Lajouad, I. El Myasse, E. K. Younes, and F. Giri, “Wind energy based conversion topologies and maximum power point tracking: A comprehensive review and analysis,” *e-Prime - Adv. Electr. Eng. Electron. Energy*, vol. 6, p. 100351, 2023, doi: https://doi.org/10.1016/j.prime.2023.100351.

[39] C. Zorn *et al.*, “Field-Data based Lab Testing of a Wind-Energy Power Converter System: Insights into Cabinet and IGBT-Module Microclimates,” in *2023 25th European Conference on Power Electronics and Applications (EPE’23 ECCE Europe)*, 2023, pp. 1–10. doi: 10.23919/EPE23ECCEEurope58414.2023.10264328.

[40] P. Drexhage and S. Häuser, “SEMIKRON AN 16-001 - Effect of Humidity and Condensation on Power Electronics Systems,” Nuremberg, 2022. [Online]. Available: https://www.semikron-danfoss.com/service-support/downloads/detail/semikron-application-note-effect-of-humidity-and-condensation-on-power-electronics-systems-en-2022-01-11-rev-01.html

[41] ABB Ltd., “System description and start-up guide - ACS800-67 wind turbine converters,” Zurich, 2017.

[42] E. Kolbinger, F. Wuest, M. v. Dijk, S. Trampert, and K. Lang, “An approach for failure prediction in H3 TRB-tests,” in *2019 22nd European Microelectronics and Packaging Conference & Exhibition (EMPC)*, 2019, pp. 1–5. doi: 10.23919/EMPC44848.2019.8951836.

[43] P. W. Carlin, A. S. Laxson, and E. B. Muljadi, “The history and state of the art of variable-speed wind turbine technology,” *Wind Energy*, vol. 6, no. 2, pp. 129–159, 2003, doi: 10.1002/we.77.

[44] B. J. Baliga and S. Carlos, “Enhancement- and depletion-mode vertical-channel m.o.s. gated thyristors,” *Electron. Lett.*, vol. 15, no. 20, pp. 645-647(2), Sep. 1979, [Online]. Available: https://digital-library.theiet.org/content/journals/10.1049/el_19790459

[45] B. J. Baliga, M. S. Adler, P. V Gray, R. P. Love, and N. Zommer, “The insulated gate rectifier (IGR): A new power switching device,” in *1982 International Electron Devices Meeting*, 1982, pp. 264–267. doi: 10.1109/IEDM.1982.190269.

[46] B. J. Baliga, “Fast-switching insulated gate transistors,” *IEEE electron device Lett.*, vol. 4, no. 12, pp. 452–454, 1983, doi: 10.1109/EDL.1983.25799.

[47] V. K. Khanna, *The Insulated Gate Bipolar Transistor IGBT Theory and Design*. NJ: Wiley-Interscience, 2003.

[48] B. J. Baliga, “Switching speed enhancement in insulated gate transistors by electron irradiation,” *IEEE Trans. Electron Devices*, vol. 31, no. 12, pp. 1790–1795, 1984, doi: 10.1109/T-ED.1984.21790.

[49] N. Iwamuro and T. Laska, “IGBT History, State-of-the-Art, and Future Prospects,” *IEEE Trans. Electron Devices*, vol. 64, no. 3, pp. 741–752, 2017, doi: 10.1109/TED.2017.2654599.

[50] Infineon Technologies AG, “IGBT Modules.” [Online]. Available: https://www.infineon.com/cms/en/product/power/igbt/igbt-modules/

[51] J. Millán, P. Godignon, X. Perpiñà, A. Pérez-Tomás, and J. Rebollo, “A Survey of Wide

Bandgap Power Semiconductor Devices," *IEEE Trans. Power Electron.*, vol. 29, no. 5, pp. 2155–2163, 2014, doi: 10.1109/TPEL.2013.2268900.

[52] S. Yerra, H. S. Krishnamoorthy, and G. S. Kulothungan, "Simplified Gate Driving Strategy for GaN-Based Multi-level Buck Converters Operating at MHz Switching Frequencies," in *2021 IEEE Applied Power Electronics Conference and Exposition (APEC)*, 2021, pp. 735–740. doi: 10.1109/APEC42165.2021.9487118.

[53] D. Yan and D. B. Ma, "A Monolithic GaN Power IC With On-Chip Gate Driving, Level Shifting, and Temperature Sensing, Achieving Direct 48-V/1-V DC–DC Conversion," *IEEE J. Solid-State Circuits*, vol. 57, no. 12, pp. 3865–3876, 2022, doi: 10.1109/JSSC.2022.3201781.

[54] J. Loncarski, H. A. Hussain, and A. Bellini, "Efficiency, Cost, and Volume Comparison of SiC-Based and IGBT-Based Full-Scale Converter in PMSG Wind Turbine," *Electronics*, vol. 12, no. 2. 2023. doi: 10.3390/electronics12020385.

[55] SEMIKRON International GmbH, *Application Manual Power Semiconductors*, 2nd ed. Nuremberg: ISLE Verlag, 2015. [Online]. Available: https://www.semikron-danfoss.com/service-support/application-manual.html

[56] Infineon Technologies AG, "TRENCHSTOP™ 1200 V IGBT7 T7 Application Note," Munich, 2021.

[57] J. Liu *et al.*, "Online junction temperature extraction and aging detection of IGBT via Miller plateau width," in *2018 IEEE Applied Power Electronics Conference and Exposition (APEC)*, 2018, pp. 2813–2820. doi: 10.1109/APEC.2018.8341416.

[58] L. Li, Y. Xu, Z. Li, P. Wang, and B. Wang, "The effect of electro-thermal parameters on IGBT junction temperature with the aging of module," *Microelectron. Reliab.*, vol. 66, pp. 58–63, 2016, doi: 10.1016/j.microrel.2016.09.016.

[59] M. Hutter, C. Weber, C. Ehrhardt, and K. D. Lang, "Comparison of different technologies for the die attach of power semiconductor devices conducting active power cycling," in *CIPS 2016; 9th International Conference on Integrated Power Electronics Systems*, 2016, pp. 1–7.

[60] H. S. H. Chung, H. Wang, F. Blaabjerg, and M. Pecht, *Reliability of power electronic converter systems*. 2016. doi: 10.1049/PBPO080E.

[61] Hitachi Energy Ltd., "Press-pack IGBT and diode modules." Accessed: Nov. 02, 2024. [Online]. Available: https://www.hitachienergy.com/uk-ie/en/products-and-solutions/semiconductors/stakpak

[62] Infineon Technologies AG, "IGBT Press Packs." Accessed: Nov. 02, 2024. [Online]. Available: https://www.infineon.com/cms/en/product/power/igbt/igbt-press-packs/

[63] Semikron Danfoss, "SKiiP 7 - Designed to Meet the Challenges." Accessed: Nov. 02, 2024. [Online]. Available: https://www.semikron-danfoss.com/products/product-lines/skiip/skiip-7.html

[64] D. D. Dickson, "An overview of silicone dielectric gels," *EIC*, no. Table 3, pp. 92–95, 1975, doi: 10.1109/EIC.1975.7458502.

[65] L. Cheng, L. Wang, Z. Guan, and F. Zhang, "Aging characterization and lifespan prediction of silicone rubber material utilized for composite insulators in areas of atypical warmth and humidity," *IEEE Trans. Dielectr. Electr. Insul.*, vol. 23, no. 6, pp. 3547–3555, 2016, doi: 10.1109/TDEI.2016.005784.

[66] WACKER, "Room Temperature Vulcanizing (RTV) Silicones - Material and Processing Guidelines," 2023.

[67] F. Yan, L. Wang, H. Wang, S. Wang, and K. Gao, "High Temperature Characteristics of

Composite Materials Composed of Silicone Gel and Barium Titanate in High Voltage Power Modules," *IEEE Trans. Ind. Appl.*, vol. 59, no. 3, pp. 3648–3659, 2023, doi: 10.1109/TIA.2023.3246033.

[68] D. J. Rogers, J. Bruford, A. Ristic-Smith, K. Ali, P. Palmer, and E. Shelton, "A Comparison of the Hard-Switching Performance of 650 V Power Transistors With Calorimetric Verification," *IEEE Open J. Power Electron.*, vol. 4, pp. 764–775, 2023, doi: 10.1109/OJPEL.2023.3315348.

[69] W. Perdikakis, M. J. Scott, K. J. Yost, C. Kitzmiller, B. Hall, and K. A. Sheets, "Comparison of Si and SiC EMI and Efficiency in a Two-Level Aerospace Motor Drive Application," *IEEE Trans. Transp. Electrif.*, vol. 6, no. 4, pp. 1401–1411, 2020, doi: 10.1109/TTE.2020.3010499.

[70] J. O. Gonzalez, R. Wu, S. Jahdi, and O. Alatise, "Performance and Reliability Review of 650 V and 900 V Silicon and SiC Devices: MOSFETs, Cascode JFETs and IGBTs," *IEEE Trans. Ind. Electron.*, vol. 67, no. 9, pp. 7375–7385, 2020, doi: 10.1109/TIE.2019.2945299.

[71] M. Tencer, "Conductive aqueous layer formation at the gel-substrate interface in equilibrium with 100% RH environment," *IEEE Trans. Components Packag. Technol.*, vol. 23, no. 4, pp. 693–699, 2000, doi: 10.1109/6144.888855.

[72] C. F. Bayer, U. Waltrich, A. Soueidan, R. Schneider, E. Baer, and A. Schletz, "Enhancement of the partial discharge inception voltage of DBCs by adjusting the permittivity of the encapsulation," in *CIPS 2016; 9th International Conference on Integrated Power Electronics Systems*, 2016, pp. 1–5.

[73] U. Waltrich, C. F. Bayer, M. Reger, A. Meyer, X. Tang, and A. Schletz, "Enhancement of the partial discharge inception voltage of ceramic substrates for power modules by trench coating," in *2016 International Conference on Electronics Packaging (ICEP)*, 2016, pp. 536–541. doi: 10.1109/ICEP.2016.7486885.

[74] C. F. Bayer *et al.*, "Electrochemical Corrosion on Ceramic Substrates for Power Electronics - Causes, Phenomenological Description, and Outlook," in *CIPS 2018; 10th International Conference on Integrated Power Electronics Systems*, 2018, pp. 1–7.

[75] WACKER, "Wacker SilGel 612 A/B - Technical Data Sheet," 2020. [Online]. Available: https://www.wacker.com/h/en-us/medias/WACKER-SilGel-612-AB-en-2020.12.02.pdf

[76] J. Deltour, M.-L. Locatelli, S. Dinculescu, D. Malec, and D. Meyer, "Partial Discharges and AC Breakdown Voltage Tests on Thick Metallized Aluminum Nitride Substrates for High Voltage Power Modules," in *2023 IEEE Electrical Insulation Conference (EIC)*, IEEE, 2023, pp. 1–5. doi: 10.1109/EIC55835.2023.10177364.

[77] B. Snorradottir, P. Gudnason, R. Scheving, F. Thorsteinsson, and M. Másson, "Release of anti-inflammatory drugs from a silicone elastomer matrix system," *Pharmazie*, vol. 64, pp. 19–25, Feb. 2009, doi: 10.1691/ph.2008.8206.

[78] B. Zhang *et al.*, "Dielectric Properties Characterization and Evaluation of Commercial Silicone Gels for High-Voltage High-Power Power Electronics Module Packaging," *IEEE Trans. Dielectr. Electr. Insul.*, vol. 30, no. 1, pp. 210–219, 2023, doi: 10.1109/TDEI.2022.3225247.

[79] K. Li, B. Zhang, Z. Yang, X. Jiang, and X. Li, "Degradation behaviors of silicone gel encapsulation material with moisture intrusion," *Polym. Degrad. Stab.*, vol. 206, p. 110197, 2022, doi: https://doi.org/10.1016/j.polymdegradstab.2022.110197.

[80] H. Ardebili, C. Hillman, M. A. E. Natishan, P. McCluskey, M. G. Pecht, and D. Peterson, "A comparison of the theory of moisture diffusion in plastic encapsulated microelectronics with moisture sensor chip and weight-gain measurements," *IEEE Trans. components Packag. Technol.*, vol. 25, no. 1, pp. 132–139, 2002, doi: 10.1109/6144.991185.

[81] Z. Qiu, J. Zhang, P. Ning, and X. Wen, "Study on Moisture Absorption Characteristics of Power

Plastic Packaging Devices," in *ICEMS 2018; 21st International Conference on Electrical Machines and Systems*, 2018, pp. 788–791. doi: 10.23919/ICEMS.2018.8549152.

[82] H. G. Carter and K. G. Kibler, "Langmuir-Type Model for Anomalous Moisture Diffusion In Composite Resins," *J. Compos. Mater.*, vol. 12, no. 2, pp. 118–131, Jul. 1978, doi: 10.1177/002199837801200201.

[83] B. Gong *et al.*, "Moisture absorption characteristics of silicone rubber and its effect on dielectric properties," in *2013 Annual Report Conference on Electrical Insulation and Dielectric Phenomena*, IEEE, 2013, pp. 430–433. doi: 10.1109/CEIDP.2013.6748283.

[84] C. Lesaint, C. Babault, K. B. Liland, and L. E. Lundgaard, "Absorption of water in silicon gel," in *2014 IEEE 18th International Conference on Dielectric Liquids (ICDL)*, IEEE, 2014, pp. 1–4. doi: 10.1109/ICDL.2014.6893159.

[85] R. Shen, Y. Tu, C. Zhang, and S. Xu, "Influence of electric field on the moisture absorption characteristic of silicone rubber material," in *2016 IEEE International Conference on High Voltage Engineering and Application (ICHVE)*, IEEE, 2016, pp. 1–4. doi: 10.1109/ICHVE.2016.7800918.

[86] K. Hatori, K. Nakamura, W. Noboru, N. Soltau, and E. Wiesner, "Humidity Absorption Behavior of Silicone Gel in HVIGBT Modules," in *2021 23rd European Conference on Power Electronics and Applications (EPE'21 ECCE Europe)*, EPE Association, 2021, p. P.1-P.8.

[87] J.-H. Fabian, S. Hartmann, and A. Hamidi, "Analysis of insulation failure modes in high power IGBT modules," *IAS*, vol. 2. IEEE, pp. 799-805 Vol. 2, 2005. doi: 10.1109/IAS.2005.1518425.

[88] J. Flicker, R. Kaplar, B. Yang, M. Marinella, and J. Granata, "Insulated gate bipolar transistor reliability testing protocol for PV inverter applications," *Prog. photovoltaics*, vol. 22, no. 9, pp. 970–983, 2014, doi: 10.1002/pip.2351.

[89] C. Papadopoulos, B. Boksteen, G. Paques, and C. Corvasce, "Humidity Robustness of IGBT Guard Ring Termination," in *PCIM Europe 2019; International Exhibition and Conference for Power Electronics, Intelligent Motion, Renewable Energy and Energy Management*, 2019, pp. 1–8.

[90] Y. Gao, X. Liang, J. Wang, Z. Yan, Y. Liu, and Y. Cai, "A capacitance study of anomalous diffusion of water into HTV silicone rubber materials," *IEEE Trans. Dielectr. Electr. Insul.*, vol. 23, no. 1, pp. 368–376, 2016, doi: 10.1109/TDEI.2015.005291.

[91] K. Fischer *et al.*, "Exploring the Causes of Power-Converter Failure in Wind Turbines based on Comprehensive Field-Data and Damage Analysis," *Energies (Basel)*, vol. 12, no. 4, p. 593, 2019, doi: 10.3390/en12040593.

[92] A. J. Wileman, S. Aslam, and S. Perinpanayagam, "A road map for reliable power electronics for more electric aircraft," *Prog. Aerosp. Sci.*, vol. 127, p. 100739, 2021, doi: https://doi.org/10.1016/j.paerosci.2021.100739.

[93] M. Borghei and M. Ghassemi, "Insulation Materials and Systems for More- and All-Electric Aircraft: A Review Identifying Challenges and Future Research Needs," *IEEE Trans. Transp. Electrif.*, vol. 7, no. 3, pp. 1930–1953, 2021, doi: 10.1109/TTE.2021.3050269.

[94] C. Zorn *et al.*, "Field-Data based Lab Testing of a Wind-Energy Power Converter System : Insights into Cabinet and IGBT-Module Microclimates Keywords Multimodal vs . single stress testing", doi: 10.23919/EPE23ECCEEurope58414.2023.10264328.

[95] R. Bayerer, M. Lassmann, and S. Kremp, "Transient Hygrothermal-Response of Power Modules in Inverters-The Basis for Mission Profiling Under Climate and Power Loading," *IEEE Trans. Power Electron.*, vol. 31, no. 1, pp. 613–620, 2016, doi: 10.1109/TPEL.2015.2408117.

[96] S. Kremp, O. Schilling, and V. Müller, “Empirical study on humidity conditions inside of power modules under varying external conditions,” *CIPS 2016; 9th Int. Conf. Integr. Power Electron. Syst.*, pp. 1–6, 2019.

[97] Y. Ji *et al.*, “Investigation on Humidity Effect on Partial Discharge Considering Thermal Aging,” in *2022 International Conference on Electrical Machines (ICEM)*, IEEE, 2022, pp. 2325–2330. doi: 10.1109/ICEM51905.2022.9910815.

[98] N. Wang, I. Cotton, and K. Evans, “Impact of Thermal Cycling in Humid Environments on Power Electronic Modules,” *IEEE Trans. Components, Packag. Manuf. Technol.*, vol. 2, no. 7, pp. 1085–1091, 2012, doi: 10.1109/TCPMT.2012.2195781.

[99] M. Brincker, K. B. Pedersen, P. K. Kristensen, and V. Popok, “Passive thermal cycling of power diodes under controlled atmospheric conditions - effects on metallization degradation,” in *CIPS 2016; 9th International Conference on Integrated Power Electronics Systems*, 2016, pp. 1–6.

[100] H. Beyer, V. Sivasubramaniam, M. Bayer, and S. Hartmann, “Reliability of Lead-free Large Area Solder Joints in IGBT Modules with Respect to Passive and Active Thermal Cycling,” in *CIPS 2016; 9th International Conference on Integrated Power Electronics Systems*, 2016, pp. 1–6.

[101] M. Schäfer, O. Schilling, C. Yue, and T. Kashko, “Comparison between active and passive thermal cycling stress with respect to substrate solder reliability in IGBT modules with Cu baseplates.” pp. 674–681, 2014.

[102] A. Hambrecht, R. Klitzke, S. Lehmann, D. Wagenitz, and S. Dieckerhoff, “Transient Thermal Impedance Model based on Online-Measurement of the On-State Voltage in IGBT Converters,” in *CIPS 2016; 9th International Conference on Integrated Power Electronics Systems*, 2016, pp. 1–4.

[103] R. Khazaka, L. Mendizabal, D. Henry, and R. Hanna, “Survey of High-Temperature Reliability of Power Electronics Packaging Components,” *IEEE Trans. Power Electron.*, vol. 30, no. 5, pp. 2456–2464, 2015, doi: 10.1109/TPEL.2014.2357836.

[104] E. H. Amalu and N. N. Ekere, “Modelling evaluation of Garofalo-Arrhenius creep relation for lead-free solder joints in surface mount electronic component assemblies,” *J. Manuf. Syst.*, vol. 39, pp. 9–23, 2016, doi: 10.1016/j.jmsy.2016.01.002.

[105] V. Samavatian, H. Iman-Eini, Y. Avenas, and M. Samavatian, “Effects of Creep Failure Mechanisms on Thermomechanical Reliability of Solder Joints in Power Semiconductors,” *IEEE Trans. power Electron.*, vol. 35, no. 9, pp. 8956–8964, 2020, doi: 10.1109/TPEL.2020.2973312.

[106] H. Li, Y. Hu, S. Liu, Y. Li, X. Liao, and Z. Liu, “An Improved Thermal Network Model of the IGBT Module for Wind Power Converters Considering the Effects of Base-Plate Solder Fatigue,” *IEEE Trans. Device Mater. Reliab.*, vol. 16, no. 4, pp. 570–575, 2016, doi: 10.1109/TDMR.2016.2606483.

[107] A. Hanif, A. N. M. W. Azad, and F. Khan, “Detection of Bond Wire Lift Off in IGBT Power Modules Using Ultrasound Resonators,” in *2020 IEEE Applied Power Electronics Conference and Exposition (APEC)*, Kansas City, 2020, pp. 345–350. doi: 10.1109/APEC39645.2020.9124226.

[108] A. Hanif, D. Devoto, and F. Khan, “Bond Wire Damage Detection and SOH Estimation of a Dual-Pack IGBT Power Module Using Active Power Cycling and Reflectometry,” *IEEE Trans. Power Electron.*, vol. 35, no. 7, pp. 6761–6772, 2020, doi: 10.1109/TPEL.2019.2958898.

[109] M. Bouarroudj, Z. Khatir, J. P. Ousten, F. Badel, L. Dupont, and S. Lefebvre, “Degradation behavior of 600 V–200 A IGBT modules under power cycling and high temperature

environment conditions," *Microelectron. Reliab.*, vol. 47, no. 9, pp. 1719–1724, 2007, doi: 10.1016/j.microrel.2007.07.027.

[110] Z. Deng, M. Chen, W. Lai, X. Ding, and H. Xia, "A Comparative Study on Lifetime Models in IGBT Power Modules," in *2019 4th International Conference on Intelligent Green Building and Smart Grid (IGBSG)*, 2019, pp. 241–245. doi: 10.1109/IGBSG.2019.8886209.

[111] H. S. Chung, H. Wang, F. Blaabjerg, and M. Pecht, *Reliability of Power Electronic Converter Systems*, vol. 80. Stevenage: Stevenage: The Institution of Engineering and Technology, 2016. doi: 10.1049/PBPO080E.

[112] A. Abuelnaga, M. Narimani, and A. S. Bahman, "A Review on IGBT Module Failure Modes and Lifetime Testing," *IEEE access*, vol. 9, pp. 9643–9663, 2021, doi: 10.1109/ACCESS.2021.3049738.

[113] X. Z. Qiu *et al.*, "Review of IGBT Junction Temperature Extraction and Estimation Methods," *IOP Conf. Ser. Mater. Sci. Eng*, vol. 774, no. 1, p. 12091, 2020, doi: 10.1088/1757-899X/774/1/012091.

[114] A. Watanabe, M. Tsukuda, and I. Omura, "Real time degradation monitoring system for high power IGBT module under power cycling test," *Microelectron. Reliab.*, vol. 53, no. 9–11, pp. 1692–1696, 2013, doi: 10.1016/j.microrel.2013.07.084.

[115] A. Ibrahim, J. P. Ousten, R. Lallemand, and Z. Khatir, "Power Cycling Tests in High Temperature Conditions of SiC-MOSFET Power Modules and Ageing Assessment," in *CIPS 2016; 9th International Conference on Integrated Power Electronics Systems*, 2016, pp. 1–6.

[116] U.-M. Choi, F. Blaabjerg, S. Jorgensen, S. Jørgensen, and S. Jorgensen, "Power Cycling Test Methods for Reliability Assessment of Power Device Modules in Respect to Temperature Stress," *IEEE Trans. power Electron.*, vol. 33, no. 3, pp. 2531–2551, 2018, doi: 10.1109/TPEL.2017.2690500.

[117] U.-M. Choi, S. Jørgensen, F. Iannuzzo, and F. Blaabjerg, "Power cycling test of transfer molded IGBT modules by advanced power cycler under different junction temperature swings," *Microelectron. Reliab.*, vol. 88–90, no. June, pp. 788–794, 2018, doi: 10.1016/j.microrel.2018.07.002.

[118] A. Hanif, S. Das, and F. Khan, "Active power cycling and condition monitoring of IGBT power modules using reflectometry," *APEC*. IEEE, pp. 2827–2833, 2018. doi: 10.1109/APEC.2018.8341418.

[119] S. Bęczkowski *et al.*, "Online Vce measurement method for wear-out monitoring of high power IGBT modules," *2013 15th Eur. Conf. Power Electron. Appl. EPE 2013*, pp. 1–7, 2013, doi: 10.1109/EPE.2013.6634390.

[120] F. Forest *et al.*, "Fast power cycling protocols implemented in an automated test bench dedicated to IGBT module ageing," *Microelectron. Reliab.*, vol. 55, no. 1, pp. 81–92, 2015, doi: 10.1016/j.microrel.2014.09.008.

[121] M. A. Eleffendi and C. M. Johnson, "A Health Monitoring Framework for IGBT Power Modules," in *CIPS 2016; 9th International Conference on Integrated Power Electronics Systems*, 2016, pp. 1–6.

[122] X. Sun, M. Huang, Y. Liu, and X. Zha, "Investigation of artificial neural network algorithm based IGBT online condition monitoring," *Microelectron. Reliab.*, vol. 88–90, no. May, pp. 103–106, 2018, doi: 10.1016/j.microrel.2018.07.068.

[123] Y. Avenas, L. Dupont, and Z. Khatir, "Temperature measurement of power semiconductor devices by thermo-sensitive electrical parameters - A review," *IEEE Trans. Power Electron.*, vol. 27, no. 6, pp. 3081–3092, 2012, doi: 10.1109/TPEL.2011.2178433.

[124] A. Griffo, J. Wang, K. Colombage, and T. Kamel, “Real-Time Measurement of Temperature Sensitive Electrical Parameters in SiC Power MOSFETs,” *IEEE Trans. Ind. Electron.*, vol. 65, no. 3, pp. 2663–2671, 2018, doi: 10.1109/TIE.2017.2739687.

[125] M. H. Mohamed Sathik, S. Prasanth, F. Sasongko, and J. Pou, “Online condition monitoring of IGBT modules using voltage change rate identification,” *Microelectron. Reliab.*, vol. 88–90, no. May, pp. 486–492, 2018, doi: 10.1016/j.microrel.2018.07.040.

[126] M. H. Mohamed Sathik, S. Prasanth, F. Sasongko, and J. Pou, “Online condition monitoring of IGBT modules using current-change rate identification,” *Microelectron. Reliab.*, vol. 92, no. November 2018, pp. 55–62, 2019, doi: 10.1016/j.microrel.2018.11.013.

[127] M. H. Mohamed Sathik, S. Prasanth, F. Sasongko, J. Pou, and A. K. Gupta, “Online condition monitoring of IGBT modules using gate-charge identification,” *Conf. Proc. - IEEE Appl. Power Electron. Conf. Expo. - APEC*, vol. 2019-March, pp. 2702–2707, 2019, doi: 10.1109/APEC.2019.8722200.

[128] C. Felgemacher, B. Dombert, C. Noeding, and P. Zacharias, “IGBT Online-Temperature Monitoring using Turn-Off Delay as a Temperature Sensitive Electrical Parameter,” in *CIPS 2016; 9th International Conference on Integrated Power Electronics Systems*, 2016, pp. 1–6.

[129] H. Luo, Y. Chen, P. Sun, W. Li, and X. He, “Junction Temperature Extraction Approach With Turn-Off Delay Time for High-Voltage High-Power IGBT Modules,” *IEEE Trans. Power Electron.*, vol. 31, no. 7, pp. 5122–5132, 2016, doi: 10.1109/TPEL.2015.2481465.

[130] L. Li *et al.*, “A turn-off delay time measurement and junction temperature estimation method for IGBT,” in *2017 IEEE Applied Power Electronics Conference and Exposition (APEC)*, IEEE, 2017, pp. 2290–2296. doi: 10.1109/APEC.2017.7931019.

[131] C. Zorn and N. Kaminski, “Temperature Humidity Bias (THB) Testing on IGBT Modules at High Bias Levels,” in *CIPS 2014; 8th International Conference on Integrated Power Electronics Systems*, 2014, pp. 1–7.

[132] C. Zorn and N. Kaminski, “Acceleration of temperature humidity bias (THB) testing on IGBT modules by high bias levels,” *Proc. Int. Symp. Power Semicond. Devices ICs*, vol. 2015-June, pp. 385–388, 2015, doi: 10.1109/ISPSD.2015.7123470.

[133] C. Papadopoulos, C. Corvasce, A. Kopta, D. Schneider, G. Pâques, and M. Rahimo, “The influence of humidity on the high voltage blocking reliability of power IGBT modules and means of protection,” *Microelectron. Reliab.*, vol. 88–90, no. June, pp. 470–475, 2018, doi: 10.1016/j.microrel.2018.07.130.

[134] J. Jormanainen *et al.*, “High Humidity, High Temperature and High Voltage Reverse Bias - A Relevant Test for Industrial Applications,” in *PCIM Europe 2018; International Exhibition and Conference for Power Electronics, Intelligent Motion, Renewable Energy and Energy Management*, 2018, pp. 563–569.

[135] J. Ingman, J. Jormanainen, and E. Mengotti, “H3TRB-HVDC on SiC: A Relevant Test for Industrial Applications,” 2018. [Online]. Available: https://www.psma.com/sites/default/files/uploads/tech-forums-semiconductor/presentations/is165-h3trb-hvdc-sic-relevant-test-industrial-applications.pdf

[136] K. Li *et al.*, “Reliability Considerations of High Power IGBT Modules under High Temperature/Humidity/Bias (HTHB) Condition,” in *PCIM Europe 2019; International Exhibition and Conference for Power Electronics, Intelligent Motion, Renewable Energy and Energy Management*, 2019, pp. 1–5.

[137] D. Cimmino and S. Ferrero, “High-Voltage Temperature Humidity Bias Test (HV-THB): Overview of Current Test Methodologies and Reliability Performances,” *Electron.*, vol. 9, no.

11, p. 1884, 2020, doi: 10.3390/electronics9111884.

[138] F. Hoffmann, A. Mihaila, V. Soler, and N. Kaminski, “H3TRB Test on 6.5 kV SiC-JBS Diodes,” *CIPS 2020; 11th Int. Conf. Integr. Power Electron. Syst.*, vol. 858, no. 6, pp. 485–489, 2020.

[139] J.-H. Peters, M. Hanf, S. Clausner, C. Zorn, and N. Kaminski, “Improved HV-H3TRB robustness of a 1700 V IGBT chip set in standard power modules,” *Microelectron. Reliab.*, vol. 126, no. xxxx, p. 114211, Nov. 2021, doi: 10.1016/j.microrel.2021.114211.

[140] C. Schimpf, K. Feldmann, C. Matzner, and A. Steinke, “Failure of electronic devices due to condensation,” *Microsyst. Technol.*, vol. 15, no. 1, pp. 123–127, 2009, doi: 10.1007/s00542-008-0643-y.

[141] M. Jellesen, D. Minzari, U. Rathinavelu, P. Møller, and R. Ambat, “Investigation of Electronic Corrosion at Device Level,” *ECS Trans.*, vol. 25, Jan. 2010, doi: 10.1149/1.3321952.

[142] H. Deng, J. Meng, D. Wang, and W. Zhang, “Breakdown Voltage Impact on Lifetime of 1200V IGBT modules under H3TRB-HVDC Testing,” in *2019 IEEE 26th International Symposium on Physical and Failure Analysis of Integrated Circuits (IPFA)*, 2019, pp. 1–4. doi: 10.1109/IPFA47161.2019.8984824.

[143] J. Leppänen, G. Ross, V. Vuorinen, J. Ingman, J. Jormanainen, and M. Paulasto-Kröckel, “A humidity-induced novel failure mechanism in power semiconductor diodes,” *Microelectron. Reliab.*, vol. 123, p. 114207, 2021, doi: https://doi.org/10.1016/j.microrel.2021.114207.

[144] J. Leppänen *et al.*, “Aluminium corrosion in power semiconductor devices,” *Microelectron. Reliab.*, vol. 137, p. 114766, 2022, doi: https://doi.org/10.1016/j.microrel.2022.114766.

[145] S. Kremp and O. Schilling, “Humidity robustness for high voltage power modules: Limiting mechanisms and improvement of lifetime,” *Microelectron. Reliab.*, vol. 88–90, pp. 447–452, 2018, doi: https://doi.org/10.1016/j.microrel.2018.06.043.

[146] Z. Wu *et al.*, “SiC IGBT degradation mechanism investigation under HV-H3TRB tests,” *J. Power Electron.*, 2023, doi: 10.1007/s43236-023-00726-9.

[147] Y. Xu, Z. Hu, H. Chen, D. Li, Z. Hu, and D. Li, “Influence of Relative Humidity on the Temperature Increase of a Power Converter,” *J. Power Electron.*, vol. 15, no. 3, pp. 841–848, 2015, doi: 10.6113/JPE.2015.15.3.841.

[148] F. Wuest, O. Wittler, and M. Schneider-Ramelow, “Influence of temperature and humidity on power cycling capability of power modules,” *Microelectron. Reliab.*, vol. 114, no. October, p. 113880, 2020, doi: 10.1016/j.microrel.2020.113880.

[149] F. Hoffmann, N. Kaminski, and S. Schmitt, “Investigation on the Impact of Environmental Stress on the Thermo-Mechanical Reliability of IGBTs by Means of Consecutive H3TRB and PCT Testing,” in *2021 33rd International Symposium on Power Semiconductor Devices and ICs (ISPSD)*, 2021, pp. 371–374. doi: 10.23919/ISPSD50666.2021.9452227.

[150] F. Hoffmann, M. Hanf, N. Kaminski, and S. Schmitt, “Investigation on the Impact of Thermo-Mechanical Stress on the Humidity Ruggedness of IGBTs by Means of Consecutive PCT and H3TRB Testing,” in *2020 32nd International Symposium on Power Semiconductor Devices and ICs (ISPSD)*, 2020, pp. 376–379. doi: 10.1109/ISPSD46842.2020.9170080.

[151] Y. Wang *et al.*, “Advanced Power Cycling Test Integrated With Voltage, Current, Temperature, and Humidity Stress,” *IEEE Trans. Power Electron.*, vol. 38, no. 6, pp. 7685–7696, 2023, doi: 10.1109/TPEL.2023.3246498.

[152] Y. Wang, E. Deng, T. Wu, Y. Zhang, L. Xie, and Y. Huang, “Thermo-Hygroscopic-Mechanical Coupling Simulation Method for Power Electronics Under Power Cycling Test,” *IEEE Trans. Power Electron.*, vol. 38, no. 9, pp. 11521–11530, 2023, doi: 10.1109/TPEL.2023.3290749.

[153] BSI, *BS 1339-1:2002 - Humidity - Part 1: Terms, definitions and formulae*. 2002.

[154] World Meteorological Organization, *Guide to Metoerological Instruments and Methods of Observation*, 7th ed. Geneva: WMO, 2008.

[155] L. Alwis, T. Sun, and K. T. V. V Grattan, "Optical fibre-based sensor technology for humidity and moisture measurement: Review of recent progress," *Meas. J. Int. Meas. Confed.*, vol. 46, no. 10, pp. 4052–4074, 2013, doi: 10.1016/j.measurement.2013.07.030.

[156] B. T. DeBoi, B. W. Nelson, P. Kanatzar, F. Fraas, A. Curbow, and T. McNutt, "Analysis of Moisture-Induced Void Formations within Silicon Carbide Power Modules," in *PCIM Europe 2023; International Exhibition and Conference for Power Electronics, Intelligent Motion, Renewable Energy and Energy Management*, 2023, pp. 1–8. doi: 10.30420/566091121.

[157] J. Wisniak, "Historical development of the vapor pressure equation from dalton to antoine," *J. Phase Equilibria*, vol. 22, no. 6, pp. 622–630, 2001, doi: 10.1007/s11669-001-0026-x.

[158] National Institute of Standards and Technology (NIST), "NIST Chemistry WebBook, SRD 69 - Water." Accessed: Mar. 12, 2024. [Online]. Available: https://webbook.nist.gov/cgi/cbook.cgi?ID=C7732185

[159] J. Huang, "A Simple Accurate Formula for Calculating Saturation Vapor Pressure of Water and Ice," *J. Appl. Meteorol. Climatol.*, vol. 57, no. 6, pp. 1265–1272, 2018, doi: https://doi.org/10.1175/JAMC-D-17-0334.1.

[160] C. F. Bayer, U. Waltrich, A. Soueidan, E. Baer, and A. Schletz, "Partial discharges in ceramic substrates - Correlation of electric field strength simulations with phase resolved partial discharge measurements," in *2016 International Conference on Electronics Packaging, ICEP 2016*, The Japan Institute of Electronics Packaging, 2016, pp. 530–535. doi: 10.1109/ICEP.2016.7486884.

[161] H. Fröhlich, *Theory of Dielectrics: Dielectric Constant and Dielectric Loss*. Oxford, UK: Clarendon Press, 1958.

[162] H. Föll, "Electronic Materials," Dielectrics. Accessed: Feb. 21, 2024. [Online]. Available: https://www.tf.uni-kiel.de/matwis/amat/elmat_en/index.html

[163] Z. Ahmad, "Polymer Dielectric Materials," M. A. Silaghi, Ed., Rijeka: IntechOpen, 2012, p. Ch. 1. doi: 10.5772/50638.

[164] R. Dorey, "Chapter 4 - Microstructure–property relationships: How the microstructure of the film affects its properties," in *Micro and Nano Technologies*, R. B. T.-C. T. F. for M. and M. Dorey, Ed., Oxford: William Andrew Publishing, 2012, pp. 85–112. doi: https://doi.org/10.1016/B978-1-4377-7817-5.00004-3.

[165] A. Ward, *Dielectric materials for advanced applications*. 2016. doi: 10.13140/RG.2.1.3481.5600.

[166] G. Giannoukos, M. Min, and T. Rang, "Relative complex permittivity and its dependence on frequency," *World J. Eng.*, vol. 14, no. 6, pp. 532–537, Jan. 2017, doi: 10.1108/WJE-01-2017-0007.

[167] J. R. Lowney and R. D. Larrabee, "The use of Fick's law in modeling diffusion processes," *IEEE Trans. Electron Devices*, vol. 27, no. 9, pp. 1795–1798, 1980, doi: 10.1109/T-ED.1980.20105.

[168] C.-H. Shen and G. S. Springer, "Moisture Absorption and Desorption of Composite Materials," *J. Compos. Mater.*, vol. 10, no. 1, pp. 2–20, Jan. 1976, doi: 10.1177/002199837601000101.

[169] J. Xu, Y. Qin, and Z. An, "Overall Improvements in Outdoor Performance of ATH-free Silicone Rubbers by Direct Fluorination," in *2022 IEEE International Conference on High Voltage Engineering and Applications (ICHVE)*, 2022, pp. 1–4. doi:

10.1109/ICHVE53725.2022.9961556.

[170] A. D. Drozdov and J. deClaville Christiansen, “Modeling dielectric permittivity of polymer composites at microwave frequencies,” *Mater. Res. Bull.*, vol. 126, p. 110818, 2020, doi: https://doi.org/10.1016/j.materresbull.2020.110818.

[171] Z. Duanmu, Z. Zhang, Y. Song, and J. Deng, “Study on Dielectric Model for Capacitance-Based Nondestructive Testing of Water Content in Concrete,” *2022 IEEE 5th International Electrical and Energy Conference (CIEEC)*. pp. 1870–1875, 2022. doi: 10.1109/CIEEC54735.2022.9846360.

[172] R. Simpkin, “Derivation of Lichtenecker’s Logarithmic Mixture Formula From Maxwell’s Equations,” *IEEE Trans. Microw. Theory Tech.*, vol. 58, no. 3, pp. 545–550, 2010, doi: 10.1109/TMTT.2010.2040406.

[173] S. O. Nelson, “Measurement and calculation of powdered mixture permittivities,” *IEEE Trans. Instrum. Meas.*, vol. 50, no. 5, pp. 1066–1070, 2001, doi: 10.1109/19.963159.

[174] F. de Paulis, M. H. Nisanci, M. Y. Koledintseva, J. L. Drewniak, and A. Orlandi, “From Maxwell Garnett to Debye Model for Electromagnetic Simulation of Composite Dielectrics Part I: Random Spherical Inclusions,” *IEEE Trans. Electromagn. Compat.*, vol. 53, no. 4, pp. 933–942, 2011, doi: 10.1109/TEMC.2011.2158217.

[175] G. LaPlante, A. V Ouriadov, P. Lee-sullivan, and B. J. Balcom, “Anomalous moisture diffusion in an epoxy adhesive detected by magnetic resonance imaging,” *J. Appl. Polym. Sci.*, vol. 109, no. 2, pp. 1350–1359, Jul. 2008, doi: https://doi.org/10.1002/app.28106.

[176] G. Mitic and G. Lefranc, “Localization of electrical-insulation and partial-discharge failures of IGBT modules,” *IEEE Trans. Ind. Appl.*, vol. 38, no. 1, pp. 175–180, 2002, doi: 10.1109/28.980373.

[177] J.-H. Fabian, S. Hartmann, and A. Hamidi, “Partial Discharge Failure Analysis of AIN Substrates for IGBT Modules,” *Microelectron. Reliab.*, vol. 44, no. 9, pp. 1425–1430, 2004, doi: 10.1016/j.microrel.2004.07.111.

[178] H. Mitsudome *et al.*, “Basic study on partial discharge location in power module,” in *2016 IEEE International Conference on Dielectrics (ICD)*, 2016, pp. 451–454. doi: 10.1109/ICD.2016.7547640.

[179] H. Mitsudome *et al.*, “High accuracy partial discharge location in power module using multiple loop sensors,” in *2017 IEEE International Workshop On Integrated Power Packaging (IWIPP)*, 2017, pp. 1–5. doi: 10.1109/IWIPP.2017.7936749.

[180] P. Fu *et al.*, “Partial Discharge Measurement and Analysis in High Voltage IGBT Modules Under DC Voltage,” *CSEE J. POWER ENERGY Syst.*, vol. 4, no. 4, pp. 513–523, 2018, doi: 10.17775/CSEEJPES.2017.01190.

[181] G. Mitic, T. Licht, and G. Lefranc, “IGBT module technology with high partial discharge resistance,” in *Conference Record of the 2001 IEEE Industry Applications Conference. 36th IAS Annual Meeting (Cat. No.01CH37248)*, 2001, pp. 1899–1904 vol.3. doi: 10.1109/IAS.2001.955789.

[182] F. Yan, L. Wang, T. Yang, B. Wang, F. Yang, and L. Yu, “Design of Packaging Structure in High Voltage Power Modules to Avoid Surface Breakdown,” in *2020 IEEE Workshop on Wide Bandgap Power Devices and Applications in Asia (WiPDA Asia)*, 2020, pp. 1–5. doi: 10.1109/WiPDAAsia49671.2020.9360276.

[183] M. T. Do, J.-L. Augé, and O. Lesaint, “Partial discharges in silicone gel in the temperature range 20-150°C,” in *2006 IEEE Conference on Electrical Insulation and Dielectric Phenomena*, 2006, pp. 590–593. doi: 10.1109/CEIDP.2006.312001.

[184] K.-W. Lee *et al.*, “Partial discharge characteristics of the ultra-high voltage cable insulators according to the measuring temperature,” in *2008 International Conference on Condition Monitoring and Diagnosis*, 2008, pp. 105–108. doi: 10.1109/CMD.2008.4580241.

[185] C. Hudon, M. Chaaban, M. Belec, and D. N. Nguyen, “Effect of temperature and thermal expansion on slot partial discharge activity,” in *2007 Electrical Insulation Conference and Electrical Manufacturing Expo*, 2007, pp. 122–126. doi: 10.1109/EEIC.2007.4562602.

[186] G. Finis, A. Claudi, and G. Malin, “Dielectric breakdown strength of silicone gel under various environmental conditions,” in *2005 IEEE Russia Power Tech*, 2005, pp. 1–6. doi: 10.1109/PTC.2005.4524423.

[187] G. Finis and A. Claudi, “On the Electric Breakdown Behavior of Silicone Gel at Interfaces,” *IEEE Trans. Dielectr. Electr. Insul.*, vol. 15, no. 2, pp. 366–373, 2008, doi: 10.1109/TDEI.2008.4483454.

[188] J.-L. Augé, O. Lesaint, and A. T. Vu Thi, “Partial discharges in ceramic substrates embedded in liquids and gels,” *IEEE Trans. Dielectr. Electr. Insul.*, vol. 20, no. 1, pp. 262–274, 2013, doi: 10.1109/TDEI.2013.6451366.

[189] G. Finis and A. Claudi, “On the dielectric breakdown behavior of silicone gel under various stress conditions,” *IEEE Trans. Dielectr. Electr. Insul.*, vol. 14, no. 2, pp. 487–494, 2007, doi: 10.1109/TDEI.2007.344630.

[190] Y. Kikuchi *et al.*, “Effects of ambient humidity and temperature on partial discharge characteristics of conventional and nanocomposite enameled magnet wires,” *IEEE Trans. Dielectr. Electr. Insul.*, vol. 15, no. 6, pp. 1617–1625, 2008, doi: 10.1109/TDEI.2008.4712665.

[191] Y. Kikuchi, T. Murata, N. Fukumoto, M. Nagata, Y. Wakimoto, and T. Yoshimitsu, “Investigation of partial discharge with twisted enameled wires in atmospheric humid air by optical emission spectroscopy,” *IEEE Trans. Dielectr. Electr. Insul.*, vol. 17, no. 3, pp. 839–845, 2010, doi: 10.1109/TDEI.2010.5492257.

[192] M. Fenger and G. C. Stone, “Investigations into the effect of humidity on stator winding partial discharges,” *IEEE Trans. Dielectr. Electr. Insul.*, vol. 12, no. 2, pp. 341–346, 2005, doi: 10.1109/TDEI.2005.1430402.

[193] T. Kaji, H. Asai, H. Kojima, and N. Hayakawa, “Combined Effect of Temperature and Humidity of Magnet-Wires on Partial Discharge Inception Voltage under Inverter-Surge Voltage,” in *2018 IEEE Conference on Electrical Insulation and Dielectric Phenomena (CEIDP)*, IEEE, 2018, pp. 554–557. doi: 10.1109/CEIDP.2018.8544745.

[194] A. Rumi, A. Cavallini, and L. Lusuardi, “Combined Effects of Temperature and Humidity on the PDIV of Twisted Pairs,” in *2020 IEEE 3rd International Conference on Dielectrics (ICD)*, 2020, pp. 906–909. doi: 10.1109/ICD46958.2020.9342030.

[195] IEC, *60034-18-41 - Rotating electrical machines - Part 18-41: Partial discharge free electrical insulation systems (Type I) used in rotating electrical machines fed from voltage converters - Qualification and quality control tests*. 2014.

[196] IEC, *61287 - Railway Applications - Power Convertors Installed on Board Rolling Stock*. 2006.

[197] IEC, *61287-1 - Railway applications. Power converters installed on board rolling stock. Characteristics and test methods*. 2014.

[198] IEC, *60270+A1:2015 - High-voltage test techniques. Partial discharge measurements*. 2015.

[199] IEC, *TS 61934 - Electrical insulating materials and systems - Electrical measurement of partial discharges (PD) under short rise time and repetitive voltage impulses*. 2011.

[200] Y. Ding, Y. Wang, H. Sun, and Y. Yin, “High-Temperature Partial Discharge Characteristics of

Power Module Packaging Insulation Under Square Pulse With High Dv/Dt Based on Down-Mixing Method," *IEEE Trans. Ind. Electron.*, vol. 70, no. 7, pp. 7334–7342, 2023, doi: 10.1109/TIE.2022.3201276.

[201] H. You, Z. Wei, B. Hu, Z. Zhao, R. Na, and J. Wang, "Partial Discharge Behaviors in Power Modules Under Square Pulses With Ultrafast dv/dt," *IEEE Trans. Power Electron.*, vol. 36, no. 3, pp. 2611–2620, 2021, doi: 10.1109/TPEL.2020.3014043.

[202] A. Madonia, P. Romano, T. Hammarstrom, S. M. Gubanski, F. Viola, and A. Imburgia, "Partial discharge of gel insulated high voltage power modules subjected to unconventional voltage waveforms," in *CEIDP*, IEEE, 2016, pp. 715–718. doi: 10.1109/CEIDP.2016.7785602.

[203] T. Ebke, A. Khaddour, and D. Peier, "Degradation of silicone gel by partial discharges due to different defects," in *2000 Eighth International Conference on Dielectric Materials, Measurements and Applications (IEE Conf. Publ. No. 473)*, 2000, pp. 202–207. doi: 10.1049/cp:20000505.

[204] B. Florkowska, M. Florkowski, J. Roehrich, and P. Zydron, "The influence of PWM stresses on degradation processes in electrical insulation systems," *2010 Annu. Rep. Conf. Electr. Insul. Dielectic Phenom.*, no. 1, pp. 1–4, 2010, doi: 10.1109/CEIDP.2010.5723975.

[205] M. Sato, A. Kumada, K. Hidaka, K. Yamashiro, Y. Hayase, and T. Takano, "Degradation process of silicone-gel by internal surface discharges," in *2014 IEEE 18th International Conference on Dielectric Liquids (ICDL)*, IEEE, 2014, pp. 1–4. doi: 10.1109/ICDL.2014.6893095.

[206] Z. Yang, K. Li, X. Jiang, B. Zhang, and X. Li, "The Degradation Behaviors from Triple Junctions in IGBT Power Modules," in *2022 IEEE International Conference on High Voltage Engineering and Applications (ICHVE)*, IEEE, 2022, pp. 1–5. doi: 10.1109/ICHVE53725.2022.9961665.

[207] X. Jiang, K. Li, Z. Yang, B. Zhang, and X. Li, "Comparative Analysis on Insulation Degradation Characteristics of Two Commercial Silicone Gels," in *2022 IEEE International Conference on High Voltage Engineering and Applications (ICHVE)*, IEEE, 2022, pp. 1–5. doi: 10.1109/ICHVE53725.2022.10014508.

[208] N. Wang, I. Cotton, J. Robertson, S. Follmann, K. Evans, and D. Newcombe, "Partial discharge control in a power electronic module using high permittivity non-linear dielectrics," *IEEE Trans. Dielectr. Electr. Insul.*, vol. 17, no. 4, pp. 1319–1326, 2010, doi: 10.1109/TDEI.2010.5539704.

[209] C. Park, "Electrets: A Remedy for Partial Discharge Caused by Power Electronics Switching," *IEEE Trans. Ind. Electron.*, vol. 68, no. 12, pp. 12947–12952, Dec. 2021, doi: 10.1109/TIE.2020.3045707.

[210] K. Li, B. Zhang, X. Li, F. Yan, and L. Wang, "Electric Field Mitigation in High-Voltage High-Power IGBT Modules Using Nonlinear Conductivity Composites," *IEEE Trans. Components, Packag. Manuf. Technol.*, vol. 11, no. 11, pp. 1844–1855, 2021, doi: 10.1109/TCPMT.2021.3106962.

[211] Z. Zhang *et al.*, "Packaging of 20 kV Double-Side Cooled Silicon Carbide Diode Module With Electrical Insulation Enhanced by a Polymer-Nanoparticle Coating," in *2023 25th European Conference on Power Electronics and Applications (EPE'23 ECCE Europe)*, 2023, p. P.1-P.6. doi: 10.23919/EPE23ECCEEurope58414.2023.10264618.

[212] H. Hourdequin, L. Laudebat, M.-L. Locatelli, Z. Valdez-Nava, and P. Bidan, "Metallized ceramic substrate with mesa structure for voltage ramp-up of power modules," *Eur. Phys. Journal. Appl. Phys.*, vol. 87, Aug. 2019, doi: https://doi.org/10.1051/epjap/2019180288.

[213] M. M. Tousi and M. Ghassemi, "Combined geometrical techniques and applying nonlinear field

dependent conductivity layers to address the high electric field stress issue in high voltage high-density wide bandgap power modules," *IEEE Trans. Dielectr. Electr. Insul.*, vol. 27, no. 1, pp. 305–313, 2020, doi: 10.1109/TDEI.2019.008493.

[214] L. Zhong *et al.*, "An Integrated Structure–Material Optimization Strategy for the Packaging of High-Voltage Insulated Gate Bipolar Transistors," *IEEE Trans. Dielectr. Electr. Insul.*, vol. 29, no. 6, pp. 2163–2170, 2022, doi: 10.1109/TDEI.2022.3211225.

[215] M. Sherriff, A. Griffo, C. Jia, and C. Ng, "Investigation of the impact of temperature and humidity on the capacitance of dielectric gel used for power electronics," in *11th International Conference on Power Electronics, Machines and Drives (PEMD 2022)*, 2022, pp. 91–96. doi: 10.1049/icp.2022.1023.

[216] S. Pevec and D. Donlagic, "Miniature all-silica fiber-optic sensor for simultaneous measurement of relative humidity and temperature," *Opt. Lett.*, vol. 40, no. 23, p. 5646, 2015, doi: 10.1364/ol.40.005646.

[217] P. J. Thomas and J. O. Hellevang, "A fully distributed fibre optic sensor for relative humidity measurements," *Sensors Actuators, B Chem.*, vol. 247, pp. 284–289, 2017, doi: 10.1016/j.snb.2017.02.027.

[218] P. J. Thomas and J. O. Hellevang, "A high response polyimide fiber optic sensor for distributed humidity measurements," *Sensors Actuators, B Chem.*, vol. 270, pp. 417–423, 2018, doi: 10.1016/j.snb.2018.05.011.

[219] A. Leal-Junior, A. Frizera-Neto, C. Marques, and M. J. Pontes, "Measurement of temperature and relative humidity with polymer optical fiber sensors based on the induced stress-optic effect," *Sensors (Switzerland)*, vol. 18, no. 3, 2018, doi: 10.3390/s18030916.

[220] J. Zhang, X. Shen, M. Qian, Z. Xiang, and X. Hu, "An optical fiber sensor based on polyimide coated fiber Bragg grating for measurement of relative humidity," *Opt. Fiber Technol.*, vol. 61, no. December 2020, p. 102406, 2021, doi: 10.1016/j.yofte.2020.102406.

[221] J.-Y. Guo, B. Shi, M.-Y. Sun, C.-C. Zhang, G.-Q. Wei, and J. Liu, "Characterization of an ORMOCER®-coated FBG sensor for relative humidity sensing," *Meas. J. Int. Meas. Confed.*, vol. 171, 2021, doi: 10.1016/j.measurement.2020.108851.

[222] K. Zhang, G. Schlottig, E. Mengotti, O. Quittard, and F. Iannuzzo, "Study of moisture transport in silicone gel for IGBT modules," *Microelectron. Reliab.*, vol. 114, no. May, p. 113773, 2020, doi: 10.1016/j.microrel.2020.113773.

[223] S. Fröhling *et al.*, "Verification of Hygrothermal Simulations Using Silicone Encapsulated Climate Sensors in Continuously Operated IGBT Power Modules," in *2023 11th International Conference on Power Electronics and ECCE Asia (ICPE 2023 - ECCE Asia)*, 2023, pp. 1361–1369. doi: 10.23919/ICPE2023-ECCEAsia54778.2023.10213687.

[224] A. V Mamishev, K. Sundara-Rajan, F. Yang, Y. Du, and M. Zahn, "Interdigital sensors and transducers," *Proc. IEEE*, vol. 92, no. 5, pp. 808–845, 2004, doi: 10.1109/JPROC.2004.826603.

[225] H. Farahani, R. Wagiran, and M. N. Hamidon, *Humidity sensors principle, mechanism, and fabrication technologies: A comprehensive review*, vol. 14, no. 5. 2014. doi: 10.3390/s140507881.

[226] G. González, E. S. Kolosovas-Machuca, E. López-Luna, H. Hernández-Arriaga, and F. J. González, "Design and fabrication of interdigital nanocapacitors coated with HfO2," *Sensors (Switzerland)*, vol. 15, no. 1, pp. 1998–2005, 2015, doi: 10.3390/s150101998.

[227] P. A. Kumar, N. B. Rao, P. Akhendra Kumar, N. Bheema Rao, P. A. Kumar, and N. B. Rao, "Fractal spiral capacitor for wireless applications," *Electron. Lett.*, vol. 52, no. 6, pp. 481–483, 2016, doi: 10.1049/el.2015.3420.

[228] V. Zimmermann *et al.*, “Integration of Printed Electronics with Potted Power Electronic Modules,” in *CIPS 2020; 11th International Conference on Integrated Power Electronics Systems*, 2020, pp. 1–5.

[229] W. Chen, A. Berwald, A. Hauke, V. Zimmermann, C. F. Bayer, and M. P. M. Jank, “Integration of a humidity sensor with power electronic applications,” in *2022 IEEE Sensors*, 2022, pp. 1–4. doi: 10.1109/SENSORS52175.2022.9967313.

[230] A. Jamaluddin, U. Taufik, Y. Iriani, S. Budiawanti, and Suyitno, “Simple fabricating PCB-based inter digital capacitor for glucose biosensor,” *AIP Conf. Proc.*, vol. 1788, no. 1, p. 30092, Jan. 2017, doi: 10.1063/1.4968345.

[231] L. Urankar and P. Henninger, “Compact extended algorithms for elliptic integrals in electromagnetic field and potential computations. I. Elliptic integrals of the first and second kind with extended integration range,” *IEEE Trans. Magn.*, vol. 27, no. 5, pp. 4338–4342, 1991, doi: 10.1109/20.105059.

[232] H. Muzaffar and K. S. Williams, “Evaluation of Complete Elliptic Iintegrals of the First Kind at Singular Moduli,” *Taiwan. J. Math.*, vol. 10, no. 6, pp. 1633–1660, Dec. 2006, doi: 10.11650/twjm/1500404580.

[233] International Rectifier, “Application Note AN-983,” 2012.

[234] IEC, *60747-9:2019 - Semiconductor Devices - Part 9: Discrete devices - Insulated-gate bipolar transistors (IGBTs)*. 2019.

[235] Rohde & Schwarz, “Application Note - Tips & Tricks on Double Pulse Testing,” 2021.

[236] R. Lundin, “A handbook formula for the inductance of a single-layer circular coil,” *Proc. IEEE*, vol. 73, no. 9, pp. 1428–1429, 1985, doi: 10.1109/PROC.1985.13304.

[237] E. Husain and R. S. Nema, “Analysis of Paschen Curves for air, N2 and SF6 Using the Townsend Breakdown Equation,” *IEEE Trans. Electr. Insul.*, vol. EI-17, no. 4, pp. 350–353, 1982, doi: 10.1109/TEI.1982.298506.

[238] A. Rumi, J. G. Marinelli, D. Barater, A. Cavallini, and P. Seri, “The Challenges of Reliable Dielectrics in Modern Aerospace Applications: The Hazard of Corona Resistant Materials,” *IEEE Trans. Transp. Electrif.*, vol. 8, no. 4, pp. 4646–4653, 2022, doi: 10.1109/TTE.2022.3191064.

[239] U. Eduok, O. Faye, and J. Szpunar, “Recent developments and applications of protective silicone coatings: A review of PDMS functional materials,” *Prog. Org. coatings*, vol. 111, pp. 124–163, 2017, doi: 10.1016/j.porgcoat.2017.05.012.

[240] L. Niemeyer, “A generalized approach to partial discharge modeling,” *IEEE Trans. Dielectr. Electr. Insul.*, vol. 2, no. 4, pp. 510–528, 1995, doi: 10.1109/94.407017.

[241] I. Semenov, I. G. Folkestad, K. Niayesh, and L. Lundgaard, “Characterization of defects in aluminum nitride substrates through partial discharge measurements,” in *2022 IEEE 4th International Conference on Dielectrics (ICD)*, IEEE, 2022, pp. 380–384. doi: 10.1109/ICD53806.2022.9863543.

[242] C. F. Bayer, E. Baer, U. Waltrich, D. Malipaard, and A. Schletz, “Simulation of the electric field strength in the vicinity of metallization edges on dielectric substrates,” *IEEE Trans. Dielectr. Electr. Insul.*, vol. 22, no. 1, pp. 257–265, 2015, doi: 10.1109/TDEI.2014.004285.

[243] C. F. Bayer, U. Waltrich, R. Schneider, A. Soueidan, E. Baer, and A. Schletz, “Enhancing partial discharge inception voltage of DBCs by geometrical variations based on simulations of the electric field strength,” in *CIPS 2016; 9th International Conference on Integrated Power Electronics Systems*, 2016, pp. 1–5.

[244] S. Mukherjee, T. M. Evans, D. R. Huitink, and H. A. Mantooth, “A Partial Discharge Inception Voltage Modeling Approach,” *IEEE Open J. Power Electron.*, vol. 4, pp. 148–160, 2023, doi: 10.1109/OJPEL.2023.3241853.

[245] Y. L. Ogundiran, A. Griffo, S. Sundeep, and J. Wang, “A Novel Embedded Sensor for Partial Discharge Detection in Inverter-Fed Machines,” *IEEE Trans. Ind. Appl.*, vol. 58, no. 4, pp. 4698–4707, 2022, doi: 10.1109/TIA.2022.3177172.

[246] S. Sundeep *et al.*, “Detection of partial Discharge Activity in Thermally Aged SiC Inverter Fed Stator Winding Samples and Impact of Partial Discharges on their Lifetime,” in *IET Conference Proceedings*, 2022, pp. 271–277. doi: 10.1049/icp.2022.1062.

[247] J. Luomala and I. Hakala, “Effects of temperature and humidity on radio signal strength in outdoor wireless sensor networks,” in *2015 Federated Conference on Computer Science and Information Systems (FedCSIS)*, Polish Information Processing Society (PIPS), 2015, pp. 1247–1255. doi: 10.15439/2015F241.

[248] Y. Jinggang *et al.*, “Research on the correlation between UHF signal energy and discharge quantity of partial discharge,” in *2016 IEEE International Conference on High Voltage Engineering and Application (ICHVE)*, IEEE, 2016, pp. 1–4. doi: 10.1109/ICHVE.2016.7800798.

[249] X. Liu *et al.*, “Characteristics and Identification of Partial Discharge for Insulation Structures in High Voltage IGBT Modules Under Positive Square Wave Voltage,” *IEEE Trans. Power Electron.*, vol. 38, no. 4, pp. 5347–5359, 2023, doi: 10.1109/TPEL.2022.3232327.

[250] F.-C. Gu, H.-C. Chen, and M.-H. Chao, “Application of improved Hilbert-Huang transform to partial discharge signal analysis,” *IEEE Trans. Dielectr. Electr. Insul.*, vol. 25, no. 2, pp. 668–677, 2018, doi: 10.1109/TDEI.2017.006922.

[251] B. Chen, Y. Hu, L. Wu, and H. Li, “Partial Discharge Pulse Extraction and Interference Suppression Under Repetitive Pulse Excitation Using Time-Reassigned Multisynchrosqueezing Transform,” *IEEE Trans. Instrum. Meas.*, vol. 72, pp. 1–9, 2023, doi: 10.1109/TIM.2023.3325519.

[252] Y. Fu *et al.*, “A Partial Discharge Signal Separation Method Applicable for Various Sensors Based on Time–Frequency Feature Extraction of t-SNE,” *IEEE Trans. Instrum. Meas.*, vol. 73, pp. 1–9, 2024, doi: 10.1109/TIM.2023.3335527.

[253] A. H. Alshalawi and F. S. Al-Ismail, “Partial Discharge Detection Based on Ultrasound Using Optimized Deep Learning Approach,” *IEEE Access*, vol. 12, pp. 5151–5162, 2024, doi: 10.1109/ACCESS.2024.3350555.

[254] R. Ghosh, P. Seri, R. E. Hebner, and G. C. Montanari, “Noise Rejection and Detection of Partial Discharges under Repetitive Impulse Supply Voltage,” *IEEE Trans. Ind. Electron.*, vol. 67, no. 5, pp. 4144–4151, May 2020, doi: 10.1109/TIE.2019.2921281.

[255] P. Wang, Y. Li, A. Cavallini, J. Zhang, E. Xiang, and K. Wang, “The Influence of Relative Humidity on Partial Discharge and Endurance Features under Short Repetitive Impulsive Voltages,” in *Annual Report - Conference on Electrical Insulation and Dielectric Phenomena, CEIDP*, IEEE, Oct. 2018, pp. 506–509. doi: 10.1109/CEIDP.2018.8544905.

[256] V. T. A. Tho, J.-L. Augé, and O. Lesaint, “Partial discharges and light emission from ceramic substrates embedded in liquids and gels,” in *2011 IEEE International Conference on Dielectric Liquids*, 2011, pp. 1–4. doi: 10.1109/ICDL.2011.6015490.

[257] J. Li, Y. Liang, Y. Mei, S. Member, X. Tang, and G.-Q. Lu, “Packaging Design of 15 kV SiC Power Devices With High-Voltage Encapsulation,” *IEEE Trans. Dielectr. Electr. Insul.*, vol. 29, no. 1, pp. 47–53, 2022, doi: 10.1109/TDEI.2022.3146569.

[258] A. T. Vu Thi, J.-L. Augé, O. Lesaint, and M. T. Do, “Partial discharges in Aluminium nitrite ceramic substrates,” in *2010 10th IEEE International Conference on Solid Dielectrics*, 2010, pp. 1–4. doi: 10.1109/ICSD.2010.5568137.

[259] M. Sato, A. Kumada, K. Hidaka, K. Yamashiro, Y. Hayase, and T. Takano, “Surface discharges in silicone gel on AlN substrate,” *IEEE Trans. Dielectr. Electr. Insul.*, vol. 23, no. 1, pp. 494–500, 2016, doi: 10.1109/TDEI.2015.005412.

[260] M. Borghei and M. Ghassemi, “Characterization of Partial Discharge Activities in WBG Power Converters under Low-Pressure Condition,” *Energies (Basel)*, vol. 14, no. 17, p. 5394, 2021, doi: 10.3390/en14175394.

[261] I. Semenov, I. F. Gunheim, K. Niayesh, H. K. H. Meyer, and L. Lundgaard, “Investigation of Partial Discharges in AlN Substrates Under Fast Transient Voltages,” *IEEE Trans. Dielectr. Electr. Insul.*, vol. 29, no. 2, pp. 745–752, 2022, doi: 10.1109/TDEI.2022.3163812.

[262] H. Wang, G. Xiao, L. Wang, Y. Pei, F. Yan, and Q. Yang, “A Novel Approach to Partial Discharge Detection Under Repetitive Unipolar Impulsive Voltage,” *IEEE Trans. Ind. Electron.*, vol. 70, no. 11, pp. 11681–11691, 2023, doi: 10.1109/TIE.2022.3225830.

[263] Y. Ding, Y. Wang, and Y. Yin, “Effects of Rise Time and Pulse Width on Magnitude and Phase Distribution of the Partial Discharge in PowerModule Packaging Insulation under Square Pulse,” in *2023 IEEE 4th International Conference on Electrical Materials and Power Equipment (ICEMPE)*, 2023, pp. 1–4. doi: 10.1109/ICEMPE57831.2023.10139568.

[264] M. Xu and Z. Tan, “Calculation of townsend second ionization coefficient for photoemission at different humidities,” *IEEE Trans. Dielectr. Electr. Insul.*, vol. 21, no. 4, pp. 1764–1767, 2014, doi: 10.1109/TDEI.2014.004101.

[265] X. Li *et al.*, “A 10 kV SiC Power Module Stacked Substrate Design with Patterned Middle-layer for Partial Discharge Reduction,” in *2023 IEEE Applied Power Electronics Conference and Exposition (APEC)*, IEEE, 2023, pp. 344–349. doi: 10.1109/APEC43580.2023.10131485.